A SYSTEMS BIOLOGY APPROACH TO INVESTIGATE THE ROLE OF PEROXIREDOXINS IN RESPONSES TO HYDROGEN PEROXIDE

Lewis Elwood Tomalin

Thesis submitted in accordance with the regulations of Newcastle University for the degree of Doctor of Philosophy.

Institute for Cell and Molecular Biosciences

January 2015

Declaration

I certify that this thesis is my own work, except where stated, and has not been previously submitted for a degree or any other qualification at this or any other university.

Some of the work in this thesis has been presented in the following publications:

BROWN, J. D., DAY, A. M., TAYLOR, S. R., TOMALIN, L. E., MORGAN, B. A. & VEAL, E. A. 2013. A peroxiredoxin promotes H_2O_2 signaling and oxidative stress resistance by oxidizing a thioredoxin family protein. *Cell Rep,* 5**,** 1425-35.

VEAL, E. A., TOMALIN, L. E., MORGAN, B. A. & DAY, A. M. 2014. The fission yeast Schizosaccharomyces pombe as a model to understand how peroxiredoxins influence cell responses to hydrogen peroxide. *Biochem Soc Trans,* 42**,** 909-16.

Abstract

Maintenance of redox balance is essential for fundamental physiological processes, including growth, differentiation, migration, and circadian rhythms. However, the mechanisms by which cells maintain this balance and sense acute, dynamic redox changes under signalling and/or stress conditions are poorly defined. 2-cys peroxiredoxins (Prxs) are abundant, ubiquitous thioredoxin peroxidases with important roles in ageing and cancer. Counter-intuitively, Prxs are sensitive to hydrogen peroxide (H_2O_2)-induced inhibition of this peroxidase activity by hyperoxidation to a thioredoxin-resistant form. Prx hyperoxidation has been proposed to have various functions in signalling and protein homeostasis. However, the circumstances which cause Prx to become hyperoxidized *in vivo* remain unclear. The fission yeast *Schizosaccharomyces pombe* contains a single, well-studied 2-Cys Prx with important roles in responses to H_2O_2. Using quantitative *in vivo* and *in vitro* kinetic data, multiple mathematical models have been developed to investigate when the *S. pombe* peroxiredoxin Tpx1 becomes hyperoxidised *in vivo*. This approach suggested that Prx hyperoxidation occurs when the peroxide-buffering capacity of a cell becomes saturated. This was confirmed experimentally using both *S. pombe* and human cell lines, which suggested that the thiol-proteome is responsible for this peroxide buffering capacity. Accordingly, we propose that Prx hyperoxidation signals that the cells' antioxidant defences are overcome and that repair mechanisms need to be deployed to limit damage and restore homeostasis.

We have also used an integrated modelling and experimental approach to investigate the roles of Tpx1 in promoting the H_2O_2-induced oxidation (activation) of the AP-1-like transcription factor Pap1. This has revealed that Tpx1 has 2 roles, participating as a direct H_2O_2-transducer to initiate Pap1 oxidation and also by competitively inhibiting the thioredoxin-like protein Txl1 from reducing Pap1.

Finally, we use a simple computer model representing multiple cellular peroxidase processes to demonstrate that changes in gene expression in response to H_2O_2 limit H_2O_2-induced damage by improving the cells' ability to inhibit increases in intracellular H_2O_2 concentration. Together this work has provided new insights into the cellular mechanisms responsible for the regulation of cellular responses to H_2O_2.

ACKNOWLEDGMENTS

Firstly, I would like to thank my supervisors Dr Elizabeth Veal and Dr Daryl Shanley for their guidance, support and positivity towards this project. I would like to thank all the members of the Morgan (BAM), Whitehall (SKW) and Quinn (JQ) labs, past and present for their good banter and moral support, along with the accompanying cake and booze. I would also like to thank all members of the Systems Biology group (CISBAN), for helping me to develop my computer modelling skills. In particular I would like to thank Dr Anze Zupanic, Dr Graham Smith, Dr Piero Dalle Pezze and Dr Daryl Shanley. An extra special thank you needs to go to Dr Alison Day and Dr Jonathon Brown, without their advice and patience this PhD project would not have been possible.

I would also like to thank Dr Babis Rallis and Prof Jürg Bähler for the data they provided, Prof Chris Chang and Prof Bryan Dickinson for providing the fluorescent dye PF3 and Miss Waseema Patel for her help with the human cell culture experiments. I would also like to express my gratitude to Prof Brian Morgan and Dr John Rand for providing the Tpx1^{T86E} strain.

A final thanks needs to go to our lab technician Michelle Wray. Thanks to her hard work and diligence there was an infinite supply of agar, YE5S and EMM, without which this project would not have been possible.

This project was supported by a student bursary awarded by the Biotechnology and Biological Sciences Research Council (BBSRC).

List of Abbreviations

AhpC – Alkylhydroperoxidase

AIC – Akaiki information criterion

AMS – 4 acetamido – 4' – ((iodoacetyl) amino) stilbene – 2 2'-disulfonic acid

AP-1 – Activating protein 1

ARE – Antioxidant response element

Arg – Arginine

ASK1 – Apoptosis signal-regulating kinase

ATP – Adenosine Triphosphate

BCA – Bicinchoninic acid assay

β-ME – β-mercaptoethanol

b-Zip – Basic leucine zipper

c-CRD – C-terminal cysteine rich domain

C. elegans – *Caenorhabditis elegans*

CO_2 – Carbon Dioxide

cGpx – Classical glutathione peroxidase

CRD – Cysteine rich domain

Cu^+ – Copper ion (1+ charge)

Cu/ZnSODs – Copper/Zinc containing superoxide dismutase

Cys – Cysteine

Cys_P – Peroxidatic cysteine

Cys_P-SOH – Peroxidatic cysteine with a sulphenic acid

Cys_R – Resolving cysteine

Cys-S$^-$ – Thiolate anion

Cys-SH – Cysteine protein thiol

Cys-SOH – Cysteine with a sulphenic acid

Cys-SOOH – Cysteine with a sulphinic acid

DCFDA – 2',7'-dichlorodihydrofluorescein diacetate

DIC – Differential Interference contrast microscopy

DMEM – Dulbecco's Modified Eagles Medium

DMSO – Dimethyl sulphoxide

DNA – Deoxyribonucleic acid

DPBS – Dulbecco's phosphate buffered saline

E. coli – *Escherichia coli*

EDTA – Ethylenediaminetetraacetic acid

EGF – Epidermal growth factor

EMM – Edinburgh minimal media

ER – Endoplasmic reticulum

FCS – Foetal calf serum

Fe^{2+} – Iron ions (2+ charge)

Fe-S – Iron bound to sulphur (inside a protein)

FeSOD – Iron containing superoxide dismutase

GAPDH – Glyceraldehyde 3-phosphate dehydrogenase

Gly – Glycine

Gpx – Glutathione peroxidase

GR – Glutathione reductase

Grx – Glutaredoxin

$GS^{\cdot}$ – thiyl radical

GSH – Reduced Glutathione

GSSG – oxidised glutathione

GST – glutathione-S-transferases

H_2O_2 – Hydrogen peroxide

HCl – Hydrochloric acid

HEK293 – Human Embryonic Kidney cells (293)

His – Histidine

HRP – Horse Radish Peroxidase

IAA – Iodoacetamide

IGEPAL – Octylphenoxypolyethoxyethanol

IGF-1 – Insulin-like growth factor

kDa – Kilo-Daltons

LiAc – Lithium Acetate

LSODA – Livermore Solver for Ordinary Differential Equations

MAPK – Mitogen activated protein kinase

MAPKK – Mitogen activated protein kinase kinase

MAPKKK – Mitogen activated protein kinase kinase kinase

Mg^{2+} – Magnesium ion (2+ charge)

MnSOD – Manganese superoxide dismutase

MsrA – Methionine-sulphoxide reductase

NaCl – Sodium Chloride

NADPH – Nicotinamide adenine dinucleotide phosphate

NADH – Nicotinamide adenine dinucleotide

n-CRD – N-terminal cysteine-rich domain

NEM – N-ethylamide

NES – Nuclear export signal

NOX – NADPH oxidases

O_2^- – Superoxide

OD – Optical Density

OH· – Hydroxyl radical

OSR – Oxidative Stress Response

PBS – Phosphate buffered saline

PEG – Polyethylene glycol

PF3 – Peroxoflour-3

Phe – Phenylalanine

PHGpx – phospholipid hydroperoxide Gpx

PLB – Protein Lysis Buffer

PMSF – phenylmethanesulfonyl flouride

Prx – Peroxiredoxin

PSH – Protein Thiol

PSS – Protein disulphide

ROS – Reactive oxygen species

SAPK – Stress activated protein kinases

SBML – Systems biology markup language

S. cerevisiae – *Saccharomyces cerevisiae*

SDS – Sodium dodecyl sulfate

SDS-PAGE – SDS-Polyacrylamide gel electrophoresis

Ser – Serine

SOD – Superoxide dismutase

S. pombe – *Schizosaccharomyces pombe*

SSR – Sum of squared residuals

S. Typhimurium – *Salmonella Typhimurium*

Srx – Sulphiredoxin

TBST – Tris-buffered saline with Tween

TCA – Tri-chloro acetic acid

TNFα – Tumour Necrosis Factor *alpha*

Tpx1 – Thioredoxin Peroxidase

Tris – tris(hydroxymethyl)aminomethane)

Trr1 – Thioredoxin Reductase

Trx – Thioredoxin

TrxR – Thioredoxin Reductase

Tsa – Thiol-specific antioxidant

Txl1 – Thioredoxin-like protein

UV – Ultraviolet radiation

Yap1 – Yeast activating protein 1

Ybp1 – Yeast binding protein 1

Contents

List of Figures

Figure Title **Page**

List of Tables

Chapter 2. Materials and Methods

Chapter 3. Building a model of Tpx1 oxidation and hyperoxidation

Chapter 4. The regulation of Trx1 substrates by Tpx1

Chapter 1. Introduction

1.1 Reactive oxygen species in biological systems

The term reactive oxygen species (ROS) refers to a broad range of reactive molecules which are created from the reduction of oxygen. In biological systems ROS are produced as an unavoidable by-product of aerobic metabolism, as well as other processes. Although they vary in their reactivity, ROS can cause irreversible modifications to DNA, proteins and lipids, damaging these vital cellular components. As a result, cells of all kingdoms have evolved an array of cellular mechanisms to remove ROS and repair the damage they cause. Increased oxidative modifications to cellular components correlate with ageing and age-related disorders such as cancer and neurodegeneration. This has led to the idea that the manifestation of these disorders could be the result of the accumulation of oxidative damage with age. Due to the connection between oxidative damage and disease there has been great endeavour to understand how ROS are produced and the mechanisms which prevent and repair ROS-induced damage. This first section will outline current knowledge on the sources and properties of the most common and well-studied forms of ROS found in biological systems.

1.1.1 The superoxide anion

A broad and diverse range of ROS has been detected in biological systems, around 90% of which appear to originate from the production of the superoxide anion (O_2^-) (Reaction 1) in the mitochondria as a by-product of oxidative phosphorylation (Fridovich, 1986, Boveris and Chance, 1973, Chance et al., 1979, St-Pierre et al., 2002).

(Reaction 1) $\mathbf{O_2 + e^- \rightarrow O_2^-}$

Innate inefficiencies in the reactions involving complexes I, II & III (Figure 1.1) mean that some of the electrons flowing through these complexes can “leak” and react with molecular oxygen, which under physiological conditions results in 1-3% of the oxygen molecules in the mitochondria becoming reduced to superoxide

(Chen et al., 2003, Salvador et al., 2001, Hanukoglu et al., 1993). Although the mitochondria are a major site of superoxide production, inefficiencies in other oxidising processes also contribute. For example, the oxidation and hydroxylation of foreign compounds by the cytochrome P-450 enzymes can also leak electrons to molecular oxygen (Butler and Hoey, 1993). The rapid and indiscriminate reactivity of superoxide suggests that superoxide-induced damage is likely to be confined to the mitochondria. The damaging effects of superoxide are utilised by the immune system where the activation of NADPH oxidases (NOX) in macrophages produces a *respiratory burst* generating superoxide radicals to kill the engulfed bacteria (Segal and Shatwell, 1997). Other than at the site of production, damage caused by superoxide is thought to be relativly limited compared with other oxygen radicals due to its rapid dismutation to hydrogen peroxide (H_2O_2) (Reaction 2). This process can happen spontaneously but is accelerated 4-fold via the actions of the superoxide dismutases (SODs) (Winterbourn and Hampton, 2008).

(Reaction 2) $\mathbf{2O_2^- + 2H^+ \xrightarrow{SOD} H_2O_2 + O_2}$

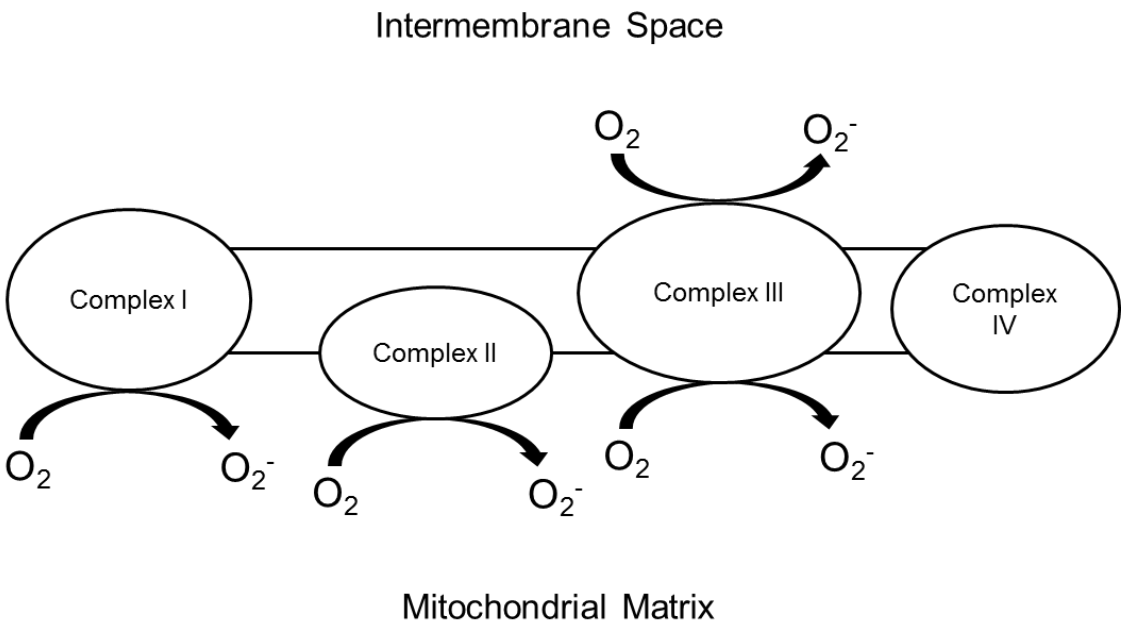

Figure 1.1: Diagram showing the formation of superoxide (O_2^-) due to electron leakage from the electron transport chain.

The diagram shows the four complexes of the electron transport chain (Complex I - IV). Complexes I, II & III are both able to leak electrons to molecular oxygen resulting in the formation of the superoxide anion in the mitochondrial matrix. Additionally, complex III can also leak electrons into the mitochondrial intermembrane space.

1.1.2 Hydrogen peroxide

H_2O_2 is not a free radical and is only selectively reactive. This allows it to diffuse further from the site of production. Its selective reactivity means that the propensity for the H_2O_2 to cause damage is limited to iron sulphur (Fe-S) containing proteins, and a sub-set of susceptible cysteine thiols (Cys-SH). Cysteine thiols normally have a high pKa of around 8.6, H_2O_2 reacts with the thiolate ($Cys\text{-}S^-$) form of the cysteine residue and therefore a microenvironment which lowers the pKa will cause a cysteine residue to be more sensitive to oxidation by H_2O_2. First order rate constants for the reaction of H_2O_2 with cysteine thiols have been shown to range from 20×10^{-6} to 20 $\mu M^{-1}s^{-1}$ (Peskin et al., 2013, Peskin et al., 2007, Winterbourn and Hampton, 2008, Rhee et al., 2012). The specificity of H_2O_2 for low pKa cysteine residues, as well as its relatively long half-life (10^{-3} s) and ability to pass through cellular membranes make H_2O_2 well-suited as a signalling molecule.

As well as its reactions with cysteine thiols, H_2O_2 is known to react with proteins containing reduced metal ions such as Fe^{2+} and Cu^+. These ions are able to reduce H_2O_2, a process referred to as the Fenton reaction (Reaction 3), resulting in the formation of the hydroxyl radical (OH·), which reacts indiscriminately with cellular components and has a much higher propensity to cause damage. Genetic perturbations which result in increased ROS production have been shown to increase damage to iron-containing proteins (Thierbach et al., 2005).

(Reaction 3) $Fe^{2+}/Cu^+ + H_2O_2 \rightarrow Fe^{3+}/Cu^{2+} + OH\cdot + OH^-$

1.1.3 The hydroxyl radical

The most common and extensively studied OH· induced oxidative modification is the oxidation of the nucleotide guanine to 8-oxo-7,8-dihydroguanine. This modification is regularly used as a biomarker for oxidative stress and indicates the potential for carcinogenesis to occur (Bruner et al., 2000). OH· is particularly damaging to lipids due to its ability to attack the –C=C– double bond in poly-unsaturated fatty acids, this forms -CH·- radical which then reacts with oxygen to form the peroxyl radical which can then react with the CH_2 of another poly unsaturated fatty acid and propagate this process. This can cause considerable

damage to cellular membranes (for review of ROS and cellular damage see Valko et al., 2004).

1.2 Role of ROS in ageing

The oxidative stress theory of ageing proposed by Denham Harman postulates that ageing is caused by the accumulation of ROS-induced damage to macromolecules which would ultimately impair cellular function and lead to ageing and age-related disease (Harman, 1956) (for review see (Bokov et al., 2004)). This ageing theory was later re-named the mitochondrial theory of ageing when it became apparent that the majority of ROS are produced by the mitochondria (Harman, 1972). It was believed that oxidative damage to the mitochondria would accumulate with age, and that the resulting damage would result in increased ROS production causing a vicious cycle of mitochondrial damage and ROS formation ultimately leading to cell death (Figure 1.2).

Although this neat and simplistic theory of ageing has now been replaced with more modern theories, the connection between mitochondrial ROS production and the healthy life span of an organism is well-established. Genetic interventions able to decrease ROS levels, particularly at the mitochondria, have been shown to have beneficial effects on lifespan in many organisms. For example, overexpression of MnSOD (Manganese-containing SOD, see 1.3.1) in *Saccharomyces cerevisiae* and in *Drosophila melanogaster* causes increased life span whilst deletion accelerates ageing (Longo et al., 1996, Longo et al., 1999, Sun et al., 2002). Furthermore, overexpression of mitochondrial catalase has been reported to delay age related phenotypes and increase lifespan in mice (Schriner et al., 2005),

Mutations of genes which effect insulin or insulin-like growth factor signalling (IGF-1-signalling) have been shown to extend lifespan. IGF-1 underlies the well-established, widely conserved link between caloric restriction and extended lifespan (Partridge and Gems, 2002, Guarente and Kenyon, 2000, Bishop and Guarente, 2007, Piper and Bartke, 2008). Studies in *Caenorhabditis elegans* show that long lived *daf-2* (an IGF-1-receptor homolog) mutants have increased expression of a number of antioxidant genes thus indicating that increased

resistance to oxidative stress may underlie the well-established link between IGF1-signalling and life span extension (Honda and Honda, 1999, Murphy et al., 2003). In mice, genetic perturbations which result in increased mitochondrial ROS production can result in increased oxidative damage, decreased life-span and increased tumour incidence, further demonstrating the link between mitochondrial ROS, ageing and disease (Thierbach et al., 2005, Lebovitz et al., 1996).

The evidence that increased mitochondrial ROS production can result in decreased life span supports the mitochondrial theory of ageing, however there are many examples that contradict this theory. For example, although overexpression of MnSOD has been shown to increase life-span in *S. cerevisiae* and in *D. melanogaster*, there are many examples where overexpression of MnSOD does not cause an extension of life span despite decreasing ROS production and ROS induced damage (Lebovitz et al., 1996, Li et al., 1995, Silva et al., 2005, Motoori et al., 2001, Jang et al., 2009). This has been demonstrated in *C. elegans* where manipulation of each of the five *C. elegans sod* genes had no effect on life-span (Doonan et al., 2008). Furthermore, none of the *C. elegans* sod genes were required for the *daf-2* mutant longevity.

Furthermore there is evidence that increased ROS production can have positive effects on lifespan. For example, in *C. elegans*, decreased glucose intake has been shown to increase mitochondrial activity resulting in an increase in ROS production. However, rather than having a detrimental effect, this increase in ROS appears to increase life-span (Schulz et al., 2007). Evidence such as this has led to the idea that, although high levels of ROS undoubtedly cause damage, low levels of ROS are actually beneficial to the cell. One explanation for the beneficial effects of ROS is a process called mitohormesis whereby exposure to low levels of ROS promotes long-term resistance to damage due to ROS-induced adaptive responses such as initiation of the unfolded protein response. For example, it was recently demonstrated in *C. elegans* that increased mitochondrial O_2^- production was required to trigger the expression of lifespan extension genes (Yang and Hekimi, 2010). It is therefore argued that the role of O_2^- in ageing may be a balance between pro-survival signalling and toxic damage to cellular components (Van Raamsdonk and Hekimi, 2012). (for reviews on mitohormesis see Ristow and Schmeisser, 2014 and Ristow and Zarse, 2010).

These studies suggest that the lifespan of an organism does not hinge entirely on ROS-induced damage, and that the way in which oxidative damage to cellular components influence the lifespan of an organism is still unclear. An interesting example of this, although somewhat of an anomaly, comes from the naked mole rat (*Heterocephalus glaber*). *H. glaber* has been shown to exhibit increased levels of oxidative damage to its cellular components, despite living much longer than other rodents of a similar size (Andziak et al., 2006). Although ROS and oxidative damage have both positive and negative roles in the lifespan and health of an organism, ageing is a most likely a complex interplay between oxidative stress and other factors. Antioxidant systems are complex and interconnected, if we are to understand the role of oxidative stress in ageing we will have to understand more about the structure and regulation of the antioxidant systems, rather than focus on individual enzymes alone.

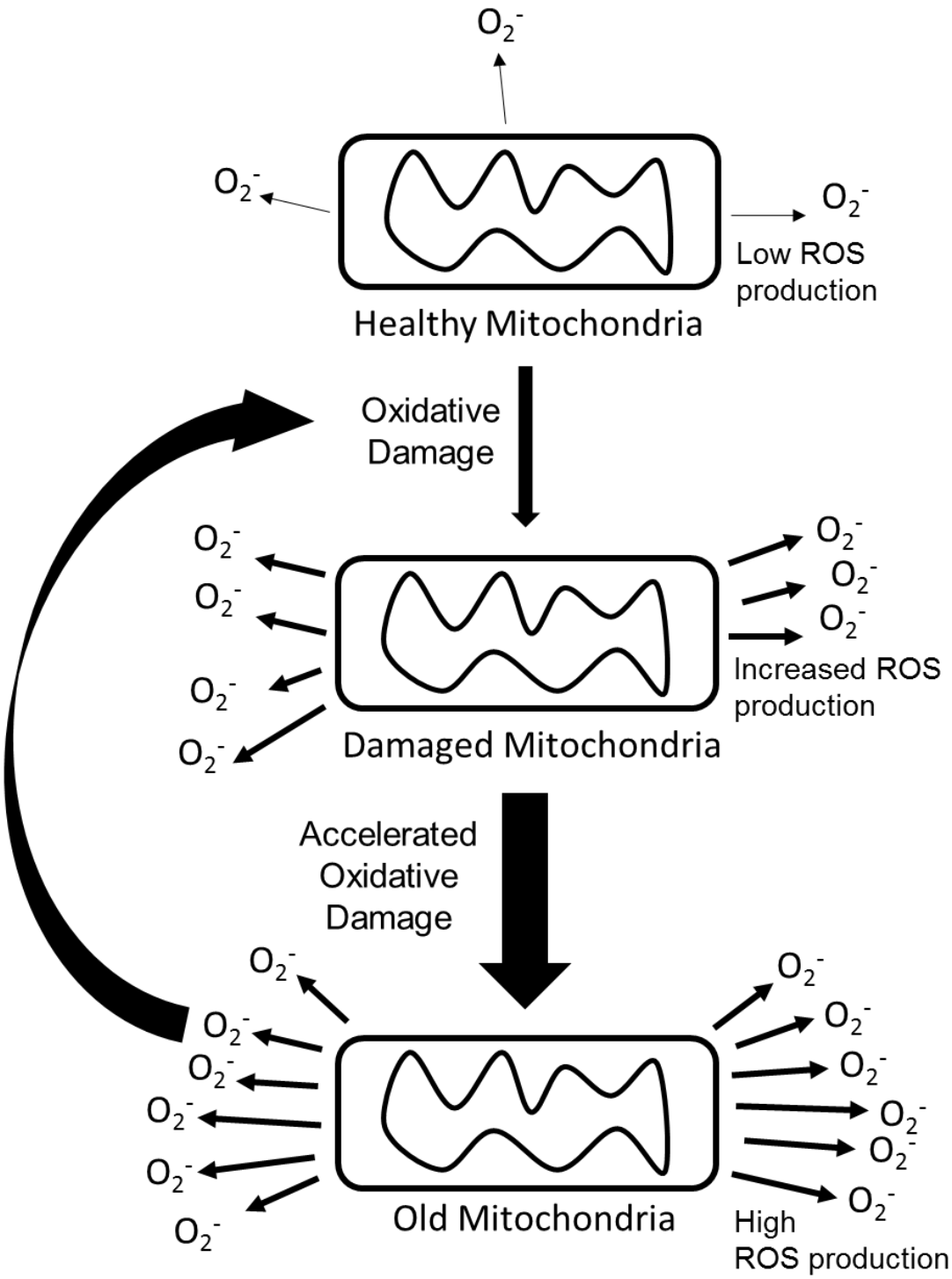

Figure 1.2: Diagram representing the mitochondrial theory of ageing

Reactive oxygen species produced by mitochondria will cause oxidative damage to mitochondrial proteins and DNA. Due to this damage, the mitochondria will produce more ROS which will accelerate the oxidative damage. This results in the accelerated formation of damaged mitochondria with age.

1.2.1 Positive roles for ROS

The evidence discussed above suggests that ROS can have positive effects on an organisms lifespan as well as detrimental damaging effects. Evidence that ROS can have pro-survival roles, as well as other positive functions, was demonstrated long before its implications in ageing were identified. An early example of this was in *E. coli* and *S. Typhimurium* where an initial low dose of H_2O_2 increased the resistance of these bacteria to a subsequent exposure of a lethal concentration of H_2O_2 (Christman et al., 1985, Demple and Halbrook, 1983). The same phenomena was also demonstrated in eukaryotes, initially in *S. cerevisiae* (Collinson and Dawes, 1992, Davies et al., 1995).

A well-established example of a positive role for ROS, not related to increased ROS-resistance, can be found in the immune system where the damaging effects of superoxide, produced by NADPH oxidases, are utilised by phagocytic cells to kill invading pathogens (Halliwell and Gutteridge, 1985, Droge, 2002). The NADPH oxidases are also present in non-immune cells where they produce an oxidative burst to initiate non-immune functions such as root growth in plants (Foreman et al., 2003) and cardiac differentiation in mammals (for a review see Veal and Day, 2011). H_2O_2 produced by the mitochondria have also been demonstrated to promote and inhibit a number of different signalling pathways (Fay et al., 2006, DeYulia and Carcamo, 2005, DeYulia et al., 2005, Ali et al., 2006, Chiarugi et al., 2003).

1.3 Antioxidant enzymes

The utilisation of ROS as a signalling molecule, but at high levels for the destruction of pathogens, make it imperative that cells control the local concentrations of ROS. Intracellular concentrations of ROS in the cell need to be controlled in such a way as to prevent damage to cellular components whilst also allowing the utilisation of healthy signalling responses. This control is achieved by a number of processes, including the removal of ROS by antioxidant enzymes, the expression of which is upregulated in response to H_2O_2. Understanding how this control is achieved will provide further insights into the complex relationship between ROS, ageing and disease.

1.3.1 Superoxide dismutase

O_2^- produced in the mitochondria or by NADPH oxidases is effectively the primary source of the majority of biological ROS (St-Pierre et al., 2002). It is therefore not surprising that prokaryotes and eukaryotes have evolved the superoxide dismutases (SODs) family of enzymes which reduce O_2^- to H_2O_2 and water (Xiang et al., 2014). This role in removing O_2^- makes SODs the first line of defence in minimising ROS-induced damage at the site of production. The SODs can be subdivided based on the identity of the ionic metal cofactor associated with the enzymes catalytic centre: iron SODs (FeSODs) are found in prokaryotes, protists and plants, copper/zinc SODs (Cu/ZnSODs) found in bacteria and the cytosol of eukaryotes and manganese SODs (MnSODs) found in prokaryotes and the mitochondrial matrix of eukaryotes. The role of the SODs in controlling ROS levels appears primarily to convert O_2^- into the less reactive H_2O_2 (for a review see Valko et al., 2006).

1.3.2 Catalase

There are a vast array of different peroxidase enzymes found within the cell of which the heme-peroxidases more commonly known as catalases are the best characterised (Zamocky et al., 2008a, Zamocky et al., 2008b, Goblirsch et al., 2011). Catalases are widely conserved and are able to convert two molecules of H_2O_2 to water and oxygen via a two-step mechanism involving the oxidation and reduction of iron (Reactions 4 & 5).

$$\text{(Reaction 4) } Fe(III) + H_2O_2 \rightarrow Fe(IV)=O + H_2O$$

$$\text{(Reaction 5) } Fe(IV)=O + H_2O_2 \rightarrow Fe(III) + H_2O + O_2$$

The reactions of catalase are very fast with apparent k_{cat} values ranging 54,000 - 833,000 s^{-1} and K_m values between 38 – 600 mM (Chelikani et al., 2004).

In mammalian cells the catalases appear to be largely localised in the peroxisomes and to a lesser extent in the mitochondrial matrix. However this is not the case for all organisms (Chaudière and Ferrari-Iliou, 1999). For example *S. pombe* catalase has been reported to be present predominantly in the cytoplasm and nucleus (Chaudière and Ferrari-Iliou, 1999, Matsuyama et al.,

2006). A broad range of human medical disorders have been attributed to catalase deficiency (for a review see Zamocky et al., 2008a). For example the genetic disease generally known as acatalasemia (Ogata, 1991) is characterised by having decreased overall catalase activity and results in the clinical problems such as oral gangrene and increased cancer incidence in adulthood (Goth et al., 2004). There is also evidence in mice that overexpression of catalase interferes with wound healing and tissue remodelling (Sen and Roy, 2008).

1.3.3 Thiol-peroxidases

Thiol-peroxidases do not utilise metal ions for their catalytic activity, but instead utilise the reversible oxidation of a redox-sensitive cysteine thiol, referred to as the peroxidatic cysteine (Cys_P) (reaction 6). The proximity of basic amino acids in the protein tertiary structure lowers the pKa of the Cys_P causing it to become sensitive to oxidation by H_2O_2 (Choi et al., 1998, Nagy et al., 2011). The resulting cysteine sulphenic acid (Cys_P-SOH), then condenses with a second cysteine, referred to as the resolving cysteine (Cys_R) to form an inter-molecular or an intra-molecular disulphide bond (reaction 7) (Chae et al., 1994a, Chae et al., 1994b, Chae et al., 1994c).

(Reaction 6) $Cys\text{-}SH + H_2O_2 \rightarrow Cys\text{-}SOH + H_2O$

(Reaction 7) $Cys\text{-}SOH + Cys\text{-}SH \rightarrow Cys\text{-}S\text{-}S\text{-}Cys + H_2O$

Two main thiol-based peroxidase families have been identified, the glutathione peroxidases (Gpxs) and the peroxiredoxins (Prxs). The Gpxs and Prxs both contain cysteine residues which are sensitive to oxidation by H_2O_2 and subsequently form disulphide bonds. However these two enzyme families are distinguished by the disulphide reductases responsible for the reduction of the resulting disulphide bond. The H_2O_2-induced disulphide in the Prxs is reduced by a protein called Thioredoxin (Trx), although it has been shown that *S. cerevisiae* Gpx3 can also be reduced by Trx (Delaunay et al., 2002). The Trxs are a family of small proteins (~11 kDa) able to reduce disulphide bonds in proteins, including the peroxiredoxins. This process results in the formation of a disulphide bond in Trx which is reduced by a thioredoxin reductase (TrxR) using electrons from NADPH. Trx and TrxR are collectively referred to as the thioredoxin system and

are responsible for the reduction of disulphide bonds in a broad range of substrates involved in many cellular processes (reviewed in Holmgren and Lu, 2010). The prokaryotic peroxiredoxin AhpC does not use Trx as a reducing agent and instead the protein AhpF is responsible via a mechanism which can use either NADH or NADPH (Poole, 1996). There are however examples of prokaryotic Prxs that utilise the thioredoxin system in their catalytic mechanism (Baker and Poole, 2003).

1.3.3.1 Glutathione

The H_2O_2-induced disulphide bond in Gpx enzymes is reduced by the tri-peptide glutathione (GSH) thus recycling the Gpx protein. GSH is a tripeptide of glutamate, cysteine and glycine (γ-L-glutamyl-L-cystinylglycine) which itself also acts as a free radical scavenger. The cysteine thiol of GSH can be oxidised to a thiyl radical ($GS^{\cdot}$) which then forms a disulphide with another GSH to make an oxidised glutathione dimer (GSSG) which is recycled by the glutathione reductases (GR) (Hayes and McLellan, 1999). In higher eukaryotes Gpx can be divided into two distinct forms, the classical Gpx (cGpx), which are soluble and tetrameric, and the phospholipid hydroperoxide Gpx (PHGpx) which are monomeric and partly membrane-bound. PHGpx is responsible for the protection of membranes against lipid peroxidation and the repair of oxidative damage to membranes (Avery and Avery, 2001). In *S. cerevisiae* Gpx1, Gpx2 and Gpx3 have been shown to be required for protection against H_2O_2 and lipid peroxidation (Inoue et al., 1999, Avery and Avery, 2001).

GSH is involved in phase-II detoxification and can be conjugated to toxic metabolites of xenobiotics via the action of glutathione-S-transferases (GST) (O'Brien and Tew, 1996). The actions of GST can also conjugate GSH to protein thiols (-SH) resulting in the formation of mixed glutathione protein disulphides, this is thought to protect proteins from damaging oxidation events (Grant, 2001). GSH is also a cofactor in the reduction of protein disulphides by the glutaredoxins (Grx). Grx are able to reduce protein disulphides, such as those in ribonucleotide reductase and are also able to reduce glutathione disulphides with other proteins (Lillig et al., 2008, Wheeler and Grant, 2004). In *S. cerevisiae* two Grx proteins

have been shown to be important for resistance to oxidative stress (Collinson et al., 2002, Wheeler and Grant, 2004).

1.3.3.2 The peroxiredoxins

The peroxiredoxins are further divided into three distinct subfamilies, characterised by differences in their catalytic mechanisms (Figure 1.3) (for review see Rhee and Woo 2012). The typical 2-Cys peroxiredoxins form homodimers in response to H_2O_2 via an intermolecular disulphide bond between two Prx monomers. The atypical 2-Cys Prxs are less common and form an intramolecular disulphide bond in response to H_2O_2. The final Prx subfamily is the 1-Cys Prxs which form a free Cys-SOH at their Cys_P in response to H_2O_2.

Prx and Gpx genes are conserved in prokaryotes and eukaryotes although their contribution to oxidative stress resistance varies between organisms (Missall et al., 2005, Navrot et al., 2006, Mariotti et al., 2012). In the budding yeast *S. cerevisiae* deletion of the typical 2-Cys peroxiredoxin Tsa1 results in sensitivity to a range of hydroperoxides and deletion of all five *S. cerevisiae* peroxiredoxins caused genomic instability as well as sensitivity to oxidative stress (Wong et al., 2004, Park et al., 2000). A second 2-Cys peroxiredoxin, Tsa2, is proposed to act synergistically with Tsa1 to confer resistance to oxidative stress (Wong et al., 2002). Deletion of either of the *S. cerevisiae* glutathione peroxidases Gpx1 and Gpx2 does not cause any obvious stress-sensitivity phenotypes although deletion of Gpx3 does cause hypersensitivity to peroxide (Inoue et al., 1999). However, the role of Gpx3 in resistance to peroxide is most likely due to its role in the activation of the stress response transcription factor Yap1 (Delaunay et al., 2002) Similarly to Tsa1, deletion of Tpx1, the only typical 2-Cys Prx found in the fission yeast *S. pombe*, also increases sensitivity to a range of hydroperoxides, whilst over expression increases resistance (Veal et al., 2004, Bozonet et al., 2005). In comparison, deletion of the *S. pombe* glutathione peroxidase Gpx1 causes only a very small decrease in resistance to oxidative stress (Paulo et al., 2014). It would appear that, with the exception of Gpx3, that the peroxiredoxins play a much more important role in resistance to oxidative stress than the glutathione peroxidases in these two divergent yeast species.

In mammalian cells six Prx isoforms have been identified. Prx1, Prx2 and Prx3 are identified as being thiol-dependent peroxidases (Chae et al., 1999). All three of these proteins are considered to be typical 2-Cys peroxiredoxins with similar catalytic efficiencies, but do differ in their cellular location. Prx1 is found predominantly in the cytoplasm and nucleus, Prx2 is also found in the cytoplasm, whilst Prx3 is targeted to the mitochondria (Chae et al., 1999). Prx4, also a typical 2-Cys peroxiredoxin, is found in the endoplasmic reticulum (ER) to be excreted from cells (Haridas et al., 1998). Prx5 is an atypical 2-Cys peroxiredoxin, and Prx6 is a 1-Cys peroxiredoxin. Peroxiredoxin expression has been demonstrated to be increased in a range of carcinomas (Jarvela et al., 2010, Karihtala et al., 2003) (for a review see Rhee and Woo, 2011).

An interesting feature of the eukaryotic typical 2-Cys peroxiredoxins is the susceptibility of the Cys-SOH sulphenic acid intermediate to hyperoxidation, by H_2O_2, to create a sulphinic acid (Cys-SOOH), this results in the loss of the thioredoxin peroxidase activity of the Prx (Yang et al., 2002). With the exception of cyanobacteria, helicobacter and *vibrio vulnificus*, sensitivity to hyperoxidation has evolved specifically in the eukaryotic peroxiredoxins. Bacterial 2-Cys peroxiredoxins, such as the *E. coli* peroxiredoxin AhpC, are much less sensitive to hyperoxidation (Wood et al., 2003b, Pascual et al., 2010). Conserved YF and GG(L/V/I)G amino acid motifs found in all hyperoxidation-sensitive Prx are responsible for this sensitivity (Wood et al., 2003b, Pascual et al., 2010, Koo et al., 2002). It is proposed that these amino acid motifs impede the disulphide formation between the Cys_P-SOH and the Cys_R-SH thus stabilising the Cys_P-SOH and making it more susceptible to further oxidisation by a second H_2O_2 molecule and form the hyperoxidised Cys_P-SOOH. The hyperoxidised form of Prx has no peroxidase activity and cannot be reduced by Trx. However, instead it is reduced by an enzyme called sulphiredoxin (Srx) (Biteau et al., 2003).

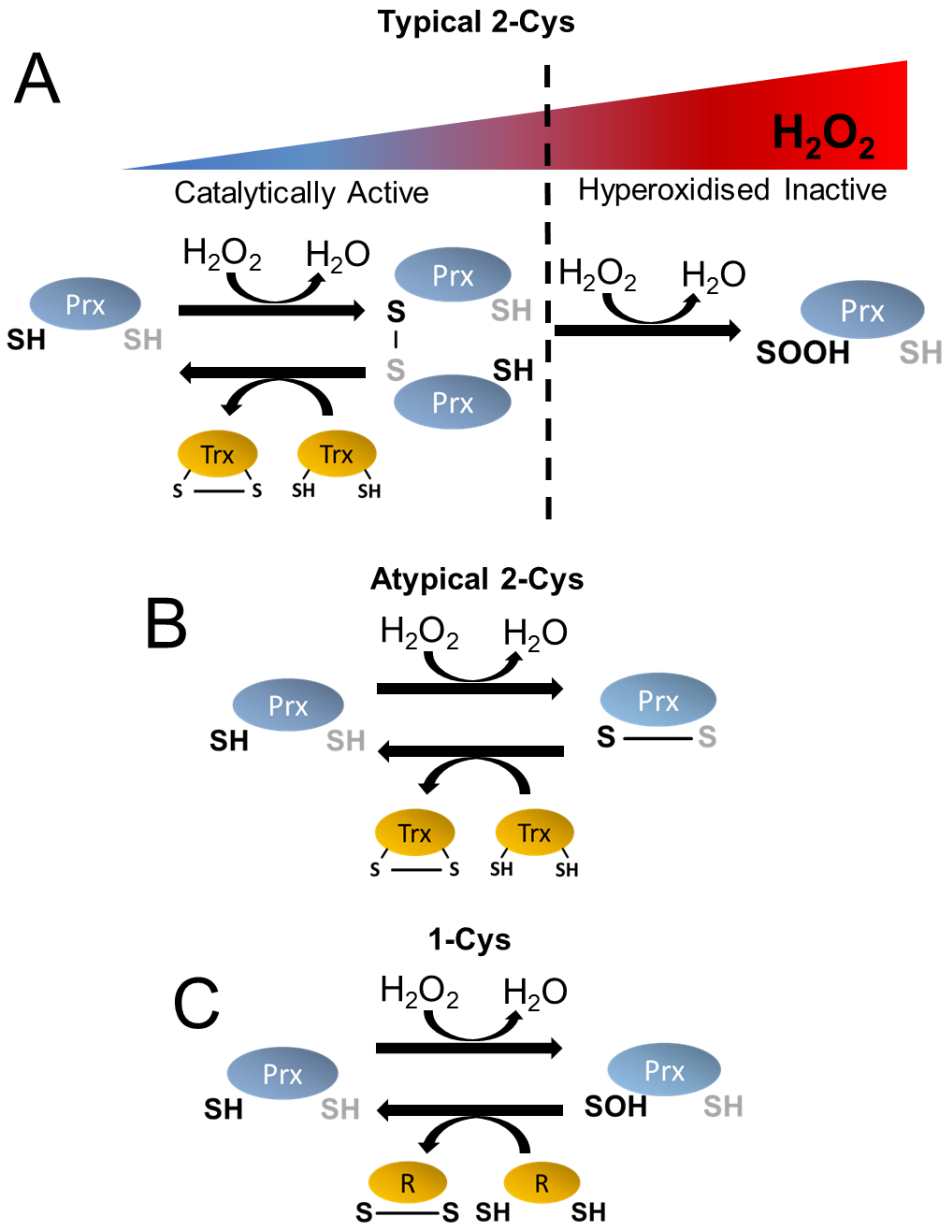

Figure 1.3: Diagrams showing the catalytic cycle for typical 2-Cys Prx, atypical 2-Cys Prx and 1-Cys Prx.

(A) The peroxidatic cysteine (black) of typical 2-Cys peroxiredoxins becomes oxidised by H_2O_2 to form a sulphenic acid. This sulphenic acid then condenses with the resolving cysteine (grey) of another peroxiredoxin molecule to form a disulphide-linked Prx homodimer. The disulphide bond in these homodimers is reduced by a protein called thioredoxin (Trx) which is oxidised by this process. At high concentrations of H_2O_2 the peroxidatic cysteine in eukaryotic typical 2-cys Prxs is susceptible to hyperoxidation to form a sulphinic acid (SOOH). (B) Atypical 2-cys peroxiredoxins form an intramolecular disulphide bond in response to H_2O_2, which is reduced by Trx. (C) 1-Cys peroxiredoxins do not form disulphide bonds, instead the H_2O_2-induced sulphenic acid (SOH) is reduced directly by a thiol-reductase although the identity of this thiol-reductase is not known.

1.3.4 Sulphiredoxin

Sulphiredoxin (Srx) was initially identified in *S. cerevisiae* as a protein showing dramatically increased expression in response to high levels of H_2O_2, whilst deletion of Srx increased sensitivity to H_2O_2 (Biteau et al., 2003). The ability of Srx to protect against oxidative stress is due to its ability to reduce sulphinic peroxiredoxins Prx-SOOH, via a mechanism which requires Trx, ATP and Mg^{2+} and thus restores the peroxidase activity of these enzymes (Biteau et al., 2003). Most organisms containing hyperoxidation-sensitive Prxs have been shown to have Srx genes, including other fungi, such as *S. pombe*, as well as animals and plants (Biteau et al., 2003, Chang et al., 2004, Bozonet et al., 2005, Basu and Koonin, 2005, Liu et al., 2006). The bacterial DNA-binding protein ParB was shown to have most homology to Srx, but has no sulphinic acid reductase activity, suggesting that eukaryotic Srx evolved from these bacterial proteins (Basu and Koonin, 2005). Over expression of Srx1 in *S. cerevisiae* has been shown to increase life span in a Tsa1-dependent manner and that this increase in life span correlated with reduced accumulation of sulphinic Tsa1 in older cells (Molin et al., 2011).

All eukaryotic Srx proteins have similar homology and all contain a conserved catalytic cysteine (Cys-99 in human Srx) essential for the reduction of Prx-SOOH as well as a conserved conserved Phe-Gly/Ser-Gly-Cys-His-Arg motif thought to be involved in the binding of ATP (Biteau et al., 2003, Basu and Koonin, 2005, Jönsson et al., 2005, Liu et al., 2006, Chang et al., 2004). Some differences in the sequence homology of Srx proteins from different kingdoms, particularly in the N-termini of the proteins has been found, however these differences are not believed to effect the catalytic activity of Srx and in plants have been shown to be responsible for the targeting of Srx to the chloroplast (Chang et al., 2004, Jönsson et al., 2005, Lee et al., 2006, Liu et al., 2006). The reduction of Cys-SOOH by Srx appears to be specific for typical 2-Cys peroxiredoxins and not the atypical 2-Cys or 1-Cys peroxiredoxins or Cys-SOOH found in GAPDH (Woo et al., 2005).

The catalytic mechanism for the reduction of Prx-SOOH by Srx is well characterised, initially Srx binds to a region in the C-terminus of Prx via a hydrophobic groove in Srx, Srx binds to reduced and hyperoxidised Prx to an equal extent and binding is independent of the Srx active site Cys-99 (Chang et al., 2004, Woo et al., 2005, Jonsson et al., 2008). Due to the requirement of ATP

and Mg^{2+} it was suggested that the formation of a sulphinic phosphoryl ester would be a likely reaction intermediate for the reduction of Prx-SOOH by Srx and that this mechanism would be common to both yeast and mammalian Srx (Biteau et al., 2003, Chang et al., 2004). A unique nucleotide binding motif in Srx is thought to stabilise the α & β phosphates of ATP and place the ATP molecule in an ideal position for the formation of a sulphinic phosphoryl ester with Prx (Jönsson et al., 2005). The formation of this sulphinic phosphoryl ester is facilitated by the initial phosphorylation of the Srx active site Cys-99 by ATP with the site of ATP cleavage between the β & γ phosphate and is dependent on Asp187 in Prx1 (Jeong et al., 2006, Lee et al., 2006, Jönsson et al., 2005). A crystal structure for hSrx in a complex with PrxI, ATP and Mg^{2+} suggests that binding of Srx causes structural rearrangements to the active site of PrxI moving the Prx-Cys_P closer to the γ-phosphate of ATP bound to Srx (Jönsson et al., 2009).

1.4 Adaptive responses to H_2O_2

Transcription factors which are activated in response to increased ROS have been identified in prokaryotes and eukaryotes (for reviews see Storz and Tartaglia, 1992, Jamieson, 1998, Faulkner and Helmann, 2011). Some of these transcription factors are responsible for the increased expression of antioxidant and repair genes. These transcriptionally regulated adaptive responses are referred to as the oxidative stress response (OSR). The OSR is regulated by a number of conserved stress response signalling pathways.

One of the first and simplest examples of a transcriptionally regulated OSR was identified in *E. coli* and *S. Typhimurium* (for a review see Storz and Tartaglia, 1992). The transcription factor OxyR contains a cysteine residue which is directly oxidised by ROS, OxyR activation then causes the induction of antioxidant genes, including those for catalase and the bacterial peroxiredoxin AhpC. Exposure to a sub-lethal concentration of H_2O_2 causes increased expression of these genes enabling the cell to survive a subsequent higher dose that would be lethal in non-pre-treated cells (Demple and Halbrook, 1983, Christman et al., 1985). There has been great interest in the mechanisms responsible for the induction of the OSR in eukaryotes. Much of this work has been done in the genetically amenable yeast

species *S. cerevisiae* and *S. pombe*. The identification of conserved OSR regulation mechanisms in these two evolutionary divergent organisms is a strong indication that these mechanisms are conserved in other eukaryotes.

1.4.1 Yap1

Transcriptional responses to oxidative stress have been extensively studied in the budding yeast *S. cerevisiae* and are dependent on the stress response transcription factor Yap1 (Schnell et al., 1992). Yap1 was first identified as an *S. cerevisiae* jun family b-Zip transcription factor able to bind to the TGACTCA sequence element which is common to the binding sites of the human transcription factor AP-1 (activating protein-1), hence Yap1 stands for yeast activating protein-1 (Moye-Rowley et al., 1989) (for review of b-Zip transcription factors see Vinson et al., 2006, Vinson et al., 2002). Early studies demonstrated the requirement of Yap1 for the increased expression of antioxidant genes as well as pleiotropic drug resistance (Schnell and Entian, 1991, Schnell et al., 1992, Wu et al., 1993). It is now established that the expression of the full set of Yap1-regulated genes requires the interaction of Yap1 with the response regulator Skn7. Yap1 and Skn7 are both required for the oxidative stress-induced expression of ~179 genes including TRX2, TRR1, TSA1 and CTT1 (Morgan et al., 1997, He and Fassler, 2005, He et al., 2009, Mulford and Fassler, 2011, Kuge and Jones, 1994, Wu and Moye-Rowley, 1994, Stephen et al., 1995, Grant et al., 1996). Exposure of *S. cerevisiae* cells to H_2O_2 results in the relocation of Yap1 from the cytoplasm to the nucleus and is dependent on three conserved cysteine residues in a cysteine rich domain (CRD) located near the C-terminal (c-CRD) of Yap1 (Kuge et al., 1997, Takeuchi et al., 1997). This region contains a nuclear export signal (NES) recognised by the nuclear exporter Crm1. The interaction between Yap1 and Crm1 is inhibited by a change in the conformational state of the c-CRD due to the formation of H_2O_2-induced disulphide bonds (Yan et al., 1998, Gulshan et al., 2005). In total Yap1 contains six cysteine residues, C303, C310 and C315 are found in an N-terminal CRD (n-CRD), whilst C598, C620 and C629 and located in the c-CRD (Figure 1.4). The induction of Yap1 disulphide bonds in response to H_2O_2 involves multiple steps. The first oxidation event is a disulphide between C310 and C315 although this does not appear to cause

nuclear accumulation of Yap1 (Okazaki et al., 2007). The second oxidation event is the formation of a disulphide bond between C303 and C598, this form of Yap1 is partially located in the nucleus (Okazaki et al., 2007, Wood et al., 2003a). Thirdly, a disulphide bond rearrangement occurs with the C310-C315 disulphide bond breaking and a new disulphide forms between C310 and C629. Finally a third disulphide bond is formed between C315 and C620. Both of these oxidised forms of Yap1 are equally nuclear and resistant to reduction (Okazaki et al., 2007, Wood et al., 2003a, Tachibana et al., 2009). Intriguingly this pattern of oxidation appears to be specific to H_2O_2-induced activation, as other Yap1 activators, such as diamide, only require the c-CRD for Yap1 nuclear localisation and Yap1-dependent gene expression (Kuge et al., 2001, Coleman et al., 1999, Azevedo et al., 2003). The nuclear import of Yap1 is mediated by a direct interaction with the protein Pse1, however this process appears to be unaffected by oxidative stress (Isoyama et al., 2001). Yap1 is therefore the first eukaryotic transcription factor discovered to be activated by the oxidation of redox sensitive cysteine residues in response to H_2O_2, similar to the *E. coli* transcription factor OxyR.

However, unlike OxyR the initial oxidation of Yap1 requires an additional H_2O_2 sensor to transduce the signal & initiate the oxidation process. Depending on the strain background, the glutathione peroxidase Gpx3 or the peroxiredoxin Tsa1 are required for the H_2O_2 induced activation of Yap1 (Delaunay et al., 2002, Veal et al., 2003, Ross et al., 2000, Okazaki et al., 2005, Tachibana et al., 2009). Upon exposure to H_2O_2 the peroxidatic cysteine in Gpx3, Cys-36, forms a sulphenic acid intermediate (Cys38-SOH) which forms a disulphide with Cys-598 in Yap1. This disulphide is then resolved to form the C303-C598 disulphide leading to Yap1 nuclear accumulation (Delaunay et al., 2002, Ma et al., 2007). Additionally the protein Ybp1 is also required for oxidation of Yap1 by Gpx3. In contrast a strain background bearing a nonsense mutation in Ybp1 utilises Tsa1 for Yap1 oxidation (Veal et al., 2003, Okazaki et al., 2005). The reversal of Yap1 activation requires reduction by the thioredoxin system, since genetic perturbations to the thioredoxin system components TRX1, TRX2 and TRR1 result in constitutive oxidation and nuclear accumulation of Yap1 and elevated expression of Yap1 dependent genes (Izawa et al., 1999, Delaunay et al., 2000, Carmel-Harel et al., 2001). The regulation of Yap1 in response to oxidative stress is therefore different to OxyR in that Yap1 is not directly oxidised by H_2O_2, instead the electrons for

oxidation are taken from Gpx3 or Tsa1 which act as H_2O_2 sensors transducing this signal to Yap1. It has been suggested that the thiol-peroxidase-mediated relay of a peroxide signal to redox regulated proteins could be a general function for all thiol-peroxidases (Gutscher et al., 2009).

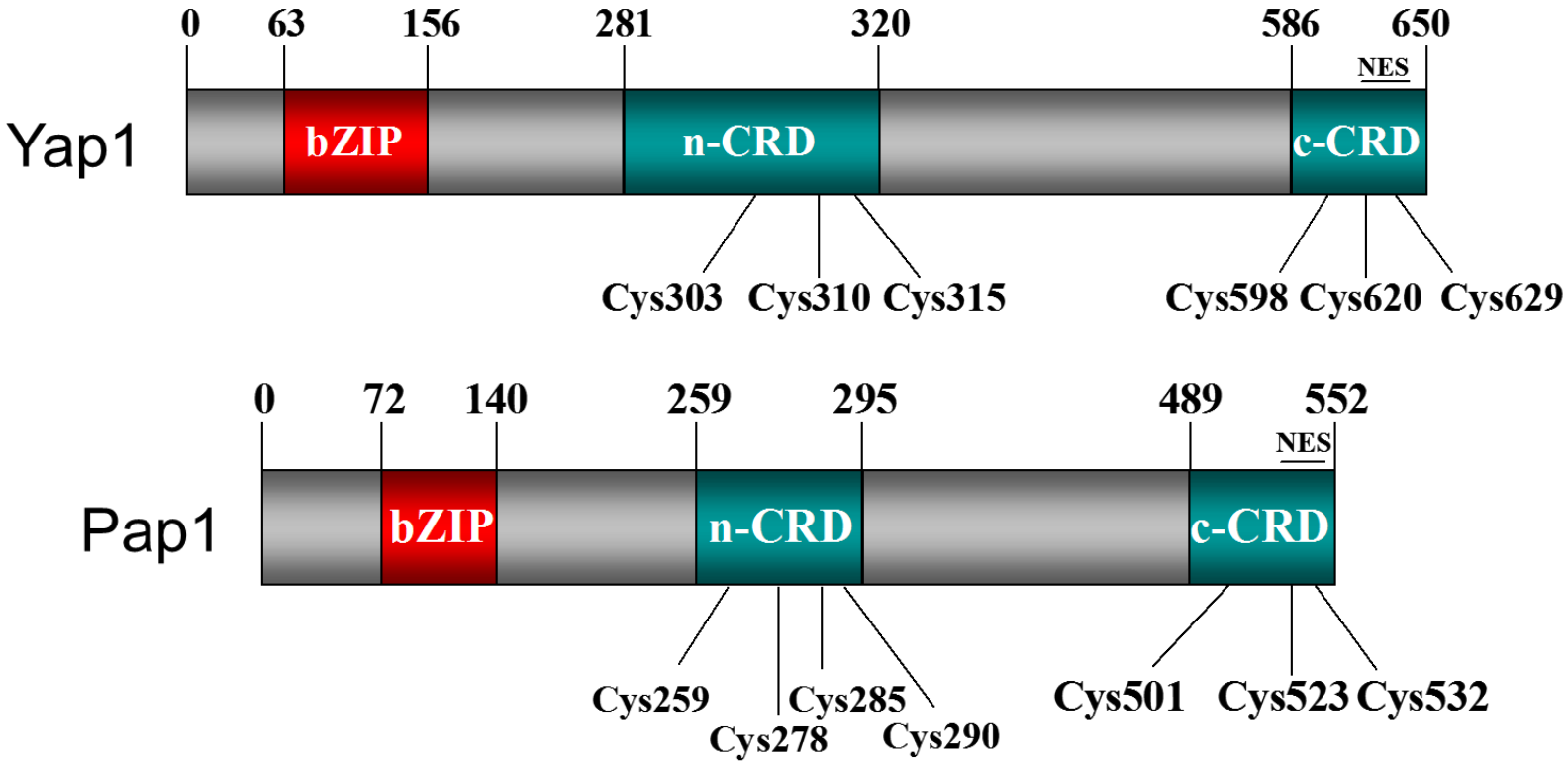

Figure 1.4: Schematic representation of the structure of the yeast bZip transcription factors, Yap1 and Pap1.

Yap1 and Pap1 contain three specific domains, the bZip domain and two cysteine rich domains, located towards the N-terminus (n-CRD) and C-terminus (c-CRD). The redox-sensitive cysteine residues located in these domains are indicated. The nuclear export signal (NES) of Yap1 and Pap1 is located within the c-CRD and is indicated (reproduced from Taylor., 2009).

1.4.2 Pap1

The regulation of the oxidative stress response in *S. pombe* is similar to *S. cerevisiae* in that it requires the AP-1 transcription factor and Yap1 homolog, Pap1 as well as the Skn7 homolog Prr1. Pap1 and Prr1 are required for the stress-induced expression of a similar set of genes to those regulated by Yap1 and Skn7 (Ohmiya et al., 1999, Ohmiya et al., 2000, Chen et al., 2008, Nakagawa et al., 2000, Vivancos et al., 2005). Similarly to Yap1, Pap1 has been demonstrated to have a role in drug resistance (Toone et al., 1998). It has been recently been suggested that Pap1 must be oxidised and nuclear, with Prr1, for antioxidant gene expression, however the reduced form of Pap1 in the nucleus with Prr1 is sufficient for drug resistance (Calvo et al., 2012, Castillo et al., 2003). Similar to Yap1, the oxidation of Pap1 in response to H_2O_2 inhibits the binding of Crm1 and results in nuclear accumulation of Pap1 (Toda et al., 1992, Toone et al., 1998, Kudo et al., 1999). Pap1 also contains two CRD domains, however the n-CRD contains four cysteine residues (C259, C278, C285, C290) and the c-CRD contains three cysteine residues (C501, C523, C532). The oxidation of Pap1 is not as well-characterised as Yap1, however there is evidence to suggest that C278, C285, C523 and C532 are oxidised in response to H_2O_2 (Calvo et al., 2013). The initial oxidation of Pap1 in response to H_2O_2 requires the *S. pombe* peroxiredoxin Tpx1. This has led to the suggestion that Tpx1 might oxidise Pap1 via a similar mechanism to the oxidation of Yap1 by Gpx3 or Tsa1 (Vivancos et al., 2005, Bozonet et al., 2005). What is clear is that the thioredoxin peroxidase activity of the *S. pombe* peroxiredoxin Tpx1 is actually required for the H_2O_2-induced activation of Pap1. However the observation that Gpx3 does not need its resolving cysteine to activate Yap1 indicates that, unlike Tpx1 and Pap1, Gpx3 can activate Pap1 independently of this peroxidase activity (Bozonet et al., 2005, Vivancos et al., 2005, Day et al., 2012). Accordingly, hyperoxidation of Tpx1 prevents H_2O_2-induced activation of Pap1 (Vivancos et al., 2005, Bozonet et al., 2005). A possible explanation for this, is that thioredoxin is responsible for the reduction of Pap1 disulphide bonds and that hyperoxidation of Tpx1 to a thioredoxin-resistant form increases the availability of reduced thioredoxin thus inhibiting Pap1 oxidation (Day et al., 2012). However, whether Tpx1 has any additional role in Pap1 activation as an H_2O_2 transducer is an outstanding question. The precise mechanism of Pap1 oxidation and its relationship with Tpx1

and the thioredoxin system is one of the key questions which will be addressed in this thesis.

1.4.3 Nrf2

In mammals the b-Zip transcription factor Nrf2 mediates the transcription of many antioxidant genes, including sulphiredoxin, as well as phase II detoxification genes (Kobayashi and Yamamoto, 2006, Itoh et al., 1997, Bae et al., 2011, Bae et al., 2008). In unstressed cells, Nrf2 is sequestered in the cytoplasm through its interaction with the repressor protein Keap1. This interaction also mediates the degradation of Nrf2 by promoting ubiquitination through the E3-ligase Cul3 (Cullinan et al., 2004, Itoh et al., 1999). Exposure to oxidants causes the dissociation of Nrf2 from Keap1 partly due to the oxidation of redox sensitive cysteine residues in Keap1 but also due to oxidative stress-induced phosphorylation of Ser40 in Nrf2 (Itoh et al., 1999, Yamamoto et al., 2008, Numazawa et al., 2003). An extra level of regulation is achieved due to the activity of the related transcriptional repressors Bach1 and Bach2. Under non-stress conditions Bach1 and Bach2 compete for ARE response elements and thus repress Nrf2 dependent gene expression (Dhakshinamoorthy et al., 2005). Changes in the intracellular redox state result in the oxidation of cysteine residues in the DNA-binding domain of Bach1; this releases them from the ARE and thus allows the activation of Nrf2-mediated gene expression (Ishikawa et al., 2005).

1.4.4 Stress-activated protein kinases

Another conserved signalling pathway, responsible for the activation of oxidative stress genes in response to H_2O_2, is the mitogen-activated protein kinase (MAPK) pathway. MAPK pathways are three tiered signalling cascades which are activated in response to a wide variety of stimuli. The first stage in the activation of MAPK signalling is the activation of a MAPK kinase kinase (MAPKKK) by an extracellular stimulus. The activated MAPKKK subsequently phosphorylates two conserved serine/threonine residues on its target MAPK kinase (MAPKK). The MAPKK then phosphorylates the threonine and tyrosine residues in a conserved Thr-X-Tyr motif in the activation loop of a MAPK. The phosphorylated MAPK can then phosphorylate a range of target proteins including transcription factors and

phosphatases responsible for the regulation of a range of cellular processes (for reviews see Chen and Thorner, 2007, Kyriakis and Avruch, 2001). Environmental stressors such as osmotic, UV and oxidative stress can activate MAPK signalling pathways. These pathways are often referred to as stress-activated protein kinases (SAPK).

In *S. cerevisiae* the Hog1 MAPK pathway, equivalent to mammalian p38/JNK is not responsible for the H_2O_2-induced expression of anti-oxidant genes (Jamieson, 1998). However, in *S. pombe* Pap1 and the MAPK Sty1 have been demonstrated to initiate two distinct but overlapping sets of OSR genes in response to H_2O_2 depending on H_2O_2 concentration (Chen et al., 2008). The initial activation of *S. pombe* MAPK signalling involves the phosphorylation of the MAPK kinase kinases (MAPKKKs or MAP3Ks) Wak1 and Win1. This initial phosphorylation is induced when H_2O_2 specifically induces the activation of a two component signal transduction pathway (Nguyen et al., 2000, Buck et al., 2001) (Figure 1.5). Two component signalling modules are absent from animals but are commonly used by bacteria and to a lesser degree by plants and fungi. There are usually used to transduce environmental stimuli (Stock et al., 2000). Indeed, two-component signalling has been proposed to promote Prr1-dependent transcriptional responses to high concentrations of H_2O_2 (Quinn et al., 2011). The MAPKKKs then phosphorylate the MAPK kinase (MAPKK) Wis1 which subsequently phosphorylates the terminal MAPK Sty1 (also known as Spc1) (Degols et al., 1996, Shiozaki and Russell, 1996, Samejima et al., 1997, Shieh et al., 1998). Sty1 then phosphorylates the transcription factor Atf1. This stabilises Atf1, by inhibiting the ubiquitin-dependent degradation of Atf1, and thus facilitates the expression of Atf1-dependent genes (Lawrence et al., 2007, Lawrence et al., 2009, Shiozaki and Russell, 1996, Wilkinson et al., 1996). It is important to note that the Atf1 does not require phosphorylation to become transcriptionally active. Phosphorylation merely facilitates Atf1-depependent gene expression by increasing the availability of Atf1. Sty1 is also responsible for maintaining the stability of *atf1*$^+$ mRNA in H_2O_2-treated cells via the actions of the protein Csx1 (Day and Veal, 2010, Rodriguez-Gabriel et al., 2003). The peroxiredoxin Tpx1 has also been demonstrated to have a key role in the regulation of MAPK signalling, Tpx1 directly oxidises Sty1 which results in the formation of a Sty1 intramolecular disulphide, a process which is essential for the H_2O_2 induced

phosphorylation of Sty1, but not other stressors, and is independent of the thioredoxin peroxidase activity of Tpx1 (Veal et al., 2004, Day and Veal, 2010)

In mammals the two major stress activated MAPKs are JNK (c-Jun N-terminal kinase) and p38 (Benhar et al., 2002, Dhillon et al., 2007). The main activators of JNK are UV radiation, inflammatory cytokines and environmental stressors. Upon activation JNK can phosphorylate and activate the transcription factors c-Jun and ATF2 (*S. pombe* Atf1 homolog). Activation of p38 occurs in response to environmental stresses such as osmotic and oxidative stress as well as inflammatory cytokines such as TNF-α and lL-1. Insulin and growth factors have also been demonstrated to activate p38 (Kyriakis and Avruch, 2001). ATF2 is the major target of p38. In mammals, the peroxiredoxins Prx1 and Prx2 have clear roles in the activation of the MAPKKK ASK1 and therefore the downstream activation of p38, although the precise role is not clear due to contradictory findings (Kim et al., 2008, Jarvis et al., 2012). For example, one study has demonstrated that knockdown of Prx1 promotes ASK1 activation (Kim et al., 2008), whilst a subsequent study found that knockdown inhibited the H_2O_2-induced activation of Ask1 (Jarvis et al., 2012). Under normal growth conditions ASK1 can be found as inactive high-molecular weight oligomers with Trx1. Exposure to H_2O_2 causes the dissociation of Trx1 and activates ASK1 (Fujino et al., 2007, Saitoh et al., 1998). At the level of the MAPK, analogous to Sty1 and Tpx1, mammalian Prx1 positively regulates p38, whilst conversely Prx2 negatively regulates the phosphorylation of p38 and JNK (Kang et al., 2004, Conway and Kinter, 2006).

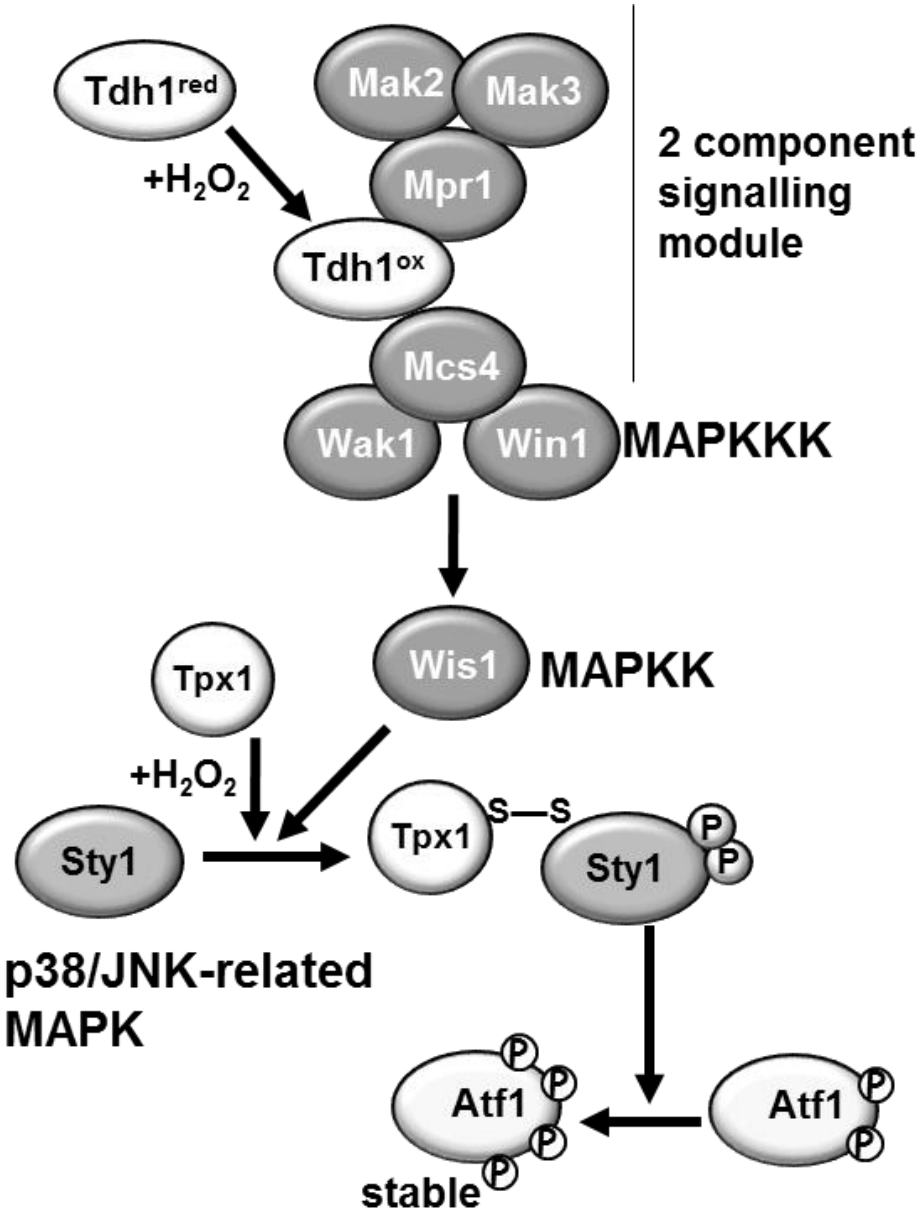

Figure 1.5: Schematic diagram showing the components of the *S. pombe* SAPK signalling pathway.

Diagram displays the two-component signalling module consisting of Mak2, Mak3 and Mpr1. The Mpr1 mediated activation of the MAPKKK Mcs4 is facilitated by the GAPDH Tdh1. The MAPKKK Wak1 and Win1 phosphorylate the MAPKK Wis1 which in turn phosphorylates the p38/JNK-related MAPK Sty1. Sty1 is also oxidised in response to H_2O_2 via a direct interaction with Tpx1. Active Sty1 will phosphorylate Atf1, this stabilises Atf1 and causes a further increase in Atf1-dependent transcription in response to H_2O_2.

1.5 Biological roles of Prx hyperoxidation

The conserved sensitivity of the eukaryotic Prxs to hyperoxidation as well as the co-evolution of Srx suggests that sensitivity to hyperoxidation is advantageous in these organisms. Indeed, the *S. pombe* mutant strain containing the hyperoxidation resistant $Tpx1^{1-181}$ displays an increased sensitivity to H_2O_2 (Koo et al., 2002). This observation that inactivation of one of the cells peroxidases is actually beneficial to the cell seems counterintuitive and has prompted the question of why have eukaryotic Prxs evolved sensitivity to hyperoxidation. One explanation, often referred to as the flood-gate model, proposes that peroxidase activity of Prx may act as a barrier to H_2O_2-signalling and suggests that Prx inactivation is important to allow the H_2O_2 messenger to oxidise target proteins (Wood et al., 2003b). However there is little evidence that a significant proportion of Prx becomes hyperoxidised in response to the low levels of H_2O_2 generated as a signalling molecule in response to growth factors (Woo et al., 2010). Although this this is contradicted by the observation that oscillations in the amount of hyperoxidised Prx have been associated with circadian rhythms across a wide range of species (for a review see Stangherlin and Reddy, 2013). Moreover, oscillations in the hyperoxidation of the mouse mitochondrial Prx, PrxIII, have been shown to be important for circadian oscillations in p38 activation and adrenal steroid synthesis (Kil et al., 2012). However, it still remains unclear whether the role of Prx hyperoxidation in these conditions is to increase the levels of H_2O_2 available for signalling. Contrary to the floodgate model, which proposes that the peroxidase activity of the Prxs is a barrier to H_2O_2 signalling, work in the fission yeast *S. pombe* has shown that the thioredoxin peroxidase activity of the *S. pombe* peroxiredoxin Tpx1 is actually required for the H_2O_2-induced activation of the AP-1 like transcription factor Pap1 (Bozonet et al., 2005, Vivancos et al., 2005). Tpx1 has also been shown have a positive role in the H_2O_2-induced activation of the MAPK Sty1 (Veal et al., 2004). Indeed the peroxiredoxins have been shown to have positive and negative in roles in redox signal transduction depending on cell type suggesting that the floodgate model does not hold true for all H_2O_2 signalling events (Choi et al., 2005, Woo et al., 2010, Kang et al., 2011, Conway and Kinter, 2006, Dangoor et al., 2012, Jarvis et al., 2012). For example, expression of Prx1 was required for activation of p38 in macrophage derived foam cells demonstrating a positive signalling role for Prx1 (Conway and Kinter, 2006).

It has recently been demonstrated that Prx1-dependent p38 activation may be due to the direct oxidation and activation of ASK1 by Prx1 (Jarvis et al., 2012). Conversely, Prx2 was shown to inhibit ASK1 activation (Jarvis et al., 2012). The ubiquitous nature of Prx1 and its high peroxidase activity means that Prx1 inhibits the activation of other H_2O_2 activated proteins. In response to growth factor signalling the peroxidase activity of Prx1 is inhibited by phosphorylation of tyrosine-194, this allows local H_2O_2 concentrations to increase and activate H_2O_2 signalling (Woo et al., 2010). Nonetheless, it is clear that Prx hyperoxidation can have downstream effects on H_2O_2 signalling suggesting that sensitivity to hyperoxidation may have evolved for its role in the regulation of H_2O_2 signalling.

As well as signalling, Prx hyperoxidation has been demonstrated to have downstream effects on protein repair. In *S. pombe*, it has been proposed that hyperoxidation of Tpx1 to a thioredoxin-resistant form is important to increase the pool of reduced thioredoxin available to support the activity of other enzymes, such as the methionine sulfoxide reductase, Mxr1, and to repair oxidatively damaged proteins (Day et al., 2012). Accordingly, hyperoxidation of Tpx1 has been shown to be important for cell survival under acute stress conditions. Hyperoxidation of Prx has also been proposed to protect cells by promoting an alternative activity for Prx to act as a chaperone, preventing protein aggregation (Jang et al., 2004, Moon et al., 2005, Olahova et al., 2008) (for a review see Kumsta and Jakob, 2009).

Part of understanding the effects that Prx hyperoxidation has on cellular behaviour is also understanding the mechanisms that influence this sensitivity and govern the conditions under which hyperoxidation can occur. For instance, although all eukaryotic Prx contain the YF and GGLG motifs conferring sensitivity to inactivation, the variation in their sensitivity to inactivation indicates that other factors also govern the sensitivity to hyperoxidation. For example, *in-vitro* studies have revealed that human Prx1 is much more sensitive to hyperoxidation than Prx3 (Peskin et al., 2013, Haynes et al., 2013). This increased sensitivity reflects a 10-fold slower rate of PrxI disulfide formation that increases the risk of further oxidation of the sulfenated peroxidatic cysteine. In addition to the intrinsic biochemical properties of the Prx itself, the sensitivity of Prx to hyperoxidation *in vivo* is also influenced by the local environment. For example, *in vitro* the ER-localised Prx, PrxIV, has a similar sensitivity to hyperoxidation to Prx1, but *in vivo*

the low abundance of disulfide reductases in the ER leads to the accumulation of PrxIV disulfides rendering hyperoxidation of PrxIV to its sulfinic form negligible (Cao et al., 2014). Thus the extent to which Prx become hyperoxidised *in vivo* will be influenced both by intrinsic properties of the Prx and its local environment such as local H_2O_2 concentration, local availability of disulfide reductases, compartmental volumes and competition with other peroxidases. Part of the work in this thesis will be addressing the question of how these factors influence when Prx hyperoxidation will occur *in vivo*.

It is clear that the increased expression of antioxidant genes is a widely conserved adaptive response to oxidative stress. As discussed above, many of the genes which display increased expression as part of the OSR, such as the Prxs, Trxs and Srxs, are also directly involved in the regulation of the signalling events that lead to the induction of the OSR. This prompts the question, what is the role of the OSR in the cellular response to oxidative stress? Although an obvious hypothesis would be that the increased expression of antioxidant genes serves to remove harmful oxidants for quickly and increase resistance to any subsequent exposures it is still unclear how these changes in gene expression will affect subsequent oxidative stress signalling events. The question of how changes in the expression of H_2O_2 signalling pathway components will affect the OSR will be addressed in this thesis. This situation where dynamic changes in signalling pathway components would result in changes to signalling is an ideal problem for systems biology.

1.6 Systems Biology

Systems Biology can be loosely defined as a field of research which attempts to understand the behaviour of biological systems from the perspective of their network properties rather than just the properties of the individual system components. Traditional, reductionist strategies to understanding biological systems have allowed scientists to piece together an understanding of the behaviour of biological systems based on the properties of their components usually consisting of biological macromolecules such as DNA and proteins. A relevant example of this are the peroxiredoxins which have well characterised oxidation and reduction mechanisms and have been demonstrated to interact

with a range of regulatory proteins across a range of species. However, when trying to understand any complex system, a detailed understanding of the system components is not enough to be able to fully predict the behaviour of the system. Instead, a broader understanding of how cellular components interact with and influence one another in a wider network is required, as well as an understanding of how the relative abundance and localisation of each protein will affect this network.

A good thought experiment to visualise this concept is to think of a box filled with engine parts. If put together in a particular way these parts will form the complex system that we call an engine. However, these same parts, connected in an alternative way, could easily be used to build something completely different. Whether it is an engine, or something else, the properties of the individual components will be the same, but the properties of the final structure will depend on how these identical components are connected. This same principle applies to biological systems where behaviour of the system is ultimately governed by the structure of the molecular or cellular network.

Similarly, two systems made from two completely different sets of component parts, could each be structured in such a way that they produce the same overall behaviour. A simple biological example for this is the well-established concept of a negative feedback loop, which occurs when an increase in a stimulus has the consequence of subsequently inhibiting that initial stimulus. A negative feedback loop can result from the interactions between biomolecules such as protein-protein interactions or via a genetic or neuronal interaction. The relationship between predator and prey in an ecological network can also be described as a negative feedback loop. All of these examples have different component parts but all result in the network property referred to as negative feedback. The work of Uri Alon has formalised the idea of network motifs and how they confer specific dynamical properties, such as negative feedback loops, to biological systems (Alon, 2007, Hart et al., 2012). Moving from a component level understanding to a network level understanding of biological systems is vital if we want to further our understanding of biology.

1.6.1 Tools and techniques in systems biology

Systems biologists use a broad range of statistical and computer modelling techniques in order to understand biological systems. One such technique, sometimes referred to as the bottom-up systems approach, is the attempt to use kinetic models to represent the key features and behaviours of small biological systems. These models use enzyme kinetic principles to describe the relationships between cell components and predict the effects that perturbations will have on this system. These predictions can then be tested experimentally and subsequently used to inform the model. If the model is unable to replicate the experimental observations it suggests the proposed model is incorrect. Alternative models can then be built and tested *in silico* until a reasonable alternative can be proposed and tested experimentally. This strategy allows researchers to infer information about the structure of a small biological network based on the experimentally observed dynamic changes of its components. This combined use of both modelling and experimental data can often provide information about a system that may not have been obvious from the experimental data alone.

1.6.2 Commonly used enzyme kinetic equations

The rates of chemical reactions can be represented using enzyme kinetic equations, the simplest of which is mass action kinetics first described by Guldberg and Waage in the late 1800s. Mass action kinetics assumes that the rate of a chemical reaction is proportional to the probability of a collision between two reactants. This probability is in turn proportional to the concentrations of these reactants. For a simple reaction, represented by equation 1, the mass action rate law can be defined using equation 2 where v is the reaction rate, k is the rate constant for the reaction and [S_1] and [S_2] are the concentrations of the substrates S_1 and S_2 respectively. The rate constant k in this instance would have units of $M^{-1}s^{-1}$.

(Equation 1) $$S_1 + S_2 = P_1$$

(Equation 2) $$v = k\,[S_1]\,[S_2]$$

Another well established and commonly used enzyme kinetic equation is the Michaelis Menten rate law (Equation 3).

$$\text{(Equation 3) } v = \frac{V_{max} \times [S]}{K_m + [S]}$$

Where *v* is equal to the rate of the reaction, V_{max} is the maximum rate of the reaction for a given concentration of enzyme, K_m is the concentration of substrate required for the reaction rate to be half V_{max} and [S] is the concentration of the substrate. The V_{max} can be calculated from equation 4 where k_{cat} is the catalytic rate constant for the enzyme and [E] is the concentration of the enzyme.

$$\text{(Equation 4) } V_{max} = k_{cat} \times [E]$$

A less common, but important enzyme kinetic equation is the ping-pong kinetic rate law (Equation 5). This is used to describe two-substrate (S_1 & S_2), enzyme (E) catalysed reactions, where the enzyme is modified (E_{mod}) by the first substrate before it reacts with second substrate (Equation 6 & 7). An example reaction displaying ping-pong kinetics is the reduction of methionine sulphoxide (Met-S-SO) by methionine disulphide reductase (MsrA) (Boschi-Muller et al., 2001, Boschi-Muller et al., 2005).

$$\text{(Equation 5) } v = \frac{(k_{cat} \times [E] \times [S_1] \times [S_2])}{(K_{m\_S_2} \times [S_1] + K_{m\_S_1} \times [S_2] + [S_1] \times [S_2])}$$

$$\text{(Equation 6) } S_1 + E \leftrightarrow S_1E \rightarrow E_{mod}$$

$$\text{(Equation 7) } E_{mod} + S_2 \leftrightarrow S_2E_{mod} \rightarrow E$$

1.6.3 Ordinary differential equations

We have briefly described that the rates of a reaction can be estimated using kinetic rate laws. We can use these rate laws to select a system of ordinary differential equations (ODEs) to represent a set of reactions. To demonstrate this, we can imagine three different chemical entities related to each other by three different reactions (Equation 8).

(Equation 8) $A \underset{k_2}{\overset{k_1}{\rightleftharpoons}} B \xrightarrow{k_3} C$

From the equation we can see that species A is converted to species B at a rate proportional to rate constant k_1, species B is converted to species A at a rate proportional to k_2 and species B is converted to species C at a rate proportional to k_3. If we assume that all reactions follow mass action kinetics, we can represent this system with a series of ODEs as follows (Equations 9 - 11).

(Equation 9) $\frac{\Delta[A]}{\Delta t} = k_2 \times [B] - k_1 \times [A]$

(Equation 10) $\frac{\Delta[B]}{\Delta t} = k_1 \times [A] - k_2 \times [B] - k_3 \times [B]$

(Equation 11) $\frac{\Delta[C]}{\Delta t} = k_3 \times [B]$

These equations are based on the reasoning that the concentration change of a given particular species ([S]) over a specific time period (Δ[S]/Δt) will be equal to the rates of all the reactions that form this species minus the rates of all reactions that consume this species. In the example of equation 9, which represents the change in [A] over time (Δ[A]/Δt), the first part of the equation (k_2 x [B]) represents the fact that the rate of conversion of species A to form species B is equal to the rate constant k_2 multiplied by the concentration of species B. The second part of the equation (-k_1 x [A]) represents the conversion of B back into A with a rate equal to k_1 x [A]. This system of ODEs can then be used to calculate the time dependent changes in the concentration of each species from an initial concentration using time course simulation algorithms.

1.6.4 Parameter estimation and identifiability

When building a computer model, the rate constants for the biochemical reactions involved are not always known, rate constants in computer models often represent an amalgamation of multiple, sometimes unknown, chemical processes and would therefore be difficult to measure experimentally (Schaber and Klipp, 2011). To overcome this problem a computer modelling technique called parameter estimation can be used. In order to use parameter estimation, a set of experimental time course data for the species in the model needs to be obtained. Parameter estimation can then be used to find a set of rate constants that allows the model to be able to simulate this data. To do this the sum of squared residuals (SSR) is calculated for a given set of model parameters p (p = (k_1, k_2, k_3) for Equation 8 model). The SSR is a quantification of the difference between the model prediction and the experimental data and is calculated using equation 12.

(Equation 12) $$SSR(p) = \sum_{i=1}^{n} \left(\frac{y_i - f(t_i, p)}{\sigma_i} \right)^2$$

Where *SSR(p)* is the sum of squared residuals for a given parameter set *p*, y_i is a set of *n* experimental data points with standard deviation σ_i, and $f(t_i, p)$ is the numerically calculated value, based on the model, at time points t_i and parameter set *p*. The parameter estimation software will find a set of values for p that produces the lowest SSR and these parameters are selected for the final model.

Sometimes not all of the reactions in a model are known. For instance, there may be a number of biochemically possible reactions but no experimental evidence to indicate which reactions are actually occurring *in vivo*. In this situation, parameter estimation can be used to determine which model is best able to describe the dynamics of the experimental data. Multiple models can be built and parameter estimation performed for each one. The model which is best able to simulate the experimental data (ie the model with the lowest SSR) can be reasoned to best represent the biology. However, adding more parameters to a model, tends to improve the fit of the model even if the added reactions are not biologically relevant. To account for this, the Akaike information criterion (AIC) (Akaike, 1973) for each model can be calculated using equation 13.

(Equation 13) $AIC = 2m - 2\ln(SSR)$

Similarly to the SSR, a lower AIC indicates a better fit to the experimental data. However the AIC also penalises models containing an increased number of parameters (*m*). This allows a fairer comparison of models containing different numbers of parameters.

Parameter estimation will not necessarily find a unique value for a particular parameter. For example a model may fit the data equally well if parameter k_1 is 0.1, 1000 or even infinite. If this situation occurs the particular parameter, in this example k_1, is non-identifiable. In this case, additional experimental data or changing the model structure is necessary in order to make the parameter identifiable. To assess whether parameters in a model are identifiable, identifiability analysis is used which also provides 95% confidence regions for each parameter (Schaber, 2012).

1.6.5 Modelling redox couples using Michaelis-Menten kinetics

A mathematical analysis of a single-cycle redoxin system (Figure 1.6) has demonstrated how the behaviour of such a system can be represented using Michaelis-Menten kinetics (Pillay et al., 2009, Pillay et al, 2011). In this analysis the single-cycle redoxin system consisted of two reactions (Equations 14 & 15) both using mass action rate laws (Equations 16 & 17). The reaction represented by equation 11 is the reduction of oxidised Thioredoxin (TrxSS), by thioredoxin reductase, utilising electrons from NADPH (Equation 14). This reaction has a rate v_1 with a mass action rate law dependent on the rate constant k_1 (Equation 16). The second reaction represents the oxidation of reduced Thioredoxin (TrxSH) by one of Thioredoxins oxidised protein substrates (PrSS) (Equation 12). This reaction has a rate v_2 with a mass action rate law dependent on the rate constant k_2 (Equation 17).

(Equation 14) $NADPH + TrxSS \rightarrow NADP + TrxSH$

(Equation 15) $TrxSH + PrSS \rightarrow TrxSS + PrSH$

(Equation 16) $v_1 = k_1 \times [NADPH] \times [TrxSS]$

(Equation 17) $v_2 = k_2 \times [TrxSH] \times [PrSS]$

This system can be represented using equations 17, 18 & 19. Equation 18 is a differential equation describing changes in the concentration of TrxSH in this single-cycle redoxin system. Equation 19 describes the concentration of TrxSH in terms of the total concentration of both TrxSH and TrxSS in the system ($[Trx]_{total}$).

(Equation 18) $\frac{\Delta[TrxSH]}{\Delta t} = k_1 \cdot [NADPH] \cdot [TrxSS] - k_2 \cdot [PrSS] \cdot [TrxSH]$

(Equation 19) $[TrxSH] = [Trx]_{total} - [TrxSS]$

Substituting equation 19 into equation 18 and solving for TrxSS results in equation 20. Equation 20 and equation 19 can then substituted into equation 17 to yield equation 21.

(Equation 20) $TrxSS = \frac{[Trx]_{total} \cdot (k_2[PrSS])}{k_1 \cdot [NADPH] + k_2 \cdot [PrSS]}$

(Equation 21) $v_2 = \frac{(k_1 \cdot [NADPH] \cdot [Trx]_{total}) \cdot [PrSS]}{\frac{k_1}{k_2} \cdot [NADPH] + [PrSS]}$

Equation 21 has the same form as the Michaelis-Menten equation (Equation 3). It can therefore be said that the V_{max} for the oxidation of TrxSH (Equation 15) in a single-cycle redoxin system can be described by $k_1 \cdot [NADPH] \cdot [Trx]_{total}$, the k_{cat} can be described by $k_1 \cdot [NADPH]$ and the K_m can be described by $k_1 \cdot [NADPH]/k_2$. This type of analysis is useful when building computer models because it demonstrates how the overall behaviour of a complex system of multiple reactions can be mathematically represented using a single reaction with multiple parameters.

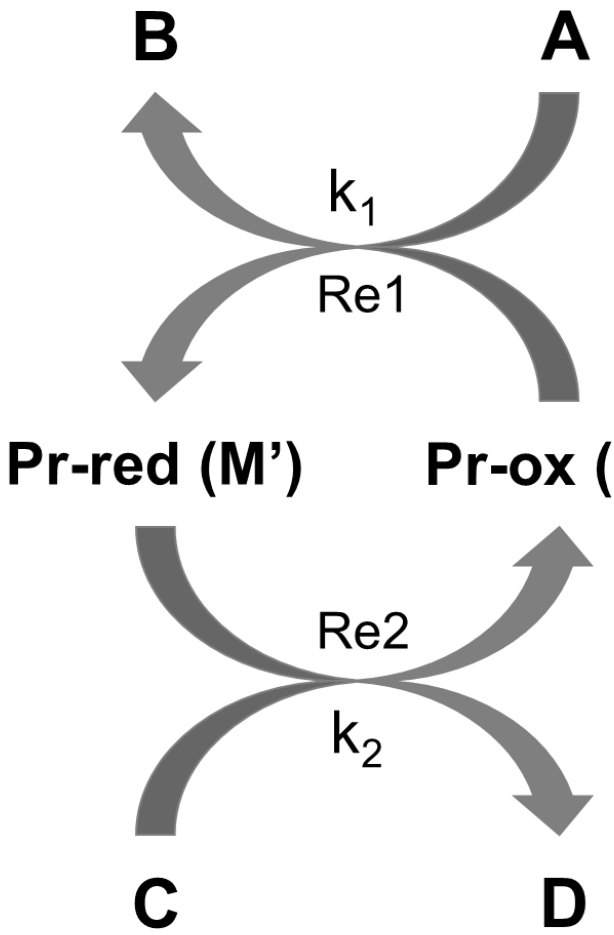

(Eq. 1)

$$v_2 = \frac{(k_1 a m_t)c}{\frac{k_1}{k_2}a + c}$$

(Eq. 2)

$$v = \frac{V_{max} \times [S]}{K_m + [S]}$$

$$V_{max} = k_1 a m_t \qquad k_{cat} = k_1 a \qquad K_m = \frac{k_1 a}{k_2}$$

Figure 1.6: A single-cycle redoxin system can be described using Michaelis-Menten kinetics.

The diagram displays the reactions of a single-cycle redoxin system comprising the reversibly oxidised protein Pr. The reduction of Pr-ox by species A (Re1) is dependent on the rate constant k_1 whilst the oxidation of Pr-red by species C (Re2) is dependent on the rate constant k_2. These reactions can be solved to create Eq.1 (m_t = M + M') which has the same form as the Michaelis-Menten equation (Eq.2). The apparent V_{max}, k_{cat} and K_m for the reduction of species C by a single cycle redoxin system can therefore be described as indicated.

1.7 Summary and Aims

Maintenance of redox balance is not only essential for minimising oxidative damage to cellular components but is required for appropriate initiation of redox-regulated signalling events. However, the mechanisms by which cells maintain this balance or sense acute, dynamic redox changes under signalling and/or stress conditions are poorly defined. The ubiquitous Prx family of thiol-peroxidases have conserved roles in signalling as well as their peroxidase functions. The hyperoxidation of the eukaryotic Prxs has been shown to play a key role in the regulation of H_2O_2-mediated signalling events as well as promoting the repair of cellular components (Day et al., 2012). However, the physiological conditions under which Prx become hyperoxidised *in vivo* are poorly defined. There are many factors governing when Prx hyperoxidation will occur *in vivo.* Hence the aim of the work in this thesis is to gain a deeper understanding of how factors such as H_2O_2 compartmentalisation and the presence of cellular peroxidases influence when Prx hyperoxidation will occur. In order to address this question experimental time course data, collected using *S. pombe*, was used to build a computer model representing the oxidation and hyperoxidation of Tpx1. It is hypothesised that this model would provide new insights into the relationship between Prx hyperoxidation and changes in intracellular H_2O_2 concentration.

Thiol-peroxidases have been shown to participate directly in the activation of Yap1 (see 1.4.1). Based on this, it has been proposed that Prx act more widely as direct H_2O_2 transducers in the oxidation of other signalling proteins. However, there is little evidence to support this. For instance it is still unclear if Tpx1 has a similar direct role in the activation of Pap1 in *S. pombe*. The aim of this study is to learn more about the potential roles of Tpx1 in the activation of Pap1. This was done by building multiple computer models, each one representing alternative mechanisms for the oxidation of Pap1 by Tpx1. By comparing the dynamics of Pap1 oxidation in these models to the experimentally observed dynamics, the objective was to identify conserved and/or distinct aspects of the thiol-peroxidase-based activation mechanisms involved in activation of AP-1 like transcription factors in *S. pombe* and *S. cerevisiae*.

Exposure to oxidative stress results in changes in the expression of many genes including peroxidases such as Prxs and Trxs. These changes cause resistance

to subsequent oxidant exposures (see 1.4). However, it is not clear how these changes in gene expression will influence signalling in response to a subsequent oxidant exposure. A further objective was to build a computer model of H_2O_2 metabolism that can be used to predict how changes in gene expression will affect the response of the cell to H_2O_2.

CHAPTER 2. Materials and Methods

2.1 Cell Culture and Maintenance

2.1.1 Growth and Maintenance of Schizosaccaromyces pombe

Schizosaccharomyces pombe strains used in this study were stored at -80°C in 50% YE5S media and 50% glycerol, from which they were propagated on YE5S agar plates (2% (w/v) agar YE5S) at 30°C. For short-term use *S. pombe* were stored on YE5S agar plates at room temperature and re-plated weekly. Unless stated otherwise, all YE5S media used in this study contained 0.5% (w/v) yeast extract, 3% (w/v) glucose and 0.74 mM adenine, 0.64 mM histidine, 0.89 mM uracil, 0.68 mM lysine and 0.76 mM leucine. For preparation of liquid cell cultures *S. pombe* cells were inoculated into 50 ml YE5S or 50 ml Edinburgh minimal media (EMM) containing 15 mM potassium hydrogen phthalate ($C_8H_5O_4K$), 15.5 mM di-sodium hydrogen orthophosphate (Na_2HPO_4), 93 mM ammonium chloride (NH_4Cl_2), 2% (w/v) glucose, 5 mM magnesium chloride ($MgCl_2.6H_2O$), 1 µM calcium chloride ($CaCl_2.2H_2O$), 13 mM potassium chloride (KCl) and 280 µM di-sodium sulphate (Na_2SO_4), 4.6 µM pantothenic acid, 81 µM nicotinic acid, 56 µM *myo*-inositol and 41 nM biotin, 0.81 µM boric acid, 0.33 µM magnesium sulphate ($MnSO_4$), 0.25 µM $ZnSO_4.7H_2O$, 0.1 µM iron chloride ($FeCl_2.6H_2O$), 0.25 µM molybdic acid, 0.6 µM potassium iodide (KI), 0.16 µM copper sulphate ($CuSO_4.5H_2O$) and 0.52 µM citric acid, supplemented with 0.48 mM histidine, 0.56 mM adenine, 0.67 mM uracil, 1.91 mM leucine and grown overnight at 30˚C with agitation. Following overnight growth, cell cultures were diluted back to an optical density (OD595) of 0.1 (~2 x 10^6 cells/ml) and then grown to mid-log phase (OD595 of 0.3 - 0.5) for use in experimentation. For cell cultures of the Δ*trx1* or Δ*trx1*Δ*txl1* strains, which are auxotrophic for cysteine, the growth media was also supplemented with 0.52 mM cysteine. All *S. pombe* strains used in this study are listed in Table 2.1.

Table 2.1 S. pombe strain names and genotypes used in this study

Strain	Genotype	Source
972	*h⁻*	Lab stock
CHP429	*h⁻ ade6-M216 leu1-32 his7-366 ura4-D18*	Lab stock
NT4	*h⁺ ade6-M216 leu1-32 ura4-D18*	Lab stock
AD82	*h⁺ ade6 his7-366 leu1-32*	Day *et al*., 2012
JB35	*h⁻ ade6-M216 leu1-32 ura4-D18 his7-366 trx1::kan ^{mx4} Flag-trx1:ura4*	Day *et al*., 2012
JB95	*h⁺ ade6 leu1-32 ura4-D18 txl1::kan^{mx4} Flag-txl1:ura4⁺*	J. D. Brown
JB116	*h⁺ ade6 leu1-32 ura4-D18 txl1::kan^{mx4} Flag-txl1:ura4⁺ trr1::ura4⁺*	J. D. Brown
JB113	*h? ade6 leu1-32 ura4-D18 txl1::kan^{mx4} Flag-txl1:ura4⁺tpx1::ura4⁺*	J. D. Brown
SB6	*h⁻ade6-M216 leu1-32 ura4-D18 srx1::ura4 his7-366*	Bozonet *et al*., 2005
LT1	*h⁻ ade6-M216 leu1-32 ura4-D18 his7-366 srx1::ura4⁺ Flag-srx1:leu2⁺*	This Study
JR68	*h⁺ ade6 leu1-32 ura4-D18 tpx1::ura4⁺ tpx1⁺ :LEU2*	Day *et al*., 2012
JR20	*h⁺ade6-M210 leu1-32 ura4-D18 tpx1::ura4⁺ tpx1$^{1-181}$:LEU2*	Day *et al*., 2012
JR42	*h⁺ade6-M210 leu1-32 ura4-D18 tpx1::ura4⁺ tpx1^{C169S}:LEU2*	Day *et al*., 2012
JB107	*h⁺ ade6 leu1-32 ura4-D18 txl1::kan^{mx4} Flag-txl1:ura4⁺ tpx1::ura4⁺ tpx1^{C169S}:LEU2*	J. D. Brown
JB92	*h⁺ ade6 leu1-32 ura4-D18 tpx1::ura4⁺tpx1^{C169S}:LEU2 txl1::kan^{mx4}*	J. D. Brown
JR39	*h⁺ade6-M210 leu1-32 ura4-D18 tpx1::ura4⁺ tpx1^{T86E}:LEU2*	J. Rand
VX00	*h⁺ade6 leu1-32 ura4-D18 tpx::ura4 his7-366*	Veal *et al*., 2004
LT3	*h⁺ade6-M216 leu1-32 ura4-D18 ctt1::kan ^{mx4}*	Gift from Peter Banks
EV68	*h⁺ade6 leu1-32 ura4-D18 trx1::kan^{mx4}*	Day *et al*., 2012
EV75	*h⁺ ade6 leu1-32 ura4-D18 txl1::kan^{mx4}*	E. A. Veal
AD81	*h⁻ ade6 his7-366 leu1-32 ura4-D18 trr1::ura4⁺*	A. M. Day
AD140	*h⁺ ade6 his7-366 leu1-32 ura4-D18 txl1::kan^{mx4} trx1::kan^{mx4}*	A. M. Day
AD100	*h? ade6 his7-366 leu1-32 ura4-D18 tpx1::ura4⁺trx1::kan^{mx4}*	A. M. Day
AD138	*h? ade6 his7-366 leu1-32 ura4-D18 tpx1::ura4⁺ trr1::ura4⁺*	A. M. Day
JB120	*h? ade6 his7-366 leu1-32 ura4-D18 trx1::kan^{mx4} txl1::kan^{mx4} trr1::ura4⁺*	J. D. Brown
TP108	*h⁻ leu1 ura4 pap1::ura4⁺*	Toda *et al*, 1991

Table 2.1 List of *S. pombe* strain names and genotypes used in this study

The table displays the names and genotypes of the *S. pombe* strains used in this study. For strains used in previously published work a reference is provided, otherwise the name of the researcher responsible for making the strain is indicated.

2.1.2 Growth and Maintenance of HEK293 cells

HEK293 cells were grown in a humidified CO_2 incubator at 37°C in 24 ml Dulbecco's Modified Eagles Medium (DMEM) (Sigma Aldrich) supplemented with 10% foetal calf serum (FCS) (Sigma Aldrich), 100 units/ml penicillin (Sigma Aldrich), 100 µg/ml streptomycin (Sigma Aldrich) and 2 mM L-glutamine (Sigma Aldrich) and 1% non-essential amino acids (Sigma Aldrich). Cells were split and seeded into new flasks with fresh media on a weekly basis.

2.2 Proteomic Methods

2.2.1 Acid-lysis protein extraction and H_2O_2 challenge

Liquid cultures were grown to mid-log phase (OD_{595} = 0.3 - 0.5), exposed to 0 – 6 mM H_2O_2 (Sigma) and 1 – 5 ml aliquots of cell culture was harvested at the indicated time points, by adding an equal volume of 20% (w/v) trichloro acetic acid (TCA) (Sigma Aldrich) in to polypropylene ribolyser tubes. Cells were pelleted by centrifugation (2 min 13,000 G), supernatant discarded, and the cell pellet snap frozen in liquid nitrogen, cell pellets were stored at -20 °C until required for the protein extraction. The pelleted cells were re-suspended in 10% (w/v) TCA (200 µl) and homogenised using glass beads (0.5mm, Biospec Products, Inc) and a biospec products mini bead beater (3 x 20 seconds). Cell lysates were transferred to microfuge tubes, pelleted by centrifugation (10 min 13,000 G 4˚C), washed (3 times) in 200 µl acetone followed by repelleting by centrifugation (2 min 13,000 rpm). Finally, the pellets were incubated at room temperature for 30 min in TCA buffer (100 mM Tris-HCl [pH 8.0], 1% SDS, 1 mM EDTA [pH 8.0] and 5.7 mM phenylmethanesulfonyl fluoride (PMSF)), centrifuged (3 min 13,000 G) and the supernatant removed to a fresh microfuge tube. The protein concentration of the supernatant was determined using a Pierce® BCA protein assay (Thermo Scientific).

2.2.2 Protein extraction using protein lysis-buffer (S. pombe)

Cultures were grown to mid-log (OD_{595} 0.3 – 0.5) phase and ~50 ml of culture (~5 x 10^8 cells) harvested by centrifugation at 2000 rpm for 2 min. Pellets were washed and resuspended in (200 µl) ice-cold protein lysis buffer (PLB) ((50 mM Tris-HCl [pH 7.5], 150 mM NaCl, 0.5% NP40 (IGEPAL), 10 mM Imidazole) containing protease inhibitors (2.9 µM pepstatin A, 4.7 µM leupeptin, 0.57 mM phenylmethanesulfonyl flouride (PMSF) and 1% (v/v) aprotinin)). The cell suspension was then transferred to a ribolyser tube, 750 µl ice-cold glass beads (Biospec products) were added and the cell walls were disrupted using a Mini-beadbeater (Biospec products) for 3 x 20 seconds with incubation on ice in between shakes. Another 200 µl of ice-cold PLB was added to the ribolyser tube and transferred to an eppendorf tube. The protein concentration of the solubilised protein sample was then determined using a Pierce® BCA protein assay kit (Thermo Scientific) and then snap frozen and stored at -20°C until further use. For analysis of Pap1, protein samples were treated with alkaline phosphatase (2 µl phosphatase, 5 µl phosphatase buffer in 15 µl protein sample) (Roche) for 60 min at 37°C in order to dephosphorylate Pap1 before SDS-PAGE analysis.

2.2.3 H_2O_2 challenge and protein extraction using lysis-buffer (HEK293)

A 10 cm plate of confluent HEK293 cells was washed three times with Dulbecco's phosphate buffered saline (DPBS) (Sigma), then incubated for 10 min at 37°C in DPBS supplemented, as indicated, with H_2O_2 (Sigma). Cells were washed three times in DPBS then re-suspended in 500 µl of protein lysis buffer (50 mM Tris pH 7.5, 150 mM NaCl, 0.5% NP40 (IGEPAL), 10 mM Imidazole, 2.9 µM pepstatin A, 4.7 µM leupeptin, 0.57 mM phenylmethanesulfonyl flouride (PMSF) and 1% (v/v) aprotinin). Protein extracts were clarified by centrifugation (3 min 13,000 rpm) and transferred to a clean microfuge tube. Protein concentrations of solubilised protein samples were determined using a Pierce® BCA protein assay kit (Thermo Scientific).

2.2.4 Treatment of protein samples with the alkylating agents NEM, AMS and IAA

For treatment of protein samples with the alkylating agents 4 acetamido – 4' – ((iodoacetyl) amino) stilbene – 2 2'-disulfonic acid (AMS) or with N-ethylamide (NEM), protein samples were extracted using acid-lysis (see section 2.2.1) with 25 mM AMS or 25 mM NEM added to the TCA buffer. Also after the 30 min incubation at room temperature, the samples were incubated a 37°C for 5 min before centrifugation and collection of the supernatant. For treatment with iodoacetamide (IAA) protein samples were collected using acid-lysis (see section 2.2.1) but instead of resuspending in TCA buffer, the protein pellet was resuspended in IAA buffer (100 mM Tris-HCl [pH 8.0], 1% SDS and 75 mM IAA) and incubated at 25°C for 20 min. IAA treated samples were then clarified by centrifugation (3 min 13,000 rpm). The protein concentration of AMS, NEM and IAA treated samples were determined using a Pierce® BCA protein assay kit (Thermo Scientific). For Pap1 oxidation experiments, samples were treated with alkaline phosphatase (2 µl phosphatase, 5 µl phosphatase buffer in 15 µl protein sample) (Roche) for 60 min at 37°C in order to dephosphorylate Pap1 prior to analysis by SDS-PAGE.

2.2.5 SDS-PAGE and Western Blot analysis

Protein samples were mixed with an equal volume of 2x SDS loading dye (625 mM Tris-HCl, pH 6.7, 50% (v/v) glycerol, 10% (v/v) sodium dodecyl sulphate (SDS), 0.5% (w/v) Bromophenol Blue) with or without addition of beta-mercaptoethanol (50 µl beta mercaptoethanol in 950 µl SDS page loading dye). Sample volumes equivalent to 1 - 40 µg of protein (indicated in figure legends) were subjected to electrophoresis using 8 – 15 % SDS polyacrylamide gel. Gel recipes were based on the SDS (denaturing) discontinuous buffer system of Laemmli (Laemmli, 1970). Following electrophoresis, proteins were transferred to Protran™ nitrocellulose transfer membrane (Amersham) using a Bio-Rad mini transfer apparatus. Following protein transfer, the membrane was blocked with bovine serum albumin (BSA) (10 % (w/v) in TBST [1 x TBS (1 mM Tris-HCl [pH 8.0], 15 mM NaCl), 0.01% (v/v) Tween 20]) for 30 min at room temperature. The membranes were then probed overnight at 4°C with 1° antibodies (1/1000 in 5%

BSA in TBST) (see Table 2.2 for antibody details), washed 3 time times with TBST (5 min) and then incubated with horseradish peroxidase (HRP) conjugated 2° antibodies (1/2000 in 5 % BSA) for 60 min at room temperature. Finally, membranes were washed 3 times in TBST (5 min) and developed using the Pierce® ECL 2 Western Blotting Substrate (Thermo Scientific) and a digital image was acquired using a Typhoon™ 9400 (GE Healthcare).

Table 2.2 Antibodies used in this study

Name	Details	Source
α-Tpx1	rabbit anti-Tpx1 polyclonal	*Day et al., 2012*
α-SO2/3	mouse anti-peroxiredoxin-SO2/3 monoclonal	(LabFrontiers) (*Woo et al., 2003*)
α-Pap1	rabbit anti-Pap1 polyclonal	Gift from Prof Nic Jones and Dr Caroline Wilkinson
α-FLAG	mouse anti-FLAG monoclonal (m2)	Sigma-Aldrich
α-Actin	mouse anti-Actin monoclonal	Sigma-Aldrich

Table 2.2: Antibodies used in this study.

The names, details and source of all of the antibodies used in this study.

Table 2.3 Oligonucleotide primers used in this study

Primer	Sequence 5' - 3'
*Nde1*Srx1F	CAAGCT**CATATG**ACTTCGATTCACACTGGC
*BamH1*Srx1B	AACTGA**GGGCTA**ATCACTATCCAAAAATTTATTG
*Nco1*SrxpromB	TCAGTT**CCATGG**GATGGTTAAAATGAATGAAAGA
*Pst1*SrxpromF	CAAGCT**CTGCAG**TGTCGCTCAGTCCTTCTTTA
SrxintcheckF	TTGAAGTATTGACCTTACTTCT
nmtendabi	GCAGCTTGAAATGGGCTTCC
ctt1checkF	GCTTTTGAATAGAAGAATACTA
ctt1checkR	AAGCCTTAGACCTTATTTATAT

Table 2.3: Oligonucleotide primers used in this study.

The name and sequence of all of the oligonucleotide primers used in this study. The relevant restriction sites are in bold.

Table 2.4 Plasmids used in this study

Plasmid	Reference
pRep1	Craven *et al*., 1998
pRip1	Craven *et al*., 1998
pRep1 *tpx1*$^{+}$	Veal *et al*., 2004
pRep1 *tpx1*^{T86E}	Dr J Rand (unpublished)
pRep1 *tpx11*$^{1-181}$	Day *et al*, 2012
pRep41 *FLAGsrx1*	Bozonet *et al*, 2005
pRep41 *promFLAGsrx1*	This Study (2.5.7)
pRip1 *promFLAGsrx1*	This Study (2.5.7)

Table 2.4: Plasmids used in this study.

The names and sources of all of the plasmids used in this study.

2.3 Fluorescence methods for the detection of ROS

2.3.1 Measuring the depletion of extracellular H_2O_2 using PeroXOquant

PeroXOquant Quantitative Peroxide Assay kit with aqueous compatible formulation (Thermo scientific) was used according to manufacturer's protocol. Cultures of 972 *S. pombe* cells were grown in EMM media to OD_{595} of 0.5. H_2O_2 was added to the growing cultures at a final concentration of 50 μM. 20 μl of *S. pombe* cell were taken at 0 - 1800 seconds, mixed in a 96-well microplate with 200 μl of working solution (freshly prepared according to manufacturer's instructions). The mix was incubated at room temperature for 20 min. Absorbance at 560 nm was measured using a TECAN infinite M200 plate reader. The blank value (EMM without hydrogen peroxide) was subtracted from all sample measurements.

2.3.2 Detection of Intracellular ROS using H_2DCFDA

Methods were adapted from (Dirmeier et al., 2002). Aliquots of 2 mM H_2DCFDA (2',7'-dichlorodihydrofluorescein diacetate, Fluka) dissolved in DMSO were stored at -80°C in the dark. H_2DCFDA was added to 10 ml of exponentially growing *S. pombe* (972) grown in EMM (supplemented with adenine, leucine, uracil and histidine) to a final concentration of 10 µM. After a further 90 min incubation (30°C, with agitation), 1 ml aliquots of DCFDA-loaded cells were transferred to microfuge tubes and incubated with 0 – 10,000 µM H_2O_2 for 10 min. Cells were pelleted by centrifugation at 6000 G for 30 s, supernatant removed and the cell pellet re-suspended in 20 µl EMM. The re-suspended cells were mounted on a microscope slide with a coverslip placed on top. The cells were then examined under the 10x, 40x and 65x objective lens using Zeiss Axioskop fluorescent microscope (Excitation 450-490 nm, Emission 515 nm) and images were taken at identical exposures. Alternatively, subsequent to incubation with H_2O_2, the samples were washed once with PBS then resuspended in 1 ml PBS (137 mM NaCl, 2.7 mM KCl, 10 mM Na_2HPO_4, and 1.8 mM KH_2PO_4 pH 7.4). 200 µl aliquots of this cell suspension were transferred to a 96 well plate and their fluorescence quantified using a TECAN infinite M200 plate reader (excitation 495 nm, emission 529 nm).

2.3.3 Measuring changes in intracellular H_2O_2 concentration using PF3 (S. pombe and HEK293)

The H_2O_2 sensitive fluorescent probe PF3-Ac (Dickinson et al., 2010) was added to 10 ml (2 x 10^7) exponentially growing *S. pombe* cells (OD 0.4 – 0.5) to a final concentration of 5 µM and incubated at 30°C in the dark for 20 minutes. After 20 min the cells were washed once in an equal volume of PBS then re-suspended in an equal volume of PBS. HEK293 cells were incubated for 20 min in DPBS containing 5 µM PF3-Ac, washed three times then re-suspended in DPBS to a final concentration of 2 x 10^6 cells/ml. Following re-suspension, 200 µl aliquots (4 x 10^6 *S. pombe* cells, 4 x 10^5 HEK293 cells) of PF3-labelled cells, unlabelled cells and PBS controls were transferred to a 96 well plate. Fluorescence measurements were made at 529 nm following excitation at 495 nm using a TECAN Infinite M200PRO plate reader and the average fluorescence of the unlabelled cells was deducted to calculate fluorescence due to PF3 (F). Measurements were taken 0 and 60 seconds before addition of H_2O_2 to determine the basal rate of reaction of PF3 with endogenously produced H_2O_2 $(\Delta F/\Delta t)_{no\_stress}$ (Eq. 1).

$$\left(\frac{\Delta F}{\Delta t}\right)_{no\_stress} = \frac{F_{t60} - F_{t0}}{60} \quad (Eq. 1)$$

Fluorescence measurements were then made 30, 60 and 120 seconds following addition of H_2O_2 (0 – 500 µM) and used to calculate the rate of change of fluorescence $(\Delta F/\Delta t)_{stress}$ (Eq. 2).

$$\left(\frac{\Delta F}{\Delta t}\right)_{stress} = \frac{F_{t120} - F_{t30}}{90} \quad (Eq. 2)$$

The rate of fluorescence change due to exogenous H_2O_2 ($\Delta F/\Delta t$) was calculated using Eq.3 and plotted against H_2O_2 concentration using the graphics and statistics package R.

$$\left(\frac{\Delta F}{\Delta t}\right) = \left(\frac{\Delta F}{\Delta t}\right)_{stress} - \left(\frac{\Delta F}{\Delta t}\right)_{no\_stress} \quad (Eq.3)$$

The R linear model function (Wilkinson and Rogers, 1973, Chambers., 1992) was used to calculate the derivative and 95% confidence interval for the change ($\Delta F/\Delta t$) when H_2O_2 is increased from 0 – 100 µM H_2O_2 (*S. pombe*) or increased from 0 – 20 µM (HEK293 cells). This gradient was extrapolated using the equation y = mx + c and plotted on the same axis as the ($\Delta F/\Delta t$) data.

2.4 Sensitivity Tests

2.4.1 Halo Tests

~2 x 10^4 exponentially growing *S. pombe* cells were pipetted along separate lines radiating towards a filter paper disk (Whatman microfiber paper) soaked in 1 µl of between 0.3 - 30% (v/v) H_2O_2. Plates were incubated at 30°C for 2-4 days and the zone of growth inhibition around the filter assessed for each strain.

2.4.2 Dilution Assays

Cells were grown to mid-log phase and serial 10-fold dilutions were spotted onto solid media containing varying concentrations of H_2O_2 using a 96-well plate replica plater (Sigma-Aldrich). Plates were then incubated at 30°C for 2-4 days and a digital image was taken using an ordinary desktop scanner (HP Scanjet G2710).

2.5 Molecular Biology Techniques

2.5.1 Polymerase Chain Reaction

PCR reactions to amplify DNA fragments for strain construction and for diagnostic purposes were performed using the High Fidelity (HF) PCR system in a final volume of 50 µl. Reaction mixes contained 1 µl of template DNA (972, LT1 or LT3), 5 µl of 10x buffer with $MgCl_2$ (supplied with enzyme), 200 µM of each dNTP (dATP, dCTP, dTTP, dGTP), 50 pmol of each oligonucleotide primer and 0.75 µl (3.5 units/µl) of HF polymerase. All HF PCR reaction were performed in a Multigene II PCR machine (Labnet) under the following conditions:

Step (1) Denature: 2 min at 94˚C

Step (2) Denature: 30 sec at 94˚C

Step (3) Annealing: 30 sec at 48 - 56˚C

Step (4) Elongation: 1 min / kilobase (kb) at 72˚C

Steps (2) to (4) repeated for 35 cycles

Step (5): 10 min at 72˚C

Hold at 10˚C

The oligonucleotide primers used in this study were synthesised by Eurogentec (UK) or Primer Design (UK) and are listed in Table 2.3. PCR products were analysed by electrophoresis on a 1% (w/v) agarose gel prepared and run in 1 x TAE (40 mM Tris acetate, 1 mM EDTA [pH8.0]). Gels were stained with 0.02% (w/v) ethidium bromide and a digital image was acquired using a Gel doc 1000 (Biorad). For use in cloning, PCR products were isolated using an QIAquick® Gel extraction Kit according to the manufacturer's instructions.

2.5.2 Bacterial Growth Conditions

Escherichia coli were grown in Luria Broth (LB) (2% (w/v) Bacto tryptone, 1% (w/v) Bacto yeast extract, 1% (w/v) NaCl, pH 7.2). For the formation of solid media 2 % (w/v) Bacto agar was added. LB media containing 0.1 mg/ml ampicillin (Sigma-aldrich) (LB Amp^+) was used for the growth of *E. coli* transformed with plasmids carrying the ampicillin resistance gene.

2.5.3 Genomic DNA Extraction (S. pombe)

A nichrome wire inoculation loop (Microspec.org) was used to collect a sample of *S. pombe* cells (CHP429) directly from a YE5S agar plate. The cells were then washed in 1 ml H_2O and resuspended in 200 µl DNA breakage buffer (10 mM Tris-HCl [pH 8.0], 1 mM ethylenediaminetetra acetic acid (EDTA) [pH 8.0], 100 mM sodium chloride (NaCl), 1% (w/v) sodium dodecyl sulphate (SDS), 2% (v/v) Triton X-100), 200 µl glass beads (425-600 microns, Sigma) and 200 µl phenol:chloroform. The cells were disrupted using a Hybaid Ribolyser (power 5 for 20 sec), a further 500 µl DNA breakage buffer was added and the tubes were vortexed. The aqueous layer was then separated by centrifugation (5 min, 13,000 rpm) and transferred to a fresh tube. The DNA was precipitated by the addition of 1/10 volume of 3 M sodium acetate [pH 5.2] and 2 volumes of 100% ethanol (EtOH). The DNA was pelleted by centrifugation (15 min, 13,000 rpm), washed in 70% EtOH, air dried and resuspended in 100 µl H_2O.

2.5.4 Transformation, Propagation and Isolation of Plasmids (E. coli)

E. coli SURE cells (*e14-(mcrA$^-$) Δ(mcrCB$^-$hsdSMR$^-$mrr)171 endA1 supE44 thi- 1 gyrA96 relA1 lac redB recJ umuC::Tn5 (Kan^r) uvrC [F'proAB laclZ Δmis Tn10 (Tel^r)*]), were used for the propagation and isolation of plasmids. Competent SURE cells were transformed with plasmid DNA using standard techniques (Maniatis *et al*., 1982). 100 µl of competent cells were incubated on ice with 1-2 µl (5 – 10 µg) plasmid DNA for 30 min, subjected to a heat shock (42˚C) for 2 min and 1 ml LB was added before incubation at 37˚C for 45 – 60 min. The cells were then plated onto LB agar plates containing ampicillin and incubated overnight at 37˚C. Plasmid DNA was isolated from *E. coli* cells using a GenElute™ Plasmid Miniprep Kit according to the manufacturer's instructions.

2.5.5 Transformation of S. pombe

Plasmid and PCR-derived DNA were introduced into *S. pombe* cells using the lithium acetate (LiAc) method described by Moreno *et al* (Moreno et al., 1991).

Cells were grown to mid-log phase (~ OD_{595} 0.5, ~ 1 x 10^7 cells/ml) in YE5S media. Cells were pelleted by centrifugation at 2000 rpm for 2 min, washed twice in equal volumes of sterile H_2O followed by 1 ml LiAc/TE solution (100 mM LiAc [pH 7.0], 10 mM Tris-HCl [pH 7.5], 0.1 mM EDTA [pH 8.0]) and resuspended in LiAc/TE at 1 x 10^9 cells/ml. ~ 2 µg plasmid DNA and an equal concentration of salmon sperm carrier DNA were then added to 100 µl cells incubated at room temperature for 10 min. 260 µl PEG/LiAc/TE (100 mM LiAc [pH 7.0], 1 x TE and 50% (v/v) polyethylene glycol (PEG) 4000) was added to the transformation mixture and the cells incubated at 30°C for 30 - 60 min with agitation. After the addition of 43 µl dimethyl sulphoxide (DMSO) (Sigma Aldrich), the cells were incubated at 42°C for 5 min and then washed in 1 ml dH_2O. The cells were then resuspended in 100 µl dH_2O and spread onto EMM agar plates supplemented with the appropriate amino acids. Plates were incubated at 30°C for 3 – 5 days until colonies appeared.

2.5.6 Restriction Endonuclease Digestion, Phosphatase Treatment and DNA Ligation Reactions

Restriction digests were performed using standard techniques (Sambrook *et al*., 1989). Enzymes and buffers were supplied from Promega and Fermentas. The digested vector was dephosphorylated using an alkaline phosphatase isolated from calf intestine (Roche Diagnostics). The vector and fragment DNA was purified using a QIAGEN gel purification kit according to the manufacturer's instructions and then ligated at a ratio of approximately 1 vector: 5 fragment molecules using T4 DNA ligase (Promega) and 10 x T4 DNA ligase buffer incubated overnight at 15˚C.

2.5.7 Plasmid Constructs

The plasmids constructed in this study are listed below:

1. pRep41 *promFLAGsrx1*

The *Srx1* promoter sequence was amplified by PCR from CHP429 *S. pombe* genomic DNA using the *Nco1*SrxpromB and the *Pst1*SrxpromF oligonucleotide primers (Table 2.2). The PCR product was isolated as described above (see section 2.5.1), digested with the *Nco1* and *Pst1* restriction endonucleases and ligated into pRep41 *FLAGsrx* (Bozonet et al., 2005) which had also been digested with *Nco1* and *Pst1*.

2. pRip1 *promFLAGsrx1*

A DNA fragment containing the Srx1 promoter sequence and an N-terminally FLAG-epitope-tagged Srx1 gene was obtained by digesting the plasmid pRep41 *promFLAGsrx1* with the *Pst1* and *Bam*H1 restriction endonucleases. This digestion product was then ligated into pRip1, which had also been digested using *Pst1* and *Bam*H1.

All plasmids used in this study are listed in Table 2.4.

2.5.8 Chromosomal Gene Tagging (FLAG-Srx1)

An *S. pombe* strain expressing an N-terminally FLAG-epitope tagged Srx1 gene, under the control of its natural promoter, from its natural locus, was created using the non-replicating pRip1 *promFLAGsrx1* (described in 2.5.7). This construct was linearised by digestion with the restriction endonuclease *HinDIII*, and the digestion product was transformed into Δ*srx1* (SB6) *S. pombe* cells. Transformants were screened by growth on solid EMM medium lacking uracil and leucine to select for transformants containing the *ura4*$^{+}$ and *leu2*$^{+}$ markers. Integration at the correct chromosomal loci was confirmed by PCR using the oligonucleotide primers *SrxintcheckF* and *nmtendabi* as well as sequencing of genomic DNA extracts. Finally western blot analysis was used to verify that cells were expressing FLAG-epitope tagged Srx1 (see 5.5, Figure 5.4).

2.6 Mathematical Methods

2.6.1 Model Construction, Simulation and graphical representation of simulation data

All computer models used in this study were built using the biochemical network simulator COPASI (version 4.13, build 87) (Hoops et al., 2006) (www.copasi.org) which supports the Systems Biology Markup Language (SBML). It was assumed that the species concentrations used in our model simulations would be high enough to negate any stochastic effects. Accordingly, all time course simulations were performed in COPASI using the deterministic Livermore Solver for Ordinary Differential Equations (LSODA) algorithm (Petzold, 1983) using the default parameters. Steady-state flux calculations were performed using the COPASI steady-state calculation function using the default parameters. All simulation data was exported as a text file (.txt) using Notepad (Microsoft) and further manipulation and graphical representation of the data was performed using the R software environment.

2.6.2 Calculating the intracellular concentration of S. pombe proteins and estimation of the volume of the intracellular compartment (Vol_{int}).

The intracellular concentration of specific *S. pombe* proteins were estimated using published data for the global quantification of the *S. pombe* proteome (Marguerat et al., 2012). The supplementary data accompanying the Marguerat *et al*, (2012) paper provides absolute values for the copy number per cell (cpc) for the entire *S. pombe* proteome and was used to calculate the intracellular concentration of a specific *S. pombe* proteins using equation 4 (Eq. 4).

$$M = \frac{cpc}{N_A \times Cell_{Vol}} \ (Eq. 4)$$

Where *M* is the molar intracellular concentration of a specific *S. pombe* protein, *cpc* is the copy number per cell for that protein, N_A is the Avagadro constant 6.02

x 10^{23} mol^{-1} and $Cell_{Vol}$ is the mean volume of an exponentially growing (OD595 ~ 0.5, in EMM) wild-type (972) *S. pombe* cell measured as 126 μm^3 using a cell counter and analyser system (CASY®, Schärfe System). An estimate for the total intracellular volume (Vol_{int}) of an OD_{595} = 0.4 wild-type (972) *S. pombe* culture was calculated using equation 5 (Eq. 5) where $Cell_{num}$ is the number of *S. pombe* cells in a 50 ml culture and equal to 4 x 10^8 (OD 0.1 = 2 x 10^6 cells/ml).

$$Vol_{int} = Cell_{vol} \times Cell_{num} \ (Eq. 5)$$

2.6.3 Generating a quantitative data set representing the oxidation of Tpx1 and Pap1

Western blot analysis (see section 2.2) was used to detect Tpx1 proteins in AMS-treated cell extracts from *S. pombe* cells exposed to a range of H_2O_2 concentrations (see Chapter 3 for details) and digital images were acquired using a Typhoon™ 9400 (GE Healthcare). Tpx1 containing bands were quantified using the densitometry software package ImageQuantTL (GE Healthcare). Equal size lanes were drawn over each individual protein containing lane and the minimum profile background-subtraction method was applied. Individual bands to be quantified were selected manually ensuring that the size of the quantification area for a particular oxidation state was conserved between lanes. The volume (see ImageQuantTL help section for details on band volume) of material in each quantification area was then exported to Excel (Microsoft) for further analysis.

An estimate of the concentration of Tpx1 protein in each band was then made. This estimate was based on the assumption that that the fraction of material in an individual band, relative to the total volume of material that bands lane, is proportional to the fraction of total cellular Tpx1 in that band (Eq. 5).

$$\frac{Volume\ of\ individual\ band}{Total\ volume\ of\ all\ bands\ in\ lane} \propto \frac{Amount\ of\ Tpx1\ in\ band}{Total\ Tpx1\ in\ cell} \ (Eq. 5)$$

The total concentration of Tpx1 in an *S. pombe* cell was calculated to be ~ 4 µM (see 2.6.2). The concentration of Tpx1 in a particular oxidation state could

therefore be estimated by dividing the volume of the band representing that oxidation state by the total volume of all bands in that lane and multiplying by 4 µM. This allowed the creation of a quantitative data set representing the changes in the concentration of each Tpx1 oxidation state in response to multiple concentrations of H_2O_2 at different time points. A quantitative data set for the changes in oxidation state of Pap1 (see Chapter 4 for details) was created using the same general method. The total concentration of Pap1 in an *S. pombe* cell calculated at ~ 0.0245 µM (see 2.6.2). It is appropriate to note that this method of quantification assumes that total Tpx1/Pap1 in the cell is the same in each sample. This is a reasonable assumption since genome-wide measurements of expression changes in response to H_2O_2 indicate that total Tpx1 and total Pap1 do not change significantly at the time points used in this study (Lackner et al., 2012).

2.6.4 Generating a quantitative data set representing changes in Trx1-red

Western blot analysis (see section 2.2) was used to detect changes in the level of Trx1-red in AMS-treated cell extracts from *S. pombe* cells (JB35 (FLAG-Trx1)) exposed to a range of H_2O_2 concentrations (see Chapter 4 for details) and digital images were acquired using a Typhoon™ 9400 (GE Healthcare). Equal size lanes were drawn over each individual protein containing lane and the minimum profile background-subtraction method was applied. The bands representing Trx1-red in each lane were selected manually ensuring that the size of the quantification area for each band was conserved between lanes. The volume (see ImageQuantTL help section for details on band volume) of material in each quantification area was then exported to Excel (Microsoft) for further analysis. To calculate the fraction of Trx1-red each sample, relative to the non-H_2O_2-treated samples, the volume of material in each Trx1-red band was divided by the volume of material in the Trx1-red detected in the non-H_2O_2-treated sample. The total concentration of Trx1 in an *S. pombe* cell was calculated to be ~ 0.7 µM (see 2.6.2). Therefore, to estimate the concentration of Trx1-red in each sample, the fraction of Trx1-red, relative to the non-treated samples were multiplied by 0.7 µM.

2.6.5 Generating a quantitative data set representing changes in Srx1

Based on two global quantification studies of the *S. pombe* (972) proteome no Srx1 protein could be detected in H_2O_2 treated and non-stressed exponentially growing *S. pombe* cells (Marguerat et al., 2012, Lackner et al., 2012). Therefore an alternative method was used to estimate the initial concentration Srx1 in none-stressed cells, as well as measure changes in Srx1 protein levels in response to H_2O_2. Western blot analysis (see section 2.2) was used to detect changes in the level of Srx1 in NEM-treated cell extracts from *S. pombe* cells (LT1 (FLAG-Srx1)) exposed to 0 – 1 mM H_2O_2 for up to 90 min (see Chapter 5 for details). An NEM-treated protein sample of non-H_2O_2-treated sample FLAG-Trx1 (JB35) cells was ran on the same gel on the same gel as the FLAG-Srx1 cell extracts. The volume of material in each FLAG-Srx1 band, relative to the FLAG-Trx1-red band, was calculated and then multiplied by 0.7 µM (intracellular Trx1 concentration, see 2.6.4). These values were then used as an estimate for the concentration of FLAG-Srx1 in each sample.

2.6.6 Parameter estimation and identifiability analysis for model of in vivo oxidation of Tpx1 (Chapter 3)

All parameter estimation was performed using the parameter estimation function in COPASI (ver 4.13, build 87). The quantitative data from each Tpx1 oxidation experiment was saved as individual .txt files (see appendix B) and mapped to COPASI. As well as the Tpx1 oxidation data, the quantitative measurements for the removal of extracellular H_2O_2 (see 2.3.1) was also mapped for inclusion in the parameter estimation. Finally a mock data set which assumes a steady-state, non-stressed intracellular H_2O_2 concentration of 1 nM was also included in the parameter estimation based on the broad range of experimental evidence (reviewed in (Stone and Yang, 2006)) that normal physiological intracellular [H_2O_2] is in the nanomolar region in a range of organisms. The parameters calculated using parameter estimation are detailed in Chapter 3 (Table 3.6).

Using this data set and the alternative models of Tpx1 oxidation (See Chapter 3 for details) parameter estimation was performed 500 times from random initial parameter values using the Levenberg-Marquardt algorithm (Marquardt, 1963).

The parameter sets calculated by each of the 500 parameter estimations, along with the sum of squared residuals (SSR) for that parameter set, were exported as .txt files and all further analysis and graphical representation was performed using R. The SSR values, and the number of parameters estimated (m) were used to calculate the Akaike information criterion (AIC) (Akaike, 1973) each parameter set using equation 6 (Eq. 6).

$$AIC = 2m - 2\ln(SSR) \ (Eq. 6)$$

Identifiability analysis for the model parameters was performed in COPASI (ver 4.13, build 87) using the methods described by Schaber (2012) (Schaber, 2012). This required the calculation of one-dimensional likelihood profiles for each of the model parameters. This was done by performing multiple parameter estimations with the parameter of interest fixed at different values. The effect that changing the value of this parameter has on the SSR, calculated by each parameter estimation, was plotted to create a one-dimensional likelihood profile for that parameter. The 95% confidence region (p) for that likelihood profile was then calculated using equation 7.

$$p = SSR \times \left(1 + \frac{m}{n-m}\right) \times F^{\alpha}_{m,n-m} \ (Eq. 7)$$

Where SSR is the lowest SSR estimated, m is equal to the number of parameters in the model, n is the number of data points used to parameterise the model and $F^{\alpha}_{m,n-m}$ is the α quantile of the F-Ratio-distribution of m and n. $F^{\alpha}_{m,n-m}$was calculated using the F distribution function qf() in R (Johnson et al., 1995), using the value 0.95 (to indicate 95% confidence) as the first argument, followed by m and n-m as the second and third arguments. Plotting of the one-dimensional likelihood profiles, as well as the calculation and plotting of the 95% confidence intervals, were all performed using R.

2.6.7 Parameter estimation for the model of in vivo oxidation of Tpx1 and Trx1 (Chapter 4)

Parameter estimation for the *in vivo* model of Tpx1 and Trx1 oxidation was performed similarly to the model of *in vivo* Tpx1 oxidation (2.6.6) however the concentration of reduced Trx1 (2.6.4) was also included in the parameter estimation data set. Furthermore, additional parameters were included for estimation (Chapter 4, Table 4.5).

2.6.8 Calculating a chi^2 value to assess the correlation between simulation and experimental data

The chi^2 (χ^2) representing the correlation between the simulation and the experimental data was calculated using equation 8 (Eq. 8).

$$\chi^2 = \sum \left(\frac{sim(t) - data(t)}{\sigma\big(data(t)\big)} \right)^2 \quad (Eq. 8)$$

Where sim(t) is the simulation data for a given time point "t", data(t) is the experimental data for time point "t" and σ(data(t)) is the standard deviation of data(t). As a rule of thumb, if the calculated chi squared value is less than or equal to 2x the number of data points the simulation can be said to be a good fit to the experimental data.

Chapter 3. Building a model of Tpx1 oxidation and hyperoxidation

3.1 Introduction

As discussed in chapter 1 three theories have been proposed for the biological purpose of Prx hyperoxidation (Figure 3.1). The flood gate hypothesis (Figure 3.1 A) proposes that the Prxs can act as a barrier to H_2O_2 signalling and suggests that hyperoxidation/inactivation is a mechanism which allows local H_2O_2 levels to increase and thus facilitate H_2O_2 dependent signalling events (Wood et al., 2003b). A second theory for the biological role of Prx hyperoxidation relates to the finding that Prx molecules are able to form high molecular weight oligomeric complexes (Jang et al., 2004, Moon et al., 2005). These high molecular weight structures have been demonstrated to act as protein chaperones, able to protect proteins from oxidative damage. The observation that Prx hyperoxidation actually facilitates Prx oligomer formation has led to the suggestion that hyperoxidation evolved as a mechanism to promote the chaperone activity of Prx (Figure 3.1 B) (Jang et al., 2004, Moon et al., 2005). Finally, the hyperoxidation of the *S. pombe* peroxiredoxin Tpx1, has been demonstrated to increase the levels of reduced Trx1 (Figure 3.1 C). This suggests that hyperoxidation is a mechanism which increases the availability of Trx1 for reduction of oxidised protein substrates, allowing the repair of damaged proteins (Day et al., 2012).

These findings each provide clues as to why hyperoxidation occurs. However it is less clear under which conditions hyperoxidation occurs *in vivo*. As discussed in chapter 1 *in vitro* strategies have provided much information about the biochemistry of the peroxiredoxins. However, *in vivo* Prx oxidation has been demonstrated to be influenced by other factors such as compartmentalisation, the availability of reductases and local H_2O_2 concentration (Cao et al., 2014). A computer modelling approach allows the integration of all the available information on Prx biochemistry, compartmentalisation and the relative abundance of thioredoxin system components. Accordingly, this is expected to provide a more comprehensive understanding of under what conditions Prx becomes hyperoxidised *in vivo*.

When building the models, the general biochemical principles underlying Prx oxidation were taken into account. However many of the biochemical rates were obtained using experimental data from the fission yeast *S. pombe*. *S. pombe* contains a single 2-Cys Prx Tpx1. This makes analysis and interpretation of Tpx1 *in vivo* oxidation data easier than in mammalian systems which have multiple Prxs. Oxidation of Tpx1 has been well characterised and the genetic amenability of *S. pombe* has led to the development of Tpx1 mutants with altered sensitivity to hyperoxidation (Koo et al., 2002). Finally, there are a number of post-genomic resources available for *S. pombe* including the genome-wide quantification of absolute mRNA and protein levels (Marguerat et al., 2012) which provide accurate concentration data to inform our model.

Previously published computer models containing peroxiredoxin reactions (Pillay et al., 2011, Adimora et al., 2010) have modelled Prx oxidation and hyperoxidation using a simple method which did not separately take into account each of the Prx oxidation states. Studies of Prx oxidation in human and yeast cells have described the formation of three distinct Prx disulphide homodimers in response to H_2O_2 but no comprehensive mechanism has been established to describe the dynamics of these Prx species (Peskin et al., 2013, Jara et al., 2007, Haynes et al., 2013). Here we have built the first detailed model of Prx hyperoxidation able to describe all of these Prx oxidation states. This increases confidence in the conclusions drawn from this model since they are based on an accurate representation of Prx biochemistry. The rest of this chapter describes the development of the computational model of Prx oxidation as well as experimental evidence to support the main predictions of the model.

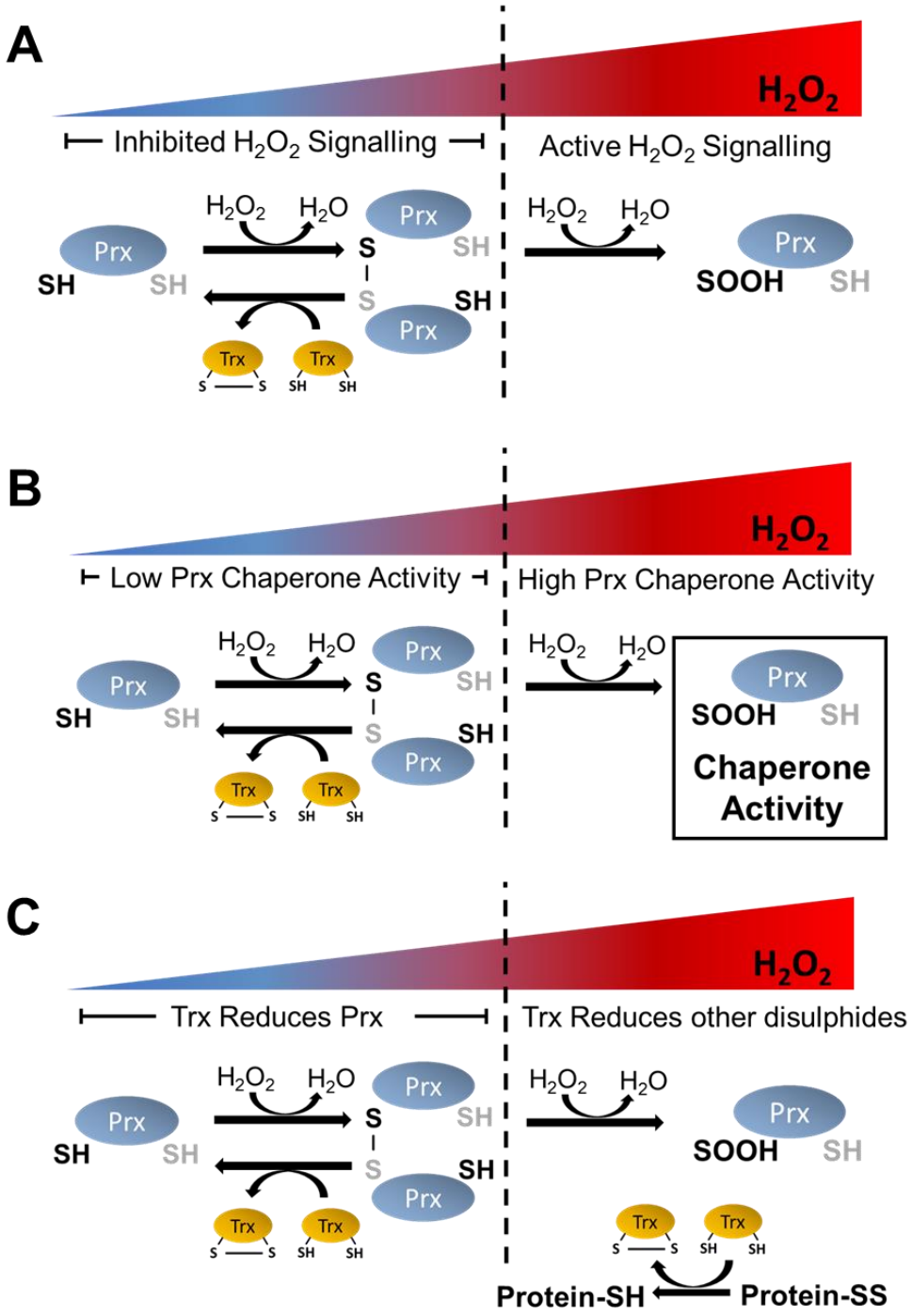

Figure 3.1: Diagrams representing the three proposed theories for the purpose of Prx hyperoxidation.

(A) The flood gate hypothesis (Figure 3.1 A) proposes that the Prxs can act as a barrier to H_2O_2 signalling and proposes that the hyperoxidation/inactivation of Prx is a mechanism to allow local H_2O_2 levels to increase and thus facilitate H_2O_2 dependent signalling events. (B) A second theory proposes that Prx hyperoxidation is a mechanism that increases the chaperone activity of Prx. (C) The third theory suggests that Prx hyperoxidation is a mechanism which increases the availability of Trx1, allowing the repair of damaged proteins.

3.2 Preliminary Modelling of H_2O_2 dynamics and Peroxiredoxin oxidation

To test and develop methods for simulating Prx oxidation we began by building a number of preliminary models based on previously published data and fundamental biological principles. Examining the behaviour of these preliminary models provided us with useful insight into how the model structure would influence the dynamics of peroxiredoxin oxidation.

3.2.1 Modelling the in vitro oxidation of human Prx2 in the absence of redox cycling

A previously published *in vitro* assay investigated the oxidation of purified human Prx2 & Prx3 at a range of H_2O_2 concentrations (10 µM – 5000 µM) in the absence of any reducing agents such as Trx1 (Peskin et al., 2013). Using SDS-PAGE and LC/MS methods the team demonstrated that both of these peroxiredoxins were able to form a range of different oxidation states upon exposure to H_2O_2 (Figure 3.2). The different oxidation states (outlined in Figure 3.3) included Prx homodimers containing either a single disulphide bond (Prx-ox#1), two disulphide bonds (Prx-ox#2) or a single disulphide bond with a sulphinic acid on the remaining peroxidatic cysteine (Prx-ox:SOOH). The existence of these three distinct Prx homodimers has also been observed in the *S. pombe* peroxiredoxin Tpx1 using western blot methods (Jara et al., 2007) and is likely to be a general feature of all the typical 2-Cys peroxiredoxins.

This assay demonstrated very clearly that, in the absence of disulphide recycling the relative abundance of these three dimers was dependent on H_2O_2 concentration (Figure 3.2). At the lowest concentrations Prx-ox#1 was the most prominent dimer but as H_2O_2 was increased Prx-ox#2 become more prominent, increasing the concentration further caused Prx-ox:SOOH to become the prominent dimer.

At the point of commencing this PhD project, there was no published model of Prx oxidation that takes into account all three of these Prx homodimers and there was no definitive description of the reactions relating them. Therefore a series of potential models to represent Prx oxidation were constructed and their ability to simulate the findings of Peskin et al (2013) was tested. It was clear from the data

that there were a number of essential reactions that would need to be included to explain the data (Figure 3.4, Table 3.1). However there were four biochemically feasible reactions which were not necessarily required to explain the data. These reactions were referred to as “optional reactions” (Figure 3.4 Table 3.1). A series of models containing all the different possible combinations of optional reactions were created and the ability of these models to simulate the data from Peskin *et al* (2013) was tested.

Optional reaction 1 (Opt1) represents the oxidation of the unbound Cys_P-SH in the Prx-ox#1 dimer by H_2O_2. Initially this reaction was considered to be essential to explain the appearance of the Prx-ox#2 dimer. Indeed in Peskin *et al* (2013) this reaction was suggested to be equally sensitive to H_2O_2 as the Cys_P-SH in the Prx-SH monomer. However, when a model was built using the reaction Opt1, this model was unable to simulate the changes in Prx-ox#2 concentration after H_2O_2 exposure (Figure 3.5 A). Instead of Opt1, we hypothesised that an alternative reaction, Opt2 (Figure 3.4), could be used to describe the formation of Prx-ox:SOH and might allow the model to accurately simulate changes in Prx-ox#2 concentration. The reaction Opt2 assumes that Prx-ox:SOH can form via the reaction of two Prx-SOH monomers (Figure 3.4). Indeed, a model containing both Prx-ox:SOH formation routes, Opt1 and Opt2, was better able to simulate the changes in Prx-ox:SOH concentration (Figure 3.5 B). Furthermore, a model containing Opt2 only was equally able to simulate the experimentally observed dynamics of Prx-ox#2 (Figure 3.5 C). When simulating the effects of Opt1 and Opt2 on the dynamics of Prx-ox#2, Opt3 (Figure 3.4) was assumed to be the only route of Prx-ox:SOOH formation and Re4 was assumed to have the rate constant k_{hyp_ox} (Figure 3.5).

Interestingly, the finding that the reaction Opt2 is required to accurately simulate the dynamics of Prx-ox#2 formation suggests that the formation of Prx-ox:SOH via the reaction of two Prx-SOH monomers could be the dominant route for the formation of Prx2-ox#2 in the *in vitro* assay.

There was some ambiguity as to the best method for describing the dynamics for the hyperoxidised Prx species (Prx-ox:SOOH and Prx-SOOH). A number of *in vivo* studies have demonstrated that Prx-ox:SOOH always precedes Prx-SOOH formation and therefore that Prx-ox:SOOH will form via Opt3 and that Prx-SOOH

must be produced by the reduction of the disulphide bond in Prx-ox:SOOH (Jara et al., 2007). However in the *in vitro* assay Prx-SOOH was detected despite the absence of disulphide reductases, this indicates that *in vitro* Prx-SOOH must be able to form through Re4. This provides two possible biochemically feasible explanations for the formation of Prx-ox:SOOH, the oxidation of the Cys_P-SOH in Prx-ox:SOH by H_2O_2 (Opt3) or the reaction between a Prx-SOOH and Prx-SOH monomer (Opt4). However, neither of these models was able to accurately describe the dynamics of Prx-ox:SOOH and Prx-SOOH formation (Figure 3.5 D & E). Specifically, the experimental data demonstrated that Prx-ox:SOOH would form after treatment with a lower H_2O_2 concentration than Prx-SOOH, whereas both models predicted each hyperoxidised form would appear at the same concentration (Figure 3.5 D & E). Adapting the model so that the rate constant $k_{slow\_hyp\_ox}$ used for re4 was ten-fold slower than k_{hyp_ox} used for Opt3, caused the model to simulate Prx-ox:SOOH formation at a lower H_2O_2 concentration than Prx-SOOH (Figure 3.5 F). This demonstrates that during the *in vitro* oxidation of Prx2, both routes of hyperoxidation (Re4 & Opt3) must occur in order to explain the data provided that the Cys_P-SOH of the Prx-SOH monomer is less sensitive to oxidation by H_2O_2 than the Cys_P-SOH in Prx-ox:SOOH.

To summarise, this preliminary model has demonstrated that in order to explain the dynamics of the *in vitro* oxidation of Prx2 in the absence of redox cycling the oxidation of the Cys_P-SH in Prx-ox#1 (Opt1) is not required. This is based on the observation that a model containing Opt2, instead of Opt1, was sufficient to simulate the dynamics of Prx-ox#2 (Figure 3.5 C). In addition to this, the model required two hyperoxidation reactions (Re4 & Opt3) to accurately simulate the *in vitro* dynamics of Prx-SOOH and Prx-ox:SOOH, but the rate constant for Re4 ($k_{slow\_hyp\_ox}$) needed to be slower than for Opt3 (k_{hyp_ox}). These findings will be taken into account when building the *in vivo* model of Prx oxidation and hyperoxidation described in the following sections.

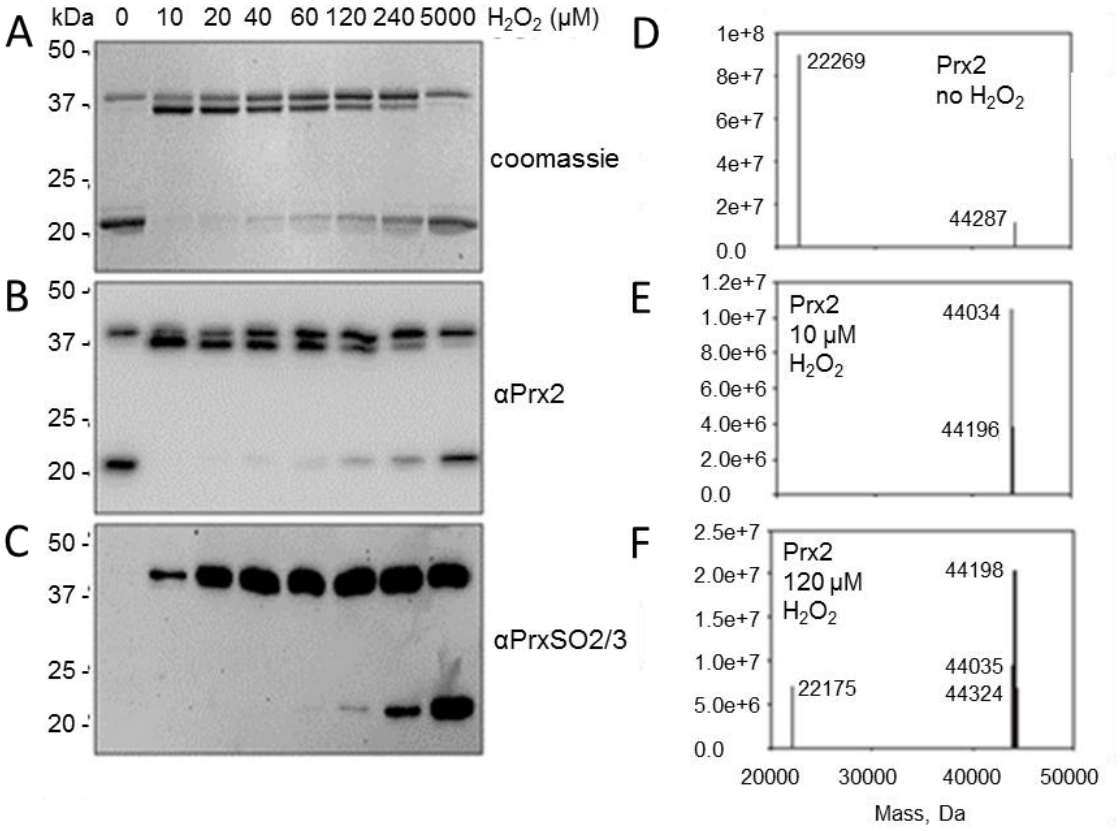

Figure 3.2: SDS-PAGE and mass spectrometry methods identify multiple oxidation states for Prx2 (adapted from Peskin et al, 2013).

The oxidation of human Prx2 was investigated using an *in vitro* assay. Purified Prx2 was incubated with the indicated [H_2O_2] for 300 seconds (see Peskin et al, 2013 for detailed methods). The reactions mixtures were then separated using SDS-PAGE and Prx protein was visualised using (A) coomassie staining or western blotting with (B) αPrx2 antibodies or (C) αPrxSO2/3 antibodies. LC/MS analysis was used to measure the mass and signal intensity of alternative Prx oxidation states in reaction mixtures containing (D) no H_2O_2 (E) 10 μM H_2O_2 and (F) 120 μM H_2O_2.

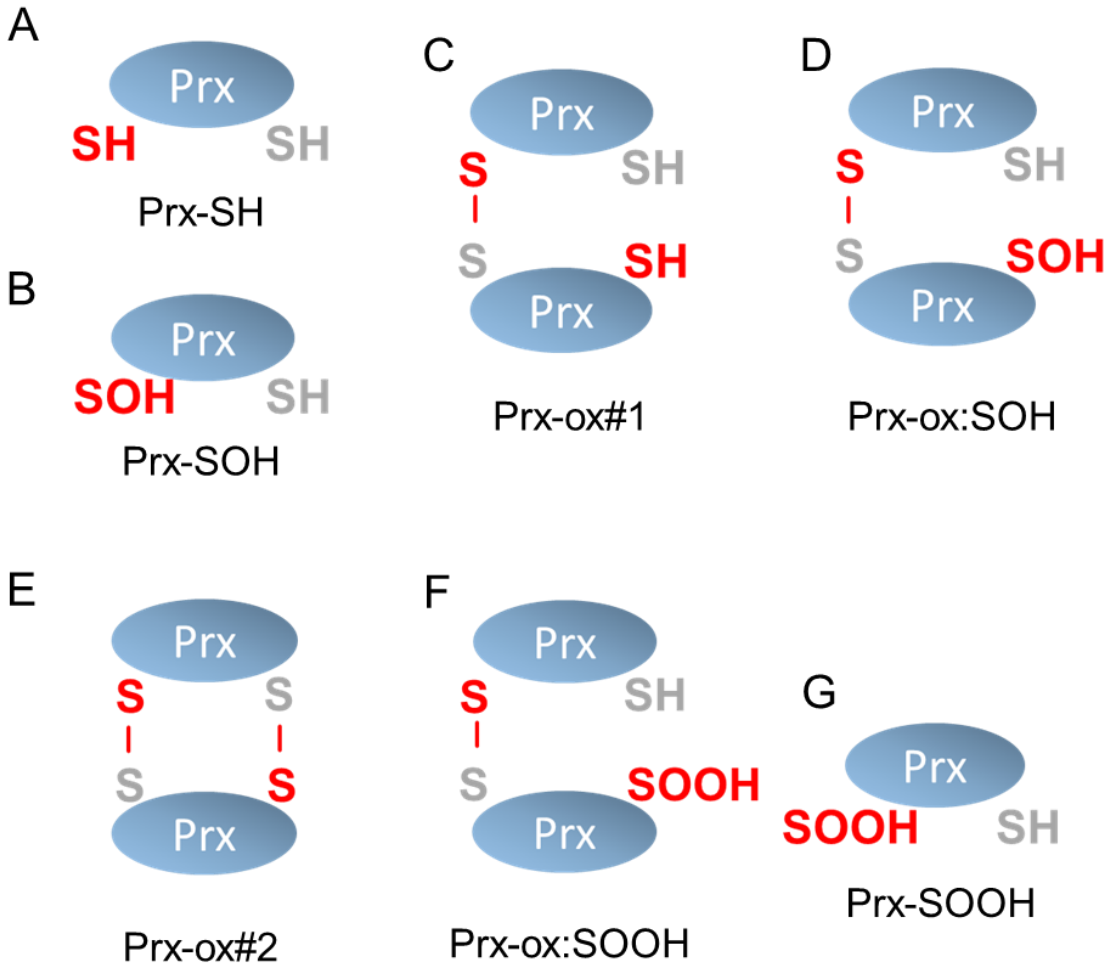

Figure 3.3: Diagrams representing experimentally detected and inferred Prx monomer and homodimer oxidation states.

The diagrams show the oxidation state of the peroxidatic cysteine (Cys_P) (red) and the resolving cysteine (Cys_R) (grey) in all of the experimentally detected and inferred (A, B, G) Prx monomers and (C, D, E, F) homodimers. The Cys_P and Cys_R exist as either a reduced-thiol (SH) state, an oxidised sulphenic-acid state (SOH), a disulphide bonded (S–S) state or an hyperoxidised sulphinic-acid (SOOH) state. The names given to each form of Prx are written beneath each diagram.

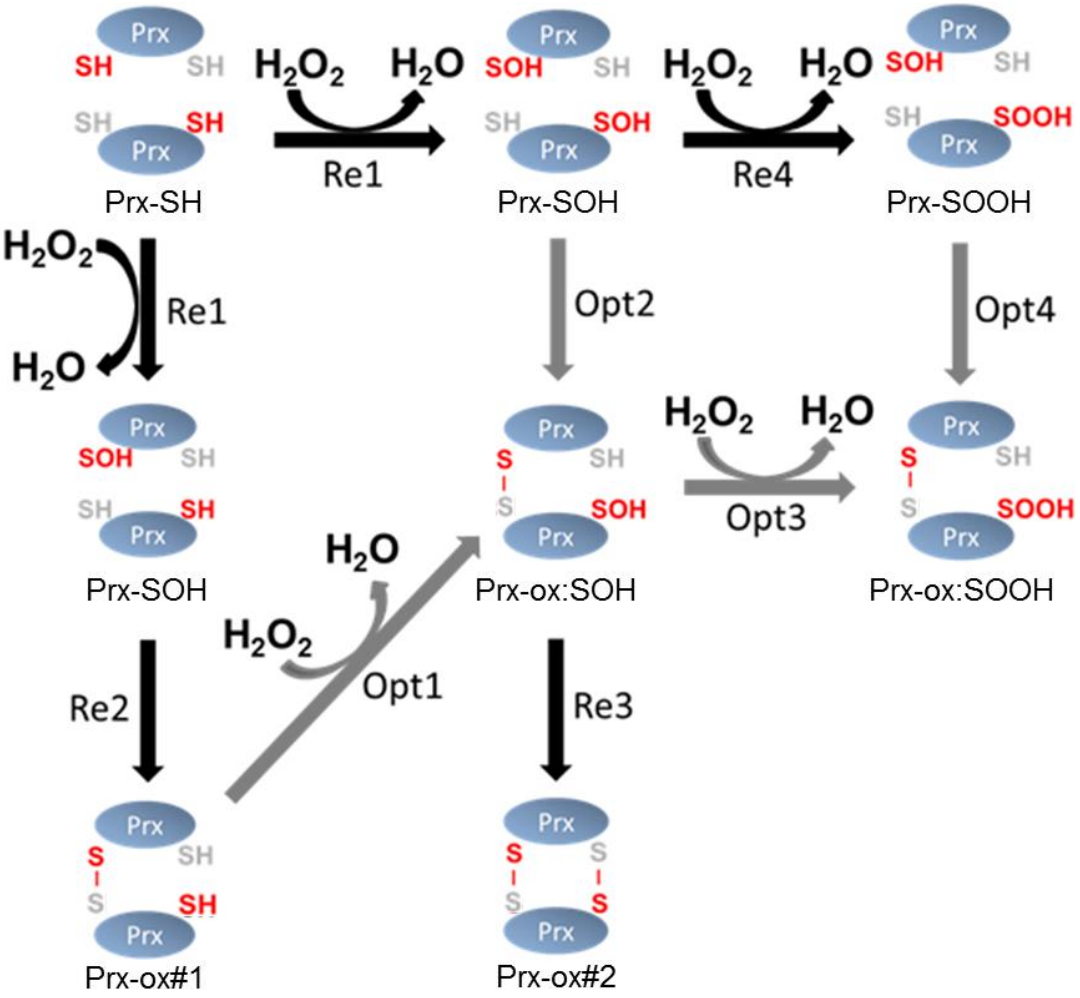

Figure 3.4: Diagram representing the computer model of *in vitro* Prx oxidation without disulphide reduction.

The diagram displays the Prx species that were included in the computer model of *in vitro* Prx oxidation. The diagram also displays the reactions included in the model, including the four essential reactions (Re1-4) and the four optional reaction (Opt1-4). (Cys_P in red) (Cys_R in grey).

Table 3.1 Rate laws for the Prx oxidation model

Reaction	Rate law
Re1	$k_{cys\_ox}[PrxSH][H_2O_2]$
Re2	$k_{disulph\_form}[PrxSOH][PrxSH]$
Re3	$k_{disulph\_form}[Prxox:SOH]$
Re4	(k_{hyp_ox}) or $(k_{slow\_hyp\_ox})[PrxSOH][H_2O_2]$
Opt1	$k_{cys\_ox}[Prxox][H_2O_2]$
Opt2	$k_{disulph\_form}[PrxSOH][PrxSOH]$
Opt3	$k_{hyp\_ox}[Prxox:SOH][H_2O_2]$
Opt4	$k_{disulph\_form}[PrxSOH][PrxSOOH]$

Table 3.1: Rate laws for the model of *in vivo* Prx oxidation without disulphide reduction.

The table displays the rate equations used for the reactions in the model of *in vivo* Prx oxidation (Figure 3.3).

Table 3.2 Parameters for the model

Parameter	Value	Units	*ref*
[PrxSH]	5	µM	Peskin et al, 2013
k_{cys_ox}	20	$\mu M^{-1} s^{-1}$	Peskin et al, 2013
$k_{disulph\_form}$	2	$(\mu M^{-1} s^{-1})$ or (s^{-1})	Peskin et al, 2013
k_{hyp_ox}	0.012	$\mu M^{-1} s^{-1}$	Peskin et al, 2013
$k_{slow\_hyp\_ox}$	0.0012	$\mu M^{-1} s^{-1}$	NA

Table 3.2: Initial parameters used in the model of *in vivo* Prx oxidation without disulphide reduction.

The table displays the values and units for the parameters used in the model of *in vivo* Prx oxidation (Figure 3.3 & Table 3.1).

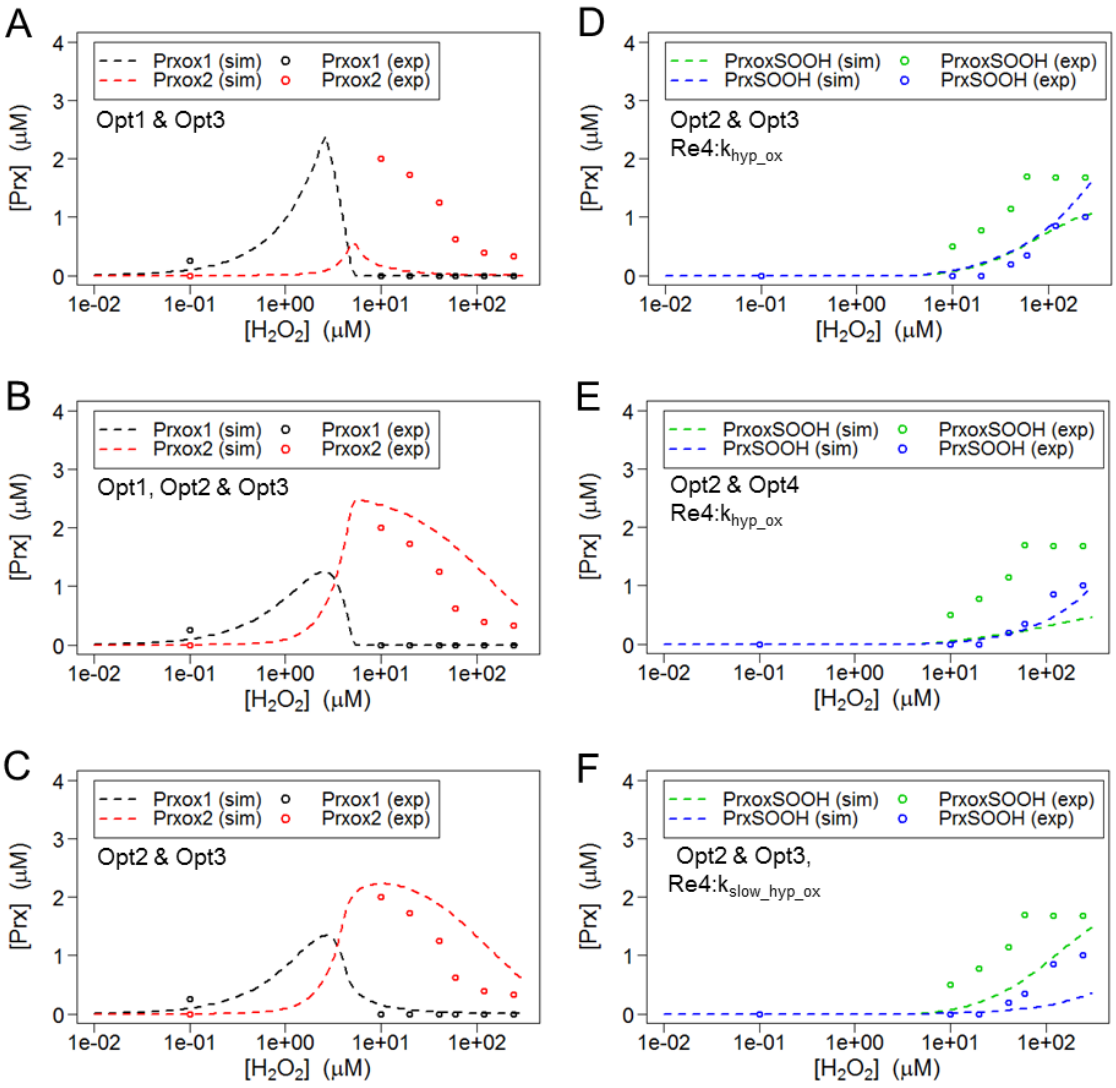

Figure 3.5: Comparison of model simulation data from the alternative models of Prx oxidation with experimental data for the *in vitro* oxidation of Prx2.

Alternative computer models of *in vivo* Prx oxidation, built using the indicated optional reactions (Opt1-4 Figure 3.3) were used to simulate the formation of the indicated Prx oxidation states in response to 0 – 120 µM H_2O_2. Most (A - E) of the model simulations used the parameter k_{hyp_ox} (Table 3.1 & 3.2) for simulating Re4, although one simulation (F) was performed using the value $k_{slow\_hyp\_ox}$ for simulating Re4. The simulation data was plotted against the experimental data for the *in vivo* oxidation of Prx2 (taken from Peskin *et al*, 2012).

3.2.3 *Modelling the movement of H_2O_2 between the extracellular and intracellular environment.*

To gain a deeper understanding into the relationship between extracellular and intracellular H_2O_2 and how this is affected by membrane permeability and H_2O_2 metabolism a simple model was built to represent a cell culture environment (Figure 3.6, Table 3.3). The model included two compartments, the first compartment represents the extracellular space (culture media) and the other represents the intracellular space. The model was built so that H_2O_2 added to the extracellular space would be able to diffuse into and out of the intracellular space down its concentration gradient, forming an equilibrium (re1 & re2). H_2O_2 inside the cell was subject to reduction by the cells peroxidase machinery (re3), which was modelled using Michaelis-Menten kinetics. The model of a cell culture environment was used to predict the effects that changes to the parameters K_m, V_{max} and $k_{H2O2perm}$ would have on the intracellular H_2O_2 ($[H_2O_2]_{int}$) concentration after addition of increasing concentrations of H_2O_2 to the culture media ($[H_2O_2]_{ex}$) (Figure 3.7).

The model predicted a bi-phasic relationship between $[H_2O_2]_{ex}$ and $[H_2O_2]_{int}$ (Figure 3.7); a low $[H_2O_2]_{ex}$ caused very little change in $[H_2O_2]_{int}$ however as $[H_2O_2]_{ex}$ increases, a critical $[H_2O_2]_{ex}$ concentration is reached above which $[H_2O_2]_{int}$ will increase linearly with $[H_2O_2]_{ex}$. The model predicted that the concentration of $[H_2O_2]_{ex}$ required to cause an increase in $[H_2O_2]_{int}$ is influenced by the parameters K_m, V_{max} and $k_{H2O2perm}$ (Figure 3.7). Increasing the rate constants K_m or $k_{H2O2perm}$ were both predicted to cause an increase in $[H_2O_2]_{int}$ at lower concentrations of $[H_2O_2]_{ex}$ (Figure 3.7 A & C), whilst increasing V_{max} was predicted to raise the concentration of $[H_2O_2]_{ex}$ required to cause an increase in intracellular H_2O_2 (Figure 3.7 B). The predictions of this preliminary model suggest that for a cell with a constant H_2O_2 membrane permeability (constant $k_{H2O2perm}$), the activity of a low K_m peroxidase process will inhibit increases in the intracellular H_2O_2 concentration after exposure to low concentrations of extracellular H_2O_2.

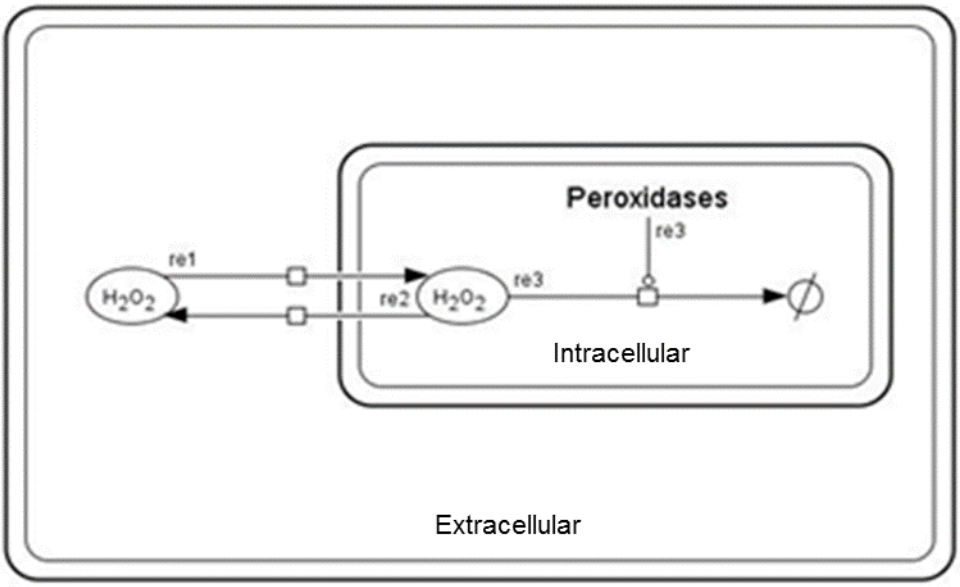

Figure 3.6: Diagram for the model of H_2O_2 dynamics in a cell culture environment.

The diagram displays the compartments (Intracellular & Extracellular) and reactions (re1-3) used to model the movement of H_2O_2 in a cell culture environment. Re1 and re2 represent the movement of H_2O_2 between the extracellular and intracellular space, whilst re3 represents the metabolism of H_2O_2 by cytoplasmic peroxidases.

Table 3.3 Rate laws for the cell culture model

Reaction	Rate law
Re1	$k_{H2O2\_perm} \cdot Vol_{ex} \cdot [H_2O_2]_{ex}$
Re2	$k_{H2O2\_perm} \cdot (Vol_{ex}/Vol_{int}) \cdot [H_2O_2]_{int} \cdot Vol_{int}$
Re3	$V_{max} \cdot [H_2O_2]_{int}/(K_m + [H_2O_2]_{int})$

Table 3.3: Rate equations for the model of H_2O_2 movement in a cell culture environment.

This table displays the rate equations used to model of movement of H_2O_2 in a cell culture environment.

Table 3.4 Initial parameter values for cell culture model

Parameter	Value	Units
k_{H2O2_perm}	1×10^{-4}	$l^{-1}\ s^{-1}$
V_{max}	200	$\mu M\ s^{-1}$
K_m	10	µM
$[H_2O_2]_{int}$	0	µM
$[H_2O_2]_{ex}$	0	µM
Vol_{ex}	0.05	l
Vol_{int}	8.1×10^{-6}	l

Table 3.4: Initial parameter values for the model of H_2O_2 movement in a cell culture environment.

This table displays the initial values of the parameter used to the model the movement of H_2O_2 movement in a cell culture.

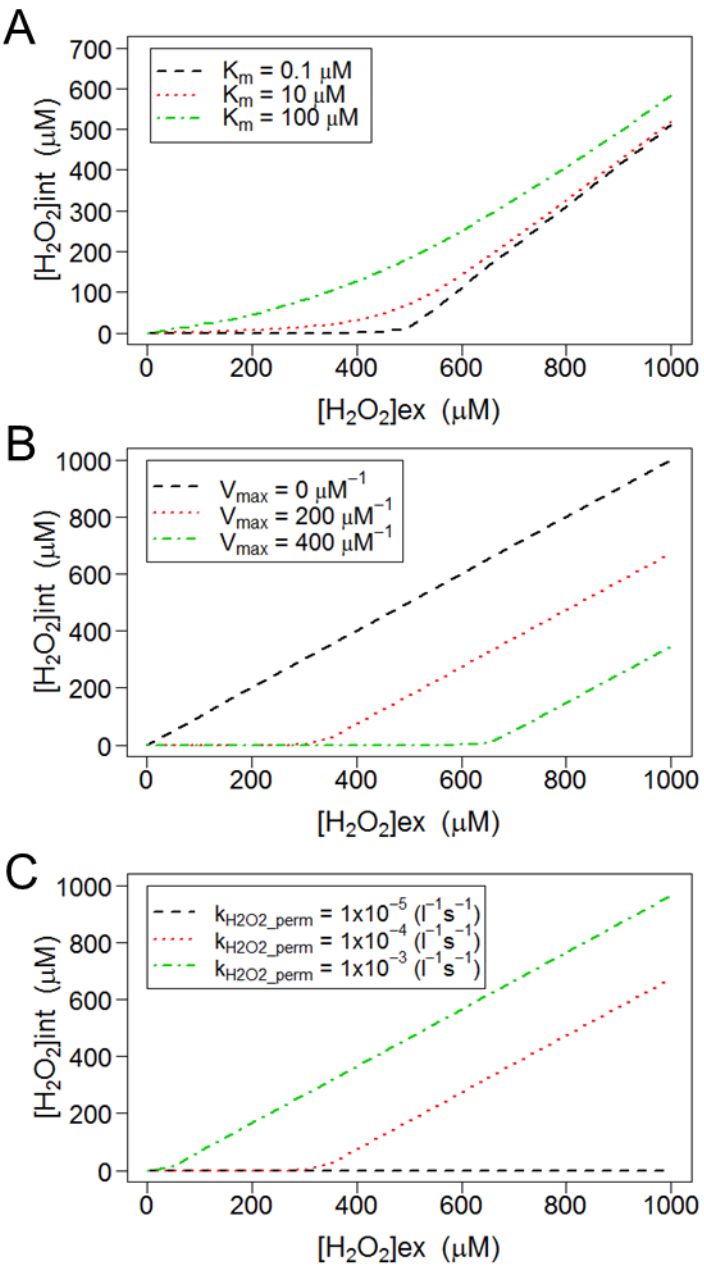

Figure 3.7: The model predictions for the effect of K_m, V_{max} and k_{H2O2_perm} on the dynamics of H_2O_2 compartmentalisation.

The model of H_2O_2 movement in a cell culture was used to simulate the effect that increasing the extracellular H_2O_2 concentration ($[H_2O_2]_{ex}$, x-axis) would have on the intracellular H_2O_2 concentration ($[H_2O_2]_{int}$, y-axis). Multiple simulations were performed using different values (indicated in legends) for the parameters (A) K_m, (B) V_{max} and (C) k_{H2O2_perm}. All other parameters were set to the initial values (Table 3.4).

3.3 Identifying key features of peroxiredoxin oxidation by studying the *in vivo* oxidation of Tpx1

The insights provided by preliminary models of *in vitro* Prx oxidation and H_2O_2 compartmentalisation provided a framework on which to build a model representing the *in vivo* oxidation of the *S. pombe* peroxiredoxin Tpx1. Next, experimental data for the oxidation of Tpx1 was collected to inform the model. The purpose of this model was to identify key features of the *in vivo* oxidation of Tpx1 and, with the help of parameter estimation techniques, test the ability of the model to replicate these experimentally observed key features, indicating that the model provides an accurate description of the biology.

3.3.1 Examination of the in vivo oxidation of Tpx1 after 20 seconds exposure to H_2O_2 confirms that three distinct Tpx1 homodimers form following exposure to H_2O_2.

In order to identify key features of Peroxiredoxin oxidation we investigated the *in vivo* oxidation of Tpx1 following a 20 seconds exposure of exponentially growing cells to 0-6000 µM H_2O_2 (Figure 3.8). Protein extracts were prepared under acidic conditions and then treated with the alkylating agent AMS which reacts with free Cys-SH residues in proteins and increase the molecular weight by approximately. (0.5 kDa). The decreased mobility of proteins containing AMS-modified Cys allows the electrophoretic separation of Tpx1 monomers and dimers with different oxidation states. AMS-treated proteins were analysed by western blot using anti-Tpx1 antibodies and multiple Tpx1-containing bands were detected (Figure 3.8A). Before addition of H_2O_2 two Tpx1 containing bands were detected (Figure 3.8A) with mobility of ~20 kDa and ~40 kDa consistent with representing reduced Tpx1 monomers (Tpx1-SH) and Tpx1 dimers respectively. The Tpx1-SH band was 3-5 times more intense than the band at ~40 kDa (Figure 3.7A). Treatment with H_2O_2 decreased the intensity of the Tpx1-SH monomer band and resulted in the formation bands at ~40 kDa, as well as higher molecular weight bands (>40 kDa) (Figure 3.8A). All of these bands were sensitive to the reducing agent beta-mercaptoethanol (Figure 3.9) confirming that these bands are disulphide complexes.

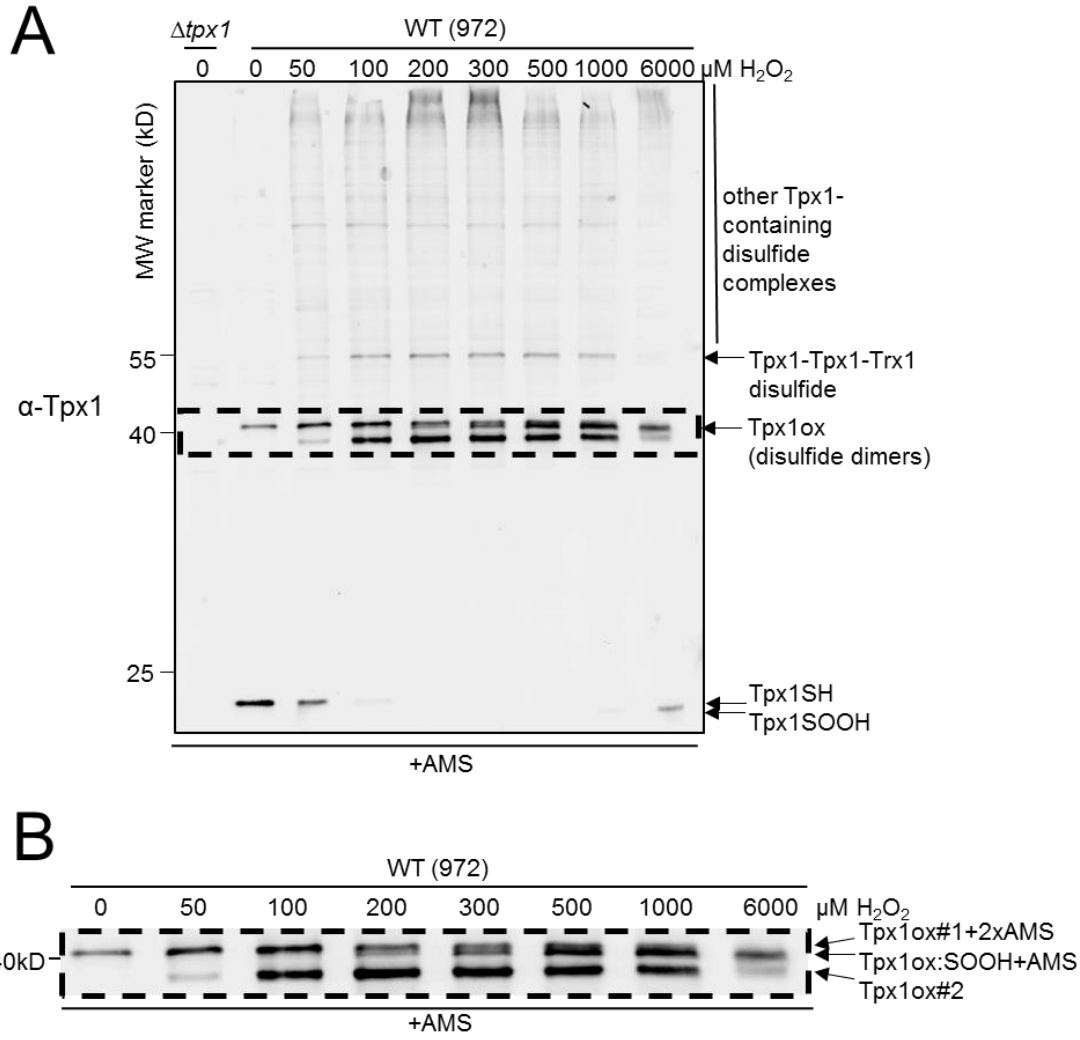

Figure 3.8: Tpx1 undergoes oxidation to multiple redox states following exposure to different concentrations of H_2O_2.

Western blot analysis (anti-Tpx1 antibodies) of (A-B) AMS-treated protein extracts from wild-type (972) and Δ*tpx1* mutant cells treated, as indicated, for 20 s with 0-6 mM H_2O_2 reveals that Tpx1 undergoes oxidation to a number of redox states following exposure to H_2O_2. The absence of bands in Δ*tpx1* mutant cells indicates that all the bands detected in wild-type cells represent Tpx1 or Tpx1-containing complexes. (B) A magnified image of the ~40 kD region outlined by the dotted line in (A) shows that 3 different Tpx1-containing disulphide dimers (Tpx1ox) are detected following treatment with concentrations ≥200 μM.

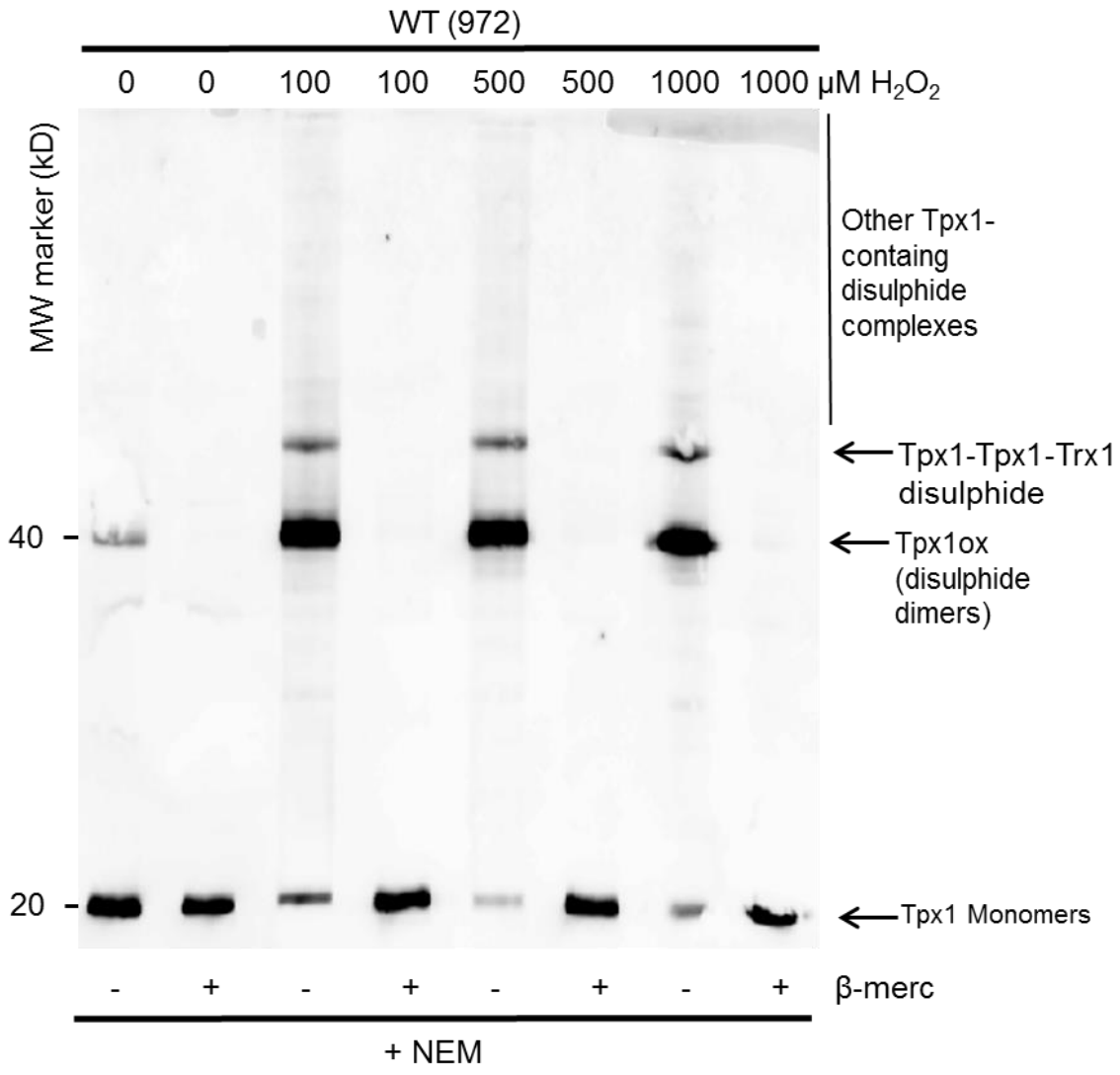

Figure 3.9: Tpx1-disulphide dimers (40 kDa) are reduced to monomers (20 kDa) by beta-marcaptoethanol treatment.

Western blot analysis (anti-Tpx1 antibodies) of NEM-treated protein extracts from wild-type (972) cells treated, as indicated, for 20 s with 0 - 1000 µM H_2O_2, with or without beta-mercaptoethanol (β-merc).

The mobility of the 40 kDa bands suggests that they represent Tpx1 disulphide homodimers. Although, it is difficult to resolve these bands, a zoomed image reveals three distinct bands (Figure 3.8B). The differences in the mobility of these three Tpx1 dimer bands suggested they contain post translational modifications, such as phosphorylation or oxidation, which have altered their mobility through the gel (Figure 3.8). Indeed, peroxiredoxin dimers with different redox states have been observed previously both *in vivo* and *in vitro* for human and *S. pombe* peroxiredoxins (Cox et al., 2009, Peskin et al., 2013, Jara et al., 2007). To establish that the three bands represent Tpx1 disulphide dimers with three different oxidation states we compared the mobility of these proteins when treated with two different thiol-reactive agents AMS and NEM (Figure 3.10). Due to its high molecular weight (0.5 kDa) binding of AMS will decrease the mobility of bands containing reduced cysteine thiols (Cys-SH) in the gel, whilst the low weight of NEM (0.0125 kDa) causes a negligible change in mobility. In samples treated with NEM, only one Tpx1-containing band was detected at 40 kDa (Figure 3.10). However, AMS treatment resulted in the detection of one, two or three bands depending on H_2O_2 concentration (Figure 3.9). This indicates that the three forms of Tpx1 represented dimers with different numbers of AMS molecules bound. Before treatment with H_2O_2 only one Tpx1 disulphide dimer band could be detected, this band showed a decrease in mobility after AMS treatment when compared to NEM suggesting that this band contains reduced cysteine thiols (Figure 3.10). After 200 µM H_2O_2 treatment, three Tpx1 disulphide bands were detected in the AMS-treated samples. The similar mobility of one of these bands to the band in the NEM-treated samples, suggested this band is AMS-resistant, indicating it contains no reduced cysteine thiols, consistent with it representing Tpx1 disulphide dimers containing two disulphide bonds (Tpx1-ox#2) (Figure 3.10). The lowest mobility band, indicating it contained 2 cysteine thiols that had reacted with AMS is consistent with it representing a Tpx1 disulphide dimer containing a single disulphide bond (Tpx1-ox#1). The third band, detected after treatment with 200 µM, had a mobility between Tpx1-ox#1 and Tpx1-ox#2, consistent with the binding of a single AMS molecule to a single reduced cysteine thiol. This is most likely the Tpx1 disulphide dimer containing a single disulphide bond and a hyperoxidised Cys_P (Tpx1-ox:SOOH) with the remaining Cys_R available to react with AMS. These results confirm that the three distinct Tpx1

disulphide dimers described here have the same redox states as previously described for *S. pombe*

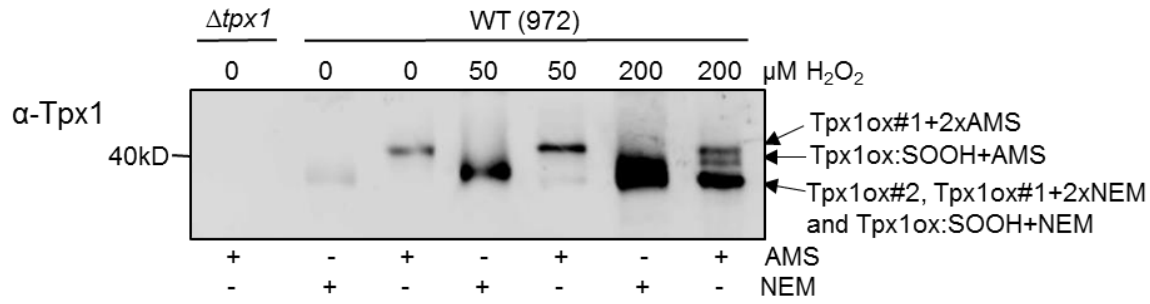

Figure 3.10: Comparison of NEM and AMS-treated proteins suggests three different Tpx1 dimers.

Western blot analysis (anti-Tpx1 antibodies) of NEM- or AMS-treated protein extracts from wild-type (972) or Δ*tpx1* (VX00) cells treated, as indicated, for 20 s with 0 - 200 μM H_2O_2.

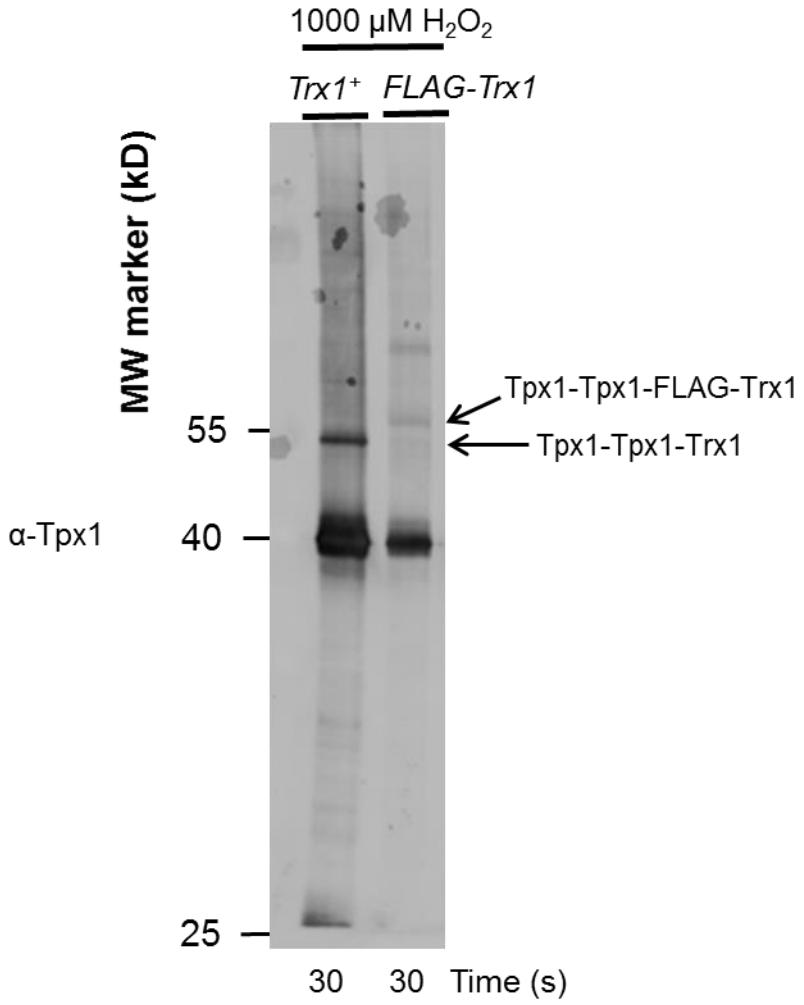

Figure 3.11: H_2O_2 treatment results in the formation of complex between Tpx1 and Trx1.

Western blot analysis (anti-Tpx1 antibodies) of NEM-treated protein extracts from wild-type (CHP429) or FLAG-*trx1* (JB35) cells treated for 30 s with 1000 μM H_2O_2. A band with a mobility of 55 kDa was detected in both strains, however this band had a slower mobility through the gel in the strain containing FLAG-Trx1. This suggests that this band represents a complex between a Tpx1 disulphide dimer and Trx1 (Tpx1-Tpx1-Trx1).

and human peroxiredoxins (Cox et al., 2009, Peskin et al., 2013, Jara et al., 2007). As well as the bands at 40 kDa a band at 55 kDa was also detected. The molecular weight of this band was consistent with a complex between a Tpx1-Tpx1 disulphide and Trx1 (Tpx1-Tpx1-Trx1). Indeed, the increased MW of this complex in cells expressing FLAG-Trx1 is consistent with this interpretation (Figure 3.11) and suggested that this complex is a reaction intermediate for the reduction of Tpx1-ox#2 by Trx1.

Having identified three Tpx1 homodimers with distinct redox states, our data suggests that the relative intensities of these dimers is dependent on H_2O_2 concentration, with Tpx1-ox#1, Tpx1-ox#2 and Tpx1-ox:SOOH being most prominent at the lowest, mid and high H_2O_2 concentrations respectively. This pattern of oxidation is similar to *in vitro* analysis of Prx2 & Prx3 conducted by Peskin et al (2013) suggesting that this might be a common feature of all peroxiredoxins. The ability of the preliminary model (Figure 3.4) based on the Peskin et al (2013) data to simulate this pattern of oxidation (Figure 3.5) suggested that the same set of Prx oxidation reactions might be able to describe the *in vivo* data. There was however a notable difference between the *in vitro* and *in vivo* data. The *in vitro* data found that hyperoxidised Prx-ox:SOOH was detected even at the lowest H_2O_2 concentrations, however *in vivo* Tpx1-ox:SOOH was not detected until treatment with $[H_2O_2]_{ex} \geq 200$ µM (Figure 3.8 & 3.10). Although this difference between the *in vivo* and *in vitro* sensitivity of Prx hyperoxidation could reflect differences in the sensitivity of Tpx1 and Prx2 to hyperoxidation, it was also postulated that it could be due to a fundamental *in vivo* mechanism not present *in vitro*.

3.3.2 Identifying Key Features of in vivo Peroxiredoxin oxidation: Time course data for the in vivo oxidation of Tpx1

To investigate the levels of hyperoxidation of Tpx1 *in vivo* we collected time course data following treatment for 0 – 600 seconds with 100 µM and 200 µM H_2O_2. After addition of 100 µM H_2O_2 (Figure 3.12) two Tpx1 containing bands (Tpx1-ox#1 & Tpx1-ox#2) were detected at 40 kDa, as seen previously (Figure 3.8 & 3.10). The relative intensities of Tpx1-ox#1 and Tpx1-ox#2 did not appear to change over the duration of the time course. Importantly, and in agreement to

the previous data (Figure 3.8 & 3.10), no Tpx1-ox:SOOH was detected over the duration of the 100 µM time course (Figure 3.12). In contrast, treatment with 200 µM H_2O_2 (Figure 3.13) resulted in the formation of Tpx1-ox#1, Tpx1-ox#2 and Tpx1-ox:SOOH dimers. The intensity of the Tpx1 dimer bands decreased over the time course and was coupled with the formation of a new Tpx1-containing band at 20 kDa (Figure 3.13). The increased mobility of this new band, compared to the AMS-reactive Tpx1-SH monomer band, detected before addition of H_2O_2, suggests it has fewer AMS-reactive cysteine thiols. This is consistent with this band representing the hyperoxidised Tpx1-SOOH monomer (Figure 3.13) previously shown to form at higher H_2O_2 concentrations (Bozonet et al., 2005). The 200 µM time course data suggests that Tpx1-ox:SOOH is converted over time to Tpx1-SOOH, with maximal hyperoxidation by 240 seconds. This was confirmed using anti-Prx-SO2/3 antibodies (Figures 3.14 & 3.15A) that specifically recognises the hyperoxidised form of 2-cys Prx, including Tpx1 (Woo et al., 2005, Day et al., 2012). Studies investigating the *in vivo* hyperoxidation of *S. pombe* in response to H_2O_2 have also shown that Prx-ox:SOOH dimers are detected prior to Prx-SOOH monomers and are therefore in agreement with these findings (Jara et al., 2007).

As discussed in section 3.3.1 the *in vivo* dynamics for the formation of the Tpx1 homodimers (Figure 3.8) were similar to the dynamics for the *in vitro* oxidation of Prx2. However, one important difference was that Prx2 hyperoxidation was detected at all H_2O_2 concentrations *in vitro*, whereas Tpx1 hyperoxidation was only detected *in vivo* in cells exposed to H_2O_2 concentrations higher than 100 µM (Figure 3.8, 3.12, 3.13). This suggests that there could be a process which is inhibiting Prx hyperoxidation at lower H_2O_2 concentrations *in vivo* that is not present *in vitro*. To confirm that there is no Tpx1 hyperoxidation after exposure to 100 µM H_2O_2 we compared samples from 100 & 200 µM samples using western blot analysis using anti-PrxSO2/3 antibodies (Figure 3.15A). This confirmed that there is no Tpx1 hyperoxidation after exposure to 100 µM H_2O_2 (Figure 3.15A). Time course data for Tpx1 hyperoxidation at 500 µM and 1000 µM H_2O_2 indicate that Tpx1 hyperoxidation is maximal by 1 min, earlier than in cells treated with 200 µM H_2O_2 (Figure 3.15). This indicates that increased extracellular H_2O_2 concentration results in an increased rate of formation of Tpx1-SOOH (Figure 3.15B). The intensity of the Tpx1-Tpx1-Trx1 band changed in parallel to the

intensity of the Tpx1-ox#2 band (Figure 3.8, 3.12, 3.13). Importantly, western blot analysis of beta-mercaptoethanol-treated samples suggest that total Tpx1 levels did not change throughout the 600 seconds time courses (Figure 3.12 & 3.13) in agreement with other published data (Lackner et al., 2012).

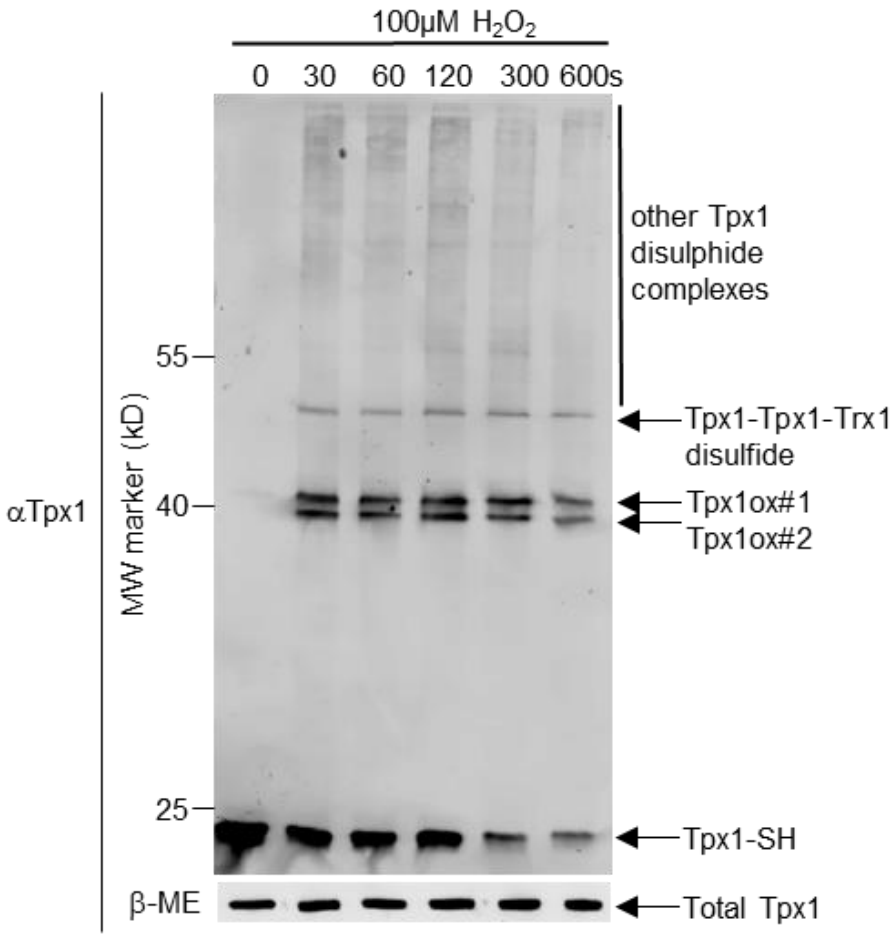

Figure 3.12: Changes in Tpx1 oxidation over time following treatment with 100 μM H_2O_2.

Western blot analysis (anti-Tpx1 antibodies) of AMS-treated protein extracts from wild-type (972) and Δ*tpx1* (VX00) mutant cells treated with 100 μM H_2O_2 for 0-600 s shows how the oxidation of Tpx1 changes with time. Western blot analysis of beta-mercaptoethanol (βME)-treated samples, run on a separate gel (lower panel) indicates there are no changes in total Tpx1 levels over the 600 second time course.

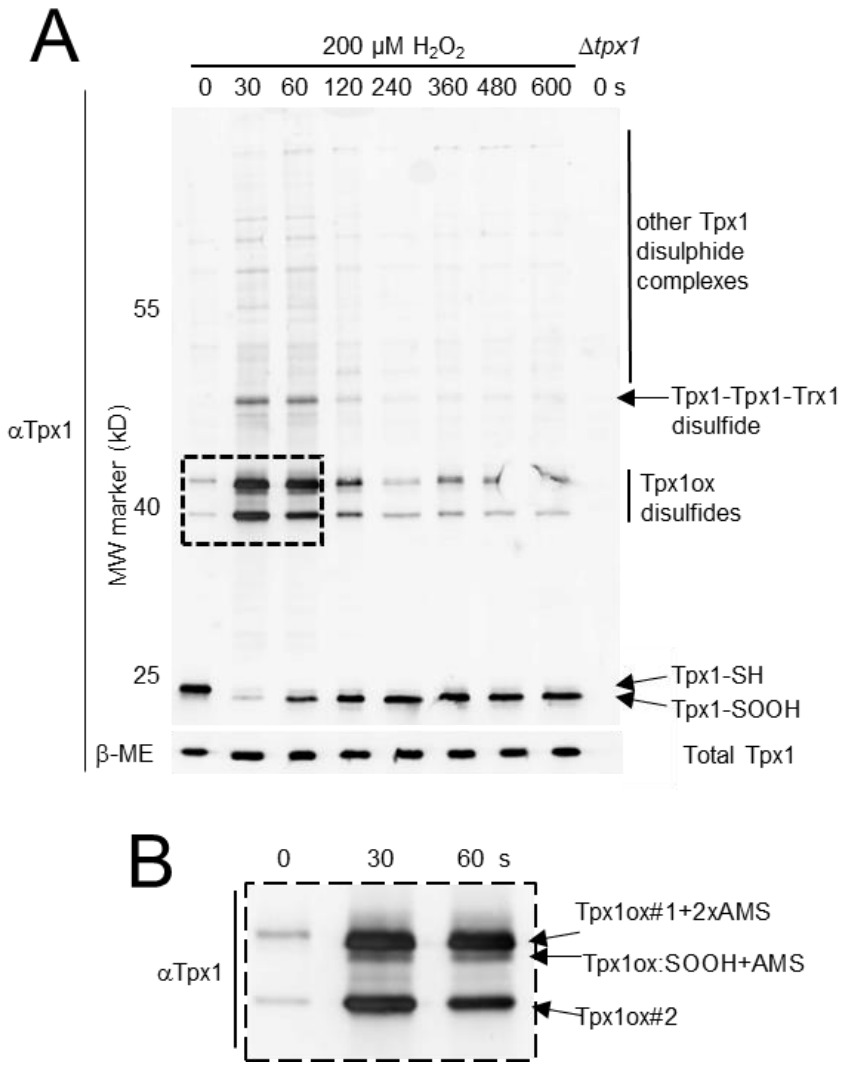

Figure 3.13: Changes in Tpx1 oxidation over time following treatment with 200 µM H_2O_2.

Western blot analysis (anti-Tpx1 antibodies) of AMS-treated protein extracts from wild-type (972) and Δ*tpx1* (VX00) mutant cells treated with 200 µM H_2O_2 for 0-600 s shows how the oxidation of Tpx1 changes with time. Western blot analysis of beta-mercaptoethanol (βME)-treated samples, run on a separate gel (lower panel) confirms that differences between lanes reflect changes in Tpx1 oxidation rather than total Tpx1 levels. (B) A section of the blot, outlined by the dotted line, is magnified and shown in the lowest panel to allow the additional Tpx1ox form, Tpx1ox:SOOH, present in cells treated with 200 µM H_2O_2, to be seen more clearly.

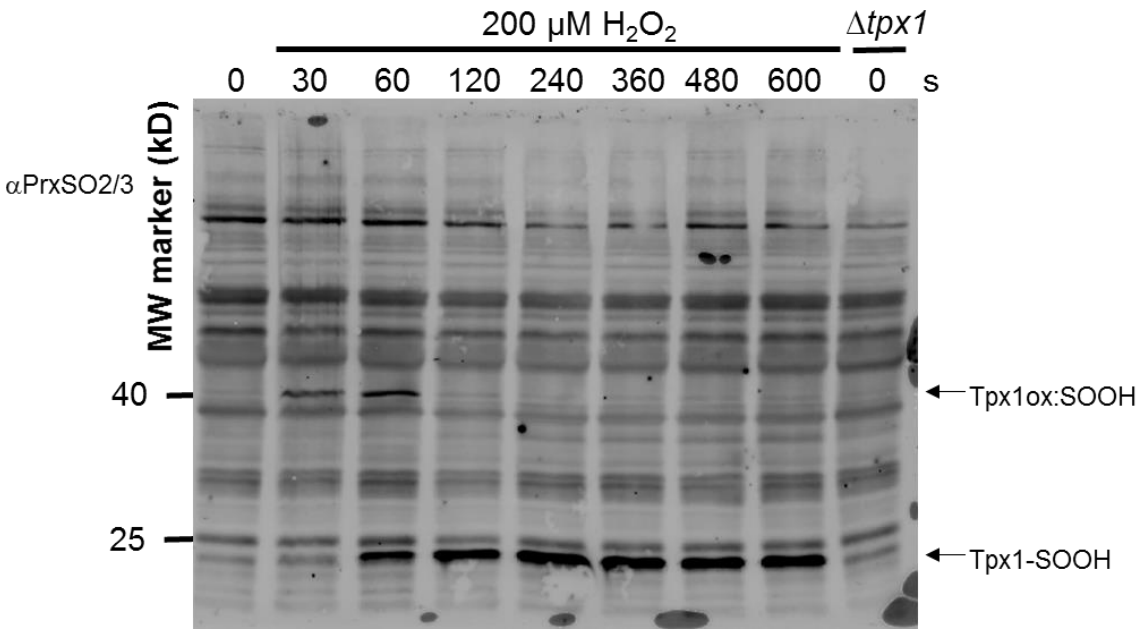

Figure 3.14: Changes in Tpx1 hyperoxidation over time following treatment with 200 µM H_2O_2.

Western blot analysis (anti-PrxSO2/3 antibodies) of AMS-treated protein extracts from wild-type (972) and Δ*tpx1* mutant cells treated with 200 µM H_2O_2 for 0-600 s shows how the hyperoxidation of Tpx1 changes with time.

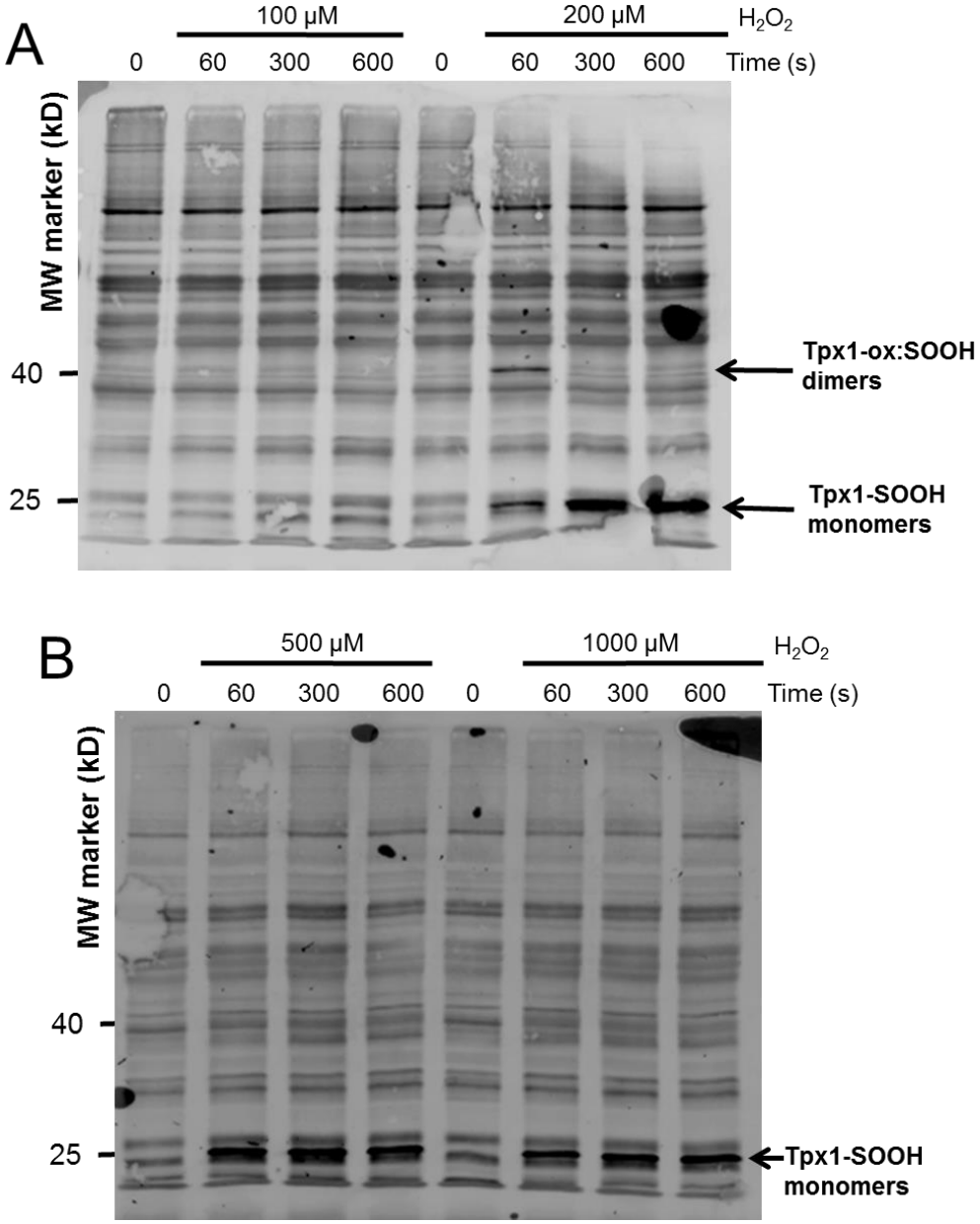

Figure 3.15: The kinetics of hyperoxidation of Tpx1 following exposure to increasing H_2O_2 concentrations.

Western blot analysis of levels of hyperoxidized Tpx1, detected using antibodies specific to the sulphinylated and sulphonylated forms of Prx (α-PrxSO2/3) in wild-type (972) *S. pombe* cells before and following exposure, for the indicated time, to 100, 200, 500 or 1000 µM H_2O_2.

3.4 Selecting a suitable model for the *in vivo* oxidation of Tpx1

Having identified the key features of the *in vivo* oxidation of Tpx1 that the model would need to replicate, computer models were constructed to represent the *in vivo* oxidation and hyperoxidation of Tpx1. As discussed below we constructed three potential models for *in vivo* Tpx1 oxidation (Figure 3.16, Table 3.5). Each model contained a core set of essential reactions. Three optional reactions, indicated in Figure 3.16, were also included. The rate equations for the reactions were based on mass action kinetics apart from Opt3, representing H_2O_2 metabolism by non-Tpx1 cellular peroxidases, which was modelled using Michaelis-Menten kinetics (Table 3.5). Rate constants for these reactions were either taken from the literature or measured experimentally. Remaining rate constants were estimated using parameter estimation (see 2.6.6). The quantitative data set used for parameter estimation was based on the relative intensities of different Tpx1 oxidation states, identified from the Tpx1 western blots and on measurements of [H_2O_2] in the cell media (see 2.3.1, 2.6.3). The suitability of each model to simulate the experimental data was assessed using quantitative measures of the model fit to the whole data set (SSR & AIC), as well as taking into account the fit to the data for individual Tpx1 species (Chi^2) (see 2.6).

3.4.1 Parameter estimation results for each model

We performed 500 parameter estimations for each of the three models using our quantitative data for the concentrations of each Tpx1 oxidation state and extracellular H_2O_2 concentration (see 2.6.3). The sum of squared residuals (SSR) and the Akaike information criterion (AIC) (Akaiki. 1973) (see 1.6.4 and 2.6.6) for each of the 500 parameter sets, for each model, were calculated. The SSR and AIC are quantitative assessments of the fit of the simulation data to the entire experimental data set such that a lower SSR/AIC indicates a better fit to the experimental data.

Table 3.4 summarises the results of the parameter estimations for each model. The model with the lowest AIC parameter set was Model C which found a parameter set with an AIC of 74.8 but was only found in 0.2% of the 500

estimations (Table 3.6). The model with the next lowest AIC parameter set was Model A which produced parameter sets with an AIC of 76.7 in 65% of the 500 parameter estimations (Table 3.6). The parameter estimations for Model B found parameter sets with an AIC of 88 which was found in 44% of the 500 estimations (Table 3.6). The frequency distributions of the AIC values calculated for the 500 parameter sets for each model were plotted (Figure 3.18).

Of the three models, the lowest AIC parameter set was found for Model C, which fit the data with an AIC of 74.8. This suggested that Model C could be the most accurate representation of the experimental data. However many of the parameters predicted for Model C differed grossly from what could be reasonably predicted based on published values. For example, the first order rate constant $k_{disulph\_form3}$ which was predicted to be 500 s^{-1} but has actually been calculated as between 2 – 20 s^{-1} based on *in vitro* experimental data (Peskin et al., 2013).

In contrast, the parameters predicted for Model A, which had a slightly higher AIC of 77.6, were all reasonably similar to experimentally measured rate constants. For example the parameters $k_{disulph\_red1}$, $k_{disulph\_red2}$ were predicted to be 0.190 (0.09 – 1.55) and 0.143 (0.06 – 1.3) $\mu M^{-1}s^{-1}$ respectively and are in good agreement with experimentally determined rate constants for the reduction of Prx disulphides by Trx1, which are in the region 0.1 $\mu M^{-1}s^{-1}$ (Trujillo et al., 2007, Pineyro et al., 2011). It is worth noting that the rate constant for $k_{disulph\_red3}$ was predicted to be 0.029 $\mu M^{-1}s^{-1}$, ~10 fold lower than $k_{disulph\_red1}$ & $k_{disulph\_red2}$. If this parameter is correct then this suggests that Trx1 is less efficient at reducing the disulfide bond in Tpx1-ox:SOOH compared with the other Tpx1 disulfide dimers, although there have been no experimental measurements to verify this. The first order rate constant for Tpx1 disulfide formation (rate constant $k_{disulph\_form2}$) of 3.44 s^{-1} estimated for our model was in a similar range to the rates of disulphide formation estimated from *in vitro* experimental investigations (Peskin et al., 2013) for human Prx1 and Prx3 (2 s^{-1} and 20 s^{-1} respectively).

A frequency distribution was plotted for each parameter in the 327 AIC = 77.6 parameter sets for Model A. Each parameter followed a normal distribution (Figure 3.18), with a narrow range, indicating that the same set of parameters was found in each of the 327 estimations. Identifiability analysis (Schaber, 2012) indicated that all of the parameters were identifiable (Figure 3.19). Where data

was available, experimentally measured rate constants were found to be within 95% confidence regions for each parameter. To summarise, parameter estimation was used to find a unique, identifiable, biologically reasonable set of parameters for Model A (Table 3.7). Model A, with this parameter set, was therefore selected as the most accurate representation of *in vivo* Tpx1 oxidation.

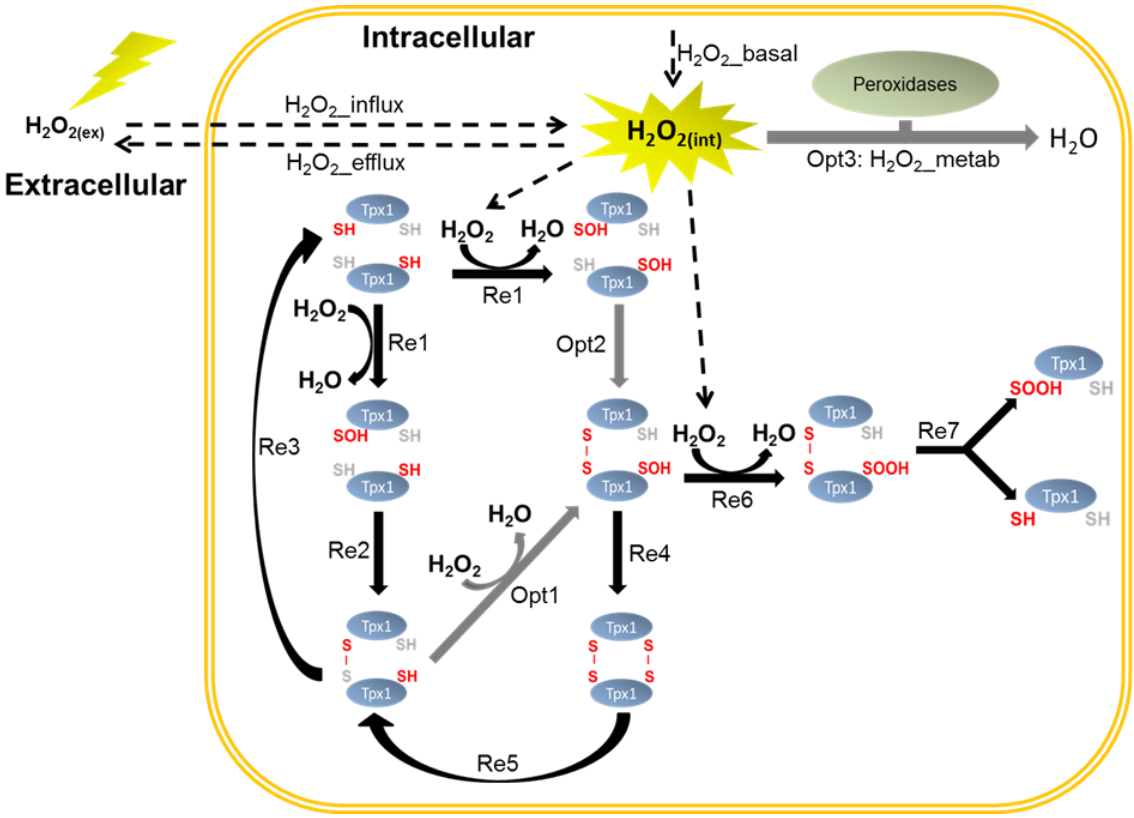

Figure 3.16: Alternative models for the *in vivo* oxidation of Tpx1

The diagram displays the compartments (extracellular & intracellular), biochemical reactions and Tpx1 oxidation states used in the alternative computer models of *in vivo* Tpx1 oxidation. The essential reactions (Re1-7) are indicated in black and the three optional reactions (Opt1-3) are labelled in grey. Re3. Re5 and Re6 require reduced Trx1 (Trx1red), this is indicated in Table 3.5. In these reactions Trx1red is oxidised to Trx1ox, which can be reduced back to Trx1red by the reaction called Trx1 reduction, shown in Table 3.5.

Table 3.5 Rate laws for the Tpx1 oxidation model reactions

Reaction	Rate law
H_2O_2_influx	$k_{H2O2\_perm} \cdot Vol_{ex} \cdot [H_2O_2]_{ex}$
H_2O_2_efflux	$k_{H2O2\_perm} \cdot (Vol_{ex}/Vol_{int}) \cdot [H_2O_2]_{int} \cdot Vol_{int}$
H_2O_2_basal	V_{basal}
Re1	$k_{cys\_ox}[Tpx1SH][H_2O_2]_{int}$
Re2	$k_{disulph\_form1}[Tpx1SOH][Tpx1SH]$
Re3	$k_{disulph\_red1}[Trx1red][Tpx1ox\#1]$
Re4	$k_{disulph\_form3}[Tpx1ox:SOH]$
Re5	$k_{disulph\_red2}[Trx1red][Tpx1ox\#2]$
Re6	$k_{hyp\_ox}[Tpx1ox:SOH][H_2O_2]_{int}$
Re7	$k_{disulph\_red3}[Trx1red][Tpx1ox:SOOH]$
Trx1 reduction	$k_{Trx1\_red}[Trx1\text{-}ox]$
Opt1	$k_{cys\_ox2}\ [Tpx1ox\#1][H_2O_2]_{int}$
Opt2	$k_{disulph\_form1}[Tpx1SOH][Tpx1SOH]$
Opt3	$V_{max\_H2O2\_metab}[H_2O_2]_{int}/K_{m\_H2O2\_metab} + [H_2O_2]_{int}$

Table 3.5: Rate laws used for the computer model of the *in vivo* Tpx1 oxidation.

The rate laws used for each of the reactions in the computer model of *in vivo* Tpx1 oxidation.

Table 3.6. Parameter Estimation results summary

	Model A	Model B	Model C
Optional Reactions	Opt2, Opt3	Opt1, Opt3	Opt2
Unique sets found	141	146	137
Lowest SSR para set	128	132	509
Lowest AIC set	77.6	88	74.8
Times Found (in 500)	327	218	1

Table 3.6: Summary of the parameter estimation results for alternative models of Tpx1 oxidation

The table summarises the parameter estimation results for three alternative computer models for *in vivo* Tpx1 oxidation. Each model contained different combinations of the three optional reactions, as indicated in the table. The table displays the number of unique parameter sets found as well as the lowest SSR and AIC values found for each model, and the number of time this value was found.

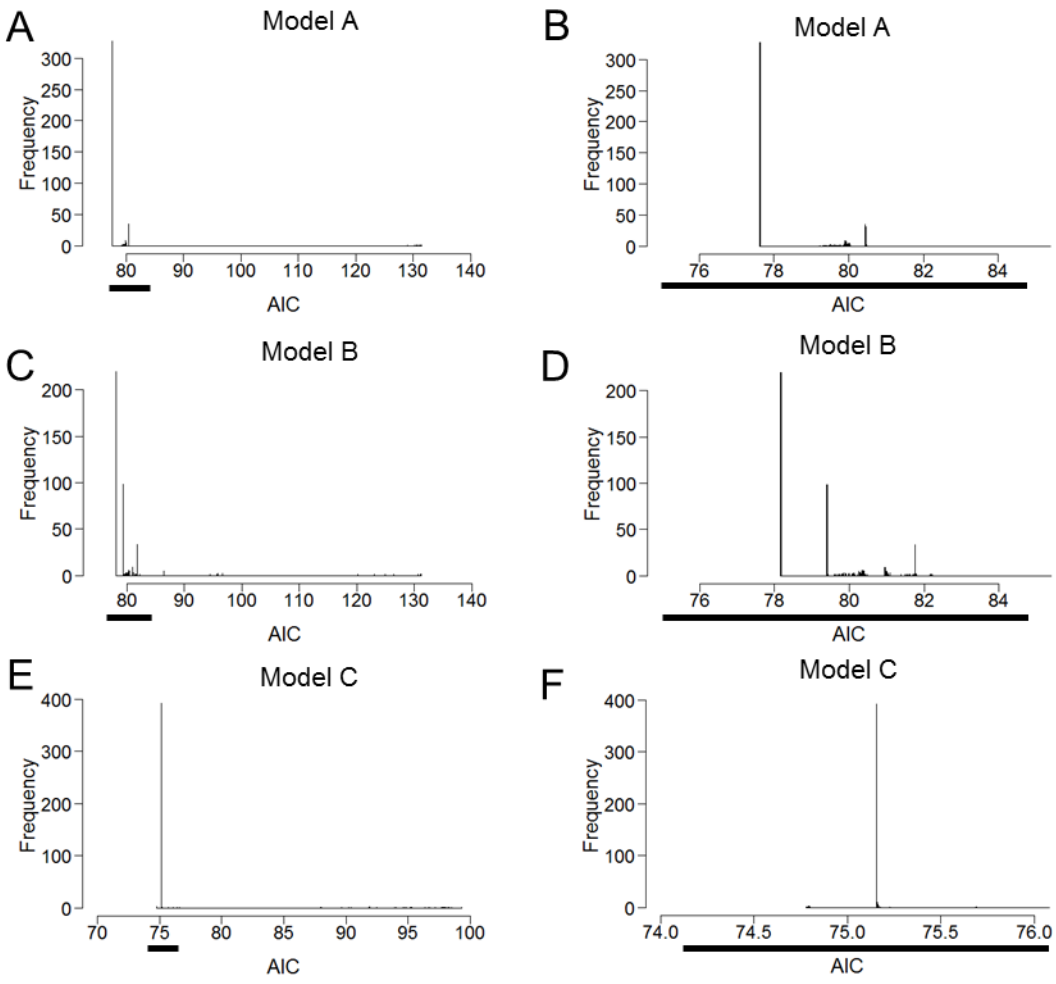

Figure 3.17: Frequency distributions for the AIC values calculated for each of the 500 parameter sets found for the Tpx1 oxidation models.

The plots show the frequency distributions for the AIC values calculated from the 500 parameter sets found for the models indicated. Two plots have been made for each model one displaying all 500 AIC values (A, C, E), and one showing the AIC values close to the most frequent value (B, D, F) (indicated with black line).

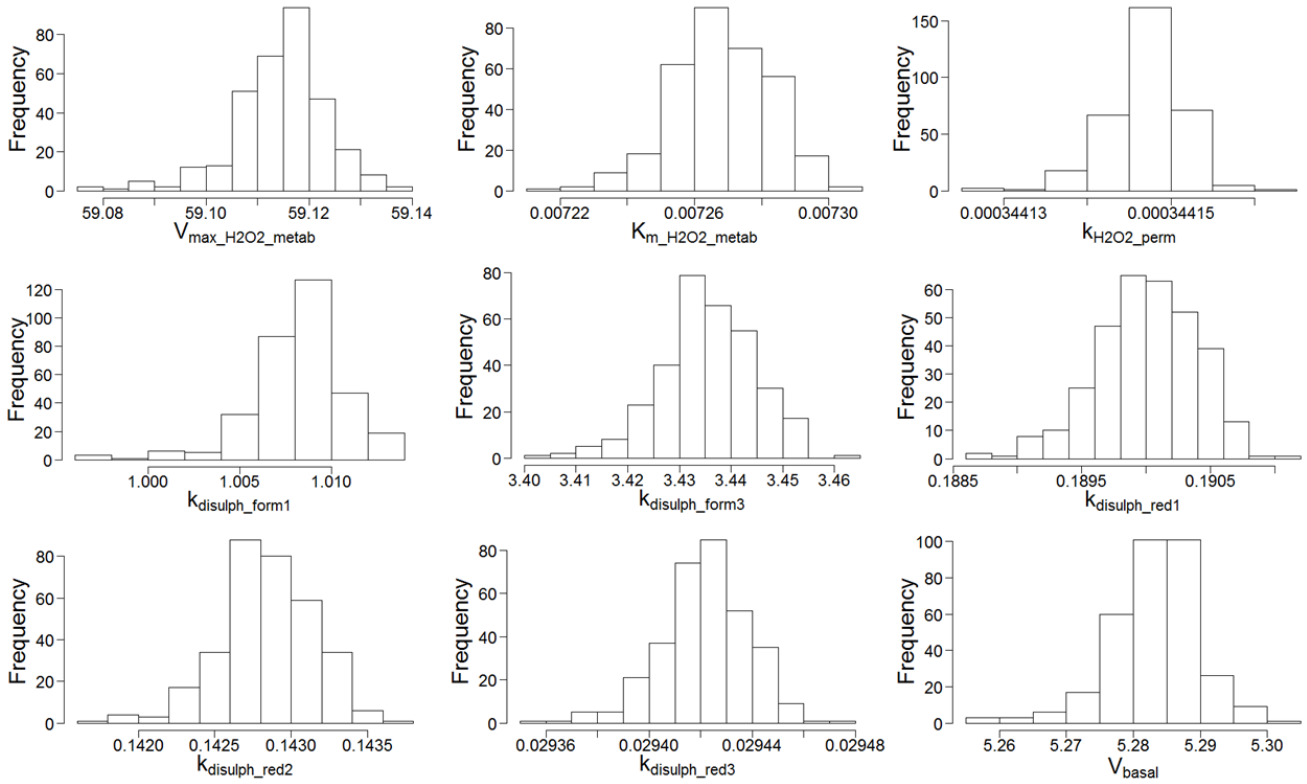

Figure 3.18: Frequency distributions for individual parameters estimated for the model of Tpx1 oxidation.

Parameter estimation found 327 parameter sets with an AIC of 77.6. The frequency distributions for each parameter in these 327 parameter sets are shown. Each parameter displayed a normal distribution indicating that all 327 parameter sets predicted a similar value for each parameter.

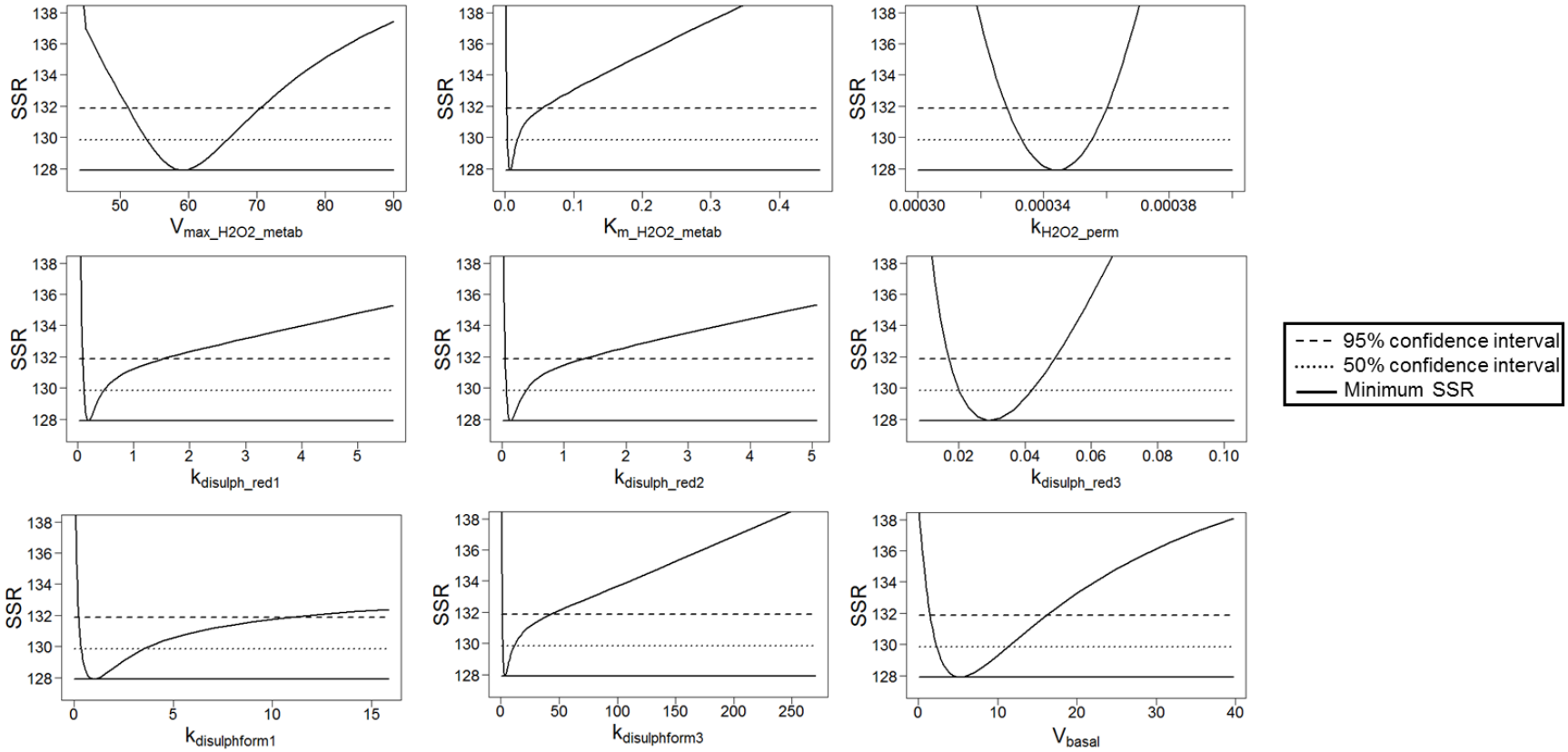

Figure 3.19: Identifiability analysis for the parameters used in the final model of *in vivo* Tpx1 oxidation.

One-dimensional contour plots for each of the parameters in the model calculated using identifiability analysis. The dotted lines represent the 50% and the dashed lines the 95% confidence intervals for each parameter and the solid line the minimum SSR as indicated.

Table 3.7 Parameters for model of in vivo Tpx1 oxidation

Parameter	Value	Units	*ref*	95% Conf. Interval
[Tpx1SH]	4	µM	Marguerat et al, 2012	NA
[Trx1red]	0.7	µM	Marguerat et al, 2012	NA
k_{H2O2_perm}	3.44×10^{-4}	$l^{-1}\ s^{-1}$	Parameter Estimation	3.29×10^{-4} - 3.59×10^{-4}
$V_{max\_H2O2\_metab}$	59	$\mu M\ s^{-1}$	Parameter Estimation	51 - 70
$K_{m\_H2O2\_metab}$	0.007	µM	Parameter Estimation	0.003 - 0.053
k_{cys_ox}	20	$\mu M^{-1}\ s^{-1}$	Peskin et al, 2013	NA
$k_{disulph\_form1}$	1.01	$\mu M^{-1}\ s^{-1}$	Parameter Estimation	0.25 - 11
$k_{disulph\_form2}$	3.44	s^{-1}	Parameter Estimation	1.5 - 43
$k_{disulph\_red1}$	0.190	$\mu M^{-1}\ s^{-1}$	Parameter Estimation	0.09 - 1.55
$k_{disulph\_red2}$	0.143	$\mu M^{-1}\ s^{-1}$	Parameter Estimation	0.06 - 1.3
$k_{disulph\_red3}$	0.029	$\mu M^{-1}\ s^{-1}$	Parameter Estimation	0.017 - 0.048
k_{Trx_red}	34	$\mu M^{-1}\ s^{-1}$	Oliveira et al, 2010	NA
k_{hyp_ox}	0.012	$\mu M^{-1}\ s^{-1}$	Peskin et al, 2013	NA
Vol_{ex}	0.05	l	Measured	NA
Vol_{int}	5.20E-05	l	Measured	NA
V_{basal}	5	$\mu M\ s^{-1}$	Parameter Estimation	1.48 - 16.2

Table 3.7: Parameters used in in the final model for the *in vivo* oxidation of Tpx1 (Model A).

The table lists the parameters used in the model of *in vivo* Tpx1 oxidation. The parameters were either found using parameter estimation, measured experimentally or found in the literature as indicated. The 95% confidence intervals for each of the parameters is also indicated.

3.4.2 Model A is able to simulate the experimentally observed dynamics of Tpx1 oxidation and H_2O_2 metabolism.

Using the AIC = 77.6 parameter set predicted by parameter estimation (Table 3.7), Model A was used to simulate Tpx1 oxidation after a 20 second exposure to 0 – 1000 µM H_2O_2 (Figure 3.20) or a 600 second exposure to 100 and 200 µM H_2O_2 (Figure 3.21 & 2.22). Model A was also used to simulate decrease in the extracellular H_2O_2 concentration up to 2000 seconds following an initial dose of 50 µM H_2O_2 (Figure 3.20A). The simulation data and experimental data were plotted on the same axis along with the Chi^2 value for each of the model species (Figures 3.20, 3.21, 3.22).

In general, the simulated dynamics of Tpx1 oxidation after 20 seconds exposure to H_2O_2 were in a good agreement with the experimental data (Figure 3.20). As a rule of thumb, if the Chi^2 value for the simulated data is less than 2x the number of data points, it can be said that the model has a good fit to the data. The model simulations displayed in Figure 3.20 were not able to meet this rule, and could therefore be said to not fit the data. However, we felt that this contradicted the visual analysis which clearly demonstrated that, in general, the model was a good representation of the dynamics of the experimental data. Once exception to this is the simulation for the change in Tpx1-ox#2 concentration, which underestimated the concentration of Tpx1-ox#2 that is formed after exposure to H_2O_2 concentrations greater than 200 µM (Figure 3.20D). This suggested that although model A fits the data better than the two alternative models B & C there were still limitations in its ability to accurately represent the biology. Importantly, Model A accurately simulated our experimental observation that there would be no formation of either of the hyperoxidised Tpx1 forms (Tpx1-ox:SOOH & Tpx1-SOOH) at H_2O_2 concentrations below 200 µM (Figure 3.20E & F). This is important since the absence of Prx hyperoxidation at lower H_2O_2 concentrations was the key difference between the *in vitro* and *in vivo* Prx oxidation data.

Model A was then used to simulate time course data for the oxidation of Tpx1 after exposure to 100 µM and 200 µM H_2O_2 (Figures 3.21 & 3.22). Plotting the simulation data against the experimental data suggests that the model is a good representation of the dynamics of Tpx1 oxidation, although some of the Chi^2 values did contradict this. Notably, the model correctly predicted that no Tpx1-

ox:SOOH or Tpx1-SOOH would be formed during the 100 µM time course (Figure 3.21D & E). Moreover the 200 µM simulation accurately predicted the experimentally observed dynamic changes in the concentrations of Tpx1-ox:SOOH and Tpx1-SOOH (Figure 3.22D - E).

To further test the ability of model A to accurately represent Tpx1 oxidation, its ability to simulate the experimental data for the formation of Tpx1-SOOH at 500 and 1000 µM H_2O_2 was tested (Figure 3.23). These time courses demonstrated that exposure to 500 µM and 1000 µM H_2O_2 caused Tpx1-SOOH to accumulate faster *in vivo* than exposure to 200 µM H_2O_2. Indeed, treatment with 1000 or 500 µM H_2O_2 resulted in maximum hyperoxidation of Tpx1 by 60 seconds (Figure 3.15). Model A simulated that increasing H_2O_2 concentration increased the rate of Tpx1-SOOH accumulation (Figure 3.23). The ability of model A to predict the formation of Tpx1-SOOH at 500 and 1000 µM H_2O_2 (Figure 3.23) experimental data which was not used to parameterise the model, validates model A and further indicates that this model is an accurate representation of the *in vivo* oxidation of Tpx1.

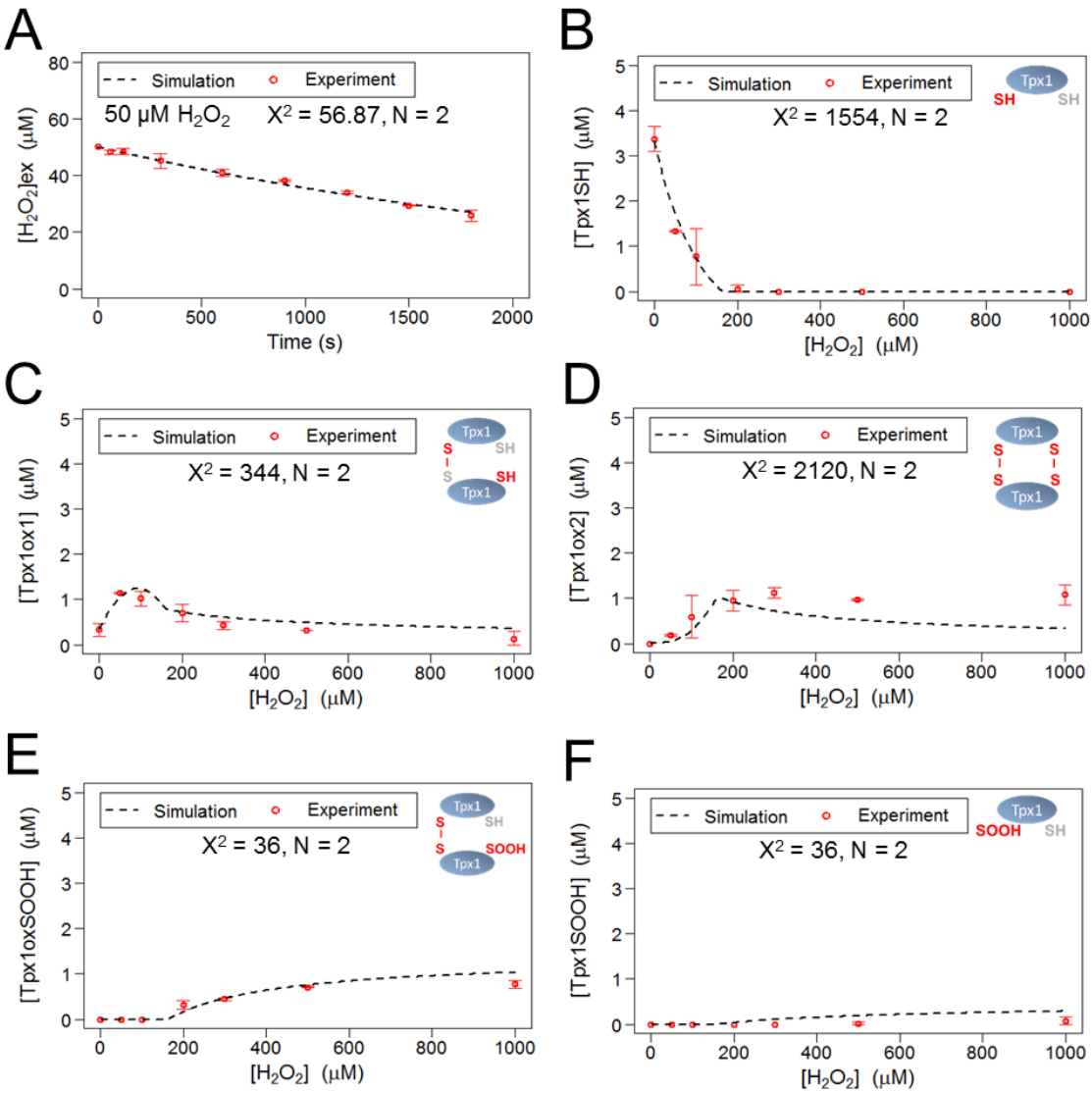

Figure 3.20 Qualitative analysis of the fit of the model to the experimental data following 20 second exposure to 0 – 1000 µM H_2O_2.

Plots show simulated and experimentally determined concentrations of (A) extracellular H_2O_2, (B) reduced Tpx1; Tpx1SH (C) single Tpx1 disulfides; Tpx1ox#1 (D) double Tpx1 disulfides; Tpx1ox#2 (E) disulfide bonded hyperoxidised Tpx1; Tpx1ox:SOOH (F) hyperoxidised Tpx1 monomer; Tpx1SOOH in wild-type *S. pombe* following 20 second exposure to between 0 and 1000 µM H_2O_2. Simulated data derived from the model were plotted against the experimental data used in the parameter estimation. Chi^2 (χ^2) values and number of repeat experiments (N) are shown. Error bars represent standard deviation.

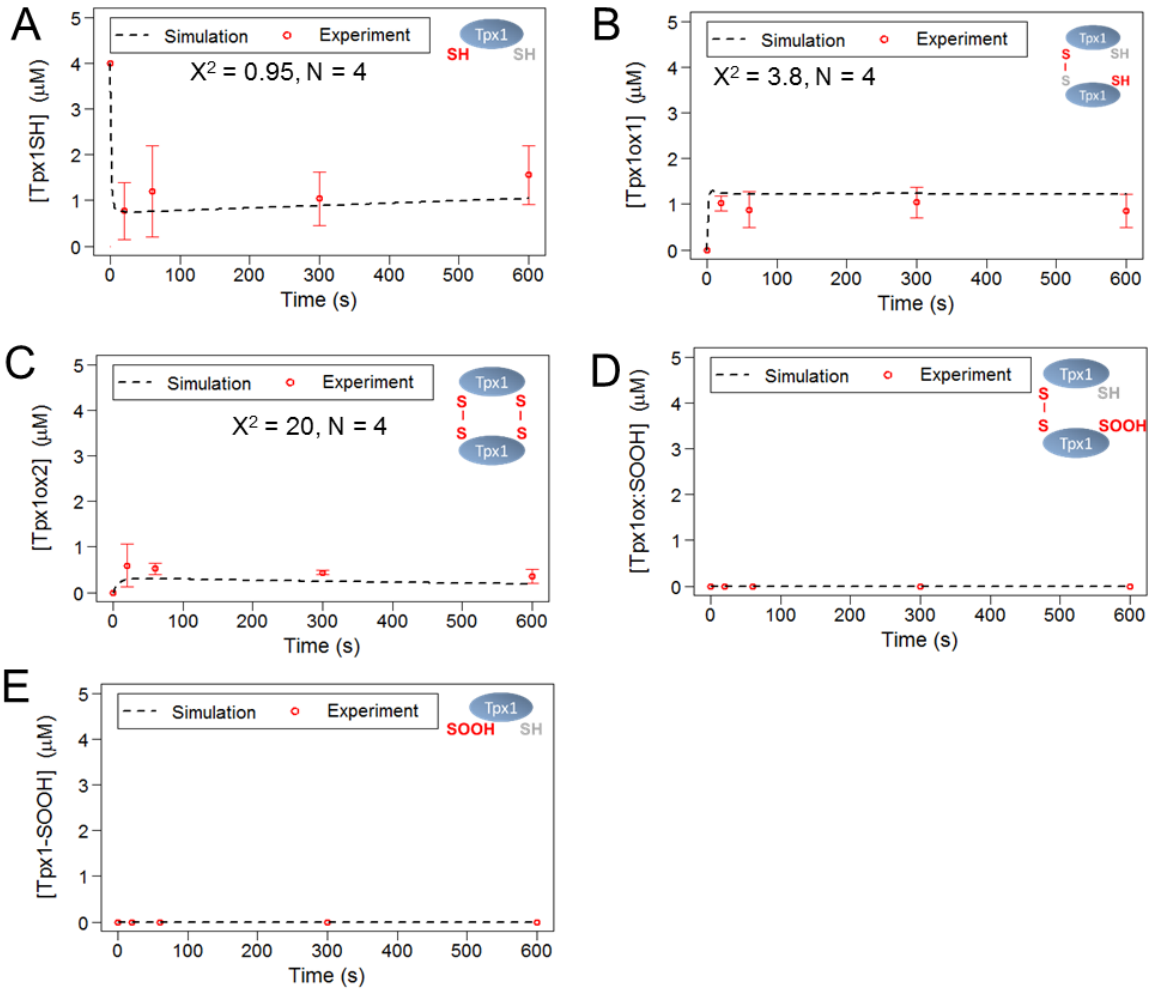

Figure 3.21 Qualitative analysis of the fit of the model to the experimental data for between 0 - 600 s exposure to 100 µM H_2O_2.

Plots show simulated and experimentally determined concentrations of (A) reduced Tpx1; Tpx1SH (B) single Tpx1 disulphides; Tpx1ox1 (C) double Tpx1 disulphides; Tpx1ox2 (D) disulphide bonded hyperoxidised Tpx1; Tpx1oxSOOH (E) hyperoxidised Tpx1 monomer; Tpx1SOOH in wild-type *S. pombe* following 0 - 600 s treatment with 100 µM H_2O_2. Simulated data derived from the model were plotted against the experimental data used in the parameter estimation. Chi^2 (χ^2) values and number of repeat experiments (N) are shown. Error bars represent standard deviation.

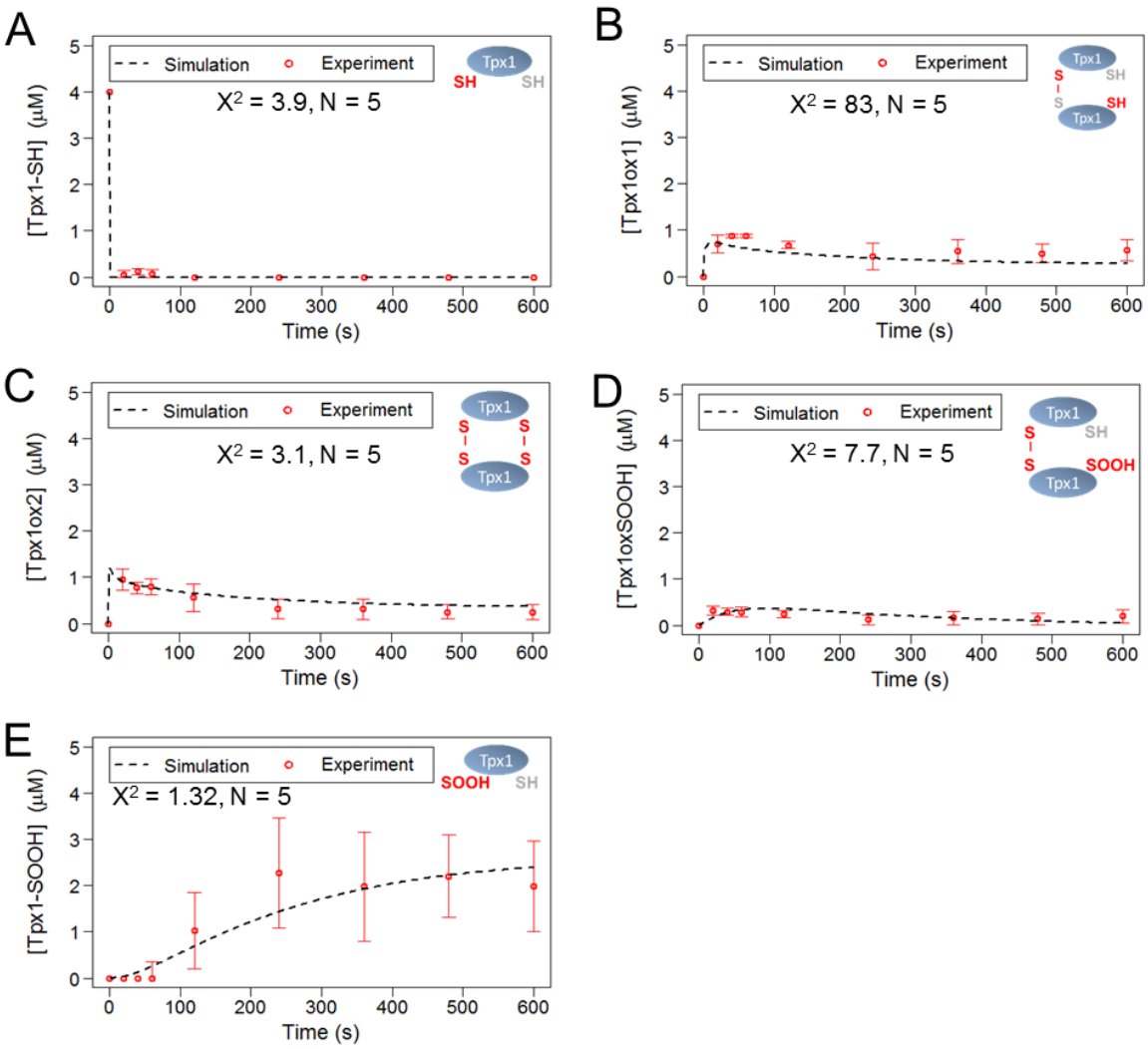

Figure 3.22 Qualitative analysis of the fit of the model to the experimental data for between 0 - 600 s exposure to 200 µM H_2O_2.

Plots show simulated and experimentally determined concentrations of (A) reduced Tpx1; Tpx1SH (B) single Tpx1 disulphides; Tpx1ox1 (C) double Tpx1 disulphides; Tpx1ox2 (D) disulphide bonded hyperoxidised Tpx1; Tpx1oxSOOH (E) hyperoxidised Tpx1 monomer; Tpx1SOOH in wild-type *S. pombe* following 0 - 600 s treatment with 200 µM H_2O_2. Simulated data derived from the model were plotted against the experimental data used in the parameter estimation. Chi^2 (χ^2) values and number of repeat experiments (N) are shown. Error bars represent standard deviation.

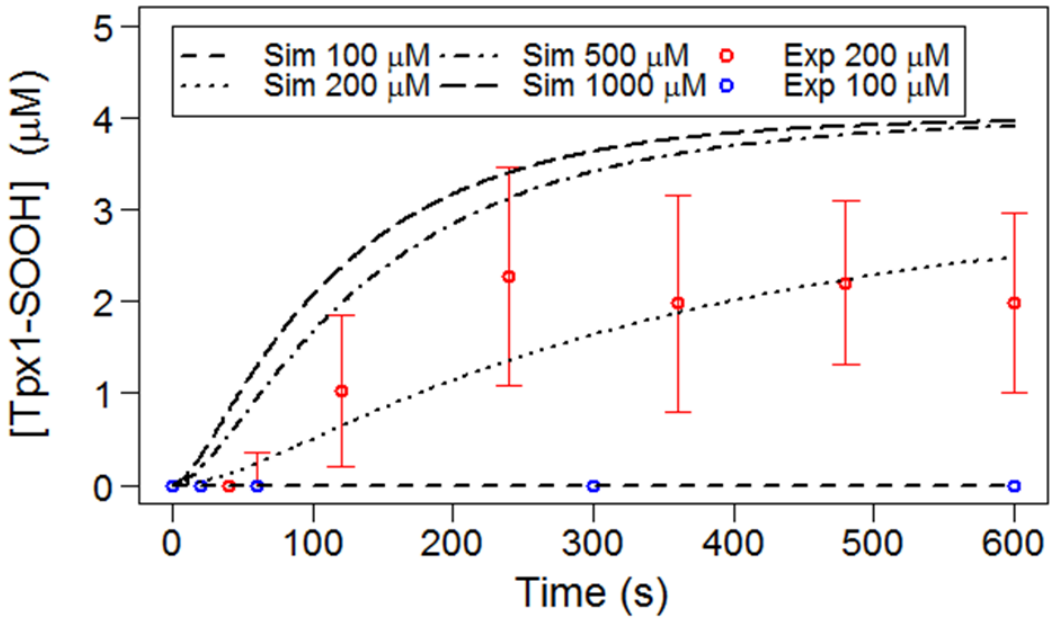

Figure 3.23: Model prediction for the effects of increasing H_2O_2 on the formation of Tpx1-SOOH from 0 – 600 seconds.

The model was used to simulate Tpx1-SOOH formation after a 0 – 600 second exposure to 100, 200, 500 and 1000 µM H_2O_2. The simulation data was plotted against the experimental data for the concentration of Tpx1-SOOH after a 0 – 600 s exposure to 100 & 200 µM H_2O_2.

3.4.3 The alternative models, Model B and Model C less accurately simulate the dynamics of Tpx1 oxidation compared to model A

To further test whether Model A is a more accurate representation of Tpx1 oxidation than the alternative models we used Model B and Model C to simulate the oxidation of Tpx1 (Figure 3.24). Although the alternative models were able to simulate some of the experimentally observed features of Tpx1 oxidation, as described below there were many examples where Model A was clearly better able to fit the data than Model B and Model C (Figure 3.24).

The simulation data for Model B indicates that this model is unable to accurately simulate the dynamics of Tpx1-ox#1 and Tpx1-ox#2 (Figure 3.24A - C). In particular, Model B failed to simulate Tpx1-ox#2 formation after a 600 s exposure to 100 µM H_2O_2 (Figure 3.24C). Model B and the preliminary model containing the reaction Opt1 both assume that the Cys_P-SH in Prx-ox#1 can be oxidised by H_2O_2 to form Prx-ox:SOH (Figure 3.4 & Figure 3.16). Since both of these models were unable to accurately simulate the dynamics of Prx oxidation (Figure 3.5 & Figure 3.24C), this strongly suggests that the oxidation of Prx-ox#1 to Prx-ox:SOH does not happen *in vivo*.

The simulation data for Model C indicated that most Tpx1 will be hyperoxidised by 600 seconds following exposure to 100 µM H_2O_2 (Figure 3.24D & E). However, experimentally no hyperoxidised Tpx1 was detected at this concentration of H_2O_2 (Figure 3.12 & 3.15 A). The absence of hyperoxidised Tpx1 after exposure to 100 µM H_2O_2 suggests the existence of a mechanism *in vivo* which is inhibiting hyperoxidation at this H_2O_2 concentration. The observation that Model A, which contains a second peroxidase process is able to simulate the dynamics of Tpx1 hyperoxidation, whilst model C does not, is consistent with another peroxidase process, which is in competition with the hyperoxidation reaction inhibiting Tpx1 hyperoxidation (Figure 3.16, re6).

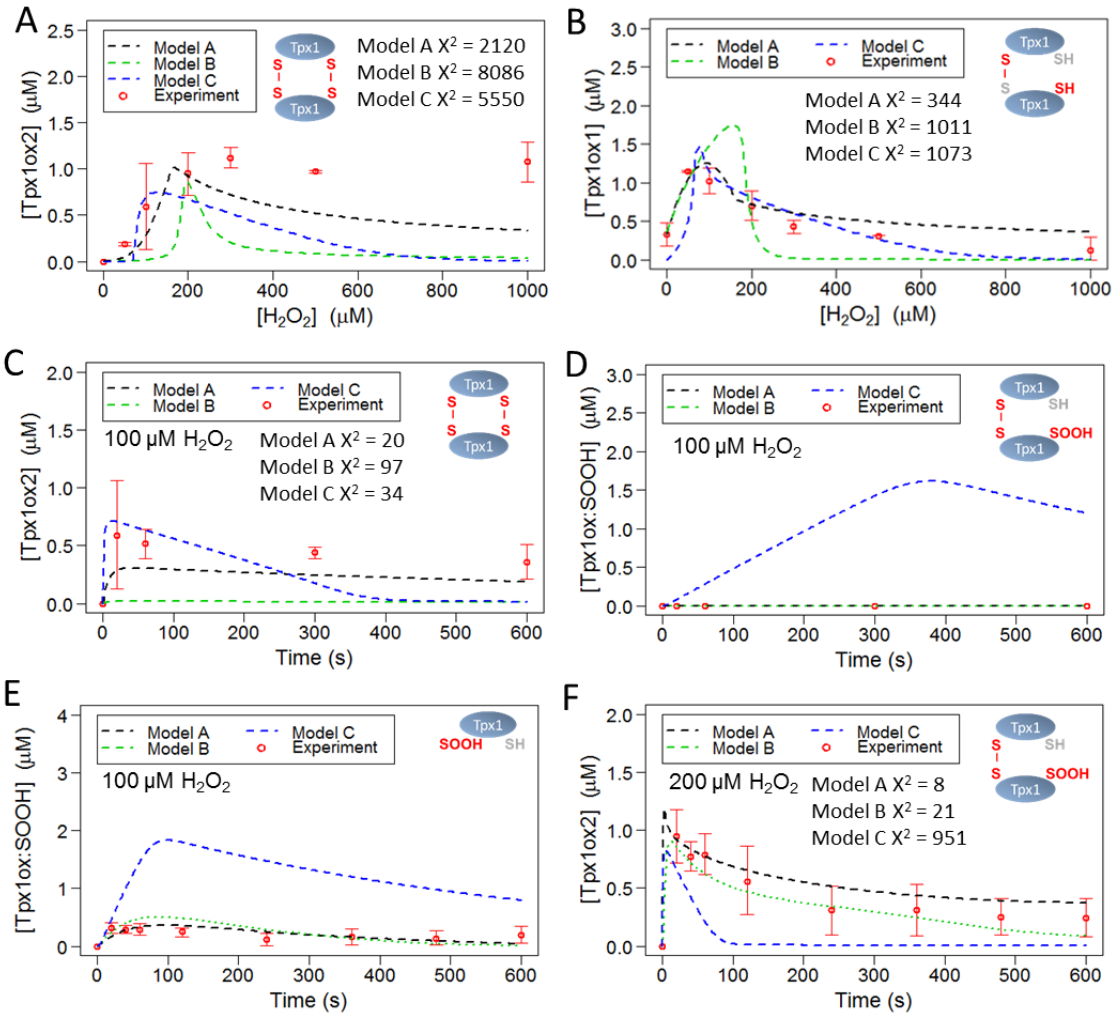

Figure 3.24: Comparison of simulation and experimental data for the alternative models of *in vivo* Tpx1 oxidation.

The alternative models of *in vivo* Tpx1 oxidation were used to simulate (A & B) the formation of Tpx1-ox#2 and Tpx1-ox#1 after a 0 – 20 second exposure to 0 – 1000 μM H_2O_2, (C – E) changes in the concentration of Tpx1-ox#2, Tpx1-ox:SOOH and Tpx1-SOOH after 0 – 600 second exposure to 100 μM H_2O_2 and (F) changes in the concentration of Tpx1-ox:SOOH after a 0 – 600 seconds exposure to 200 μM H_2O_2. Simulation data was plotted against the experimental time course data for Tpx1 oxidation. Chi^2 (χ^2) values for the correlations between the experimental and simulation data for each model are shown.

3.4.4 The model predicts a two phase relationship between intracellular and extracellular H_2O_2 concentration

Having selected Model A as the best representation of the *in vivo* oxidation of Tpx1, this model was used to predict the effect of increasing the extracellular concentration of H_2O_2 ($[H_2O_2]_{ex}$) on the intracellular H_2O_2 concentration ($[H_2O_2]_{int}$) (Figure 3.25). The model simulation predicted that $[H_2O_2]_{ex}$ < 100 µM will cause little net change in $[H_2O_2]_{int}$ however, at $[H_2O_2]_{ex}$ concentrations > 100 µM $[H_2O_2]_{int}$ will increase linearly with $[H_2O_2]_{ex}$ (Figure 3.25). These bi-phasic H_2O_2 dynamics are similar to the findings of the preliminary models of H_2O_2 movement in a cell culture environment (Figure 3.6 & 3.7). Similarly, to the cell culture model, the concentration of $[H_2O_2]_{ex}$ required to cause an increase $[H_2O_2]_{int}$ in Model A is dependent on the parameter $V_{max\_H2O2\_metab}$ and setting this parameter to 0 µM s^{-1} causes $[H_2O_2]_{int}$ to increase linearly with all $[H_2O_2]_{ex}$ concentrations (Figure 3.25A). The model therefore predicted that in order to cause an increase in $[H_2O_2]_{int}$, the rate that H_2O_2 enters the cell from the extracellular space must be faster than the V_{max} of the non-Tpx1 peroxidase process. Interestingly, the model predicts that the concentration of $[H_2O_2]_{ex}$ required to cause an increase in $[H_2O_2]_{int}$ is the same as the $[H_2O_2]_{ex}$ required of Tpx1-ox:SOOH formation (Figure 3.25B). The $[H_2O_2]_{ex}$ required for Tpx1-ox:SOOH formation is also dependent on the parameter $V_{max\_H2O2\_metab}$ (Figure 3.25B). The model is therefore suggesting that Tpx1 hyperoxidation occurs when the saturation of a non-Tpx1 peroxidase process causes an increase in $[H_2O_2]_{int}$.

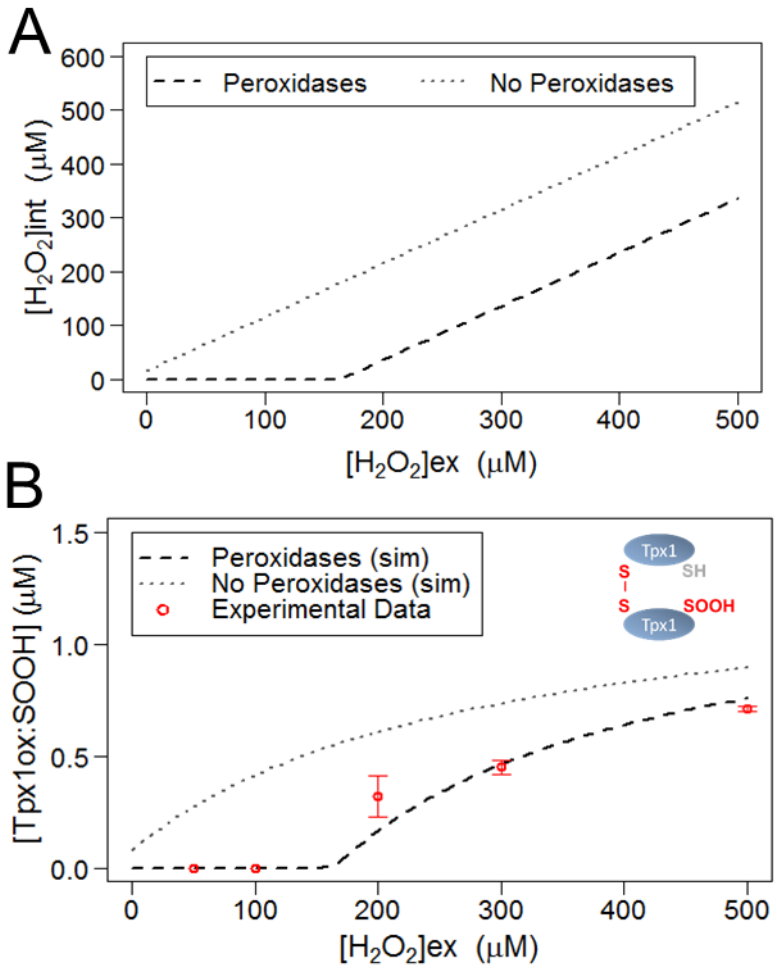

Figure 3.25: The model predicts that Tpx1 hyperoxidation will occur when cellular peroxidases become saturated.

(A) The model was used to simulate the effect that increasing extracellular H_2O_2 concentration ($[H_2O_2]_{ex}$) will have on the intracellular H_2O_2 concentration ($[H_2O_2]_{int}$). (B) The model was used to simulate the effect of $[H_2O_2]_{ex}$ on Tpx1-ox:SOOH formation. Both simulations were performed with "Peroxidases" ($V_{max\_H2O2\_metab}$ = 59 μM s^{-1}) and with "No peroxidases" ($V_{max\_H2O2\_metab}$ = 0 μM s^{-1}). The experimental data for the concentration of Tpx1-ox:SOOH after a 20 second exposure to 0 – 500 μM H_2O_2 was plotted on the same axis as the simulation data, error bars represent standard deviation of experimental data (N = 2).

3.4 Measuring intracellular H_2O_2 concentration

The model of *in vivo* Tpx1 oxidation predicted that Tpx1 hyperoxidation is preceded by an increase in intracellular H_2O_2 concentration and that this is due to the saturation of a non-Tpx1 peroxidase process (Figure 3.25B). In order to test this prediction, changes in intracellular [H_2O_2] were measured after exposure to extracellular H_2O_2. Two different ROS/H_2O_2 sensitive fluorescent dyes were used to measure changes in intracellular H_2O_2 as described below.

3.4.1 *Using DCFDA to measure intracellular H_2O_2 concentrations*

DCFDA is a commercially available and widely used ROS sensitive dye (Eruslanov and Kusmartsev, 2010, Dirmeier et al., 2002). This dye is inactive until in enters the cell after which it is activated by cellular esterase enzymes. It is important to note that DCFDA is described as a ROS-sensitive dye and is not specifically sensitive to H_2O_2. When exponentially growing *S. pombe* cells were incubated with DCFDA (see 2.3.2), then exposed to a range of H_2O_2 concentrations, fluorescence microscopy could only detect fluorescence in cells exposed to 10,000 µM H_2O_2 (Figure 3.26A). Even after treatment with 10,000 µM H_2O_2, fluorescence could only be detected in a fraction of the cells. Fluorescence measurements were also made using a plate reader (see 2.3.2) which were able to detect a small increase in fluorescence after 5,000 µM H_2O_2 and a more substantial increase at 10,000 µM H_2O_2 (Figure 3.26B).

The measured increase in fluorescence suggests that only after exposure to 10,000 µM is there any substantial increase in intracellular ROS. This disagreed with the model in that the increase in fluorescence was only detected after treatment with 10 mM H_2O_2 rather than the 0.1 mM predicted by the model (Figure 3.25). This suggested that the model prediction was incorrect. However it was possible that it reflected the lack of H_2O_2 sensitivity of DCFDA. It could be the case that DCFDA is not sensitive enough to detect an increase in H_2O_2 concentration at 0.1 mM and what we are seeing is actually an increase in other forms of ROS formed after exposure to very high concentrations of H_2O_2.

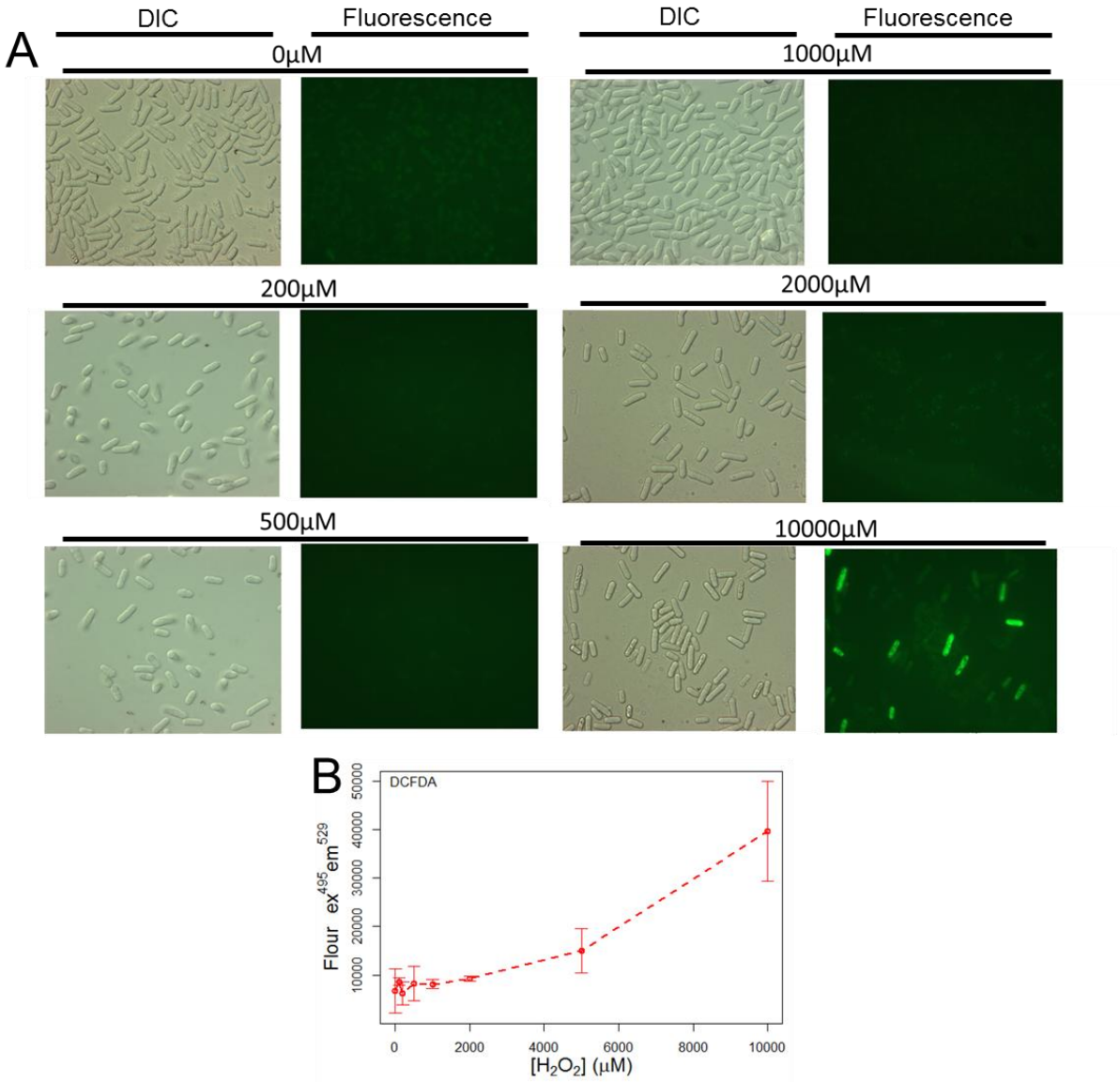

Figure 3.26: Measuring DCFDA fluorescence detected an increase in intracellular ROS concentration after treatment with 5,000 µM H_2O_2.

Exponentially growing *S. pombe* cells were exposed to H_2O_2 concentrations ranging 0 – 10,000 µM and fluorescence was detected using (A) fluorescence microscopy or (B) fluorescence plate reader methods (see 2.3.2). (A) Right hand panels show images taken using the DIC whilst the left panels show images taken using fluorescence. (B) Each H_2O_2 concentration was performed in triplicate and the error bars represent the standard deviation.

3.4.2 Using the H_2O_2 specific dye PF3 to measure intracellular H_2O_2.

Several, more sensitive, H_2O_2-specific dyes have been developed (Dickinson et al., 2010). The fluorescent dye PF3, developed by Bryan Dickinson and Chris Chang, is a semi-trappable H_2O_2-specific fluorescent dye (Dickinson and Chang, 2008). PF3 was used to measure changes in intracellular H_2O_2 in response to extracellular H_2O_2. Exponentially growing *S. pombe* cells were incubated with PF3 (see 2.3.3) and then treated with a range of H_2O_2 concentrations. PF3 fluorescence in these cells was detected using both microscope and plate reader methods.

Although we were unable to detect any fluorescence by fluorescent microscopy (data not shown), H_2O_2-induced changes in fluorescence were detected using the plate reader. Importantly, comparison of the fluorescence of PF3-treated and non-treated cells confirmed that the fluorescence was due to PF3 (Figure 3.26A). The fluorescence of the PF3 treated cells increased over time even in the absence of extracellular H_2O_2, suggesting that PF3 was sufficiently sensitive to react with endogenous H_2O_2 (Figure 3.27B). As expected addition of extracellular H_2O_2 caused the fluorescence to increase faster than in non-H_2O_2 treated cells.

Time course data for the increase in PF3 fluorescence after exposure to 0 – 500 µM H_2O_2 was collected. This data was used to calculate the rate of change of fluorescence ($\Delta F/\Delta t$) (see 2.3.3) for each H_2O_2 concentration. Plotting $\Delta F/\Delta t$ against H_2O_2 concentration (Figure 3.27C) demonstrated that $\Delta F/\Delta t$ increases with H_2O_2 concentration. Calculating the gradient (m) and the y-intercept (x) for the $\Delta F/\Delta t$ values from 0 – 100 µM and then extrapolating to 500 µM H_2O_2 using the formula y = mx + c indicated that $\Delta F/\Delta t$ was increasing disproportionately faster in the cells treated with > 150 µM H_2O_2. By assuming that $\Delta F/\Delta t$ is a proxy for $[H_2O_2]_{int}$, our data has demonstrated that increases in $[H_2O_2]_{int}$ are inhibited after exposure $[H_2O_2]_{ex}$ < 150 µM. This finding is in agreement with the prediction of our model (Figure 3.25A). The increase in $[H_2O_2]_{int}$ was also inhibited in Δ*tpx1* cells exposed to H_2O_2 < 150 µM (Figure 3.27D) indicating that this inhibition is independent of Tpx1.

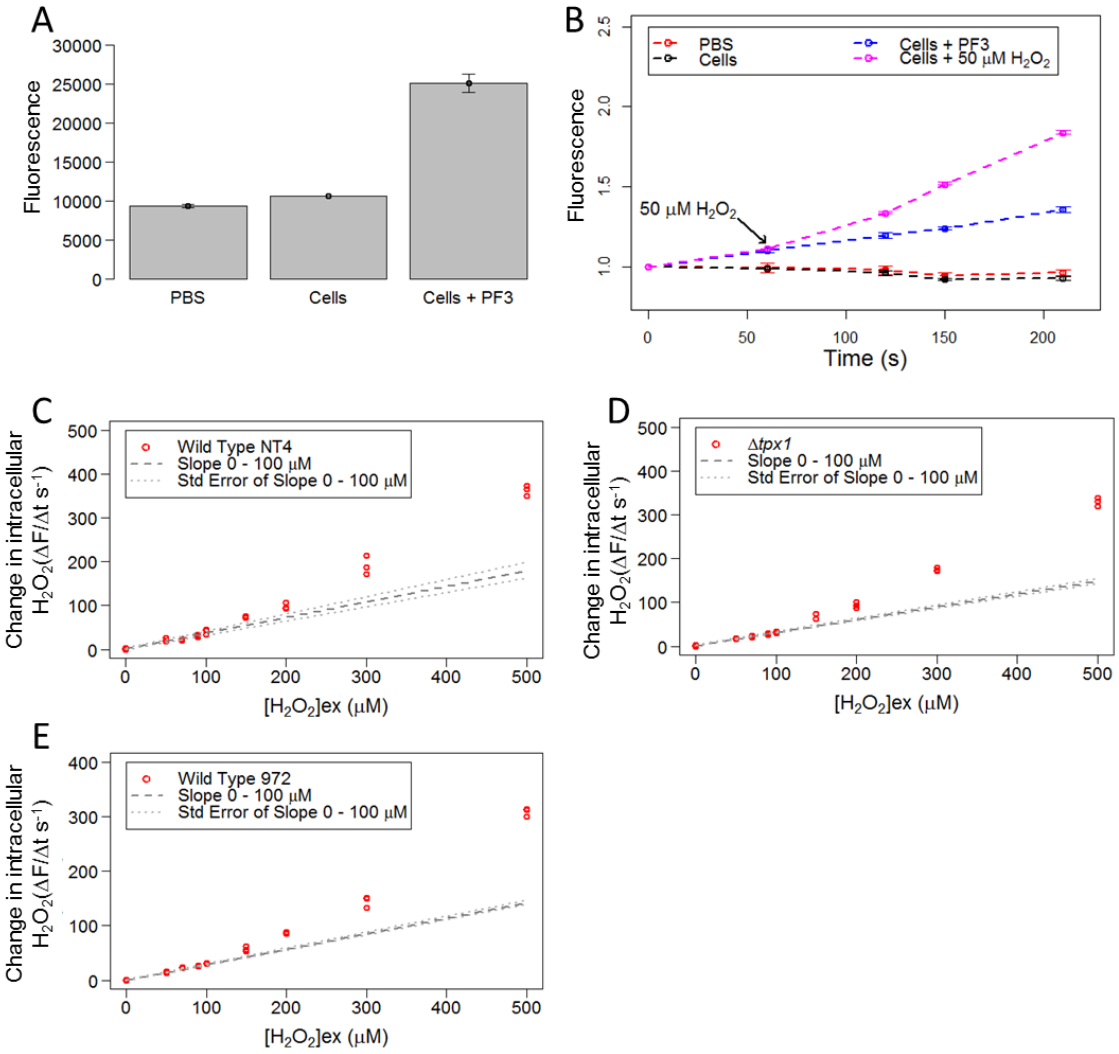

Figure 3.27: Measuring intracellular H_2O_2 using the fluorescent dye PF3.

(A) A plate reader was used to measure the fluorescence of PBS, wild-type *S. pombe* cells (NT4) suspended in PBS and PF3 treated *S. pombe* cells. Each measurement was done in triplicate and the error bars represent the standard deviation of the three measurements. (B) A plate reader was used to measure the fluorescence change over 210 seconds of PBS, *S. pombe* cells suspended in PBS, *S. pombe* cells treated with PF3 and cells treated with PF3 and 50 µM H_2O_2. The rate of change of fluorescence ($\Delta F/\Delta t\ s^{-1}$) was calculated for (C) wild-type *S. pombe* cells (NT4), (D) Δ*tpx1* (VX00) cells and (E) wild-type S. pombe cells (972) treated with 0 – 500 µM H_2O_2. The gradient and standard error of the gradient for the ($\Delta F/\Delta t\ s^{-1}$) values for 0 – 100 µM H_2O_2 treatment was extrapolated and plotted on the same axis.

3.5 The H_2O_2-buffering capacity of *S. pombe* mutants and human kidney (HEK-293) cells

The computer model predicted that increases in the intracellular H_2O_2 concentration in response to H_2O_2 < 150 µM were being inhibited by a non-Tpx1 peroxidase process (Figure 3.25). The model also predicted the saturation of this peroxidase process is responsible for increases in the intracellular H_2O_2 concentration following an extracellular exposure to H_2O_2 > 150 µM (Figure 3.25). Furthermore, the model predicted that this increase in the intracellular H_2O_2 concentration would occur prior to Tpx1 hyperoxidation (Figure 3.25B). An effective method for measuring intracellular H_2O_2 concentration was developed and used to demonstrate that, consistent with our model prediction, increases in $[H_2O_2]_{int}$ were inhibited following exposure to $[H_2O_2]_{ex}$ < 150 µM (Figure 3.27). However, it was not clear if the experimentally observed inhibition was occurring before or after Tpx1 hyperoxidation. Secondly, it was not clear if this inhibition was a general feature that is conserved in mammalian cells. Thirdly, the identity of the peroxidase process, responsible for this inhibition was unknown. To answer these questions the relationship between $[H_2O_2]_{ex}$ and $[H_2O_2]_{int}$ was measured in a range of *S. pombe* mutant cells and human kidney (HEK-293) cells.

3.5.1 Prx hyperoxidation and an increase in $[H_2O_2]_{int}$ are observed in HEK-293 after treatment with 40 µM H_2O_2.

We used PF3 to measure changes in $[H_2O_2]_{int}$ in HEK-293 cells and observed that increases in $[H_2O_2]_{int}$ were inhibited following exposure to an $[H_2O_2]_{ex}$ < 30 µM (Figure 3.28A). Using western blot, we then measured and quantified Prx hyperoxidation in HEK-293 cells exposed to 0 – 80 µM H_2O_2 for 10 min (Figure 3.28B & C). After treatment with 0 – 20 µM H_2O_2 no Prx hyperoxidation could be detected (Figure 3.28B). However, after treatment with 40 µM H_2O_2, antibodies specific for the hyperoxidised form of 2-Cys Prx detected 2-bands with a mobility of 25 kDa (Figure 3.28B). This is consistent with these bands being hyperoxidised Prx monomers, most likely Prx1 and Prx3, since Prx1 and Prx2 have the same molecular weight. This suggests that hyperoxidation of Prx might also only occur in mammalian cells once the H_2O_2 buffering capacity has been breached.

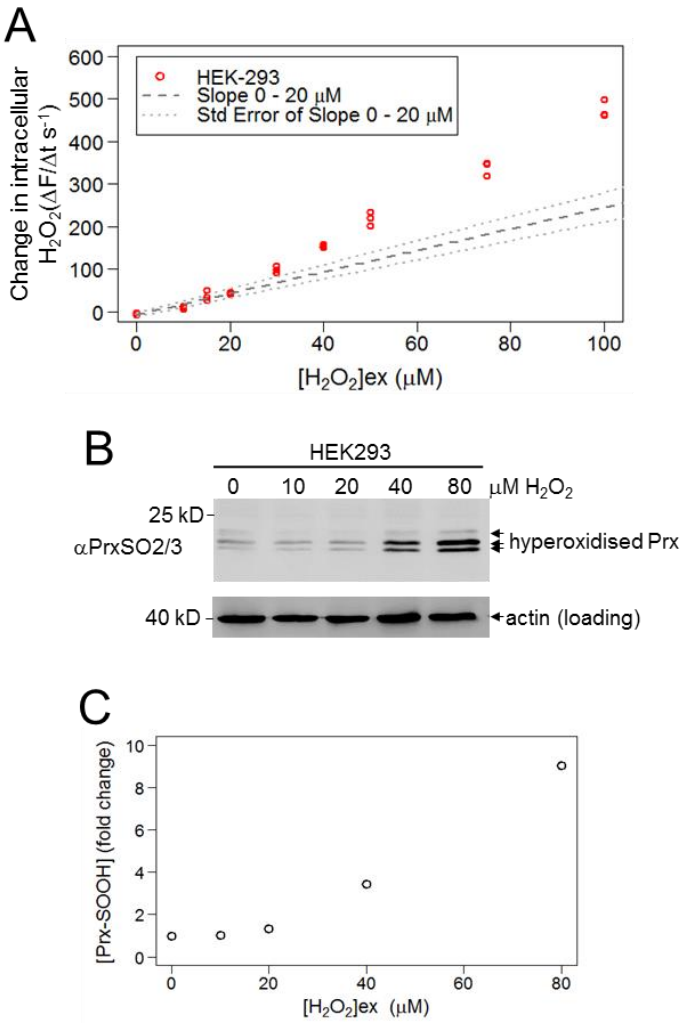

Figure 3.28: Measuring intracellular H_2O_2 and Prx hyperoxidation in HEK293 cells.

(A) The rate of change of fluorescence ($\Delta F/\Delta t\ s^{-1}$) was calculated for HEK293 cells treated with 0 – 500 µM H_2O_2. The gradient and standard error of the gradient for the ($\Delta F/\Delta t\ s^{-1}$) values for 0 – 20 µM H_2O_2 treatment was extrapolated and plotted on the same axis. (B) HEK293 cells were treated with the indicated H_2O_2 concentrations and protein samples were analysed with western blot using α-PrxSO2/3 antibodies which have affinity for hyperoxidised Prx. For use as a loading control, the blots were stripped and re-probed with α- actin antibodies. (C) The hyperoxidised Prx bands were quantified using densitometry and normalised against the intensity of the loading control bands. The fold change in band intensity, relative to the untreated cells was plotted.

3.5.2 The increase in intracellular H_2O_2 concentration is independent of Tpx1 hyperoxidation.

In order to establish whether the increase in $[H_2O_2]_{int}$ observed after exposure to $[H_2O_2]_{ex}$ > 150 µM occurs before or after Tpx1 hyperoxidation, intracellular H_2O_2 concentration was measured in two *S. pombe* mutants containing different hyperoxidation resistant forms of Tpx1. The first mutant expressed a truncated form of Tpx1, $Tpx1^{1-181}$, that is resistant to hyperoxidation (Koo et al., 2002, Day et al., 2012). The increase in $[H_2O_2]_{int}$ after exposure to $[H_2O_2]_{ex}$ > 150 µM was still observed in this mutant (Figure 3.29B) as well as the isogenic wild type for this strain (Figure 3.29A). Changes in intracellular H_2O_2 were also measured in strains containing the hyperoxidation resistant $Tpx1^{T86E}$ (Rand, Day, Veal and Morgan, unpublished work) expressed from the chromosome or plasmid (Figure 3.29C & E). Both of these strain displayed the same H_2O_2 dynamics as their isogenic wild type strains (Figure 3.29A & D). These findings suggest that, in agreement with our model, the H_2O_2-induced increase in $[H_2O_2]_{int}$ is independent of Tpx1 hyperoxidation.

3.5.3 *Inhibition of increases in the intracellular H_2O_2 concentration in S. pombe are independent of catalase but is dependent on the disulphide reductases Trx1 & Txl1*

The model indicated that the saturation of a non-Tpx1 peroxidase process is required to explain the dynamics of Tpx1 hyperoxidation and that the saturation of this process is responsible for an increase in the intracellular H_2O_2 concentration following exposure to $[H_2O_2]_{ex}$ > 150 µM (Figure 3.25). It has been shown that catalase inhibits hyperoxidation of Prx2 *in vitro* (Peskin et al., 2013). It was therefore postulated that the unknown peroxidase activity in the model, that is saturated after treatment with 150 µM H_2O_2, could be catalase. In order to test this hypothesis Δ*ctt1 S. pombe* mutant cells were made (Bioneer) in which the *ctt1* open-reading frame was replaced with the Kanamycin resistance gene Kan^{MX4} (Kim et al., 2010). This mutant was obtained from a library of deletion mutants so to confirm that the *ctt1* gene was knocked out effectively in the library strain, PCR followed by restriction digest of the PCR product was performed (see 2.5) (Figure 3.30). The Kan^{mx4} and *ctt1* PCR products produced are similar in

size. However, the *Kan^{MX4}* gene product contains a *HindIII* restriction site, which is absent from the *ctt1* product. Hence, the observation that the PCR product from the Δ*ctt1* strain was digested by the *HindIII* restriction enzyme confirms that the *ctt1* gene was disrupted in this strain.

Importantly, as expected (Paulo et al., 2014), a halo test (see 2.4.1) confirmed that loss of *Ctt1* reduced the ability of *S. pombe* to grow in the presence of high concentrations of H_2O_2 (Figure 3.31 C-E). However, the $[H_2O_2]_{int}$ measurements in the Δ*ctt1* strain (Figure 3.31 B) indicated that, similar to wild type (Figure 3.31 A), the intracellular H_2O_2 increased more rapidly after treatment with an $[H_2O_2]_{ex}$ of 150 μM. Moreover, the observation that the non-linear increase in $[H_2O_2]_{int}$ occurred in the Δ*ctt1* mutant at the same H_2O_2 concentration as the wild-type strain strongly suggests that the saturation of catalase is not responsible for the increase in H_2O_2 concentration following exposure to H_2O_2 > 150 μM.

Although it is possible that the Gpx/GSH system (Makino et al., 2008), or other subfamilies of Prx contribute to the H_2O_2-buffering capacity of *S. pombe*, this seems unlikely given the minimal effect that deletion of the genes encoding these enzymes (*gpx1*, *pmp20* or *dot5*) has on H_2O_2 resistance (Vivancos et al., 2005). Computational modelling has suggested that reversible oxidation of the thiol proteome makes an important contribution to the peroxide-buffering capacity of human cells (Adimora et al., 2010). Moreover, previous work has shown that the thiol proteome in *S. pombe* is maximally oxidised following exposure to 200 μM H_2O_2 (Garcia-Santamarina et al., 2013). Hence, we considered that reversible protein cysteine thiol oxidation might be the peroxide-removing activity that becomes saturated by 150 μM H_2O_2. The rate at which reduced protein thiols are regenerated by thioredoxin will limit the H_2O_2–removing capacity of the thiol proteome.

To test the hypothesis that the thiol proteome plays an important role in preventing increases in intracellular hydrogen peroxide we examined how extracellular H_2O_2 treatment affected intracellular H_2O_2 concentration in mutant *S. pombe* lacking both cytosolic thioredoxin family proteins, Trx1 and Txl1. Strikingly, unlike the wild type strain (Figure 3.32A), the intracellular H_2O_2 concentration in the Δ*trx1*Δ*txl1* strain increased directly proportional to the extracellular H_2O_2 concentration, even at H_2O_2 concentrations greater than 150

µM (Figure 3.32 B - D). This suggests that the H_2O_2 buffering effect seen in the wild-type strain is due to the oxidation of cellular thiols, which are subsequently reduced by thioredoxin family proteins. In one of the Δ*trx1*Δ*txl1* experiments (Figure 3.31D) there is a non-linear increase in the intracellular H_2O_2 concentration after treatment with 500 µM H_2O_2. This could imply that deletion of thioredoxin family proteins has actually increased H_2O_2 buffering, however this non-linear increase could be due to the saturation of glutathione dependent processes. It is worth noting that the maximum y-axis values for the three Δ*trx1*Δ*txl1* experiments (Figure 3.32 B-D) are lower than in the wild-type strain (Figure 3.32A). Although this creates the appearance that H_2O_2 buffering has increased in the Δ*trx1*Δ*txl1* strain, it is worth noting that the y-axis values are arbitrary due to limitations in the method. This limitation is due the fact that the gain values used by the plate reader vary between experiments. This means that y-axis values from different experiments are not comparable.

We therefore concluded that the intracellular H_2O_2 measurements in the Δ*trx1*Δ*txl1* strain indicate a loss of H_2O_2 buffering (Figure 3.32). This strongly suggests that, by reversing the oxidation of protein cysteine thiols, these thioredoxin family proteins make a major contribution to the cell's capacity to remove low levels of extracellular H_2O_2 (Figure 3.32). Together these data suggest that hyperoxidation of Prx only occurs once the peroxide-buffering capacity of the thiol proteome is saturated by H_2O_2 (Figure 3.33).

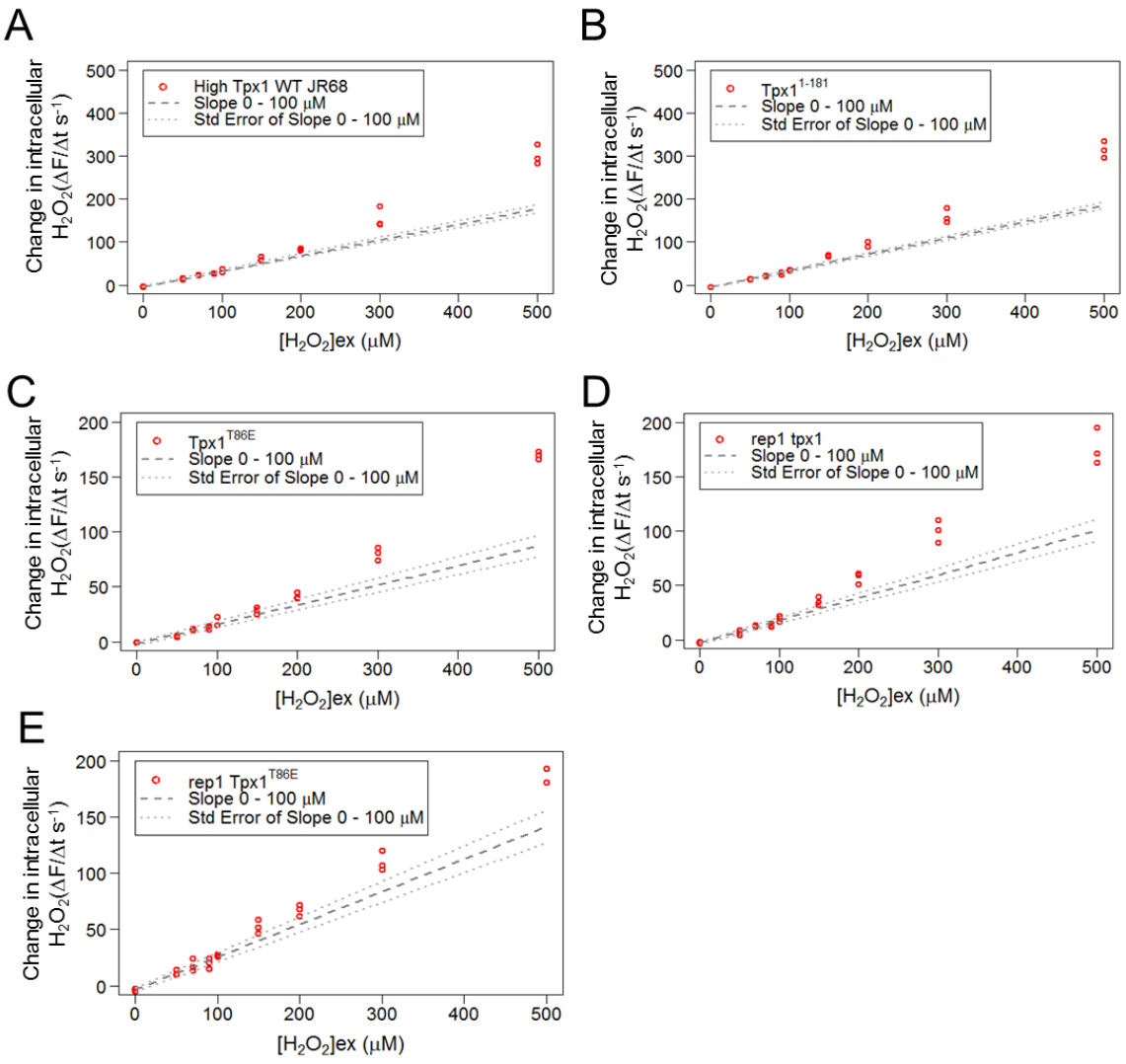

Figure 3.29: Measuring intracellular H_2O_2 concentration in hyperoxidation-resistant Tpx1 mutants.

The rate of change of fluorescence ($\Delta F/\Delta t\ s^{-1}$) was calculated for (A) wild-type *S. pombe* cells (JR68), (B) $Tpx1^{1-181}$ and (C) $Tpx1^{T86E}$ *S. pombe* cells treated with 0 – 500 µM H_2O_2. The calculations were performed using *S. pombe* cells containing plasmid (rep1) expressed Tpx1 (D) and $Tpx1^{T86E}$ (E). The gradient and standard error of the gradient for the ($\Delta F/\Delta t\ s^{-1}$) values for 0 – 100 µM H_2O_2 treatment was extrapolated and plotted on the same axis.

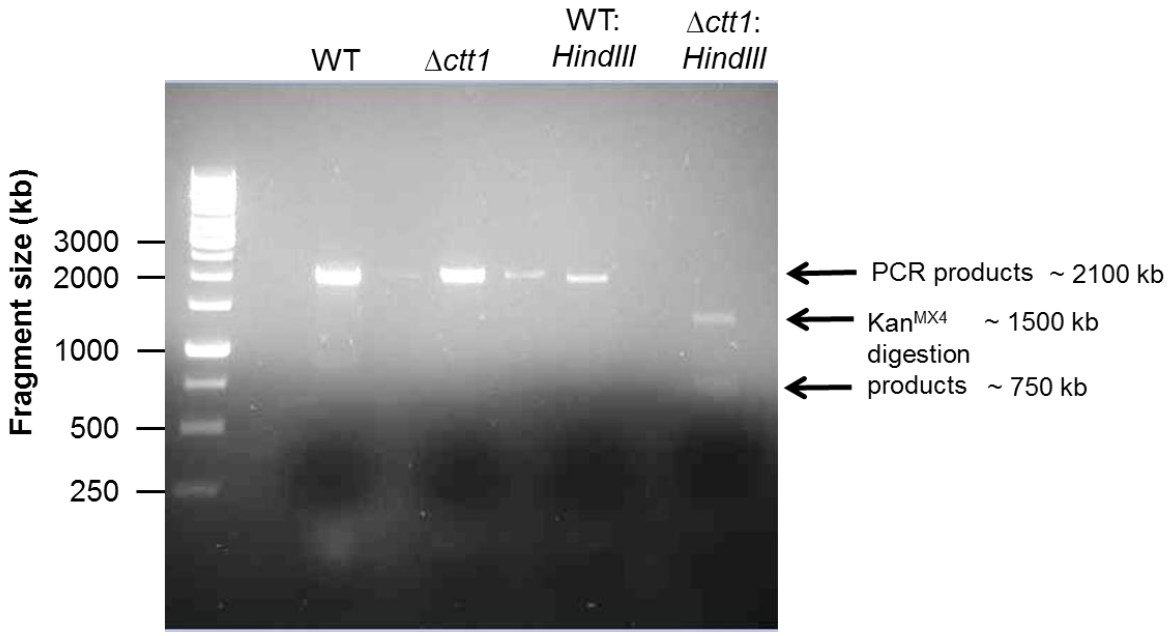

Figure 3.30: The *ctt1* gene has been effectively knocked out from the Δ*ctt1* mutant strain.

PCR was performed using the primers ctt1checkR and ctt1checkF with genomic DNA from wild-type *S. pombe* (NT4) or from the Bioneer Δ*ctt1* (LT3) strain and separated using gel electrophoresis. Samples of the PCR product were digested with the HindIII restriction endonuclease and the digestion products were separated using gel electrophoresis.

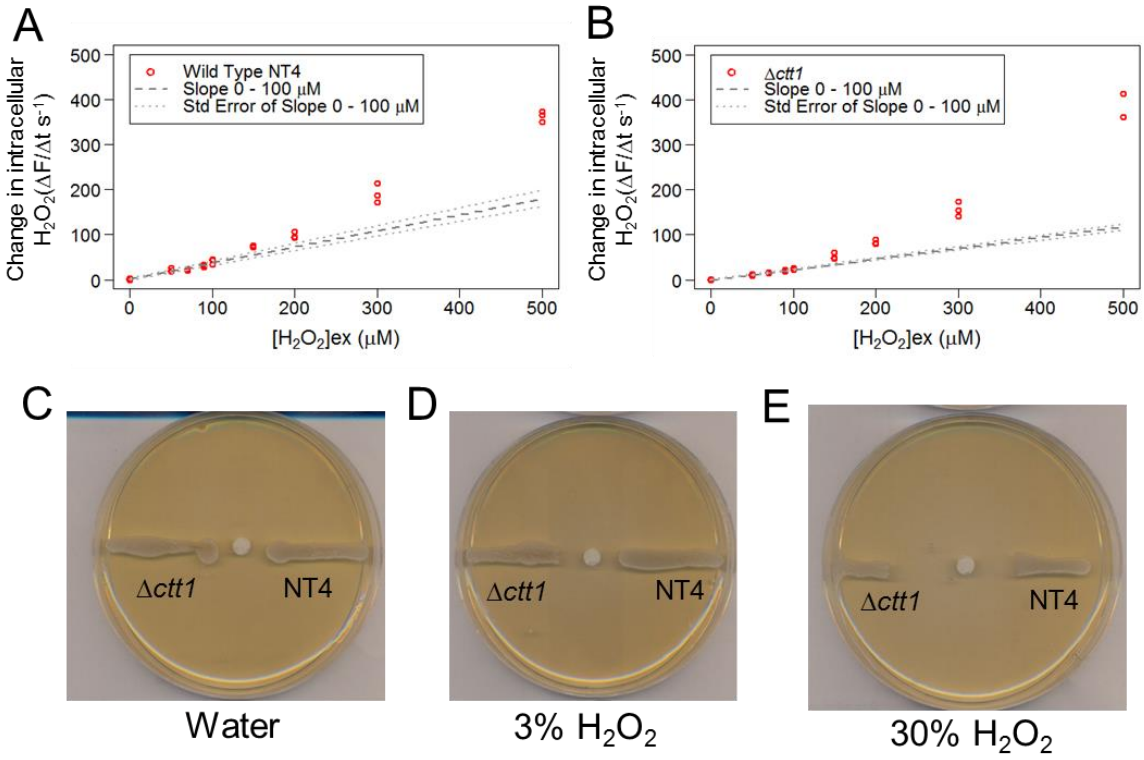

Figure 3.31: Characterisation of the Δ*ctt1* strain.

The rate of change of fluorescence ($\Delta F/\Delta t\ s^{-1}$) was calculated for (A) wild-type *S. pombe* cells (NT4) and (B) Δ*ctt1* (LT3) *S. pombe* cells treated with 0 – 500 µM H_2O_2. The gradient and standard error of the gradient for the ($\Delta F/\Delta t\ s^{-1}$) values for 0 – 100 µM H_2O_2 treatment was extrapolated and plotted on the same axis. (C - E) Wild-type (NT4) and Δ*ctt1* (LT3) *S. pombe* cells were grown on YE5S plates with filter paper soaked in (C) 1 µl of water, (D) 3% H_2O_2 or (E) 30% H_2O_2 placed in the centre of the plate.

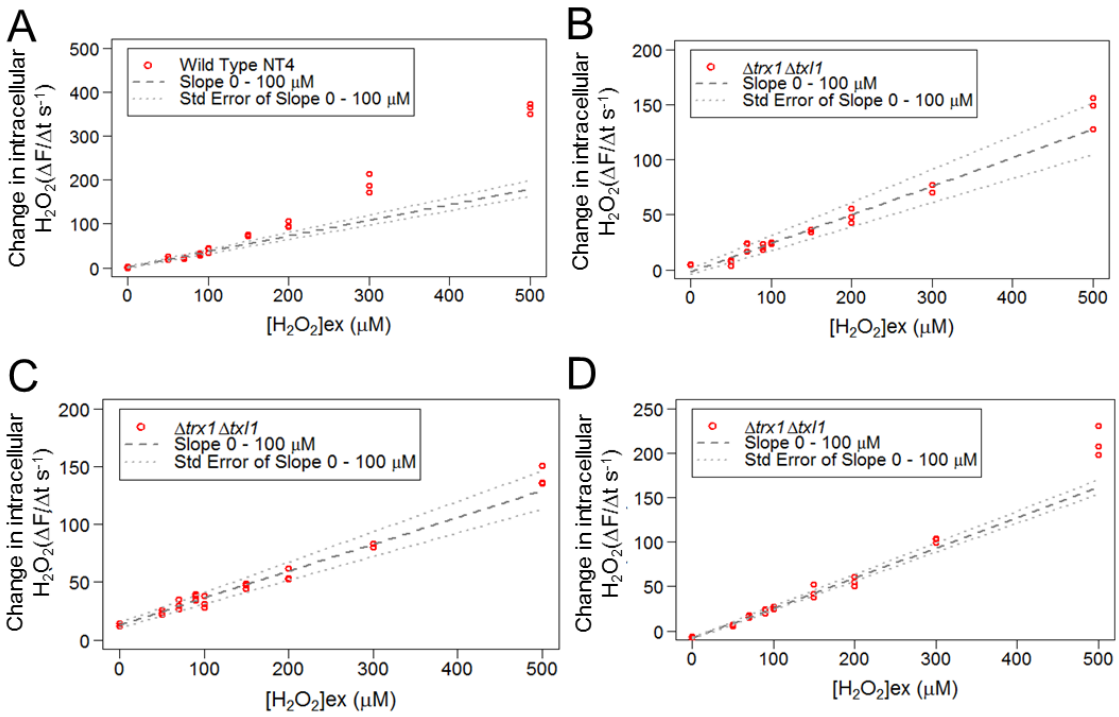

Figure 3.32: Trx1 and Txl1 are required to prevent large increases in intracellular H_2O_2 following exposure to low (< 150 µM) H_2O_2.

Increases in intracellular H_2O_2 concentration were determined as the rate of change of PF3-Ac fluorescence ($\Delta F/\Delta t\ s^{-1}$) in (A) wild-type (NT4) and (B,C & D) Δ*trx1*Δ*txl1* mutant *S. pombe* treated with 0 – 500 µM H_2O_2. The gradient and standard error of the gradient for the ($\Delta F/\Delta t\ s^{-1}$) values for 0 – 100 µM H_2O_2 treatment was extrapolated and plotted on the same axis. All three repeats for the Δ*trx1*Δ*txl1* mutants are shown.

Table 3.8 V_{max} estimates for peroxidase processes

Species	Concentration (µM)	k_{cat} (s^{-1})	V_{max} (µM s^{-1})	*ref*
ctt1	0.07	54000 - 833000	3780 - 58310	Switala *et al*, 2002
Trr1	0.9	43.7	39	Oliveira *et al*, 2010
Pgr1 (GR)	0.3	900	270	Yu and Zhou, 2007

Table 3.8 V_{max} estimates for peroxidase processes.

Values for the enzyme kinetic rate constant k_{cat} for catalase (ctt1), Thioredoxin reductase (Trr1) and glutathione reductase (Pgr1) were taken from the literature. The k_{cat} value for a given enzyme was then multiplied the estimated intracellular concentration of that enzyme (see 2.6.2) to calculate a V_{max} for the peroxidase reactions dependent on that enzyme.

3.6 Discussion

The role of peroxiredoxins in cellular responses to H_2O_2 has come under considerable scrutiny in recent years, with several functions proposed for the inactivation of their thioredoxin peroxidase activity by hyperoxidation. In this study a mathematical model describing the kinetics of oxidation of the single *S. pombe* 2-Cys Prx in response to H_2O_2 has been developed. This model has made several unexpected predictions. The first prediction is that formation of the reaction intermediate Prx-ox:SOH, which is the precursor for both Prx-ox#2 and Prx-ox:SOOH, does not form via the oxidation of the Cys_P-SH in Prx-ox#1. This is based on the observation that models containing this reaction were unable to accurately simulate the dynamics of Prx oxidation (Figure 3.4, 3.5, 3.16 & 3.24). Instead the reaction between two Prx-SOH monomers (Figure 3.4 Opt2, Figure 3.16 Opt2) allows the computer model to better simulate Prx oxidation dynamics. Based on preliminary evidence, Peskin et al (2013) suggested that the sensitivity of the Cys_P-SH to oxidation might be independent from the presence of neighbouring disulphide bonds. In contrast the models developed here suggest that Cys_P-SH will become insensitive to oxidation when the Cys_R of the same Prx molecule is in a disulphide bond. In chapter 1 it was mentioned that the sensitivity of the Cys_P-SH to oxidation by H_2O_2 is increased by the proximity of basic amino acids in the tertiary structure of the protein (Choi et al., 1998, Nagy et al., 2011). Perhaps the decreased sensitivity of the Cys_P-SH in Prx-ox#1 suggested by our model could reflect a structural rearrangement in Prx-ox#1 that distances the Cys_P from basic amino-acids, thus lowering its sensitivity to oxidation by H_2O_2.

A second prediction made by the model is that exposure to concentrations of H_2O_2 up to 100 µM produce only small increases in the intracellular H_2O_2 concentration, whereas exposure to extracellular H_2O_2 above 150 µM causes the cell's peroxide-removing capacity to be overwhelmed thus allowing intracellular H_2O_2 concentration to increase more substantially (Figure 3.25). Importantly, this prediction was experimentally confirmed (Figure 3.27). This suggests that our model is an accurate representation of the *in vivo* response of cells to extracellular H_2O_2. The model predicts that this peroxide-removing activity protects Tpx1 from hyperoxidation, and that saturation of this activity explains why hyperoxidised Tpx1 is only detected following exposure to extracellular concentrations of H_2O_2 above 150 µM. Notably, this is consistent with

experiments performed in mammalian cells which can effectively buffer extracellular H_2O_2 concentrations of 10 μM, a concentration that will cause some hyperoxidation of Prx2 *in vitro* (Miller et al., 2010, Peskin et al., 2013) but is not sufficient to cause *in vivo* hyperoxidation of Prx (Miller et al., 2010, Woo et al., 2010, Cuddihy et al., 2011). The experimental observation that the increase in $[H_2O_2]_{int}$, and the appearance of Prx hyperoxidation, both occur following treatment with H_2O_2 > 20 μM in HEK-293 cells strongly suggests that the coincident hyperoxidation of Prx and saturation of the H_2O_2 buffering capacity is conserved in human as well as yeast cells (Figure 3.28).

The finding that Tpx1 hyperoxidation only occurred once the cells peroxidase capacity becomes saturated prompted the new question of what is responsible for this peroxidase capacity. Loss of Tpx1 had a minimal effect on intracellular H_2O_2 changes compared to wild-type cell, thus indicating that the peroxidase capacity is independent of Tpx1 (Figure 3.27). Indeed, in cells expressing mutant forms of Tpx1 that are resistant to hyperoxidation, the H_2O_2 buffering capacity of *S. pombe* was unaffected (Figure 3.29). Again, this suggests that Tpx1 does not make a large contribute to the H_2O_2-buffering capacity of cells.

Catalase has been shown to inhibit Prx hyperoxidation *in vitro* (Peskin et al., 2013), moreover Δ*ctt1* mutant *S. pombe* have increased H_2O_2 sensitivity and are unable to remove high concentrations of H_2O_2 from the media (Paulo et al., 2014). Catalase therefore seemed a likely candidate responsible for the peroxide-removing activity that protects Tpx1 from hyperoxidation. However, the same relationship between extracellular and intracellular H_2O_2 concentration was observed in Δ*ctt1* mutant cells as wild-type cells suggesting that catalase is not responsible for the peroxidase buffering capacity predicted by the model (Figure 3.31). Perhaps this is unsurprising given, as discussed in the introduction (see 1.3.2), catalase is has a very high K_m for H_2O_2 (38 – 600 mM) whilst our model predicts that the peroxidase process responsible for protecting Tpx1 from hyperoxidation has a low K_m of ~ 0.007 μM (Table 3.7). Similarly an estimate of the V_{max} for catalase in *S. pombe* (4,000 – 55,000 μM s^{-1}) is much higher than the predicted V_{max} (59 μM s^{-1}) for the unknown peroxidase process (Table 3.7).

Although it is possible that the Gpx/GSH system (Makino et al., 2008), or other subfamilies of Prx contribute to the H_2O_2 buffering capacity of *S. pombe*, this

seemed unlikely given the minimal effect that deletion of the genes encoding these enzymes (*gpx1*, *pmp20* or *dot5*) has on H_2O_2 resistance (Vivancos et al., 2005). A previously published computer model has suggested that the thiol-proteome makes an important contribution to the peroxide-buffering capacity of human cells (Adimora et al., 2010). Our experimental observation that the rate of intracellular H_2O_2-induced fluorescence is directly proportional to the extracellular H_2O_2 concentration in Δ*trx1*Δ*txl1* cells strongly supports the possibility that the saturation of the thiol-proteome could be responsible for increase intracellular H_2O_2 responsible for Tpx1 hyperoxidation (Figure 3.32). Consistent with this model, the thiol-proteome becomes maximally oxidised following exposure to H_2O_2 concentrations of 200 µM (Garcia-Santamarina et al., 2013). If the total oxidation of the thiol-proteome is responsible for the increase in the intracellular H_2O_2 concentration, it would not be unreasonable to assume that the V_{max} of the Trr1-mediated reduction of Trx1 would be the similar to the parameter $V_{max\_H2O2\_metab}$ predicted for our model. Indeed, the k_{cat} for the reduction of Trx has been measured at 43 s^{-1} for *S. cerevisiae* TrxR (Oliveira et al., 2010). Assuming the k_{cat} for *S. pombe* Trr1 is similar to *S. cerevisiae* TrxR a reasonable estimate for the V_{max} for the reduction of Trx1 by Trr1 would be around 38.7 µM s^{-1} ($V_{max} = k_{cat}$ x [Trr1] = 43 s^{-1} x 0.9 µM = 38.7 µM s^{-1}) which is in the same order of magnitude of the 59 µM s^{-1} predicted for the peroxidase process in our model (Table 3.7). Also, briefly mentioned in chapter 1, was the idea that free GSH has peroxidase activity. If, instead of the thiol-proteome the peroxidase process in the model represents the complete oxidation of GSH to GSSG the parameter $V_{max\_H2O2\_metab}$ would be expected to be similar to the V_{max} for the reduction of glutathione by glutathione reductase. The k_{cat} for the *S. cerevisiae* glutathione reductase Glr1 has been measured as 900 s^{-1} (Yu and Zhou, 2007). Assuming that the *S. pombe* glutathione reductase pgr1 has a similar k_{cat}, a reasonable estimate for the V_{max} for the reduction of glutathione by glutathione reductase in *S. pombe* would be ~270 µM s^{-1} ($V_{max} = k_{cat}$ X [pgr1] = 900 s^{-1} x 0.3 µM = 270 µM s^{-1}) which is much higher than the 59 µM s^{-1} predicted for the peroxidase process in the model. This would suggest that the oxidation of glutathione will continue to contribute to the H_2O_2 buffering of the cell even when the thiol-proteome is saturated. Comparison of the V_{max} estimates for different peroxidases in the cell (Table 3.8) as well as the measurements of intracellular H_2O_2 accumulation in the

Δ*trx1*Δ*txl1* mutant, provide strong evidence that the unknown peroxidase process in the model represents the thiol-proteome (Figure 3.33).

Our model suggests that hyperoxidation only occurs when the cell's capacity for peroxide-removal is breached. This has implications towards many of the known physiological functions of Prx hyperoxidation. For example the hyperoxidation of 2-Cys Prx has been identified as a conserved feature of circadian rhythms in a diverse range of eukaryotes (for a review see (Stangherlin and Reddy, 2013)). This raises the possibility that the hyperoxidised Prx detected in each of these organisms reflects a transient, daily increase in the intracellular H_2O_2 concentration above the cell's peroxide-buffering capacity. Consistent with the possibility that a cyclic increase in ROS might be important for circadian rhythms, Nrf2, the transcription factor controlling the levels of peroxidase-removing enzymes in mammals, was recently shown to be regulated in a circadian pattern (Pekovic-Vaughan et al., 2014). If an increase in intracellular H_2O_2 is important for circadian control of cellular activities, then it is possible that loss of this regulation may contribute to the deleterious effects that can be associated with increased dietary antioxidants and constitutively activated stress defences (Wakabayashi et al., 2003).

The inactivation of 2-Cys Prx by hyperoxidation has been proposed to allow H_2O_2 to act as a signal (Wood et al., 2003). However, only a very small proportion of the total pool of 2-Cys Prx appears to become hyperoxidised under normal growth conditions/during circadian rhythms. Moreover, hyperoxidation of Prx is undetectable in response to the low H_2O_2 levels produced in response to growth factor activated NADPH oxidases (Woo et al., 2010, Cuddihy et al., 2011). As 2-Cys Prx are highly abundant, and only one of a repertoire of peroxidase enzymes, it has seemed unlikely that inactivation of such a small proportion would significantly impact on intracellular H_2O_2 levels. Indeed, as predicted by our model, our experimental data suggests that the complete inactivation of Tpx1, either by deletion or hyperoxidation, has a minimal effect on *S. pombe*'s ability to prevent the intracellular accumulation of H_2O_2 (Figure 3.27). Instead, our model is consistent with other work suggesting that hyperoxidation of Prx may have other functions in signalling or protein homeostasis (Jang et al., 2004, Phalen et al., 2006, Turner-Ivey et al., 2013, Peskin et al., 2013).

Table 3.8 V_{max} estimates for peroxidase processes

Species	Concentration (µM)	k_{cat} (s^{-1})	V_{max} (µM s^{-1})	*ref*
ctt1	0.07	54000 - 833000	3780 - 58310	Switala *et al*, 2002
Trr1	0.9	43.7	39	Oliveira *et al*, 2010
Pgr1 (GR)	0.3	900	270	Yu and Zhou, 2007

Table 3.8 V_{max} estimates for peroxidase processes.

Values for the enzyme kinetic rate constant k_{cat} for catalase (ctt1), Thioredoxin reductase (Trr1) and glutathione reductase (Pgr1) were taken from the literature. The k_{cat} value for a given enzyme was then multiplied the estimated intracellular concentration of that enzyme (see 2.6.2) to calculate a V_{max} for the peroxidase reactions dependent on that enzyme.

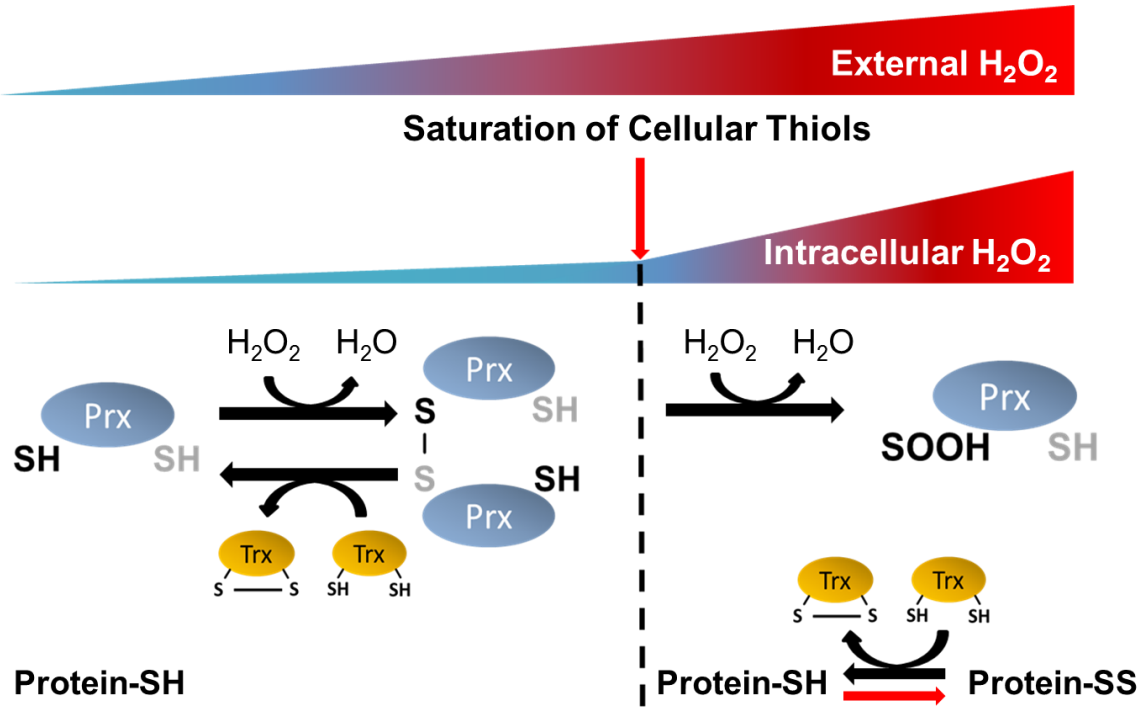

Figure 3.33: Peroxiredoxin hyperoxidation occurs when the thiol-proteome becomes saturated by H_2O_2.

Diagram summarising the findings and suggestions for Chapter 3. The results of this study suggest that as the external H_2O_2 concentration is increased, changes in the intracellular H_2O_2 concentration are inhibited due to the peroxide buffering capacity of the thiol-proteome. Under these conditions Prx will be catalytically active and Trx will be unavailable to reduce substrates other than Prx. Further increases in the external H_2O_2 concentration will cause the intracellular H_2O_2 concentration to increase, due to the saturation of the thiol-proteome peroxide buffering capacity. Under these conditions Prx will be hyperoxidised and Trx will be available to reduce protein disulphides.

Chapter 4. The regulation of Trx1 substrates by Tpx1

4.1 Introduction

The thiol-peroxidases Gpx3 and Tsa1 have been shown to be directly involved in the H_2O_2-induced activation of the stress response transcription Yap1 (Okazaki et al., 2007, Delaunay et al., 2002). Indeed, the requirement for thiol-peroxidases in the activation of transcriptional responses to H_2O_2 appears to be conserved in the fission yeast *S. pombe*, where Tpx1 is required for H_2O_2-induced activation of the transcription factors Pap1 and Atf1 (Bozonet et al., 2005, Veal et al., 2004, Vivancos et al., 2005). A direct role for thiol-peroxidases in the activation of H_2O_2-induced signalling is also proposed in mammalian cells (Winterbourn and Hampton, 2008). Indeed, the mammalian peroxiredoxins Prx1 and Prx2 have been shown to be directly involved in the activation of the MAPKKK ASK1 (Kang et al., 2004, Conway and Kinter, 2006). Although Prxs have conserved roles in the activation of H_2O_2-induced signalling events, it is unclear whether they are directly involved in the H_2O_2-induced oxidation of all H_2O_2-regulated target proteins. In the example of Yap1, it has been shown that the sulphenic acid group on Gpx3-SOH forms a disulphide bond with Yap1 which ultimately leads to the oxidation and nuclear accumulation of Yap1 (Delaunay et al., 2002). Indeed, it has been suggested that the peroxide receptor function of Gpx3, as has been observed for the activation of Yap1, could be a general function for thiol-peroxidases in a range of organisms (Winterbourn and Hampton, 2008). However, it is still unclear whether this function is conserved in *S. pombe* for the activation of Pap1 by Tpx1, since no direct disulphide bond between Pap1 and Tpx1 has been identified. If the mechanism for Pap1 activation in *S. pombe* is similar to that in its distant relative *S. cerevisiae*, this could indicate that the oxidation of redox-regulated proteins by the Cys_P-SOH in a thiol-peroxidase is a conserved H_2O_2-transducing function of many eukaryotic thiol-peroxidases.

The observation that loss of the *S. cerevisiae* thioredoxin system components Trx1, Trx2 and Trr1 results in constitutive activation of Yap1 suggests that the thioredoxin system is responsible for the reduction of Yap1 disulphides (Delaunay et al., 2000, Izawa et al., 1999, Carmel-Harel et al., 2001). A role for the thioredoxin system in the reduction of Pap1 has also been suggested, based on

the observation that the accumulation of oxidised Pap1 occurs when Trx1 is fully oxidised or deleted (Day et al., 2012). Indeed, when Tpx1 is catalytically active in cells treated with low levels of H_2O_2 Trx1 is fully oxidised and therefore unable to reduce other substrates. If Pap1 is a Trx1 substrate this could explain why the thioredoxin peroxidase activity of Tpx1 is required for the accumulation of oxidised Pap1. Consistent with this hypothesis Pap1 activation is inhibited in cells where Tpx1 is hyperoxidised (Bozonet et al., 2005, Day et al., 2012). However, together with the lack of evidence for a direct disulphide between Tpx1 and Pap1, this raises the possibility that the only role of Tpx1 in the activation of Pap1 could be to promote thioredoxin oxidation rather than act as an H_2O_2-receptor/transducer as proposed for Gpx3 in the regulation of Yap1. Instead, the initial oxidation of Pap1 could be due to direct oxidation by H_2O_2, similar to the bacterial OxyR, or perhaps by another unidentified H_2O_2 transducer.

However, there is no evidence that Trx1 is directly involved in the reduction of Pap1 (Day et al., 2012). Eukaryotic cells contain many thioredoxin like enzymes which function as cofactors for particular biochemical reactions and regulate specific signalling proteins (Lee et al., 2013). It is therefore possible the *S. pombe* thioredoxin-like protein Txl1, homologous to human TRP32/Txnl1, could also be influenced by the catalytic activity of Tpx1. In this chapter computer modelling and experimental approaches were combined to gain further insight into the relationship between Pap1, Tpx1 and the thioredoxin system.

4.2 Preliminary models of the thioredoxin system

In order to learn more about the *in silico* behaviour of redox-regulated systems, and predict how thiol-based systems and redox couples influence intracellular H_2O_2 and the activity of thioredoxin dependent reactions, we developed two preliminary models representing the thioredoxin system. 4.2.1 describes a simple model representing the reduction of the thiol-proteome by the thioredoxin system and was used to predict the effects that changes in thioredoxin system components would have on the relationship between intracellular and extracellular H_2O_2. 4.2.2 describes a second model which is an adaptation of a previously published model of the *E. coli* thioredoxin system (Pillay et al., 2011).

4.2.1 A simple model of the thiol-proteome is able to display bi-phasic H_2O_2 dynamics.

A preliminary model, discussed in the previous chapter, demonstrated that a hypothetical Michaelis-Menten peroxidase process would inhibit changes in the intracellular H_2O_2 concentration when the extracellular H_2O_2 concentration was below a particular threshold (Figure 3.6). The specific dynamics of this relationship, and the threshold of H_2O_2 required to cause an increase in the intracellular H_2O_2 concentration were predicted to be dependent on the K_m and V_{max} of the hypothetical peroxidase process (Figure 3.6). Subsequently, a detailed computer model of Tpx1 oxidation demonstrated that a hypothetical peroxidase process was required to explain the experimentally observed dynamics of Tpx1 oxidation (Figure 3.24). Based on the V_{max} value predicted for this peroxidase process, the findings of a previously published model (Adimora et al., 2010), and the experimental observation that the deletion of Trx1 and Txl1 eliminated bi-phasic H_2O_2 dynamics (Figure 3.31), this peroxidase reaction was reasoned to most likely represent the reduction of H_2O_2 by the thiol-proteome. Therefore a computer model was constructed to represent the thiol-proteome (Figure 4.1, Table 4.1 & 4.2) and its ability to inhibit increases in the intracellular H_2O_2 concentration was tested (Figure 4.2).

The preliminary model of H_2O_2 compartmentalisation discussed in chapter 3 (Figure 3.5, Table 3.3) was modified so that the hypothetical peroxidase process now represents the oxidation and reduction of the thiol-proteome (Figure 4.1, Table 4.1). This required the addition of the species PSH which collectively represents all of the H_2O_2 sensitive protein cysteine thiols in the cell. An estimate for the concentration of PSH was calculated (Table 4.2) based on data from two different studies. The first study identified a list of *S .pombe* proteins which were detected to contain oxidised cysteine following exposure to 200 µM H_2O_2 (Garcia-Santamarina et al., 2011). The intracellular concentrations of each of these proteins was then estimated based on a genome-wide quantification of the *S. pombe* proteome (Marguerat et al., 2012). Based on the assumption that each protein contains one H_2O_2-sensitive cysteine residue, the total intracellular concentration of all of the proteins identified in Garcia-Santamarina et al (2011)

was used as an estimate for the concentration of the thiol-proteome (see Appendix A). The oxidation of the thiol-proteome by H_2O_2 was represented by Re1. The model assumes that the thiol-proteome is then reduced by the thioredoxin system represented by Re2 and Re3 (Figure 4.1 & Table 4.1).

The model was used to simulate the relationship between intracellular and extracellular [H_2O_2] (Figure 4.2). Low concentrations of extracellular H_2O_2 were predicted to have little effect on the intracellular H_2O_2 concentration, whilst higher concentrations were predicted to cause a sharp increase in the intracellular H_2O_2 concentration (Figure 4.2A). The concentration of H_2O_2 required to cause an increase in the intracellular H_2O_2 concentration was dependent on the parameter k_{PSSred} which controls the rate of PSS reduction by Trx1 (Figure 4.2A). Decreasing k_{PSSred} in the model (Figure 4.2A) was predicted to decrease the concentration of $[H_2O_2]_{ex}$ required to cause an increase in $[H_2O_2]_{int}$. This effect was the same as decreasing the V_{max} parameter in the preliminary model described in chapter 3 (Figure 3.6C). Increasing the rate of thiol-oxidation, by increasing the rate constant k_{PSHox}, raised the concentration of extracellular H_2O_2 required to cause an increase in the intracellular H_2O_2 concentration. This indicates that an increase in the sensitivity or abundance of thiols in the thiol-proteome will prevent increases in the intracellular H_2O_2 concentration (Figure 4.2B). Finally, increasing the rate constant k_{Trx_red}, which represents the reduction of Trx by thioredoxin reductase, was also predicted to increase the concentration of $[H_2O_2]_{ex}$ required to cause an increase in $[H_2O_2]_{int}$ (Figure 4.2C). Together these simulations demonstrated theoretically that the removal of H_2O_2 by the thiol-proteome could reproduce the relationship between extracellular and intracellular H_2O_2 observed in the previous chapter. This supports the hypothesis that the saturation of the thiol-proteome, or at least a thiol-mediated process, is responsible for preventing increases in intracellular H_2O_2 increases in response to low extracellular doses of H_2O_2. Furthermore, this analysis of the thiol-proteome demonstrates how the peroxidase activity of the thiol-proteome can be represented using Michaelis-Menten kinetics. For example, increasing the reduction rate of Trx by increasing the rate constant k_{Trx_red} (Figure 4.2C) had the same effect on preventing increases in intracellular H_2O_2 as increasing the V_{max} of the Michaelis-Menten peroxidase process described in chapter 3 (Figure 3.6B). The fact that increasing k_{Trx_red} or V_{max} both increased the concentration of extracellular H_2O_2 required to

cause an increase in the intracellular H_2O_2 concentration indicates that the apparent V_{max} of the thiol-proteome is proportional to the rate of reduction of Trx. This is consistent with a published mathematical analysis of a single-cycle redoxin system which demonstrated that the apparent k_{cat} of a single-cycle redoxin system is proportional to the rate constant for the reduction of Trx (Pillay et al., 2009). Increasing the oxidation rate of the thiol-proteome by increasing the rate constant k_{PSSox} (Figure 4.2B) had a similar effect on the ability of the thiol-proteome to prevent increases in intracellular H_2O_2 as decreasing the K_m of the Michaelis-Menten peroxidase process described in chapter 3 (Figure 3.6A). This indicates that the apparent K_m of the thiol-proteome is inversely proportional to the sensitivity of the thiol-proteome to oxidation by H_2O_2. This is also consistent with the published mathematical-analysis of a single-cycle redoxin system which demonstrated that the apparent K_m of a single-cycle redoxin system in inversely proportional to the rate of Trx1 oxidation (Pillay et al., 2009).

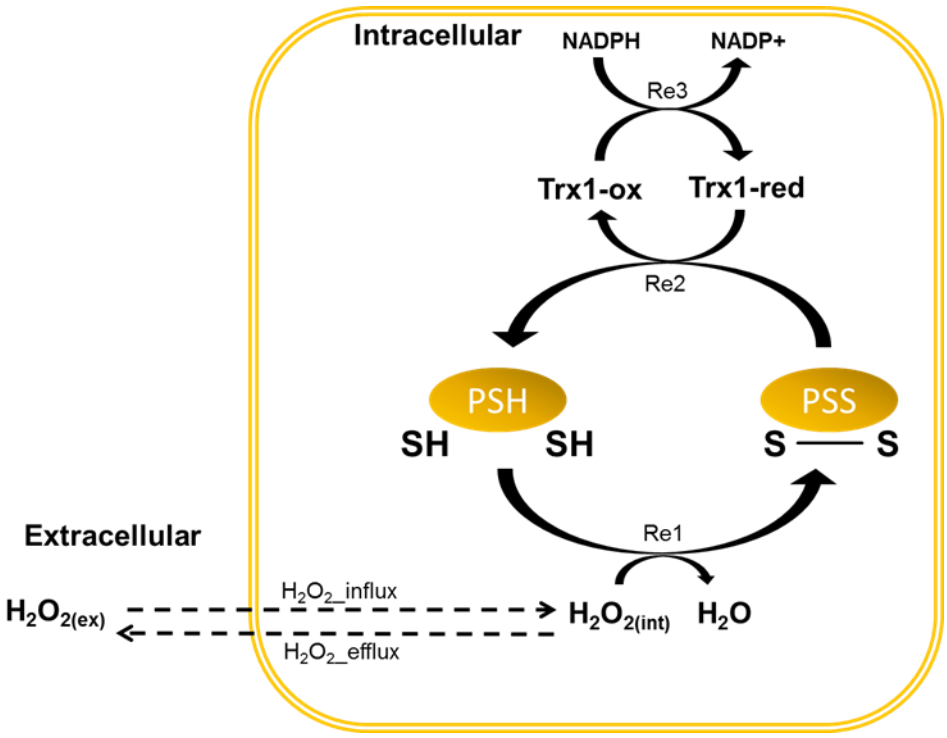

Figure 4.1: Schematic diagram for the simple model of the thiol-proteome.

The figure represents the reactions and chemical species used in the simple model of the thiol-proteome. The model contains 5 reactions, the reactions H_2O_2_influx, H_2O_2_efflux represent the movement of H_2O_2 between the extracellular and intracellular space. Re1 represents the oxidation of a protein-thiol (PSH) by H_2O_2 to form a protein disulphide (PSS) whilst Re2 represents the subsequent reduction of this PSS by the reduced form of thioredoxin (Trx1-red), resulting in the formation of oxidised thioredoxin (Trx1-ox). Trx1-ox is then subsequently reduced using electrons from NADPH via Re3.

Table 4.1 Rate laws for simple model of the thiol-proteome

Reaction	Rate law
H_2O_2_influx	$k_{H2O2\_perm} \cdot Vol_{ex} \cdot [H_2O_{2ex}]$
H_2O_2_efflux	$k_{H2O2\_perm} \cdot (Vol_{ex}/Vol_{int}) \cdot [H_2O_{2int}] \cdot Vol_{int}$
Re1	$k_{PSHox} \cdot [PSH] \cdot [H_2O_{2int}]$
Re2	$k_{PSSred} \cdot [PSS] \cdot [Trx1\text{-}red]$
Re3	$k_{Trx\_red} \cdot [Trx1\text{-}ox]$

Table 4.1: Rate laws used in the simple model of the thiol-proteome

The table displays the rate laws used for the reactions in the simple model of the thiol-proteome all of which were based on mass action kinetics.

Table 4.2 Parameters used for the simple model of the thiol-proteome

Parameter	Value	Units	*ref*
k_{H2O2_perm}	0.0001	$l^{-1}\ s^{-1}$	NA
[PSH]	82	µM	Appendix A
[PSS]	0	µM	NA
Trx1-red	0.7	µM	Marguerat et al, 2012
Trx1-ox	0	µM	NA
k_{PSHox}	1	$\mu M^{-1}\ s^{-1}$	NA
k_{PSSred}	1	$\mu M^{-1}\ s^{-1}$	NA
k_{Trx_red}	34	s^{-1}	Oliveira et al, 2010

Table 4.2: Parameters used in the simple model of the thiol-proteome.

The table displays the parameters used for the simple model of the thiol-proteome. Most of the parameters used were chosen arbitrarily (marked as NA), although the concentrations of PSH, Trx1-red and the parameter k_{Trx1_red} were taken from the literature (see section 4.2.1 for details on estimating [PSH]).

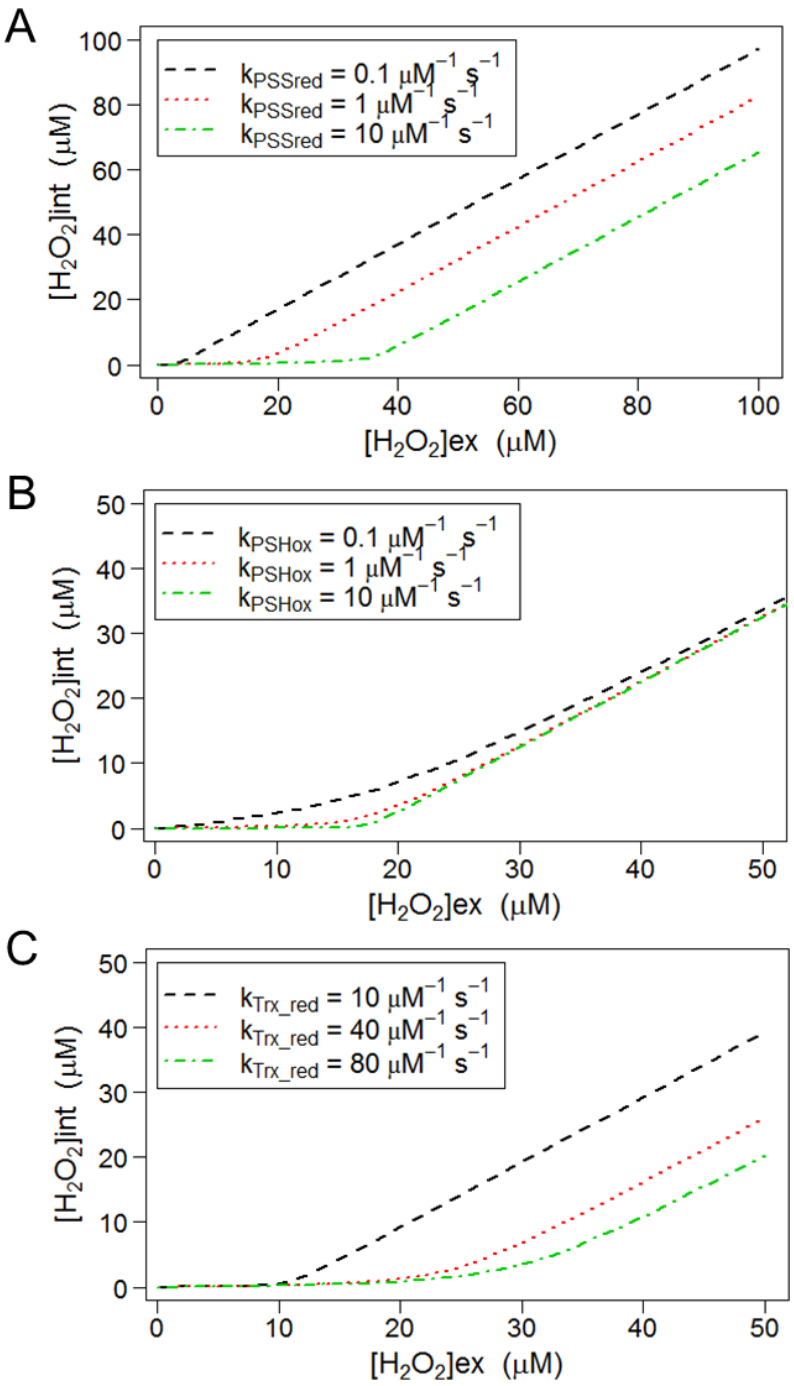

Figure 4.2: The simple model of the thiol-proteome (Figure 4.1, Tables 4.1 & 4.2) inhibits increases in the intracellular H_2O_2 concentration.

The simple model of the thiol-proteome (Figure 4.1) was used to simulate the effect of increasing extracellular H_2O_2 concentration on the intracellular H_2O_2 concentration. Simulations were performed using the indicated values of (A) k_{PSSred} (B) k_{PSHox} and (C) k_{Trx_red}. All other parameter values were as indicated in Table 4.2.

4.2.2 Preliminary Model: A kinetic model demonstrates the downstream effects of peroxiredoxin hyperoxidation on the Thioredoxin system and its substrates.

A previously published model of the *E. coli* thioredoxin system has been used to identify emergent behaviours in thioredoxin-dependent reactions resulting from the structure of the thioredoxin system (Pillay et al., 2011). Because, *E. coli* Prxs are resistant to hyperoxidation, the influence of Prx hyperoxidation on these emergent behaviours was not discussed. Since an objective of this work was to study the relationship between Tpx1 hyperoxidation and the possible Trx1 substrate Pap1, the published model of the *E. coli* thioredoxin system was adapted to predict the downstream effects of Prx inactivation would have on thioredoxin substrates. This adaptation of the *E. coli* thioredoxin system was identical to that described in Pillay et al (2011), except that reduction of NADPH by TrxR was not included. This omission was due to our assumption that NADPH would be non-limiting for the reduction of oxidised Trx by TrxR.

The adaptation of the previously published model of the *E. coli* thioredoxin system (Table 4.3 & 4.4, Figure 4.3) (Pillay et al., 2011) was used to simulate the effect of changing the concentration of TrxR on the steady-state flux though the thioredoxin reactions included in the model (Figure 4.4A). The model predicted that reducing the concentration of TrxR would cause a rapid decrease in the flux through all of the Trx-dependent reactions (re3, re4, re5). In agreement with the same simulations in Pillay et al (2011), the decrease in flux through re3, re4 and re5 had sigmoidal kinetics. This implies that fluxes through these reactions are resistant to changes in [TrxR] provided this concentration is above 0.5 µM. This hypersensitivity was not predicted for the flux through the reduction of oxidised Prx (re2), which decreased much less than the other thioredoxin-dependent reactions (Figure 4.4A). The effects of decreasing the concentration of TrxR on the flux for the oxidation of Prx by H_2O_2 (re1) was predicted to be identical to re2 (Figure 4.4). Importantly, this was in agreement with the prediction of the published model (Pillay et al., 2011) indicating that the published model has been accurately rebuilt. The model also predicted that an increase in H_2O_2 concentration would decrease the flux through the thioredoxin-dependent reactions (re3, re4, re5), with sigmoidal, hypersensitive kinetics. Increasing H_2O_2

was predicted to cause a small increase in the flux through the Prx-dependent reactions (re1 & re2) (Figure 4.4B). Again, these simulations are in agreement with the previously published predictions of this model (Pillay et al., 2011).

The model was then used to predict the effects that Prx hyperoxidation would have on the steady-state fluxes through each of the thioredoxin-dependent reactions. Decreasing the rate constant k_{Prx_red} was used to effectively mimic the accumulation of Trx-resistant Prx-SOOH. The model was used to predict the effect of reducing the rate constant k_{Prx_red} from 3000 to 0.001 μM^{-1} s^{-1} on the activity of Trx-dependent reactions (Figure 4.5A), whilst keeping all other parameters at their original values (Table 4.4). The model predicted that lowering k_{Prx_ox} would cause identical decreases in the steady state flux through the Prx reactions re1 & re2 (Figure 4.5A) indicating both Prx oxidation and reduction are inhibited. Lowering k_{Prx_red} caused a small decrease in the steady state flux through re6 indicating that Prx inactivation has decreased the demand on TrxR (Figure 4.5A). However, lowering k_{Prx_red} had no effect on the predicted steady state flux through re3, re4 & re5 (Figure 4.5A). This result indicates that Prx inactivation can act as a mechanism to decrease the demand on TrxR, but that this does not increase flux through the other Trx-dependent reactions. As demonstrated earlier (Figure 4.4A) the model predicts that lowering the concentration of TrxR will decrease the steady state flux through some of the Trx-dependent reactions, indicating that TrxR limits the flux through these reactions. However, lowering the rate constant k_{Prx_red} increased the flux through the MsrA reduction of Met-S-SO (re4) when [TrxR] was limiting (Figure 4.5B). Lowering k_{Prx_red} was also predicted to restore the flux through re4 when the concentration of H_2O_2 is high (Figure 4.5C). These results indicate that Prx inactivation will facilitate Trx-dependent reactions when the demand on TrxR is high and is in agreement with the published data indicating that hyperoxidation of *S. pombe* Tpx1 facilitates the Trx1-mediated reduction of MsrA (Mxr1) and could also be responsible for the Trx1-mediated reduction of Pap1 (Day et al., 2012).

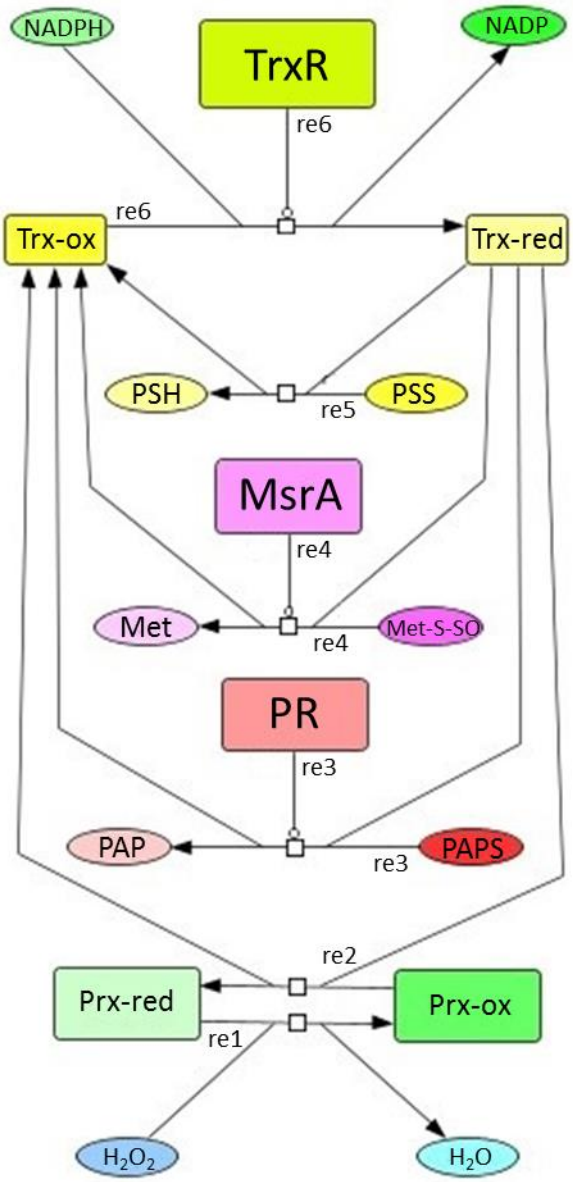

Figure 4.3: Schematic diagram representing the model of the *E. coli* thioredoxin system.

Schematic diagram displaying the biochemical species and reactions included in the model of the thioredoxin system adapted from Pillay (2011). Reaction 1 (re1) represents the oxidation of a peroxiredoxin Prx-red to Prx-ox by H_2O_2, whilst reaction 2 (re2) represents the reduction of Prx-ox by a thioredoxin Trx-red, which becomes oxidised to Trx1-ox in the process. Reaction 3 (re3) represents the reduction of 3'-phosphoadenosine-5'-phosphosulfate (PAPS) which is mediated by the enzyme PAPS reductase (PR) and requires Trx-red. Reaction 4 (re4) represents the Trx-red dependent reduction of methionine sulphoxide (Met-S-SO) by the methionine sulphoxide reductase MsrA and reaction 5 (re5) represents the reduction of protein disulphides (PSS) by Trx-red. The reduction of oxidised thioredoxin (Trx-ox) by a thioredoxin reductase (TrxR) is represented by reaction 6 (re6). NADPH was not included in the model, and is displayed on this diagram for illustration purposes only (adapted from Pillay et al., 2011).

Table 4.3 : Rate Equations for the reactions in the model of the E. coli thioredoxin system

Reaction no.	*Rate law expression*
re1	K_{Prx_ox} ([Prx-red]·[H_2O_2])
re2	K_{Prx_red} ([Prx-ox]·[Trx-red])
re3	(k_{cat_PR} ·[PR]·[PAPS]·[Trx-red])/($K_{m\_PR\_Trx}$·[PAPS] + $K_{m\_PR\_PAPS}$·[Trx-red] + [PAPS]·[Trx-red])
re4	(k_{cat_MsrA} ·[MsrA]·[Met-S-SO]·[Trx-red])/($K_{m\_MsrA\_Trx}$ ·[Met-S-SO] + $K_{m\_MsrA\_Met\text{-}S\text{-}SO}$ ·[Trx-red] + [Met-S-SO]·[Trx-red])
re5	k_{PSS_red} ([PSS]·[Trx-red])
re6	(k_{cat_TrxR} * [TrxR] * [Trx-ox]) / ([Trx-ox] + $K_{m\_TrxR\_Trx}$)

Table 4.3: Rate laws used for the reactions in the computer model of the *E. coli* thioredoxin system.

The table displays the rate laws used for the reaction in the preliminary model of the thioredoxin system. The rate laws for re1, re2 and re5 followed mass action kinetics, re6 used a Michaelis-Menten rate law. Re3 and re4 used a ping-pong rate law (see 1.6.2) as described in Pillay (2011) (adapted from Pillay et al, 2011).

Table 4.4: Parameters values used for the model of the E. coli thioredoxin system

Parameter	Value	Units	Reference
H_2O_2	0.02	µM	*Seaver et al, 2001*
H_2O	1	µM	-
Prx-red	4.88	µM	*Link et al, 1997*
Prx-ox	0	µM	*Link et al, 1997*
TrxR	4.74	µM	*Sundararaj et al, 2004*
Trx-red	1	µM	*Chinn et al, 1986*
Trx-ox	1	µM	*Chinn et al, 1986*
MsrA	2.35	µM	*Pillay et al, 2011*
Met-S-SO	970	µM	*Pillay et al, 2011*
Met	48300	µM	*Pillay et al, 2011*
PR	0.345	µM	*Pillay et al, 2011*
PAPS	0.07	µM	*Murguia et al, 1996*
PAP	1	µM	-
PSS	4.23	µM	*Pillay et al, 2011*
PSH	1	µM	-
k_{Prx_ox}	44	$\mu M^{-1} s^{-1}$	*Baker & Poole, 2011*
k_{Prx_red}	3000	$\mu M^{-1} s^{-1}$	*Baker & Poole, 2011*
k_{cat_PR}	3.5	s^{-1}	*Lillig et al, 1999*
k_{cat_MsrA}	3.7	s^{-1}	*Boschi-Muller et al, 2001*
k_{PSS_red}	0.064	$\mu M^{-1} s^{-1}$	*Pillay et al, 2009*
k_{cat_TrxR}	22.75	s^{-1}	*Chin et al, 1986*
$K_{m\_PR\_Trx}$	13.7	µM	*Lillig et al, 1999*
$K_{m\_PR\_PAPS}$	22.5	µM	*Lillig et al, 1999*
$K_{m\_MsrA\_Trx}$	10	µM	*Boschi-Muller et al, 2001*
$K_{m\_MsrA\_Met\text{-}S\text{-}SO}$	1900	µM	*Boschi-Muller et al, 2001*
$K_{m\_TrxR\_Trx}$	2.8	µM	*Williams, 1976*

Table 4.4: Parameter values for the model of the *E. coli* thioredoxin system.

The table displays the parameter values used for the preliminary model of the thioredoxin system including their units. The references in the table refer to those used in the original published model of the *E. coli* thioredoxin system (Pillay *et al*, 2011) (adapted from Pillay et al, 2011).

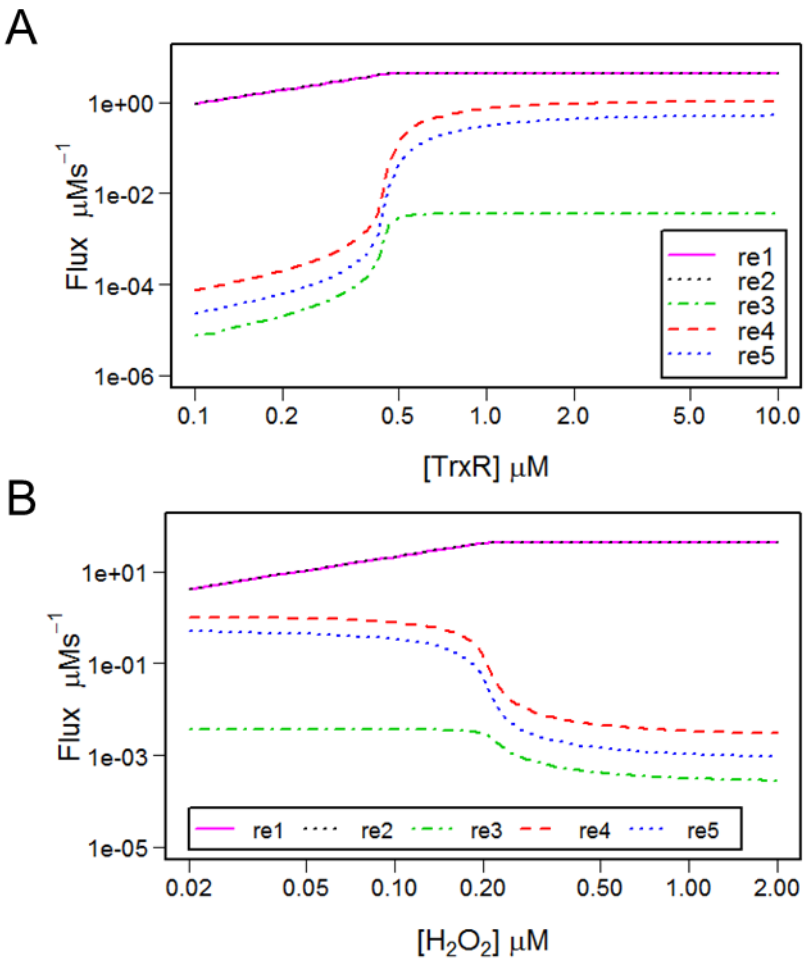

Figure 4.4: The model of the *E. coli* thioredoxin system predicts the effects that changes in [H_2O_2] and [TrxR] will have on thioredoxin substrates.

The model of the *E. coli* thioredoxin system (Figure 4.3, Table 4.4) (adapted from Pillay *et al*, 2011) was used to simulate the effects of changing (A) TrxR concentration and (B) H_2O_2 concentration on the steady state flux though thioredoxin dependent reactions.

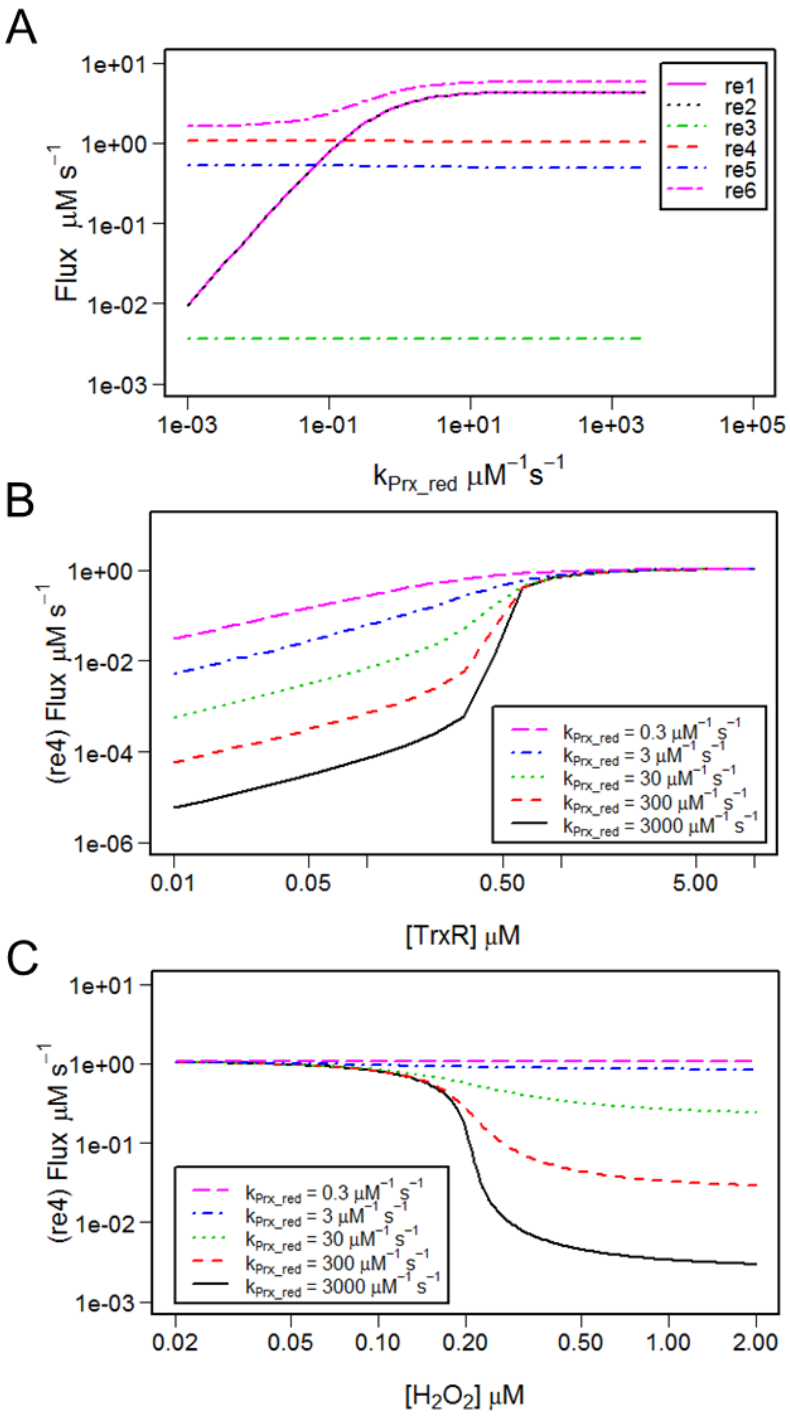

Figure 4.5: Using the model of the *E. coli* thioredoxin system (Figure 4.3) to predict the effects of the rate constant k_{Prx_red} on the steady state flux through thioredoxin dependent reactions.

(A) The model of the *E. coli* thioredoxin system was used to simulate the effect of changing the rate constant k_{Prx_red} on the flux through all of the thioredoxin dependent reactions in the model. (B) The model was used to predict the effect that changing k_{Prx_red} would have on MsrA mediated reduction of Met-S-SO (re4) at different concentrations of TrxR. (C) The model was used to predict the effect that changing k_{Prx_red} would have on MsrA mediated reduction of Met-S-SO (re4) at different concentrations of H_2O_2.

4.3 Adding *in vivo* Trx1 oxidation to the *S. pombe* computer model of Tpx1 oxidation and hyperoxidation.

The published observation that the oxidation state of Pap1 and Trx1 are closely related (Day et al., 2012) suggests that Trx1 reduces Pap1. In order to build multiple computer models of Pap1 regulation, the model of Tpx1 oxidation in chapter 3 (Figure 3.15) was adapted to accurately simulate the dynamics of Trx1 oxidation and importantly the experimentally observed feature that hyperoxidation of Tpx1 will increase the availability of reduced Trx1. To help inform this model the *in vivo* oxidation of Trx1 was measured using an *S. pombe* strain expressing a FLAG-tagged form of Trx1 from the endogenous Trx1 locus which has previously been used to study Trx1 oxidation (Day et al., 2012).

4.3.1 Measuring in vivo Trx1 oxidation in response to a 60 second exposure to 0 – 1000 µM H_2O_2

Exponentially growing cells expressing FLAG-Trx1 were collected before and following 60 seconds exposure of up to 1000 µM H_2O_2. AMS-treated proteins were analysed by western blotting using α-FLAG antibodies (Figure 4.6A). Multiple FLAG-Trx1-containing bands were detected both before and after stress, as indicated by their absence from lysate prepared from the un-tagged wild-type strain (Figure 4.6A). Before addition of H_2O_2, the mobility of the most intense FLAG-Trx1 band detected was consistent with this band representing the reduced, AMS-reactive form of Trx1 (Trx1-red) (Figure 4.6A). This is consistent with previously published work with this strain (Day et al., 2012). A lower intensity band with a molecular weight of 15 kDa (*1), slightly heavier than Trx1-red, was also detected before addition of H_2O_2 (Figure 4.6A). The higher molecular weight suggests that this could represent a form of Trx1 with post-translational modifications. This band has been previously detected (Day et al., 2012) and based on studies of *S. cerevisiae* Trx1 is suggested to represent glutathionylated Trx1 (Bao et al., 2009). The other FLAG-Trx1-containing bands, identified in the non-stressed strains, are likely to represent disulphide complexes between FLAG-Trx1 and other proteins, although comparisons with reduced samples would be necessary to confirm this.

Following a 60 second exposure of up to 100 µM H_2O_2 the Trx1-red band and the glutathionylated band decreased in intensity (Figure 4.6A). This was coupled with the appearance of a new band, with a greater mobility than Trx1-red (Figure 4.6A). The increased mobility of this new band suggests there are fewer molecules of AMS bound indicating that this band is the oxidised form of Trx1 (Trx1-ox), consistent with previously published observations (Day et al., 2012). Exposure to H_2O_2 also resulted in the decreased intensity of two bands (*2 & *3) which both had mobility ~30 – 40 kDa (Figure 4.6A). In addition to the FLAG-Trx1-ox band, exposure to 50 – 100 µM H_2O_2 caused two new higher mobility FLAG-Trx1 bands to be detected, with molecular weights of 40 kDa (*4) and 55 kDa (Flag-Trx1-Tpx1-Tpx1). These bands both reached a peak intensity after exposure to 100 µM H_2O_2 treatment and decreased in intensity after exposure to H_2O_2 > 100 µM (Figure 4.6A). The band with a mobility of 55 kDa was most likely the Trx1-Tpx1-Tpx1 trimer identified in chapter 3 (Figure 3.10). Indeed, re-probing the blot with an anti-Tpx1 antibody also detected a band at 55 kDa after treatment with 100 µM H_2O_2 consistent with this band representing Tpx1-Trx1-Trx1 trimers (Figure 4.6B). Although no follow up experiments were performed to identify the 40 kDa band (4*), and the H_2O_2-sensitive bands (*2 & *3), they were likely to represent mixed-disulphide complexes of Trx1 with another protein. It is also worth noting that the Tpx1 monomer band in the untagged wild-type strain (972) had a lower intensity compared with the monomer band in the untreated FLAG-Trx1 strain (Figure 4.6B). It is possible that this indicates that there is more Tpx1 in the FLAG-Trx1 strain. However, this has not been observed previously (Day et al., 2012). Hence it is more likely that the lane containing the wild-type sample is under loaded, although this was not confirmed (Figure 4.6B). The samples from the untagged strain also contained a Tpx1 containing band (*5) with a slightly lower mobility than the Tpx1 monomer band (Figure 4.6B). No follow up experiments were performed to identify band *5, as this band was not detected in any of the other wild-type samples analysed (eg. Figure 3.7). It was therefore assumed that its altered mobility was an experimental artifact.

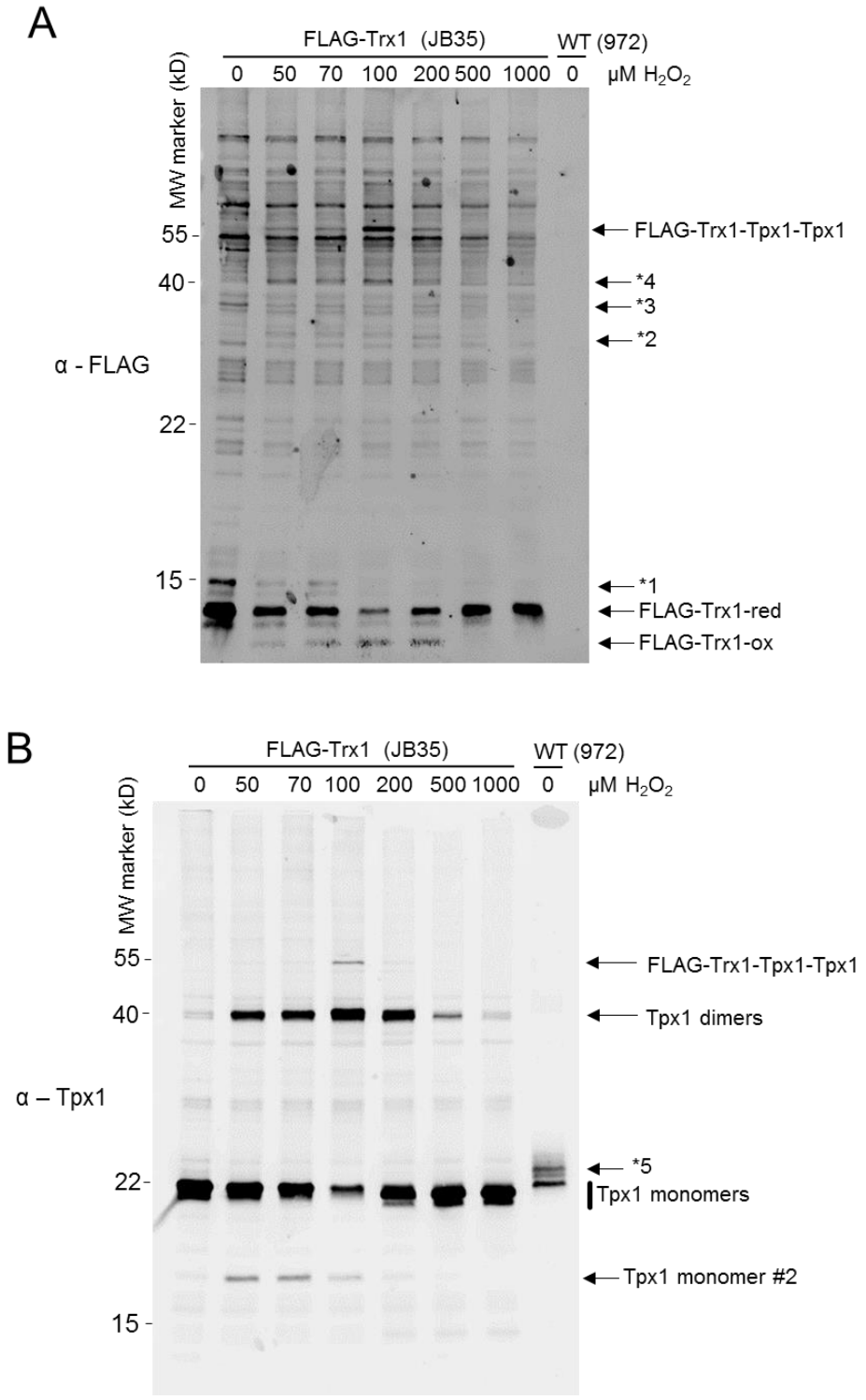

Figure 4.6: The oxidation state of FLAG-Trx1 and Tpx1 after a 60 seconds exposure to increasing concentrations of H_2O_2.

Western blot analysis of AMS-treated protein extracts from cells expressing FLAG-tagged Trx1 (JB35), or wild-type cells (972), treated as indicated with 0 - 1000 µM H_2O_2 for 60 seconds. Analysis was performed using (A) α-FLAG antibodies and (B) α-Tpx1 antibodies. The different bands detected are indicated and described in the text.

4.3.2 The dynamics of Tpx1 oxidation after a 1 min exposure to 0 – 1000 µM in the FLAG-Trx1 strain was in agreement with the dynamics of the wild-type strain.

Importantly, re-probing the western blot (Figure 4.6A) with anti-Tpx1 antibodies indicated that the dynamics of Tpx1 oxidation in the FLAG-Trx1 strain (Figure 4.6B) are similar to those observed in wild-type cells expressing untagged Trx1 (Figure 3.7). Specifically, the oxidation state of Tpx1 in the FLAG-Trx1 strain also switched from being predominantly monomeric before addition of H_2O_2, to being predominantly dimeric after exposure of up to concentrations of H_2O_2 up to 200 µM with a peak dimer intensity after exposure to 100 µM H_2O_2 (Figure 4.6B). Furthermore, as the intensity of the Tpx1 dimer bands decreased following exposure to 500 and 1000 µM, this was accompanied by an increase in the intensity of the Tpx1 monomer bands (Figure 4.6B). This was consistent with the reduction of Tpx1-ox:SOOH dimers to Tpx1-SOOH monomers observed in wild-type cells expressing untagged Trx1 (Figure 3.14B). Since this blot was originally used to investigate Trx1 oxidation this gel was not run long enough to separate reduced and hyperoxidised Tpx1-SH and Tpx1-SOOH (Figure 4.6B). Even so it could be argued that the Tpx1 monomer bands detected after exposure to 500 and 1000 µM have a slightly increased mobility compared with the monomeric band before addition of H_2O_2 (Figure 4.6B). This would indicate that these monomeric bands represent hyperoxidised Tpx1 and would be in agreement with the data presented in chapter 3.

However, a few apparent anomalies were observed regarding the oxidation of Tpx1 in the FLAG-Trx1 strain, compared with the un-tagged strain in chapter 3. Firstly, the apparent presence of two Tpx1 monomer bands with slightly different mobility, in the non-stressed cells, raised the possibility that there is hyperoxidised Tpx1 present before addition of H_2O_2 in the FLAG-tagged strain (Figure 4.6B). In contrast, there was no indication of any Tpx1 hyperoxidation before addition of H_2O_2 in wild-type cells expressing untagged Trx1 (Figures 3.14). However, western blot analysis of FLAG-Trx1-expressing cells with α-Prx-SO2/3 before and after a 300 seconds exposure to 6 mM H_2O_2 did not detect any hyperoxidised Tpx1 before addition of H_2O_2 in the FLAG-Trx1 strain (Figure 4.7). Hence, it is unlikely that the Tpx1 detected in these cells is hyperoxidised.

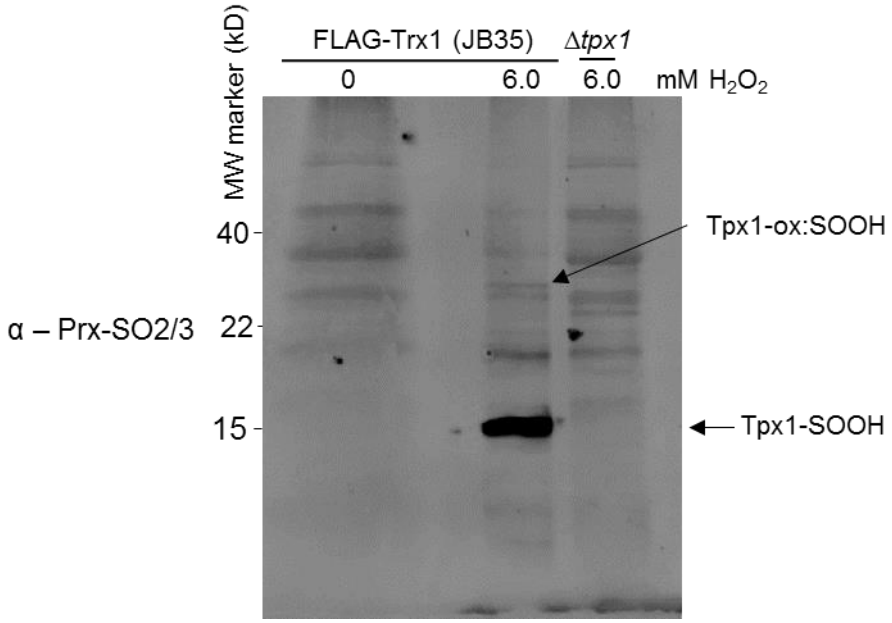

Figure 4.7: No hyperoxidised Tpx1 can be detected in FLAG-Trx1 before exposure to H_2O_2.

Western blot analysis of AMS-treated protein extracts from cells expressing FLAG-tagged Trx1 (JB35), or Δ*tpx1* (VX00) cells, treated with 0 or 6 mM H_2O_2 for 600 seconds. Analysis was performed using α-PrxSO2/3 antibodies.

4.3.3 Tpx1 is able to form an intramolecular disulphide bond

Notably a low intensity Tpx1-containing band, with a mobility just above the 15 kDa marker (Tpx1 monomer #2) was detected in cells treated with H_2O_2 less than 100 µM (Figure 4.6B). This band was most intense after exposure to 50 µM H_2O_2 and was not detected after treatment with concentrations of H_2O_2 > 100 µM. Monomeric Tpx1 runs with a mobility consistent with its predicted molecular weight of ~22 kDa (Koo et al., 2002). Therefore it was unexpected to detect such a high mobility Tpx1 band. The sensitivity of this ~15 kDa band (Tpx1 monomer #2) to the reducing agent beta-mercaptoethanol suggested that this band contains a disulphide bond (Figure 4.8). Therefore, the most plausible explanation is that this band represents a Tpx1 monomer containing an intramolecular disulphide which increases the mobility of Tpx1 through the gel. This Tpx1 monomer #2 band was not detected in AMS-treated samples (Figure 4.9), which suggests that this band may be increased during the protein extraction procedure, with AMS inhibiting its formation by preventing disulphide exchange following extraction. Even so, this band was still detected in the FLAG-Trx1 strain, despite AMS treatment. It is therefore unclear whether this band is an artefact of the experimental procedure or a genuine part of the mechanism for Tpx1 oxidation. The low intensity of this band compared with the other Tpx1 bands indicates that this band only makes up a relatively small portion of total Tpx1 (Figure 4.6B). Moreover, since the *in vivo* significance of the Tpx1 monomer #2 band was unclear this band was not included in the model.

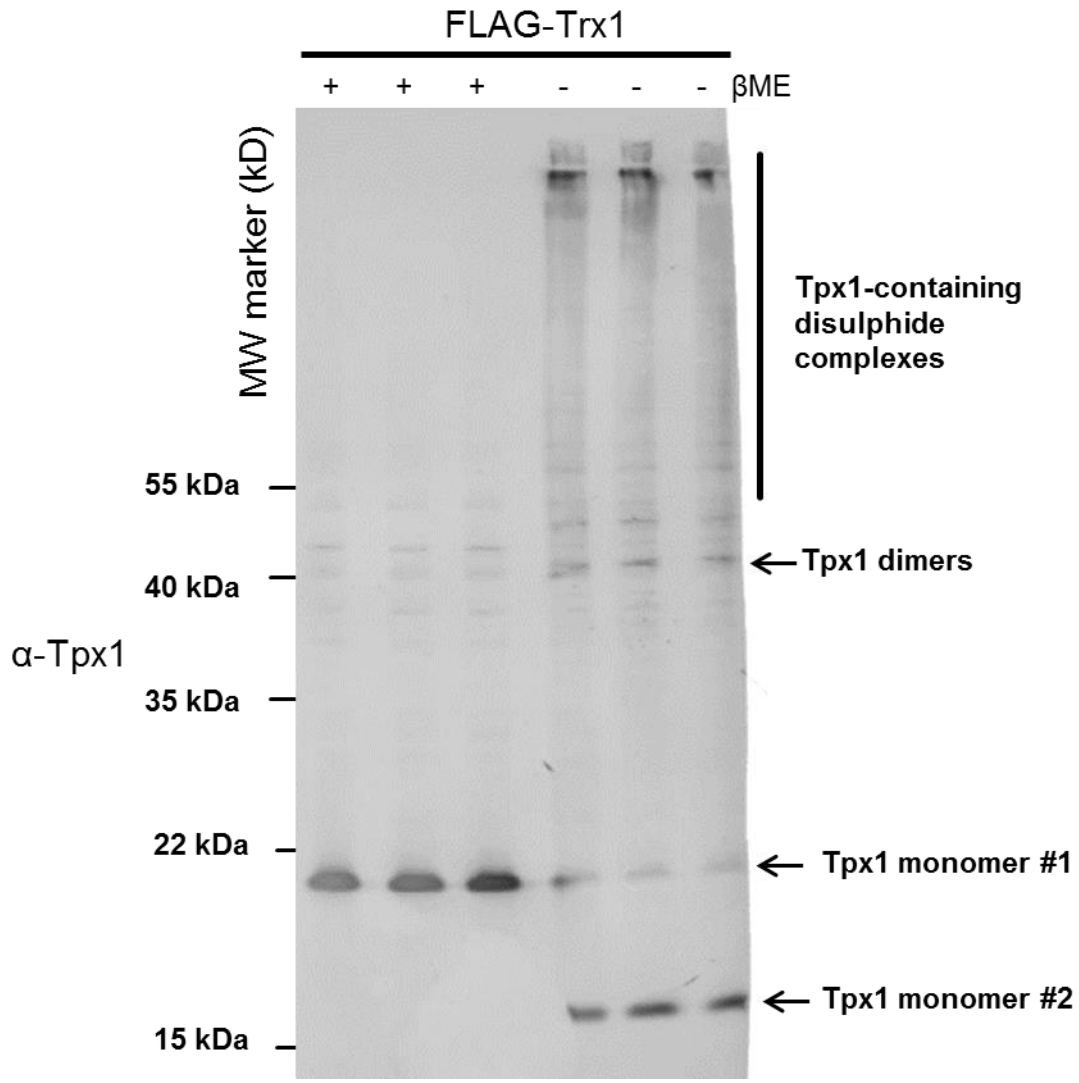

Figure 4.8: The 15 kDa Tpx1 band is reduced by beta-mercaptoethanol.

Western blot analysis of protein extracts from cells expressing FLAG-tagged Trx1 (JB35) and analysed with α-Tpx1 antibodies. Beta-mercaptoethanol treated samples were compared with non-treated samples.

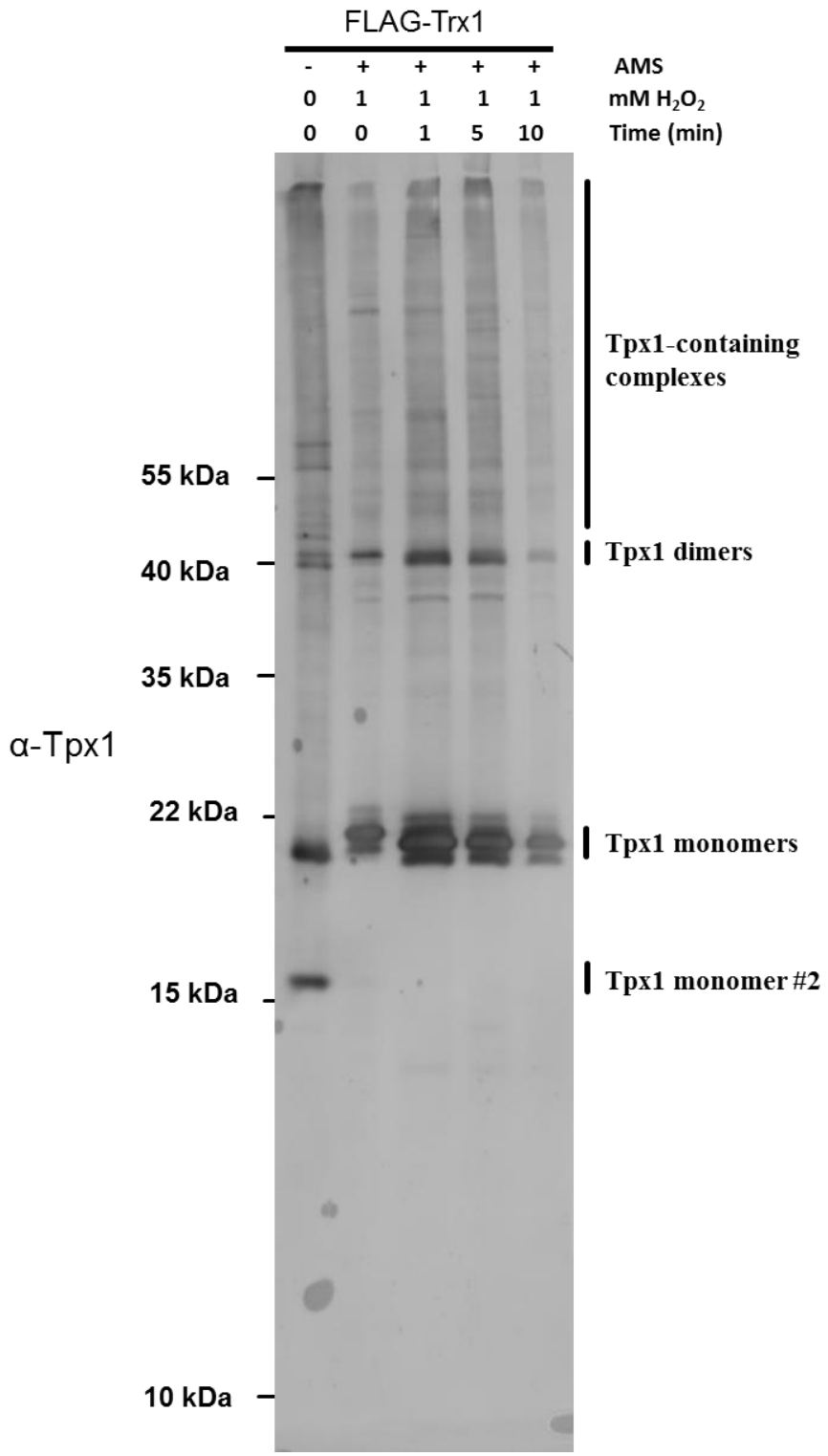

Figure 4.9: Treatment with AMS inhibits the formation of the 15 kDa Tpx1 monomer.

Western blot analysis of protein extracts from cells expressing FLAG-tagged Trx1 (JB35) treated with 0 or 1 mM H_2O_2 for up to 10 min, using α-Tpx1 antibodies. Samples were treated with AMS as indicated.

4.3.4 Measuring the in vivo oxidation of Trx1 in response to a 300 and 600 seconds exposure to 0 – 1000 µM H_2O_2.

300 seconds exposure to H_2O_2 concentrations up to 1000 µM (Figure 4.10) had a similar effect on Trx1 oxidation as a 60 seconds exposure (Figure 4.6A). This included a decrease in the intensity of the Trx1-red band when H_2O_2 was increased from 0 – 100 µM, as well as an increase in the intensity of this band when H_2O_2 was increased from 100 to 1000 µM H_2O_2 (Figure 4.10A). The appearance of new Tpx1-containing bands at 40 kDa (*4) and 55 kDa (FLAG-Trx1-Tpx1-Tpx1) was also observed at 60 seconds, again reaching peak intensity after exposure to 100 µM H_2O_2 (Figure 4.10A). However, in contrast to the 60 seconds exposure (Figure 4.6A), no Trx1-ox band was detected after 300 seconds exposure to 200 µM H_2O_2 (Figure 4.10A). Since Tpx1 is almost fully hyperoxidised to Tpx1-SOOH after a 300 second exposure to 200 µM H_2O_2 (Figure 3.12 & 3.13), absence of detectable Trx1-ox after this H_2O_2 exposure is consistent with previous work demonstrating that hyperoxidation of Tpx1 to Tpx1-SOOH increases the availability of reduced Trx1 (Day et al., 2012). Furthermore, no Trx1-ox was detected after a 600 seconds exposure to 200 µM consistent with previous work (Figure 4.10B). In contrast, 600 seconds exposure to 100 µM H_2O_2, which does not cause any Tpx1 hyperoxidation (Figure 3.11 & 3.14), resulted in the detection of Trx1-ox and other oxidised forms of Trx1 at 55 kDa (FLAG-Trx1-Tpx1-Tpx1) and 40 kDa (*4) as well as a previously un-detected Trx1 containing band with a mobility of ~35 kDa (*6) (Figure 4.10B).

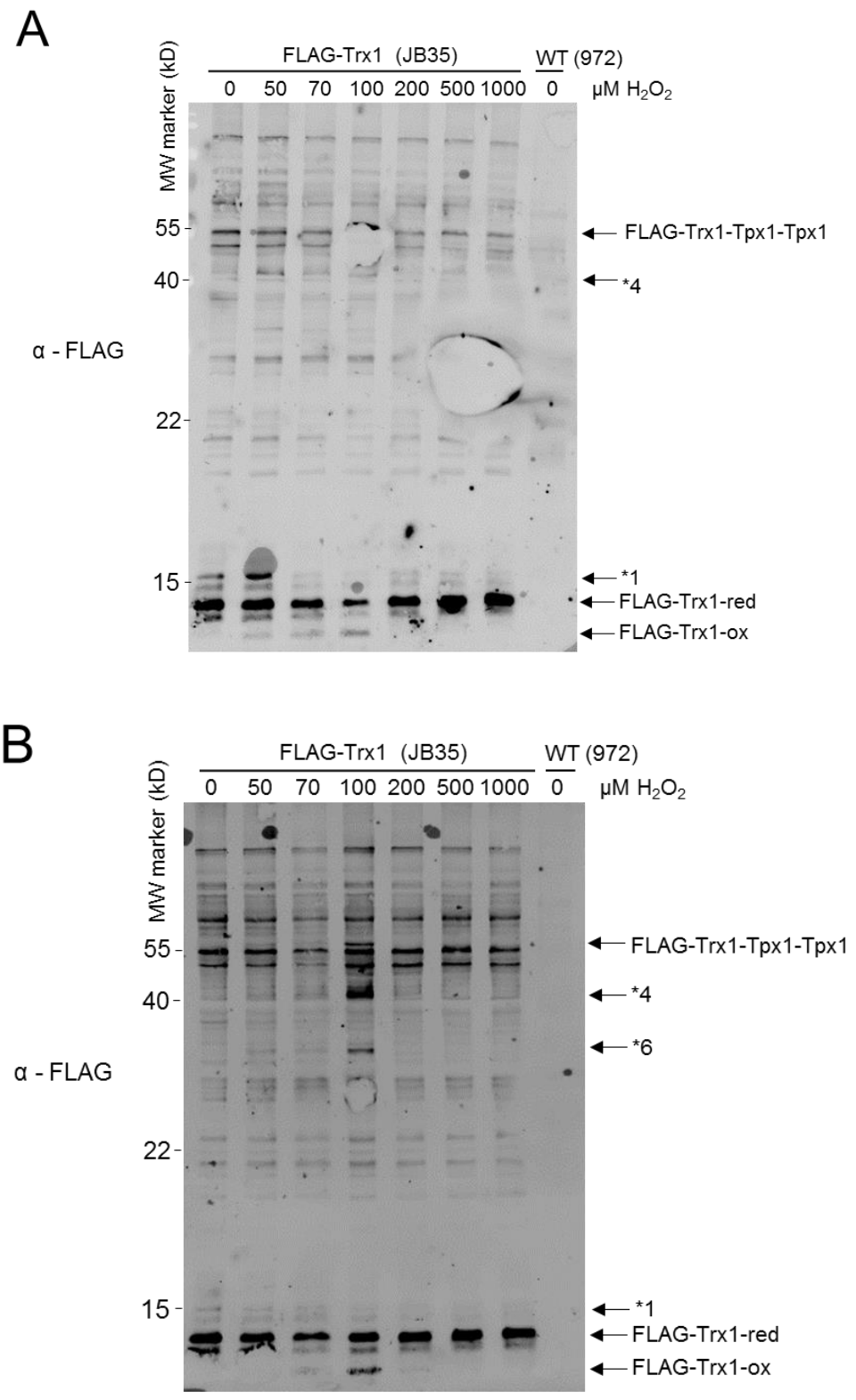

Figure 4.10: The *in vivo* oxidation of FLAG-Trx1 in response to 300 and 600 seconds exposure to increasing H_2O_2 concentration.

Western blot analysis of AMS-treated protein extracts from cells expressing FLAG-tagged Trx1 (JB35), or wild-type cells (972), treated with 0 - 1000 µM H_2O_2 for (A) 300 seconds or (B) 600 seconds. Analysis was performed using α-FLAG antibodies.

4.3.5 Accurate computer modelling of Trx1-red availability in response to H_2O_2.

The computer model of Tpx1 oxidation built in chapter 3 (Figure 3.15) focused on the accurate modelling of Tpx1 oxidation. Accurate modelling of Trx1 oxidation was not required for the model to predict that that Tpx1 hyperoxidation occurs when the cells' peroxidase capacity is overwhelmed. However, in order to use this computer model to test whether Pap1 is a substrate for Trx1, accurate modelling of Trx1 oxidation was important. The computer model described in chapter 3 was therefore adapted in order to more accurately simulate the oxidation of Trx1 (Table 4.5, Figure 4.11).

Firstly, the model was changed so that the reduction of Tpx1-ox#2 consisted of two reactions (Re6 & Re7) (Table 4.5, Figure 4.11) rather than a single reaction, as was used in the chapter 3 model (Re5) (Table 3.3, Figure 3.15). This was done so that model included the Tpx1-Tpx1-Trx1 trimer (Figure 3.10), which is an intermediate in this reaction that will decrease the availability of Trx1. Parameter estimation was then used to find a new set of parameters for the model, including the newly added reactions representing the formation and dissociation of the Tpx1-Tpx1-Tpx1 trimer. The data sets used for this parameter estimation was calculated the same as the data set used in chapter 3, except that the intensity of the Tpx1-Tpx1-Trx1 bands were also included in the quantification (Appendix B). In addition, a new set of quantitative data representing the concentration of reduced Trx1 (Trx1-red) was obtained from western blot analysis (Figures 4.6A & 4.10) (Appendix B). The rate constant for the reduction of Trx1-ox by Trr1 (k_{Trx1_red}) was also included in the parameter estimation, rather than derived from the literature, as was done in chapter 3 (Table 3.7). Parameter estimation was performed 500 times. The parameter sets with the lowest SSR had an SSR of 153.794 and were found 431 times. The most frequently predicted value for each parameter was selected for use in the model (Table 4.6). These parameters were broadly similar to the parameters predicted for the model of Tpx1 oxidation in chapter 3 (Table 3.7) indicating that the new additions to model have not dramatically affected the parameters of original model. The newly parametrised model was used to simulate the oxidation of Tpx1 in response to H_2O_2 and, similarly to the model developed in chapter 3, was in good agreement with the experimental data for Tpx1 oxidation (data not shown).

The model was then used to simulate the formation of the Tpx1-Tpx1-Trx1 trimer, which was not included in the chapter 3 model, in response to a 0 – 600 seconds exposure to 100 µM and 200 µM (Figure 4.12). This simulation data was plotted against the experimental data for the Trx1-Tpx1-Tpx1 trimer which indicated that the simulation and experimental data were broadly similar. However, it could be argued the model over predicted the concentration of Trx1-Tpx1-Tpx1 between 200 and 600 seconds after exposure to 200 µM H_2O_2 (Figure 4.12B). The model was also used to simulate the concentration of Trx1-red 0 to 600 seconds after exposure to 0 – 1000 mM H_2O_2 (Figure 4.13). Plotting this simulation data against the experimental data for Trx1 oxidation indicated that the model does not accurately simulate the changes in Trx1-red availability in response to H_2O_2 (Figure 4.13). Most notably, the model overestimated the availability of Trx1-red 60 seconds after exposure to all of H_2O_2 concentrations tested (Figure 4.13). This was particularly apparent 60 seconds after exposure to 70 and 100 µM H_2O_2 (Figure 4.13B & C). This suggests that there are biochemical processes reducing the availability of reduced Trx1 that not are not represented in this model. Given that Trx1 is likely to have many other substrates, perhaps this is not surprising. Furthermore, the observation that the model particularly overestimated the concentration of Trx1-red after exposure to 100 µM H_2O_2, suggests that these biochemical processes may potentially have the biggest impact on Trx1-red after 100 µM H_2O_2 exposure (Figure 4.13C). However, it is worth noting that the Trx1 oxidation experiments (Figure 4.6A & 4.10) were only performed once. It is therefore difficult to say confidently whether the differences between the simulation and the experimental data represent limitations of the model or experimental error.

However, the model was able to accurately simulate the published observation that the availability of reduced Trx1 increases when Tpx1 is hyperoxidised (Figure 4.13D, E & F) (Day et al., 2012). Importantly, the model accurately predicts that the concentration of Trx1-red will increase ~60 seconds after exposure to 500 and 1000 µM H_2O_2, when Tpx1 will be hyperoxidised (Figure 4.13E & F). This indicates that the model is a good representation of the relationship between Tpx1 hyperoxidation and Trx1, despite the models overestimation of the availability of Trx1-red after 70 and 100 µM H_2O_2 exposure.

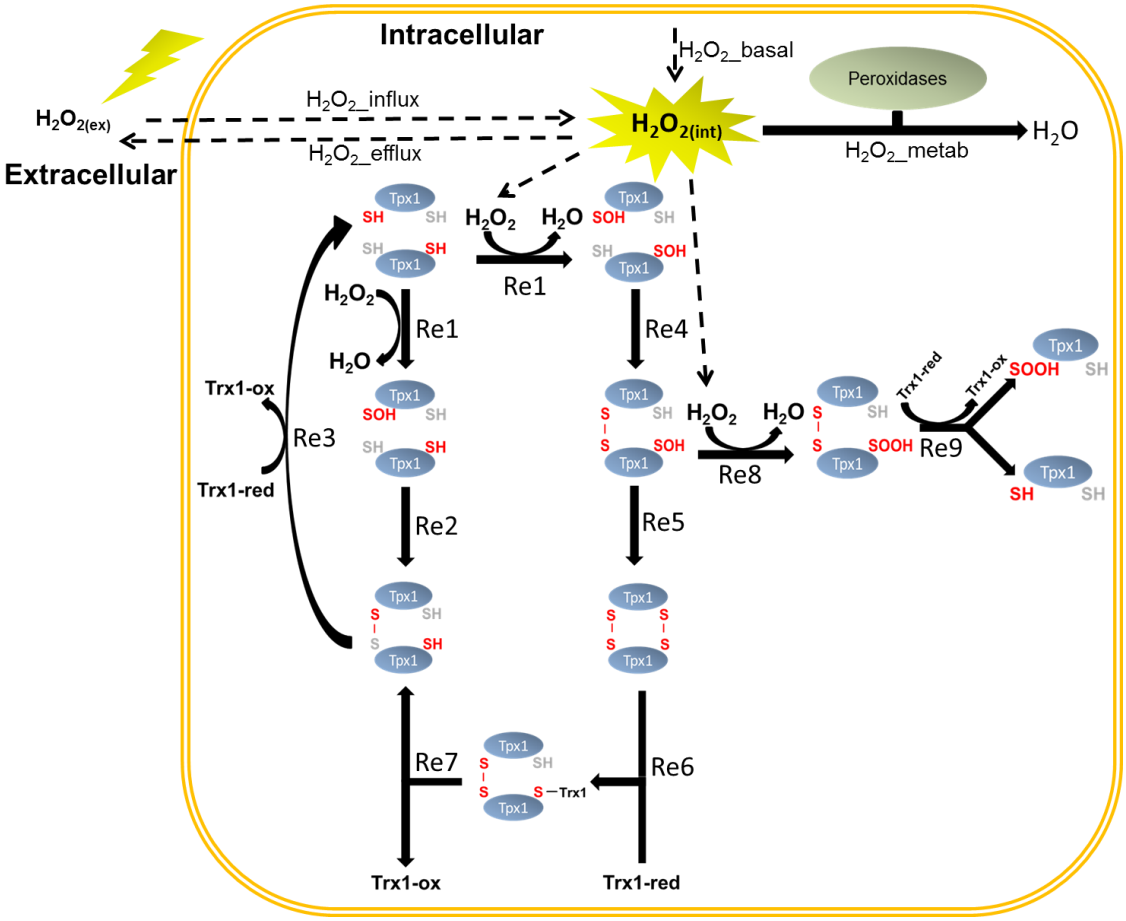

Figure 4.11: Schematic diagram for the model of Tpx1 and Trx1 oxidation.

The diagram represents the reactions used in the model of Tpx1 and Trx1 oxidation. The Tpx1 oxidation reactions are labelled (Re1 - Re9). The model also includes the reaction H_2O_2_influx and H_2O_2_efflux which represents the movement of H_2O_2 in and out of the cell respectively. Endogenous production of H_2O_2 is represented by the reaction H_2O_2_basal, whilst H_2O_2 metabolism by non-Tpx1 processes is represented by the reaction H_2O_2_metab. The reaction Re6 represents the reaction of Tpx1-ox#2 with reduced Trx1 (Trx1-red) to form a Trx1-Tpx1-Tpx1 trimer, whilst Re7 represents the dissociation of this trimer to form Tpx1-ox#1 and Trx1-ox. Re6 and Re7 were not included in the previous model of Tpx1 oxidation (Figure 3.15).

Table 4.5 Rate equations for the model of Tpx1 and Trx1 oxidation

Reaction	Rate law
H_2O_2_influx	$k_{H2O2\_perm} \cdot Vol_{ex} \cdot [H_2O_{2ex}]$
H_2O_2_efflux	$k_{H2O2\_perm} \cdot (Vol_{ex}/Vol_{int}) \cdot [H_2O_{2int}] \cdot Vol_{int}$
H_2O_2_metab	$V_{max\_H2O2\_metab}[H_2O_{2int}]/(K_{m\_H2O2\_metab} + [H_2O_{2int}])$
H_2O_2_basal	V_{basal}
Re1	k_{cys_ox}[Tpx1SH][$H2O2_{int}$]
Re2	$k_{disulph\_form1}$[Tpx1SOH][Tpx1SH]
Re3	$k_{disulph\_red1}$[Trx1red][Tpx1ox#1]
Re4	$k_{disulph\_form1}$[Tpx1SOH][Tpx1SOH]
Re5	$k_{disulph\_form3}$[Tpx1ox:SOH]
Re6	$k_{disulph\_red2a}$[Trx1red][Tpx1ox#2]
Re7	$k_{disulph\_red2b}$[Tpx1ox-Trx1]
Re8	k_{hyp_ox}[Tpx1ox:SOH][H_2O_{2int}]
Re9	$k_{disulph\_red3}$[Trx1red][Tpx1ox:SOOH]
Trx1 reduction	k_{Trx1_red}[Trx1-ox]

Table 4.5: Rate equations used for the model of Tpx1 and Trx1 oxidation.

The table displays the rate equations used for the reactions in the model of Tpx1 and Trx1 oxidation. Most of the rate laws were identical to those used in the model of Tpx1 oxidation developed in chapter 3 (Table 3.5).

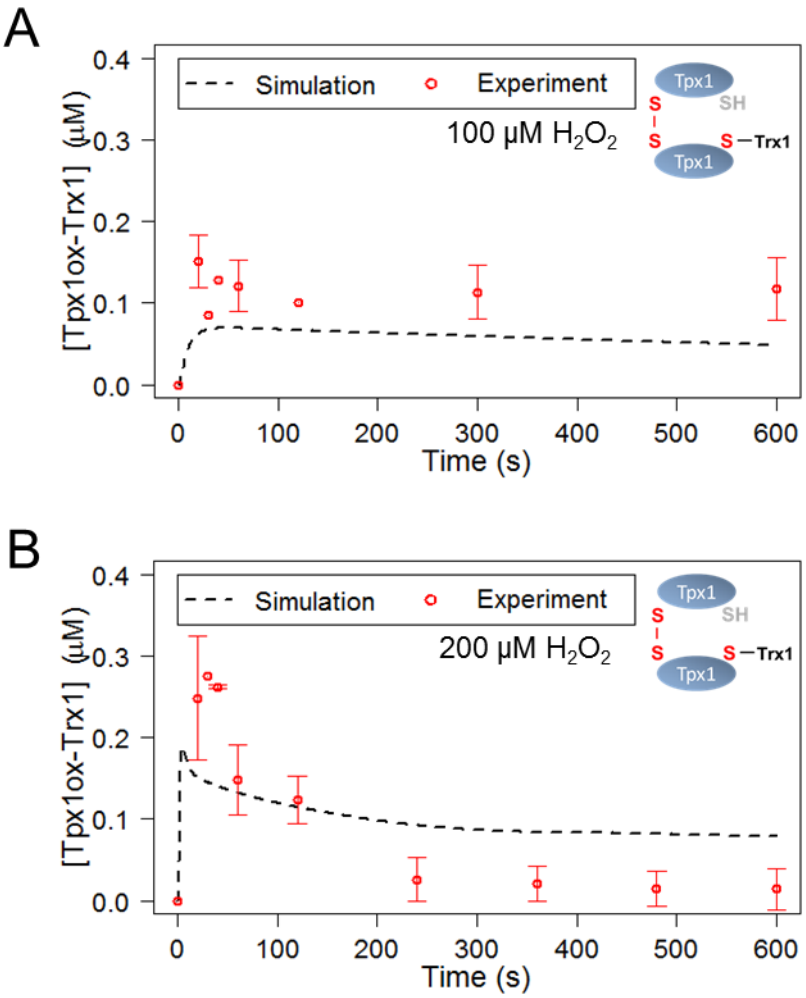

Figure 4.12: The model of Tpx1 and Trx1 oxidation is able to predict the dynamics of the Tpx1-Tpx1-Trx1 trimer.

The model of Tpx1 and Trx1 oxidation (Figure 4.11) was used to simulate the formation of the Trx1-Tpx1-Tpx1 trimer 0 – 600 seconds after exposure to (A) 100 μM H_2O_2 and (B) 200 μM H_2O_2. The experimental data for the concentration of Trx1-Tpx1-Tpx1 was plotted on the same axis as the simulation data.

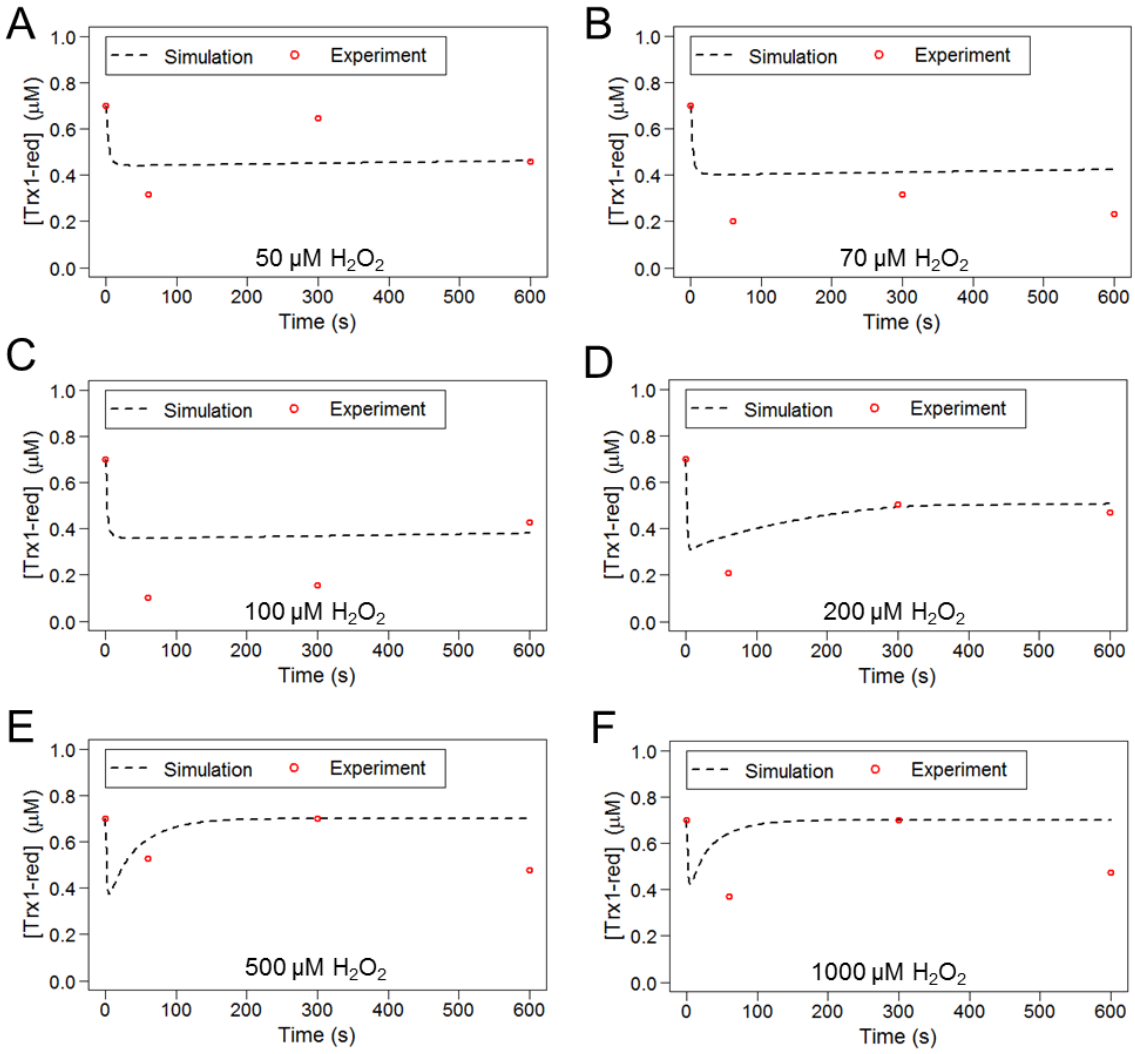

Figure 4.13: The model of Tpx1 and Trx1 oxidation is partly able to simulate the experimental data for the availability of reduced Trx1.

The model of Tpx1 and Trx1 oxidation was used to simulate changes in the concentration of reduced Trx1 (Trx1-red) up to 600 seconds after exposure to 50 – 1000 µM H_2O_2 (A – F as indicated). The experimental data for the concentration of Trx1-red was plotted on the same axis as the simulation data.

4.4 Building computer models representing potential mechanisms of Pap1 regulation

In order to explore the feasibility of the potential mechanisms for the regulation of Pap1, the computer model of Tpx1 and Trx1 oxidation was adapted to represent alternative mechanisms for Pap1 oxidation and reduction. In order to assess which of these models is the most feasible, semi-quantitative data were collected for the oxidation of Pap1 in response to multiple H_2O_2 concentrations. This included measuring the early oxidation of Pap1 (0 - 120 seconds) as well as the extended oxidation of Pap1 (0 – 60 minutes).

4.4.1 Measuring the in vivo oxidation of Pap1 in response to H_2O_2

Protein extracts from cells exposed to 200 µM H_2O_2 for 10 min (600 seconds) were treated with the alkylating agent IAA and phosphatase treated, consistent with previously published methods (Day et al., 2012). These extracts were analysed by western blot using anti-Pap1 antibodies (Figure 4.14). Before addition of H_2O_2 the most prominent Pap1 containing band migrated with a mobility between the 70 and 100 kDa markers. This mobility is lower than would be expected based on the estimated molecular weight of Pap1 (~61 kDa). However, C-terminal-tagged forms of Pap1 also run more slowly than expected (Taylor., 2009) which suggests that perhaps Pap1 undergoes an alternative post-translational modification. Treatment with IAA decreased the mobility of Pap1 through the gel (Figure 4.14), indicating that under normal growing conditions Pap1 contains reduced cysteine residues. This band is therefore likely to represent the reduced form of Pap1, consistent with published work (Day et al., 2012). A second, lower intensity, Pap1 containing band was also detected before addition of H_2O_2 (Figure 4.14). The mobility of this band was slightly higher the band representing fully reduced form of Pap1. Studies of Yap1 oxidation have identified a partially oxidised form of Yap1 with a slightly greater mobility than fully reduced Yap1, which was also detected before addition of H_2O_2 (Okazaki et al., 2007). It was therefore assumed that the greater mobility Pap1 band represents a partially oxidised form of Pap1 (Figure 4.14). Interestingly this band was only detected in the IAA-treated samples suggesting that the partially oxidised form of Pap1 becomes reduced during the extraction procedure, unless there is an

alkylating agent present to prevent the thiol-exchange (Figure 4.14). Exposure to H_2O_2 reduced the intensity of both the fully reduced and partially oxidised Pap1 bands (Figure 4.14). This decrease in intensity was coupled with an increase in the intensity of a new higher mobility band close to the 70 kDa marker (Figure 4.14). Based on previously published work the band was assumed to be the fully oxidised form of Pap1 (Figure 4.14) (Day et al., 2012). By 5 minutes after exposure to 200 µM H_2O_2 almost all of Pap1 was in the fully oxidised state (Figure 4.14). This suggests that a 5 minute exposure to 200 µM H_2O_2 is sufficient to fully oxidise most of the Pap1 in the cell. Measurements of Pap1 oxidation up 60 min (3600 seconds) after a 200 µM H_2O_2 exposure revealed that Pap1 remained fully oxidised until around 20 minutes after H_2O_2 exposure following which the reduced form of Pap1 could also be detected (Figure 4.15). 60 minutes after H_2O_2 exposure no fully oxidised Pap1 was detected, only the fully reduced Pap1 band and partially oxidised Pap1 forms (Figure 4.15). This indicates that all of the Pap1 in the cell has returned to a fully reduced state 60 minutes after exposure to 200 µM H_2O_2 (Figure 4.15). Previous studies using an epitope tagged form of Pap1, found that exposure to 200 µM H_2O_2 only caused around half of Pap1 in the cell to become fully oxidised (Vivancos et al., 2005, Day et al., 2012). Our observation, using anti-Pap1 antibodies, that all cellular Pap1 is fully oxidised by 200 µM H_2O_2 suggests the epitope tag used in the previous studies may inhibit Pap1 oxidation. A high molecular weight Pap1-containing band was also detected after H_2O_2 exposure, but only at time points where fully oxidised Pap1 was also detected (Figure 4.15). The high molecular weight of this band suggests that it could be a complex containing Pap1. Intriguingly, the observation that this band is only detected when Pap1 is oxidised suggests that this complex could be an intermediate in the reduction of oxidised Pap1.

Pap1 oxidation was also measured 0 – 30 min (0 – 1800 seconds) after exposure to 500 µM H_2O_2 (Figure 4.16). Similar to a 200 µM exposure, treatment with 500 µM H_2O_2 resulted in the detection of the fully oxidised Pap1 band (Figure 4.16). However, unlike treatment with 200 µM H_2O_2, fully reduced Pap1 was still detected after a 500 µM treatment (Figure 4.16) indicating that 500 µM H_2O_2 treatment does not oxidise all of the cellular Pap1 protein. This fully reduced Pap1 band was detected 30 min after 500 µM H_2O_2 exposure at which time the oxidised Pap1 band were not observed (Figure 4.16). These observations suggest that

Pap1 is able to return to its fully reduced, pre-stress, oxidation state much sooner after 500 µM H_2O_2 exposure (Figure 4.16) compared with 200 µM exposure (Figure 4.15).

Pap1 oxidation was also measured after a 0 - 10 minutes (600 seconds) exposure to 100 µM H_2O_2 (Figure 4.17). All three Pap1 oxidation states were detected after exposure to 100 µM H_2O_2, the relative intensity of all three bands appeared unchanged from 30 – 600 seconds after exposure (Figure 4.17). This suggests, that 100 µM H_2O_2 does not oxidise all of the Pap1 protein in the cell (Figure 4.17). For example almost all Pap1 was in a fully oxidised state 10 min (600 seconds) after exposure to 200 µM H_2O_2 (Figure 4.14 and 4.15), whilst the reduced form of Pap1 could still be detected 600 seconds after 100 µM H_2O_2 treatment (Figure 4.17). Notably, although treatment with 100 or 500 µM H_2O_2 did not cause all of the Pap1 to become oxidised, the initial oxidation of Pap1 was faster after 500 µM H_2O_2 treatment (Figure 4.18). The initial rate of Pap1 oxidation was similar after 500 and 1000 µM H_2O_2 treatments (Figure 4.19) indicating that this rate is maximal at 500 µM.

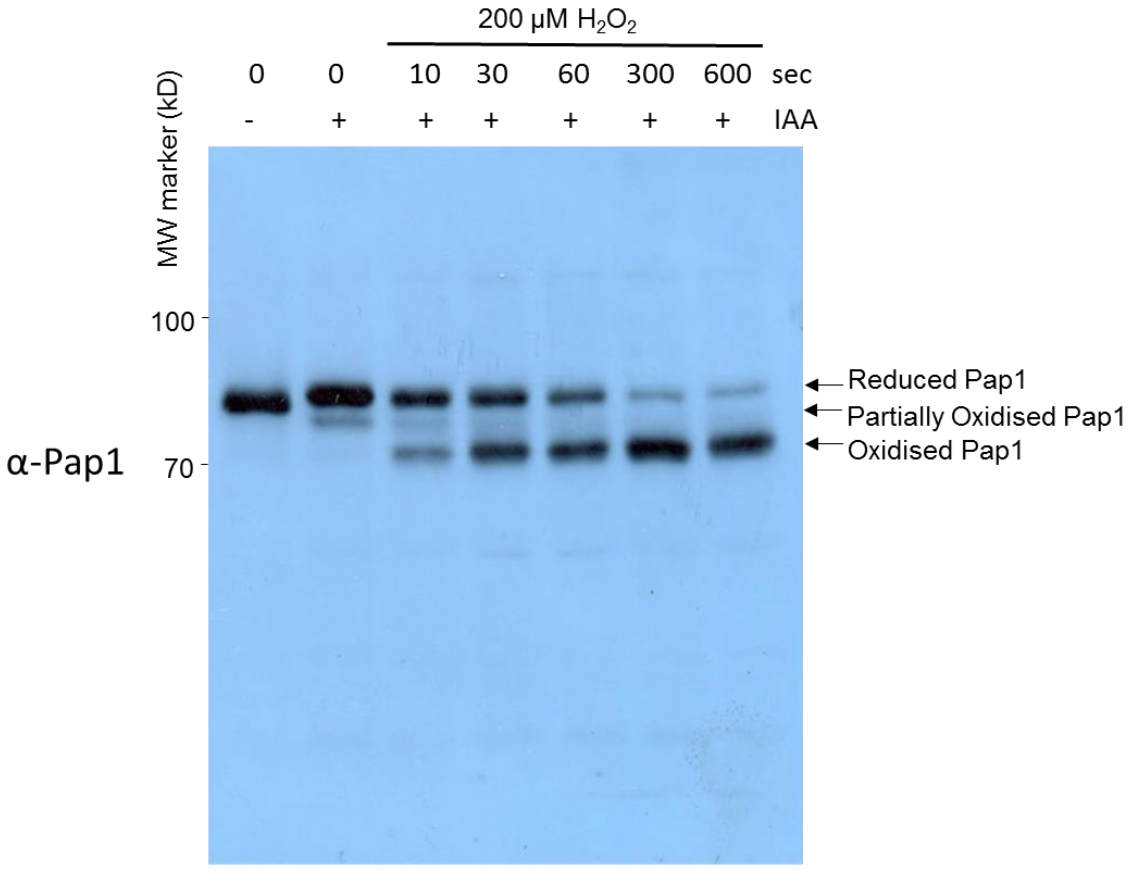

Figure 4.14: Pap1 oxidation 0 - 600 seconds after exposure to 200 µM H_2O_2.

Western blot analysis, using α-Pap1 antibodies, of protein extracts taken from wild-type (NT4) cells were exposed to 200 µM H_2O_2 for 0 to 600 seconds. Protein extracts were treated with IAA as indicated (kindly provided by Dr A M Day).

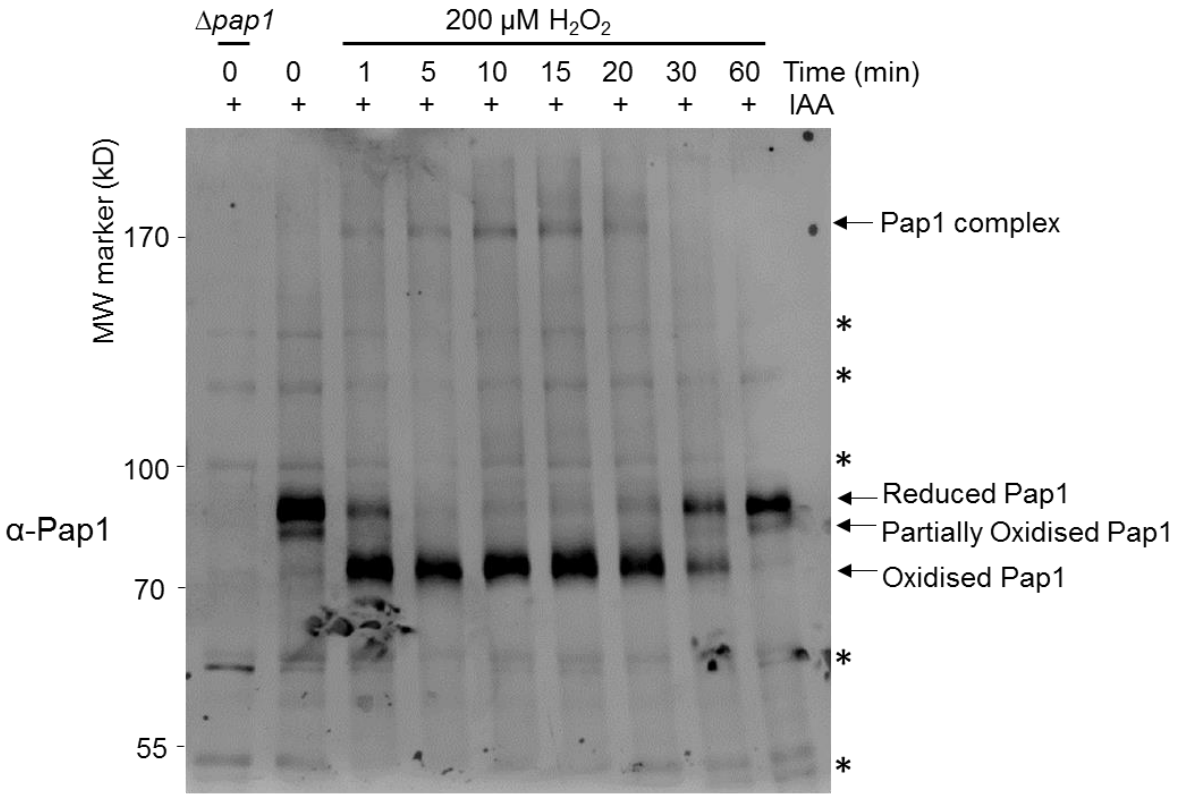

Figure 4.15: Pap1 oxidation 0 - 60 min after exposure to 200 μM H_2O_2.

Western blot analysis, using α-Pap1 antibodies, of IAA-treated protein extracts from wild-type (NT4) cells and Δ*pap1* (TP108) cells. The wild-type cells were exposed to 200 μM H_2O_2 for 0 to 60 minutes (3600 seconds). Non-specific bands present in the Δ*pap1* cells are marked with an asterisk (*).

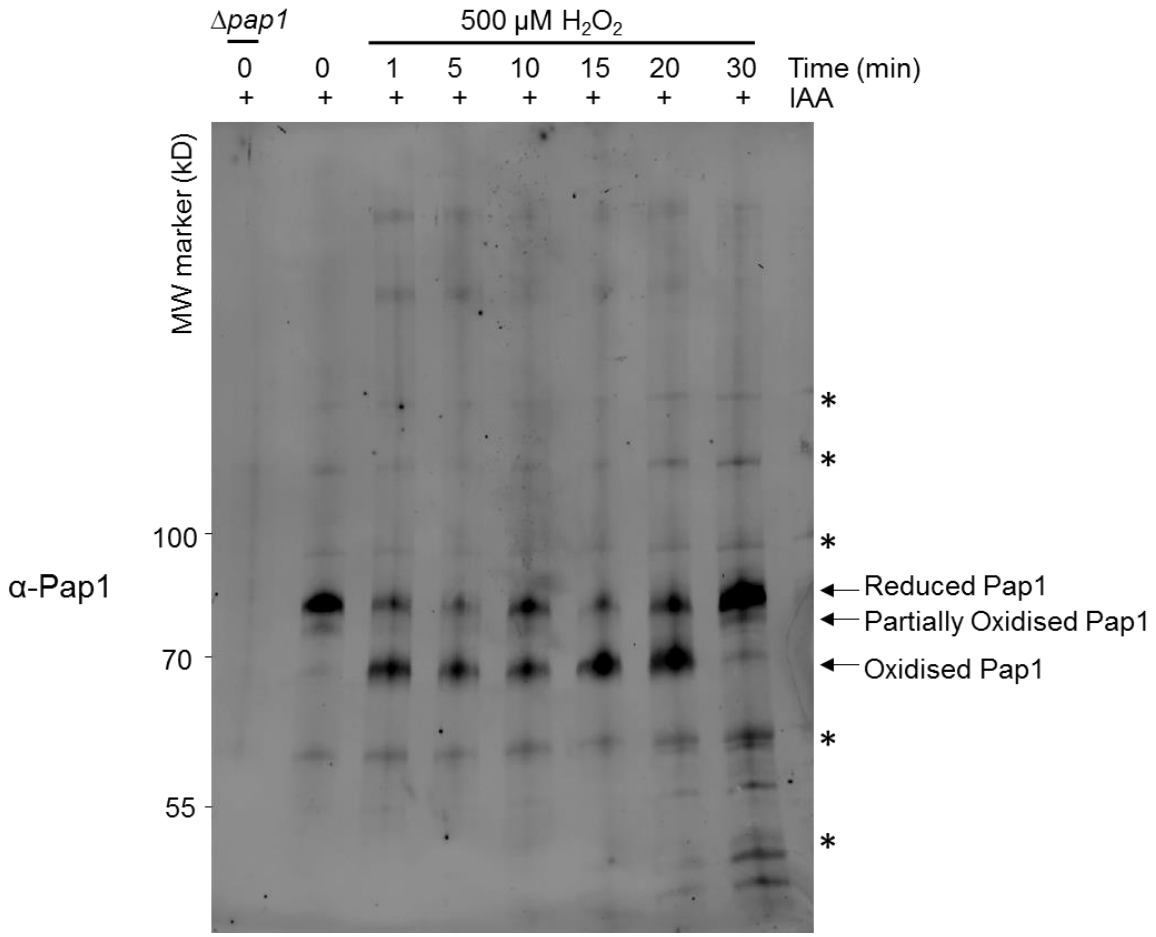

Figure 4.16: Pap1 oxidation 0 - 30 min after exposure to 500 μM H_2O_2.

Western blot analysis, using α-Pap1 antibodies, of IAA-treated protein extracts from wild-type (NT4) cells and Δ*pap1* (TP108) cells. The wild-type cells were exposed to 200 μM H_2O_2 for 0 to 30 minutes (1800 seconds). Non-specific bands are marked with an asterisk (*).

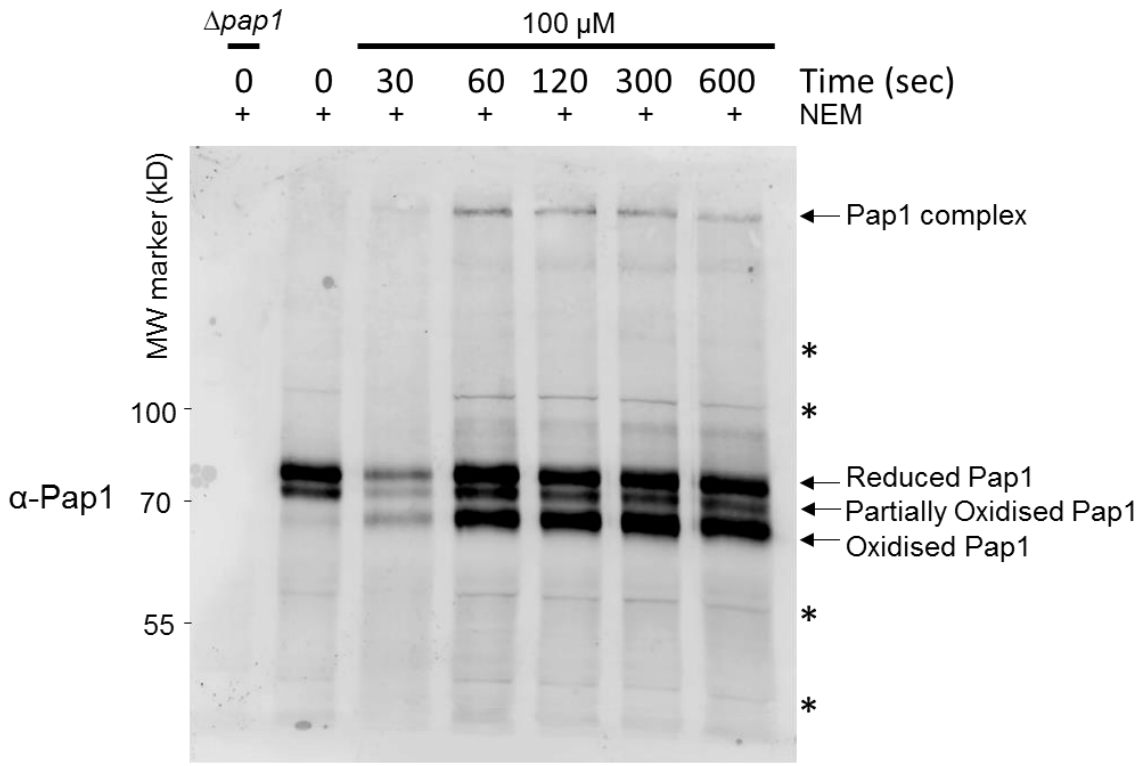

Figure 4.17: Pap1 oxidation 0 - 600 seconds after exposure to 100 µM H_2O_2.

Western blot analysis, using α-Pap1 antibodies, of NEM-treated protein extracts from wild-type (NT4) cells and Δ*pap1* (TP108) cells. The wild-type cells were exposed to 200 µM H_2O_2 for 0 to 600 seconds. Non-specific bands are marked with an asterisk (*).

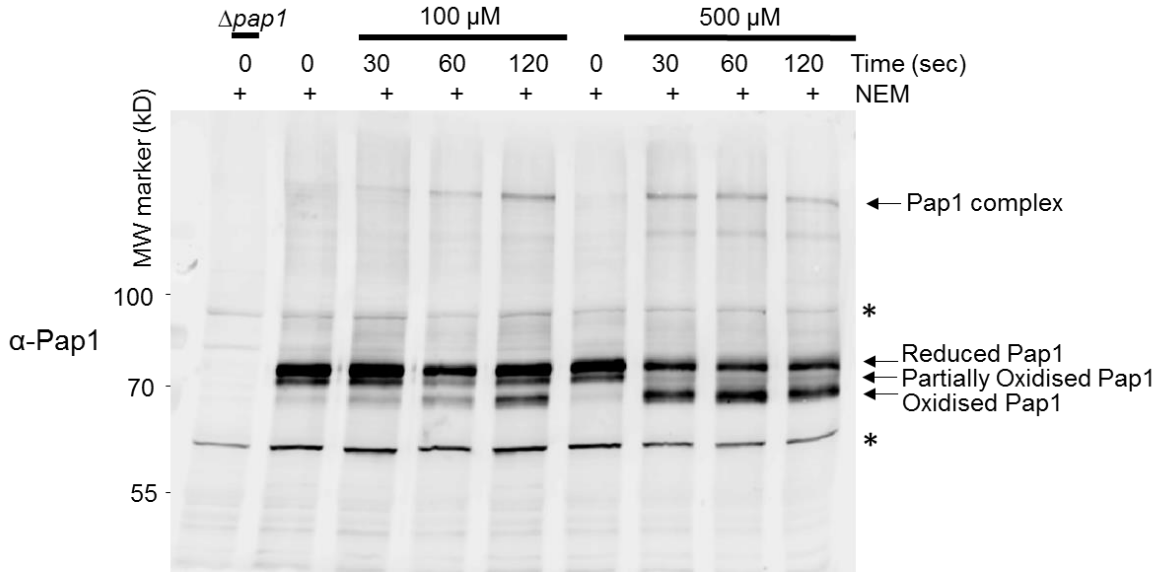

Figure 4.18: Pap1 oxidation 0 - 120 seconds after exposure to 100 & 500 µM H_2O_2.

Western blot analysis, using α-Pap1 antibodies, of NEM-treated protein extracts from wild-type (NT4) cells and Δ*pap1* (TP108) cells. The wild-type cells were exposed to 100 µM or 500 µM H_2O_2, as indicated, for 0 to 120 seconds. Non-specific bands are indicated with an asterisk (*).

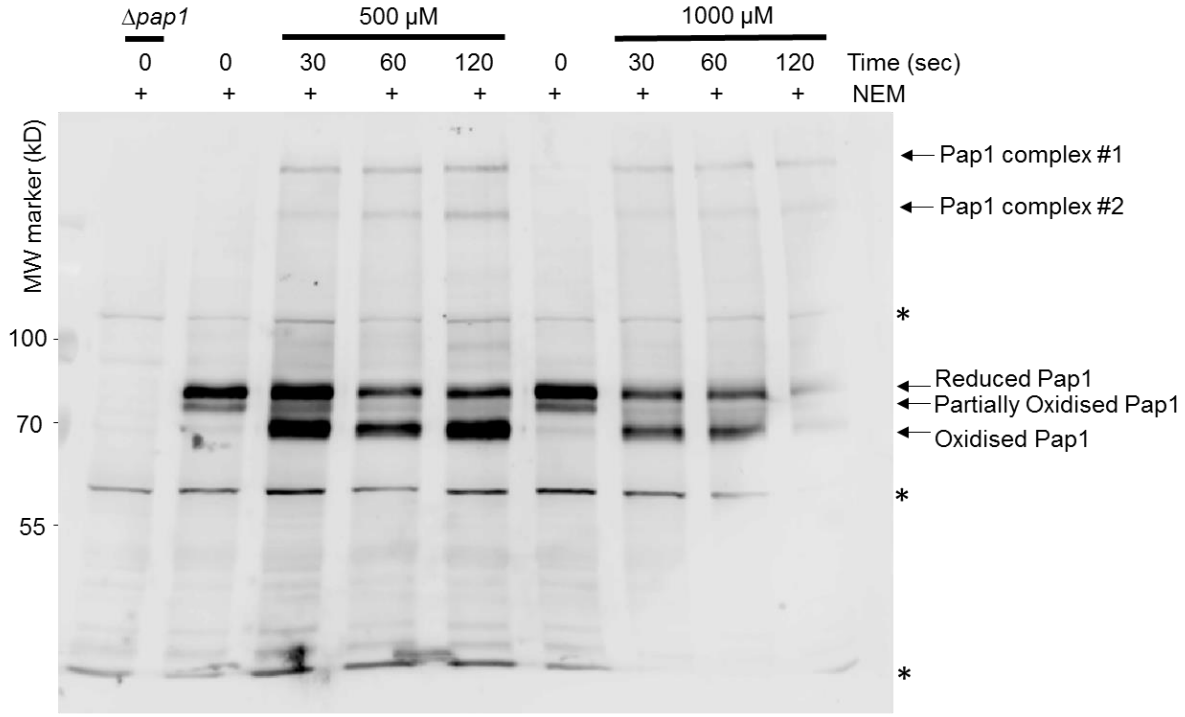

Figure 4.19: Pap1 oxidation 0 - 120 seconds after exposure to 500 & 1000 µM H_2O_2.

Western blot analysis, using α-Pap1 antibodies, of NEM-treated protein extracts from wild-type (NT4) cells and Δ*pap1* cells. The wild-type cells were exposed to 500 µM or 1000 µM H_2O_2, as indicated, for 0 to 120 seconds. Non-specific bands not present in the Δ*pap1* cells are indicated with an asterisk (*).

4.4.2 Testing the ability of alternative mechanisms of Pap1 regulation to simulate the experimental data.

The computer model of Tpx1 and Trx1 oxidation was adapted to make three computer models each representing a potential mechanism for the oxidation and reduction of Pap1 (Table 4.6 & 4.7). Each model was then used to simulate the oxidation of Pap1 in response to different concentrations of H_2O_2. By comparing the simulation data for each model to the experimentally observed dynamics of Pap1 oxidation an assessment was made as to which mechanism of Pap1 regulation was most likely. The mechanisms tested were, Pap1 is directly oxidised by H_2O_2 (Model A), directly oxidised by Tpx1-SOH (Model B) or directly oxidised by Tpx1-ox#1 (Model C). All models assumed Pap1 is reduced by Trx1.

4.4.2.1 Direct oxidation by H_2O_2 cannot explain the experimentally observed dynamics of Pap1 oxidation from 0 to 120 seconds.

As discussed in chapter 1 (see 1.4), an oxidation sensitive cysteine residue in the bacterial stress response transcription factor OxyR has been shown to be directly oxidised by H_2O_2, resulting in the activation of this transcription factor (for review see (Storz and Tartaglia, 1992). This raises the possibility that direct oxidation of a cysteine residue in Pap1, by H_2O_2, could also be the mechanism for the activation of Pap1. Although the H_2O_2-induced activation of Pap1 is inhibited in a Δ*tpx1* mutant, suggesting that direct oxidation by H_2O_2 is not the activation mechanism, it could be possible that the only role of Tpx1 in the activation of Pap1 is to inhibit the Trx1-mediated reduction of Pap1 (Bozonet et al., 2005, Day et al., 2012, Vivancos et al., 2005). Loss of Tpx1 would increase the availability of reduced Trx1, and this could be sufficient to keep Pap1 in a reduced state, despite the presence of H_2O_2 and would therefore explain the inhibition of H_2O_2 induced Pap1 oxidation.

To test this hypothesis two new reactions were added to the model of Tpx1 and Trx1 oxidation (Model A, Table 4.6). The first reaction (Model A, Table 4.6, Figure 2.20) represents the direct oxidation of Pap1 by H_2O_2 and is dependent on the rate constant k_{Pap1ox}. The second reaction (Table 4.6, Figure 4.20) represents the reduction of Pap1 by Trx1 and is dependent on the rate constant $k_{Pap1red}$. Both

reactions were assumed to follow mass action kinetics (Table 4.6). This model was used to simulate the effect that different values of $k_{Pap1red}$ and k_{Pap1ox} would have on the concentration of oxidised Pap1 (Pap1-ox) 1 min after exposure to 0, 100, 200 & 500 µM H_2O_2 (Figure 4.21). These simulations were compared to the experimentally observed concentrations of Pap1-ox (Figure 4.21). One set of simulations was performed based on the assumption that Pap1 contains a H_2O_2-sensitve cysteine residue which is equally as sensitive to oxidation as the Cys_P-SH in Tpx1 (20 $\mu M^{-1}s^{-1}$, see Table 3.7). To represent this the rate constant k_{Pap1ox} was set at a value of 20 μM^{-1} s^{-1} for these simulations (Figure 4.21A). In these simulations Trx1 was assumed to have similar affinity for Pap1 disulphides as for Tpx1, the rate constant k_{Papred} was therefore given a value of 0.1 μM^{-1} s^{-1} (Figure 4.21A). This model predicted that a 1 min exposure to 200 µM H_2O_2 would result in the formation of more Pap1-ox compared to 1 min exposure to 100 µM (Figure 4.21A). This is in agreement with the experimental data (Figure 4.21A). However, the model predicted that a 1 min after exposure to 200 or 500 µM H_2O_2 would result in the same, maximal, concentration of Pap1-ox (Figure 4.21A). This disagrees with the experimental data which indicated that treatment with 500 µM H_2O_2 would result in less oxidised Pap1 (Figure 4.21A, 4.14 & 4.16).

A similar set of simulations were performed but this time assuming the cysteine in Pap1 is much less sensitive to oxidation by H_2O_2, than Tpx1 (Figure 4.21B). To represent this, the rate constant k_{Pap1ox} was set to 0.01 μM^{-1} s^{-1}, whilst $k_{Pap1red}$ still set to 0.1 μM^{-1} s^{-1} (Figure 4.21B). This model predicted that Pap1-ox would not be detected after a 1 min treatment with 100 µM H_2O_2. Also, this model predicted that more Pap1-ox would be detected 1 min after treatment with 500 µM H_2O_2 than with 200 µM (Figure 4.21B), in disagreement with the experimental data. Indeed, none of the simulations made using Pap1 model A were able to simulate the experimentally observed feature that treatment with 500 µM H_2O_2 results in less Pap1-ox formation than is observed following 200 µM (Figure 4.21). This suggests that direct oxidation of Pap1 by H_2O_2 and subsequent reduction by Trx1 is not a suitable mechanism to explain the experimentally observed dynamics of Pap1 oxidation.

Table 4.6 Reaction equations and rate laws for the alternative models of Pap1 regulation

Reaction description	Reaction	Rate law
(Pap1 model A) Pap1 is oxidised by H_2O_2	Pap1-red + $H_2O_{2(int)}$ -> Pap1-ox	k_{Pap1ox}[Pap1-red][H_2O_{2int}]
(Pap1 model B) Pap1 is oxidised by Tpx1-SOH	Pap1-red + Tpx1-SOH -> Pap1-ox + Tpx1-SH	k_{Pap1ox}[Pap1-red][Tpx1-SOH]
(Pap1 model C) Pap1 is oxidised by Tpx1-ox#1	Pap1-red + Tpx1-ox#1 -> Pap1-ox + 2 x Tpx1-SH	k_{Pap1ox} [Pap1-red][Tpx1-ox#1]
(All Pap1 models) Pap1 is reduced by Trx1	Pap1-ox + Trx1-red -> Pap1-red + Trx1-ox	$k_{Pap1red}$ [Pap1-ox][Trx1-red]

Table 4.6: Reaction equations and rate laws for the alternative models of Pap1 regulation.

The table displays the reaction equations and the rate laws used for the alternative models of Pap1 oxidation. These reactions were added to the model of Tpx1 and Trx1 oxidation to make to full models (Table 4.5). A description of each reaction and the model it used in is displayed in the left hand column.

Table 4.7 Initial Pap1 concentrations used in the models of Pap1 regulation

Species	Initial Concentration	*ref*
Pap1-red	0.0245 µM	Marguerat et al, 2012
Pap1-ox	0 µM	Marguerat et al, 2012

Table 4.7: Initial Pap1concentrations used in the alternative models of Pap1 regulation.

The table displays the initial concentration of Pap1-red and Pap1-ox used in the alternative models of Pap1 regulation. The total concentration of cellular Pap1 was estimated to be ~0.0245 µM based on published data (Marguerat et al, 2012) (see 2.6.2).

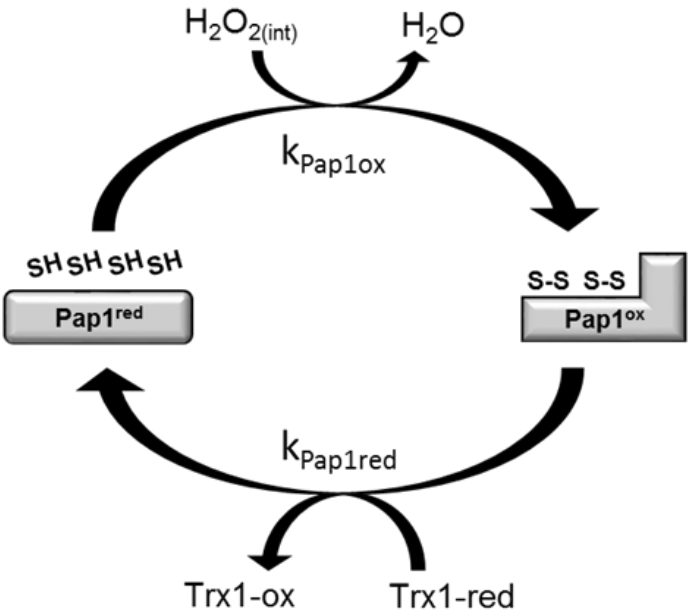

Figure 4.20: Schematic diagram representing the direct oxidation of Pap1 by H_2O_2 and subsequent reduction of Pap1 by Trx1.

Schematic diagram showing the Pap1 dependent reactions added to the computer model of Tpx1 and Trx1 oxidation (Table 4.5) to make Pap1 model A (Table 4.6). Pap1 model A represents the direct oxidation of Pap1 by H_2O_2 and subsequent reduction by Trx1 which are dependent on the rate constants k_{Pap1ox} and $k_{Pap1red}$ respectively.

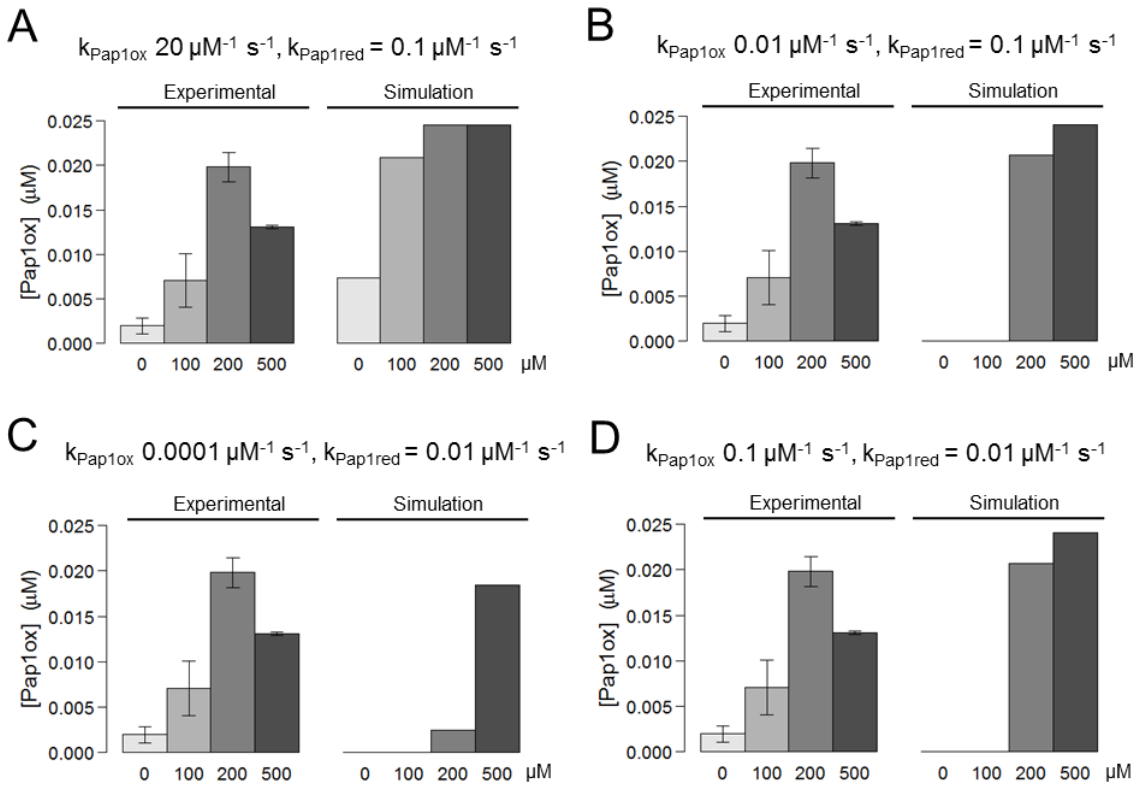

Figure 4.21: Direct oxidation of Pap1 by H_2O_2 and subsequent reduction by Trx1 (Pap1 model A) does not accurately simulate the dynamics of Pap1 oxidation after 60 second exposure to 0 – 500 µM H_2O_2.

Pap1 model A, which assumes Pap1 is directly oxidised by H_2O_2 and subsequently reduced by Trx1 (Figure 4.20), was used to simulate the concentration of oxidised Pap1 (Pap1-ox) 1 min after exposure to 0 – 500 µM H_2O_2. Four simulations were performed (A - D) with each simulation using different values for the parameters k_{Pap1ox} and $k_{Pap1red}$ as indicated above each bar chart. The simulation results are represented by the right hand bars and the experimental data is represented by the left hand bars. The error bars represent the standard deviation of multiple measurements (0 µM n = 9, 100 µM n = 3, 200 µM, n = 3 and 500 µM n = 3).

4.4.2.2 The oxidation of Pap1 by the Tpx1-SOH monomer is able to simulate the dynamics of Pap1 oxidation.

As discussed in chapter 1 (1.4.2) and section 4.1, the *S. cerevisiae* Pap1 homolog, Yap1, has been shown to be directly oxidised by the thiol-peroxidase Gpx3 via a mechanism which involves the formation of a disulphide bond between Gpx3-SOH and Yap1 (Delaunay et al., 2002). Given that that the *S. pombe* thiol-peroxidase Tpx1 is required for the H_2O_2-induced oxidation of Pap1 (Day et al., 2012) it is reasonable to suggest that, similarly to Yap1 and Gpx3, Pap1 might be directly oxidised by the sulphenic form of Tpx1 (Tpx1-SOH). To represent this possibility two new reactions were added to the model of Tpx1 and Trx1 oxidation (Model B, Table 4.6, Figure 4.22). The first reaction represents the direct oxidation of Pap1 by Tpx1-SOH, which is dependent on the rate constant k_{Pap1ox} (Table 4.6, Figure 4.22). The second reaction represents the reduction of Pap1 by Trx1, which is dependent on the rate constant kPap1red (Table 4.6, Figure 4.22). This model was used to simulate the concentration of Pap1-ox 1 min after exposure to 0 – 500 µM H_2O_2 using different values for the parameters $k_{Pap1red}$ and k_{Pap1ox} (Figure 4.23). In order to assess the ability of each parameter set to simulate the initial oxidation of Pap1, several key dynamic features were looked for. Firstly, the model should predict an increase in Pap1-ox when H_2O_2 concentration is increased from 0 to 100 µM. Secondly an H_2O_2 increase from 100 to 200 µM H_2O_2 should result in a further increase in Pap1-ox. Finally, increasing the H_2O_2 concentration from 200 to 500 µM H_2O_2 should cause a decrease in Pap1-ox. Unlike model A (Figure 4.20 & 4.21), all of the parameter values tested for model B were able to simulate these key features of Pap1 oxidation (Figure 4.23).

It was clear that the ability of model B to simulate the initial oxidation of Pap1 was better than model A. However, an assessment of which model B parameter set was best, needed to be made. The model that used a k_{Pap1ox} value of 0.1 μM^{-1} s^{-1} and a $k_{Pap1red}$ of 0.1 μM^{-1} s^{-1} (Figure 4.23A) predicted a Pap1-ox concentration of 0.01 µM after treatment with 100 µM H_2O_2 for 60 seconds. This was close to the mean of the experimentally measured value of ~0.008 µM 1 min after 100 µM H_2O_2 treatment, and within the standard deviation of the measured values (Figure 4.23A). However, the simulated concentrations of Pap1-ox after 200 µM and 500 µM H_2O_2 treatments were ~0.01 µM and ~0.007 µM, both of which were around

half of their experimentally measured values (Figure 4.23A). Similarly, the model which used a k_{Pap1ox} value of 0.1 μM^{-1} s^{-1} and a $k_{Pap1red}$ of 0.01 μM^{-1} s^{-1}, accurately predicted the experimentally measured Pap1-ox concentration after 200 µM treatment, but did not accurately predict the measured values after 100 µM and 500 µM treatment (Figure 4.23D). The only model which was able to accurately predict more than one of the experimentally measured Pap1-ox concentrations was the model using a k_{Pap1ox} value of 0.04 μM^{-1} s^{-1} and a $k_{Pap1red}$ of 0.01 μM^{-1} s^{-1} (Figure 4.23C). This model accurately simulated the concentration of Pap1-ox 1 min after exposure to 100 & 500 µM H_2O_2 (Figure 4.23C), although did under estimate the concentration of Pap1-ox after a 200 µM H_2O_2 exposure (Figure 4.23C). We therefore decided that the 0.04 μM^{-1} s^{-1}, $k_{Pap1red}$ of 0.01 μM^{-1} s^{-1} parameter set enabled the best fit to the data (Figure 4.23C). Although other parameter sets were tested, none of these sets were able to accurately simulate the experimentally measured Pap1-ox concentrations after 100, 200 and 500 µM H_2O_2 treatments (data not shown).

Although none of the model B simulations accurately simulated all of the Pap1-ox data, in contrast to model A, model B was able to simulate the key dynamic features of Pap1-ox formation (Figure 4.23). This suggests that direct oxidation of Pap1 by Tpx1-SOH is more likely to represent the mechanism of Pap1 oxidation than oxidation by H_2O_2.

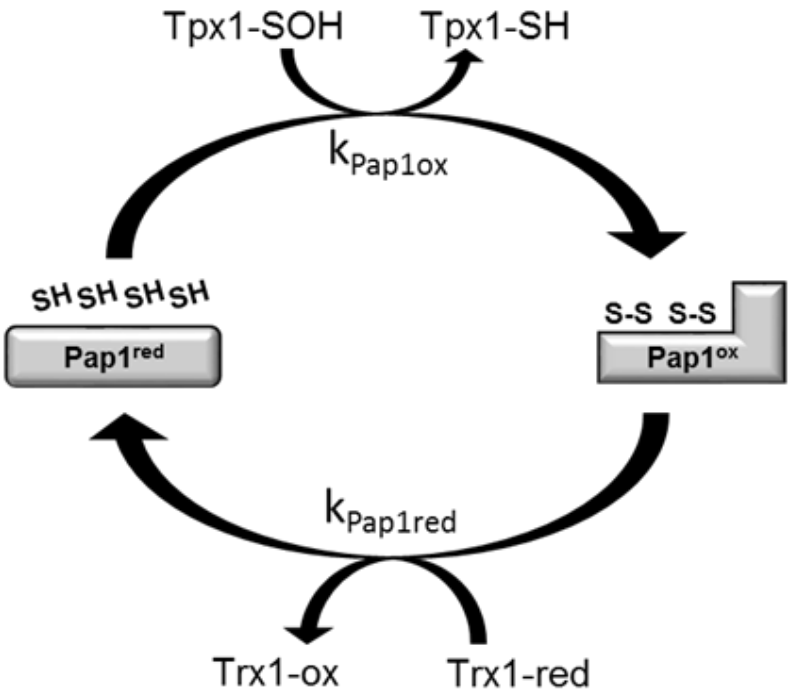

Figure 4.22: Schematic diagram representing the direct oxidation of Pap1 by Tpx1-SOH and subsequent reduction of Pap1 by Trx1.

Schematic diagram showing the Pap1 dependent reactions added to the computer model of Tpx1 and Trx1 oxidation (Table 4.5) to make Pap1 model B (Table 4.6). Pap1 model B represents the direct oxidation of Pap1 by Tpx1-SOH and subsequent reduction by Trx1 which are dependent on the rate constants k_{Pap1ox} and $k_{Pap1red}$ respectively.

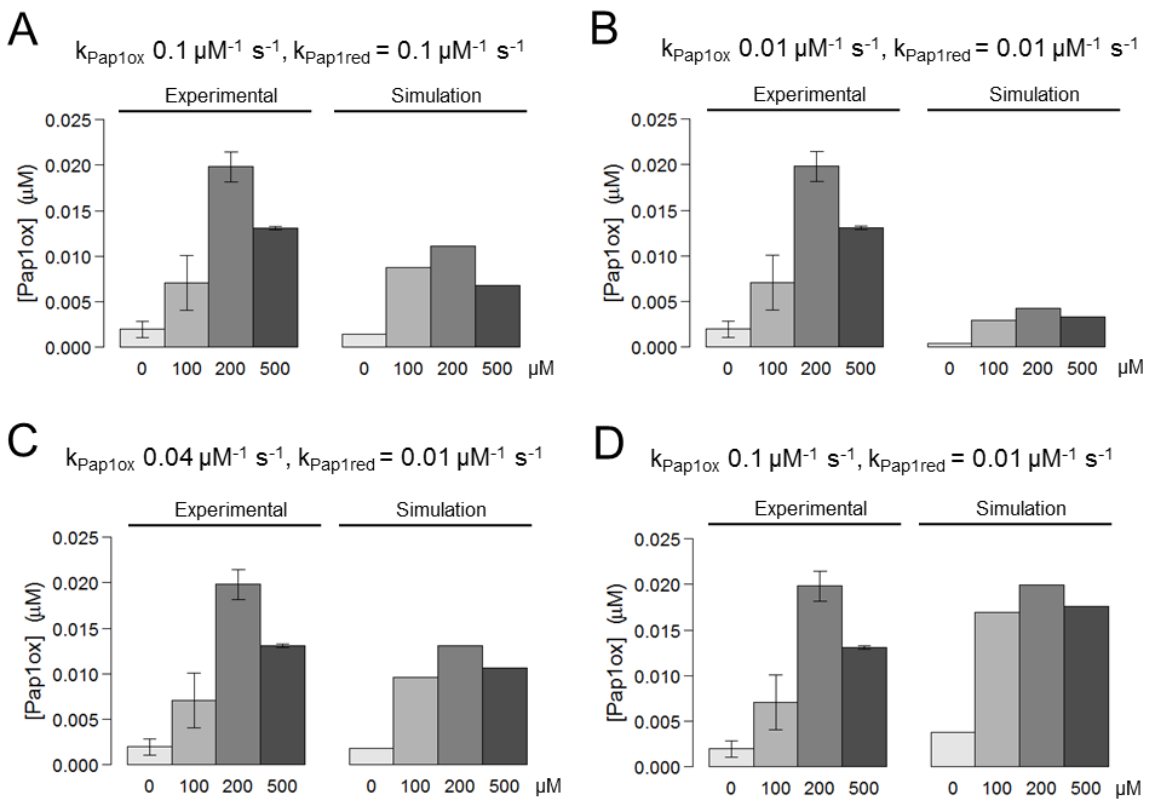

Figure 4.23: Direct oxidation of Pap1 by Tpx1-SOH and subsequent reduction by Trx1 (Pap1 model B) is able to simulate the dynamics of Pap1 oxidation after 60 second exposure to 0 – 500 μM H_2O_2.

Pap1 model B, which assumes Pap1 is directly oxidised by Tpx1-SOH and subsequently reduced by Trx1 (Figure 4.22), was used to simulate the concentration of oxidised Pap1 (Pap1-ox) 1 min after exposure to 0 – 500 μM H_2O_2. Four simulations were performed (A - D) with each simulation using different values for the parameters k_{Pap1ox} and $k_{Pap1red}$ as indicated above each bar chart. The simulation results are represented by the right hand bars and the experimental data is representing by the left hand bars. The error bars represent the standard deviation of multiple measurements (0 μM n = 9, 100 μM n = 3, 200 μM, n = 3 and 500 μM n = 3).

4.4.2.3 The Pap1 mediated reduction of Tpx1-ox#1 cannot explain the experimentally observed dynamics of Pap1 oxidation after a 60 seconds exposure to H_2O_2.

Another potential mechanism for the oxidation of Pap1 could be that Pap1 behaves as a disulphide-reductase and is able to reduce oxidised Tpx1 (Table 4.6, Figure 4.24). For example, rather than be oxidised by Tpx1-SOH, Pap1 might instead directly reduce Tpx1 disulphide bonds such as the one in Tpx1-ox#1. To represent this, two new reactions (Pap1 model C, Table 4.6, Figure 4.24) were added to the computer model of Tpx1 and Trx1 oxidation (Table 4.5). This model was used to simulate the concentration of oxidised Pap1 after a 60 seconds exposure to 0 – 500 µM H_2O_2 using different values for the parameters $k_{Pap1red}$ and k_{Pap1ox} (Figure 4.25). Similar to Pap1 model B, all of the Pap1 model C simulations were able to simulate the experimentally observed feature that less Pap1-ox will form after exposure to 500 µM compared to a 200 µM H_2O_2 exposure (Figure 4.25). This suggests that model C can also simulate some of the observed features of Pap1 oxidation. However, model C always predicted that peak Pap1 oxidation would occur after treatment with 100 µM rather than 200 µM H_2O_2 (Figure 4.25). Furthermore, some of the model C simulations greatly overestimated the amount of oxidised Pap1 before addition of H_2O_2 (Figure 4.25A & C). For these reasons, it was concluded that Pap1 model B is a better representation of Pap1 oxidation than Pap1 models A & C. Accordingly, this evidence suggests it is more likely that Pap1 becomes oxidised by direct oxidation of Pap1 by Tpx1-SOH (Figure 4.22) than direct oxidation by H_2O_2 (Figure 4.20) or Pap1 behaving as a disulphide reductase (Figure 4.24).

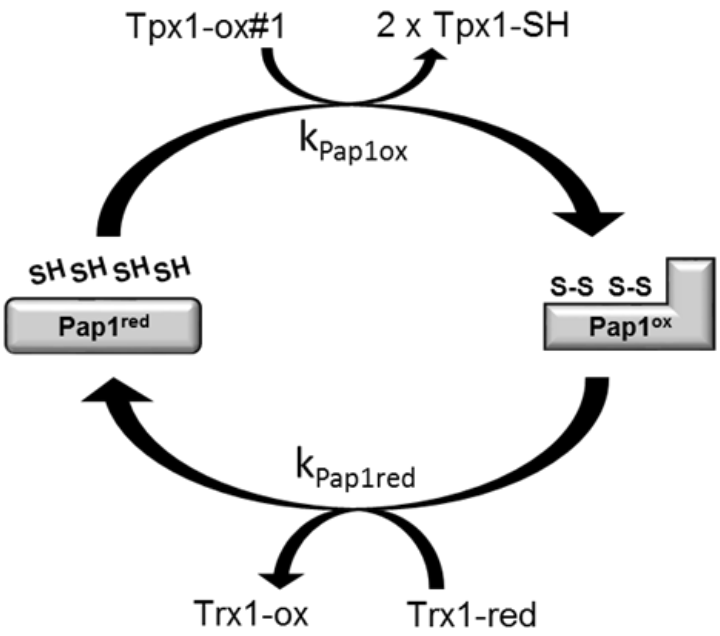

Figure 4.24: Schematic diagram representing the reduction of Tpx1-ox#1 by Pap1 and subsequent reduction of Pap1 by Trx1.

Schematic diagram showing the Pap1 dependent reactions added to the computer model of Tpx1 and Trx1 oxidation (Table 4.5) to make Pap1 model C (Table 4.6). Pap1 model C represents the reduction of a Tpx1 homodimer (Tpx1-ox#1) by Pap1, which results in the formation of two reduced Tpx1 monomers (Tpx1-SH). This reaction is dependent on the rate constant k_{Pap1ox}. The oxidised form of Pap1 (Pap1-ox) is then subsequently reduced Trx1, and is dependent on the rate constants $k_{Pap1red}$.

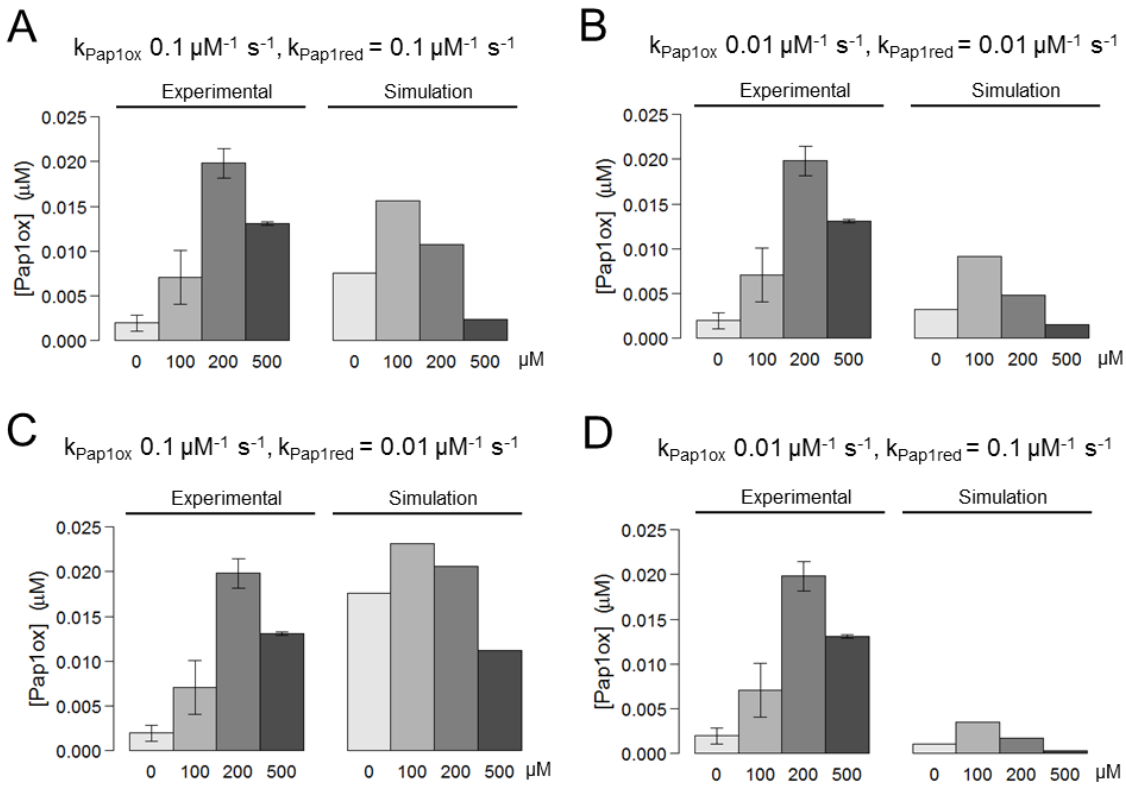

Figure 4.25: The reduction of Tpx1-ox#1 by Pap1 and the subsequent reduction of oxidised Pap1 by Trx1 (Pap1 model C) is not able to simulate experimentally observed Pap1 oxidation after 60 second exposure to 0 – 500 μM H_2O_2.

Pap1 model C, which assumes Tpx1-ox#1 is reduced by Pap1 and that oxidised Pap1 is reduced by Trx1 (Figure 4.24), was used to simulate the concentration of oxidised Pap1 (Pap1-ox) 1 min after exposure to 0 – 500 μM H_2O_2. Four simulations were performed (A - D) with each simulation using different values for the parameters k_{Pap1ox} and $k_{Pap1red}$ as indicated above each bar chart. The simulation results are represented by the right hand bars and the experimental data is representing by the left hand bars. The error bars represent the standard deviation of multiple measurements (0 μM n = 9, 100 μM n = 3, 200 μM, n = 3 and 500 μM n = 3).

4.4.2.4 The model of Pap1 oxidation is not able to accurately simulate the extended (0 – 60 min) oxidation of Pap1.

The computer model of Pap1 oxidation which assumed Pap1 is oxidised by Tpx1-SOH and subsequently reduced by Trx1 (Pap1 model B, Table 4.6, Figure 4.22) was best able to simulate the experimental data for the early oxidation (0 – 60 seconds) of Pap1 (Figure 4.23) compared with the other models tested (Figure 4.21 & Figure 4.25). Furthermore, using the parameter values k_{Pap1ox} = 0.04 and $k_{Pap1red}$ = 0.01 μM^{-1} s^{-1}, together with the parameter values calculated for the model of Tpx1 and Trx1 oxidation (Table 4.5) most accurately predicted the concentrations of Pap1-ox 1 min after a 100 µM and 500 µM exposure (Figure 4.23). This model was also able to accurately simulate the formation of Pap1-ox from 0 – 600 seconds after exposure to 100 µM H_2O_2 as well as steady state Pap1 oxidation (Figure 4.26A & B). However, this model was unable to accurately simulate the experimentally observed formation of Pap1-ox 0 - 3600 seconds after exposure to 200 µM (Figure 4.26C). Specifically, the experimental data demonstrated the vast majority of Pap1 is fully oxidised up to 30 min (1800 seconds) after exposure to 200 µM H_2O_2 (Figure 4.15), but that after 30 min the concentration of oxidised Pap1 rapidly decreases, such that Pap1 is fully reduced by 60 min (Figure 4.15). Although Pap1 model B was able to simulate the near complete oxidation of Pap1 30 min (1800 seconds) after exposure to 200 µM H_2O_2 (Figure 4.26C), it was unable to simulate the experimental observation that Pap1 would be almost fully reduced by 60 min (3600 seconds) (Figure 4.26C). Furthermore, Pap1 model B was unable to simulate the experimentally observed changes in Pap1-ox concentration 30 min (1800 seconds) after exposure to 500 µM H_2O_2 (Figure 4.26D). The experimental data demonstrated that, after an initial oxidation, Pap1 is only fully reduced 30 min after H_2O_2 exposure (Figure 4.16). In contrast, model B predicted that Pap1 would already be reduced approximately 10 min after H_2O_2 exposure (Figure 4.26D). This suggests that factors not represented in this model influence the dynamics of the oxidation/reduction of Pap1 *in vivo*.

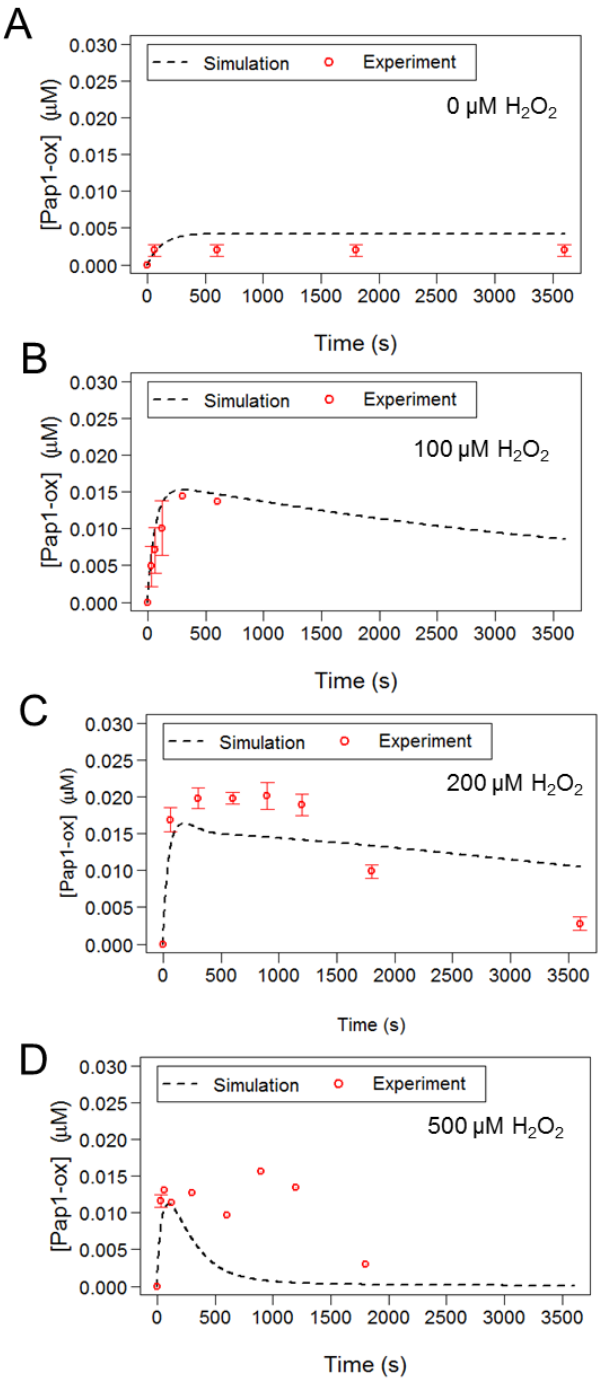

Figure 4.26: Pap1 model B is unable to simulate the levels of Pap1 oxidation observed over an extended time course following exposure to H_2O_2.

The model of Pap1 oxidation (Model B, Table 4.6, Figure 4.22) was used to simulate changes in the concentration of oxidised Pap1 (Pap1-ox) 0 – 3600 seconds after exposure to (A) 0 µM, (B) 100 µM, (C) 200 µM and (D) 500 µM H_2O_2. The experimental data for the concentration of Pap1-ox (red circles) was plotted on the same axis as the simulation data (black dashed line). Error bars represent the standard deviation of repeated measurements (0 µM n = 9, 100 µM n = 3, 200 µM, n = 3 and 500 µM n = 3). Data points without error bars indicate that no repeat measurements were made.

4.5 Investigating a potential role for the thioredoxin-like protein Txl1 in the reduction of Pap1

None of the computer models of Pap1 oxidation were able to accurately simulate all of the experimentally observed features of Pap1 oxidation. This suggests that none of the three Pap1 regulation mechanisms tested completely represents the actual *in vivo* mechanism of Pap1 regulation. *S. pombe* contains a second thioredoxin family protein, Txl1. A series of experiments was therefore performed in order to establish whether Txl1 has a role in the regulation of Pap1.

4.5.1 Pap1 is able to form a disulphide bond with Txl1

Pap1 oxidation was measured in the thioredoxin-peroxidase deficient *tpx1*^{C169S} mutant background (Figure 4.27). In the *tpx1*^{C169S} mutant, the resolving cysteine (Cys_R) has been replaced by a serine residue, this prevents the formation of Tpx1 disulphide dimers and therefore inhibits the Tpx1 catalytic cycle (Day et al., 2012). Interestingly, in this strain, the H_2O_2-induced oxidation of Pap1 was inhibited (Figure 4.27A & B). Instead H_2O_2 treatment caused the formation of high molecular weight Pap1 disulphide complexes (Figure 4.27A). One of these complexes, also detected in the non-H_2O_2 treated cells displayed a mobility shift in cells containing a FLAG-tagged Txl1 protein (Figure 4.27B). It was therefore reasoned that this band represents a complex between Pap1 and Txl1. In contrast, Trx1 was not present in any of these complexes (data not shown). This Pap1-containing band was not detected in Δ*txl1 tpx1*^{C169S} cells confirming that this band represents a complex between Pap1 and Txl1 (Figure 4.27B). Furthermore, the H_2O_2-induced oxidation of Pap1 was restored in Δ*txl1 tpx1*^{C169S} cells (Figure 4.27B). These data raised the possibility that Txl1, rather than Trx1, directly reduces Pap1.

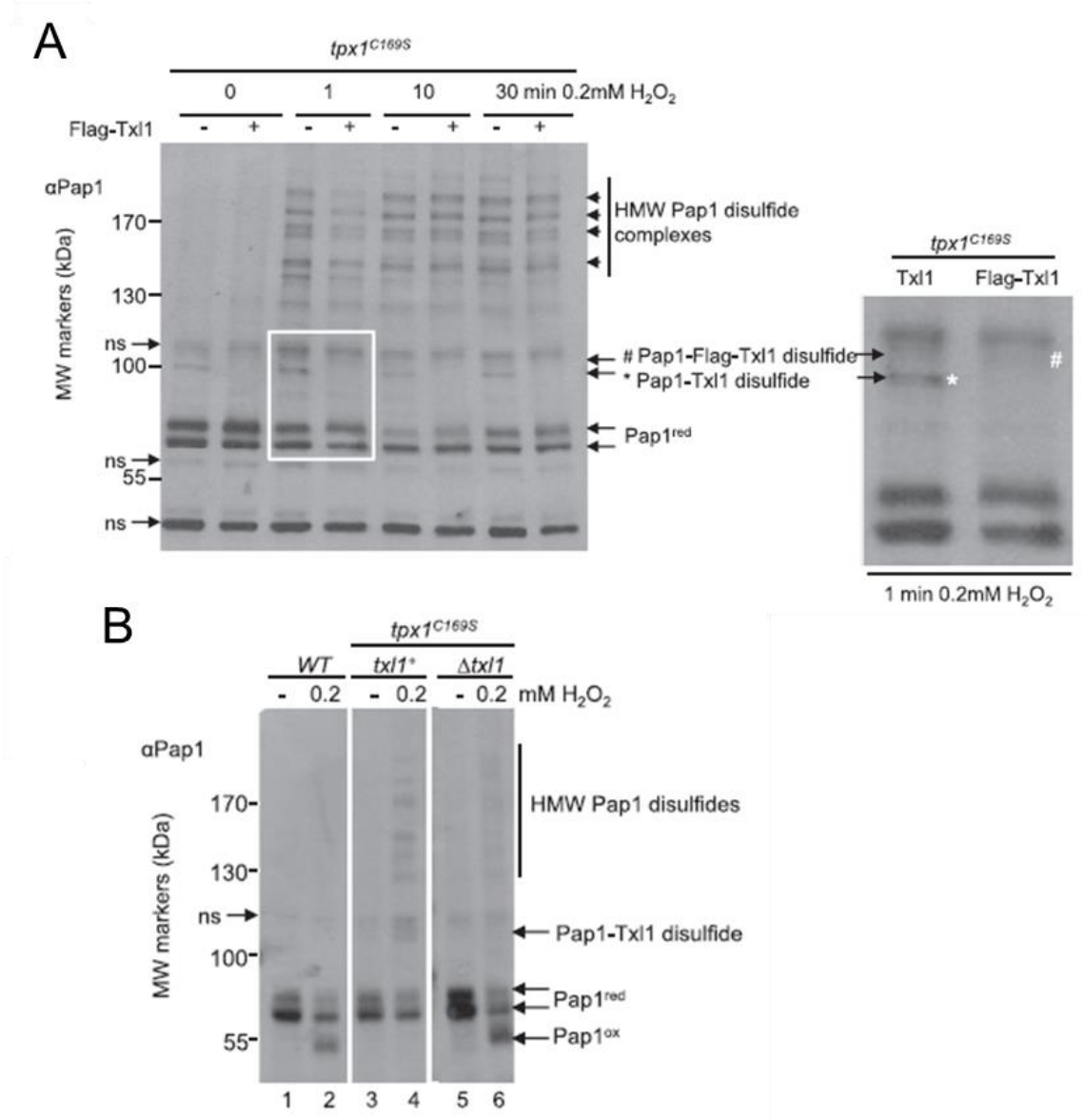

Figure 4.27: Txl1 forms disulphide complexes with Pap1 and inhibits normal H_2O_2-induced oxidation of Pap1 in cells expressing the thioredoxin peroxidase defective *tpx1*^{C169S}.

Western blot analysis, using Pap1 antibodies, of the redox status of Pap1 in (A) cells expressing *tpx1*^{C169S} and coexpressing either *txl1*$^{+}$ or FLAG-Txl1 from their normal chromosomal loci before and following treatment with 0.2 mM H_2O_2 for the indicated times. Bands with a mobility that is consistent with Txl1-Pap1 (*) and FLAG-Txl1-Pap1 (#) disulphides are indicated on the blot and in a selected area (white rectangle) magnified on the right-hand side of the panel. (B) Western blot analysis of wild-type (AD82) cells, and either *txl1*$^{+}$ or Δ*txl1* cells coexpressing *tpx1*^{C169S} from the normal chromosomal locus, before and following treatment with 0.2 mM H_2O_2 for 1 min (data provided by Dr Alison Day and Dr Jonathon Brown).

4.5.2 The effect of Tpx1, H_2O_2, and Trr1 on Txl1 oxidation

The detection of a disulphide complex between Txl1 and Pap1 strongly suggests that Txl1 is directly responsible for the reduction of oxidised Pap1 (Figure 4.27). However, it was not known whether Tpx1 is a substrate for Txl1 as well as Trx1, or whether Txl1 is a substrate for Trr1. To gain further insight into the relationship between Txl1,Tpx1 and Trr1, Txl1 oxidation was measured using a *S. pombe* cells expressing FLAG epitope tagged Txl1 (FLAG-Txl1) expressed from its natural locus. The oxidation of FLAG-Txl1 in response to a 0 – 30 min exposure to 200 µM H_2O_2 was measured using western blot analysis of AMS treated samples (Figure 4.28). Prior to H_2O_2 treatment FLAG-Txl1 was detected with a mobility consistent with the molecular weight of Txl1 (32 kDa) (Figure 4.28A). A lower mobility band was also detected before addition of H_2O_2 but was also present in samples from wild-type cells expressing the untagged form of Txl1, indicating this was non-specific (Figure 4.28A). After a 1 min exposure to 200 µM H_2O_2 of a, greater mobility FLAG-Txl1 band was detected (Figure 4.28A). The higher mobility of this new band is consistent with fewer AMS molecules being bound to Txl1 and indicates that this represents FLAG-Txl1 with an intramolecular disulphide bond (Txl1-ox) (Figure 4.28A). This therefore indicates that the lower mobility band detected before H_2O_2 addition represents the reduced form of Txl1 (Txl1-red). 10 minutes after exposure 200 µM H_2O_2 the intensity of the Txl1-red band had increased slightly but the intensity of this band did not return to pre-stress levels until 30 min after H_2O_2 exposure (Figure 4.28A). Notably, FLAG-Txl1 was constitutively completely oxidised in Δ*trr1* FLAG-Txl1 cells (Figure 4.28A). This is a strong indication that Trr1 is responsible for the reduction of oxidised Txl1. Furthermore, loss of Tpx1 (Δ*tpx1 FLAG-txl1*) prevented the H_2O_2-induced oxidation of Txl1 (Figure 4.28B). Moreover although, oxidised Txl1 was detected after a 1 min exposure to 6 mM H_2O_2, Txl1 returned to being fully reduced 10 min after exposure to 6 mM H_2O_2 (Figure 4.28C). This is consistent with the H_2O_2-induced oxidation of Txl1 requiring catalytically active Tpx1. This is also consistent with Txl1 being responsible for the reduction of Pap1, which occurs very rapidly in cells exposed to these concentrations of H_2O_2 (Day et al, 2012).

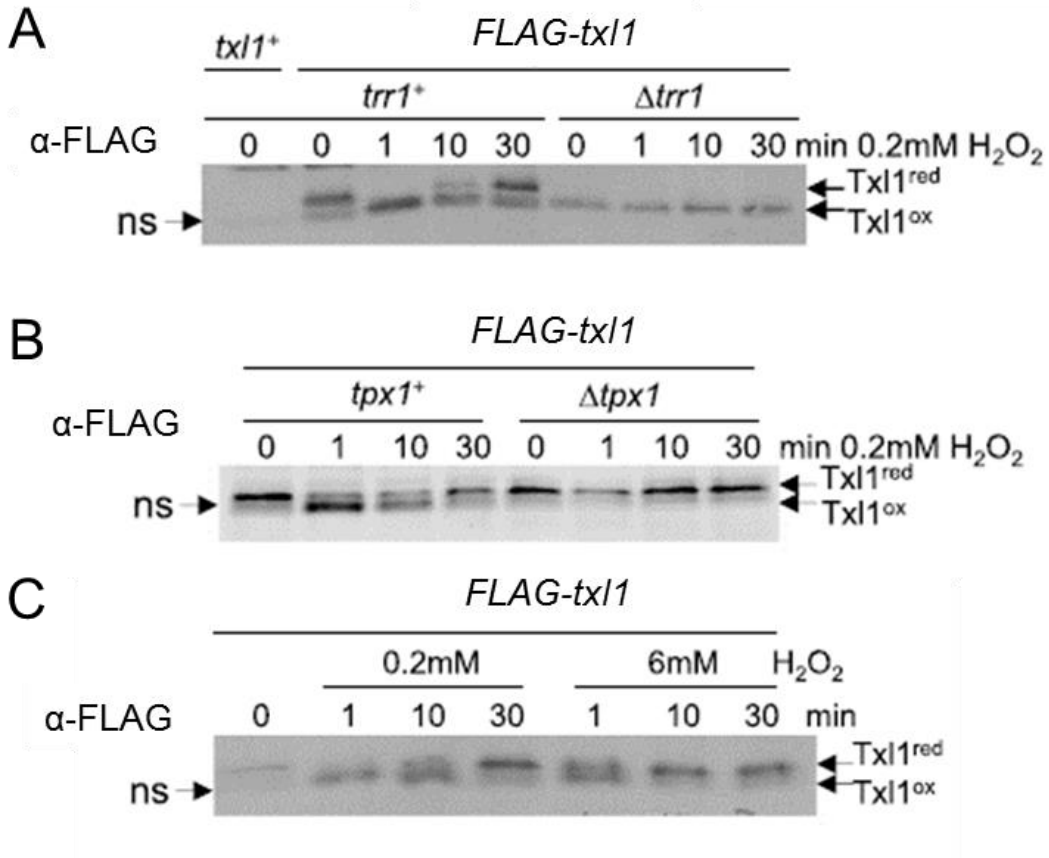

Figure 4.28: Effect of H_2O_2, Trr1, and Tpx1 on oxidation of Txl1.

Western blot analysis, using α-FLAG antibodies, of AMS-treated protein extracts from (A) wild-type, *FLAG-txl1* (JB95), (A) *FLAG-txl1 Δtrr1* (JB116) and (B) *FLAG-txl1 Δtpx1* (JB113) cells before and after a 30 min exposure to 0.2 mM or (C) 6 mM H_2O_2. None specific bands are indicated with ns and bands representing the oxidised and reduced forms of Txl1 are indicated with $Txl1^{ox}$ and $Txl1^{red}$ respectively. (Data provided by Dr Alison Day and Dr Jonathon Brown.)

4.5.3 A computer model in which Pap1 is reduced by Txl1 is better able to simulate the extended oxidation of Pap1

The detection of a Txl1-Pap1 complex in $Tpx1^{C169S}$ cells (Figure 4.27) and correlation between Txl1 and Pap1 oxidation (Figure 4.28, 4.15) highlights the possibility that Txl1 is responsible for the reduction of oxidised Pap1. This suggests that a feasible mechanism for Pap1 regulation could be that Pap1 is oxidised by Tpx1-SOH and then subsequently reduced by Txl1. To test the feasibility of this mechanism the computer model of Pap1 oxidation (Model B, Table 4.6, Figure 4.22) was adapted so that Txl1, not Trx1 was responsible for the reduction of Pap1-ox (Table 4.8). When building this model the assumption was made that Trx1 and Txl1 compete for the same pool of Trr1 (Figure 4.29). To represent this competition, the reduction of Trx1-ox was modelled using two reactions, in which Trx1-ox and Trr1 form a complex (Trx1-Trr1) dependent on the parameter $k_{Trx1red1}$ (Table 4.8). The Trx1-Trr1 complex then dissociates to form reduced Trx1 and Trr1 dependent on the rate constant $k_{Trx1red2}$ (Table 4.8). The reduction of oxidised Txl1 (Txl1-ox) by Trr1 was modelled using mass action kinetics dependent on the rate constant $k_{Txl1red}$ (Table 4.8). Parameter estimation was used to estimate values for the rate constants $k_{Trx1red1}$, $k_{Trx1red2}$ and $k_{Txl1red}$ using the quantitative data sets for the oxidation of Tpx1, Trx1 and Pap1. All other parameter values were set to those used for the model of Tpx1 and Trx1 oxidation (Table 4.5) and $k_{Pap1red}$ and k_{Pap1ox} were set to 0.01 and 0.04 $\mu M^{-1}\ s^{-1}$ respectively (Table 4.8). Using this set of rate constants (Table 4.9), the model was used to simulate the changes in Pap1-ox in response to 100, 200 and 500 µM H_2O_2 (Figure 4.30). Plotting the simulation data against the experimental data for the concentration of Pap1-ox revealed that the model was still unable to simulate the decrease in Pap1-ox 1800 s (30 min) after exposure to 200 µM H_2O_2 (Figure 4.30B). However, the model did more accurately simulate the experimental data for changes in Pap1-ox levels in response to 500 µM H_2O_2 (Figure 4.30C). Specifically, in accordance with the experimental data, the computer model in which Pap1-ox is reduced by Txl1 predicted that Pap1 would return to being fully reduced at a much later time point than Pap1 model B (Pap1 is reduced by Trx1) (Figure 4.22, Figure 4.30C & D). This provides further evidence that Txl1 rather than Trx1 is responsible for the reduction of Pap1.

Table 4.8 Reaction equations and rate laws for the model of Pap1 reduction by Txl1

Reaction description	Reaction	Rate law
Formation of a Trx1-Trr1 complex	Trx1-ox + Trr1 -> Trx1-Trr1	$k_{Trx1red1}$[Trx1-ox][Trr1]
Dissociation of Trx1-Trr1 complex	Trx1-Trr1 -> Trx1-red + Trr1	$k_{Trx1red2}$[Trx1-Trr1]
Oxidation of Pap1 by Tpx1-SOH	Pap1-red + Tpx1-SOH -> Pap1-ox + Tpx1-SH	k_{Pap1ox} [Pap1-red][Tpx1-SOH]
Reduction of Pap1-ox by Txl1-red	Pap1-ox + Txl1-red -> Pap1-red + Txl1-ox	$k_{Pap1red}$ [Pap1-ox][Txl1-red]
Reduction of Txl1-ox by Trr1	Txl1-ox + Trr1 -> Txl1-red + Trr1	$k_{Txl1red}$ [Txl1-ox][Trr1]

Table 4.8: Reaction equations and rate laws used for the computer model of Pap1 reduction by Txl1

The table displays the reaction equations and the rate laws used for the computer model of Pap1 reduction by Txl1. These reactions were added to the model of Tpx1 and Trx1 oxidation (Table 4.5). A description of each reaction is displayed in the left hand column.

Table 4.9 Parameter values used in the computer model of Pap1 reduction by Txl1

Species	Initial Value	*ref*
Pap1-red	0.0245 µM	Marguerat et al, 2012
Pap1-ox	0 µM	NA
Trr1	0.9 µM	Marguerat et al, 2012
Trx1-Trr1	0 µM	NA
Txl1-red	0.163 µM	Marguerat et al, 2012
Txl1-ox	0 µM	NA
k_{Pap1ox}	0.04 μM^{-1} s^{-1}	see 4.4.2
$k_{Pap1red}$	0.01 μM^{-1} s^{-1}	see 4.4.2
$k_{Txl1red}$	0.0008 μM^{-1} s^{-1}	parameter estimation
$k_{Trx1red1}$	1.3 μM^{-1} s^{-1}	parameter estimation
$k_{Trx1red2}$	3.8 s^{-1}	parameter estimation

Table 4.9: Parameter and rate laws used for the computer model of Pap1 reduction by Txl1

The table displays the initial parameter values used for the computer model of Pap1 reduction by Txl1. These values were either calculated using data from the literature (Marguerat et al, 2012) (see 2.2.2) or estimated using parameter estimation.

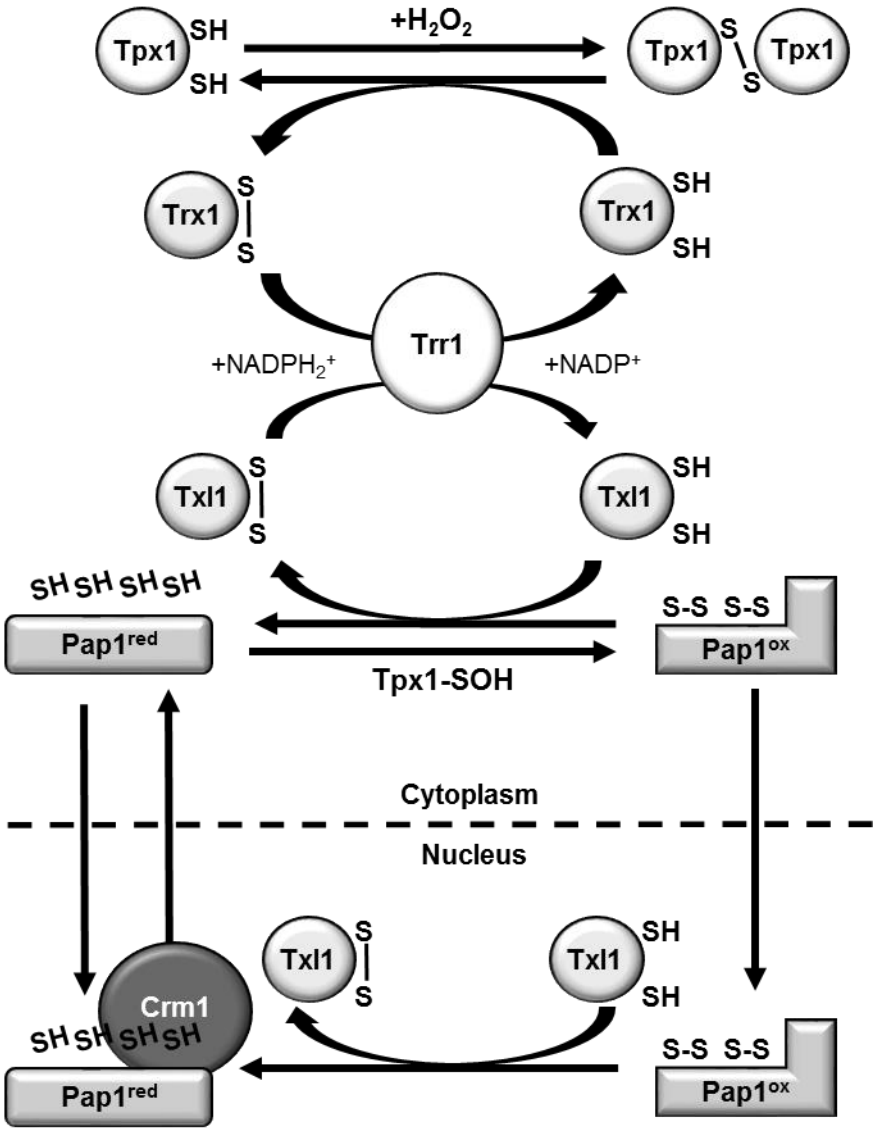

Figure 4.29: Proposed mechanism for the regulation of Pap1 by Tpx1 and the thioredoxin system.

Diagram representing the proposed mechanism of Pap1 regulation by the thioredoxin system based on the evidence described in chapter 4. Pap1 is oxidised by Tpx1-SOH which results in the nuclear accumulation of Pap1 due to the inhibition of Crm1 mediated nuclear export. Oxidised Pap1 is reduced by Txl1 resulting in Pap1 re-entering the cytoplasm due to the action of Crm1. Trx1 is oxidised in response to H_2O_2 due to the Trx1 mediated reduction of Tpx1 disulphides. Oxidised Trx1 competes with oxidised Txl1 for the same pool of Trr1.

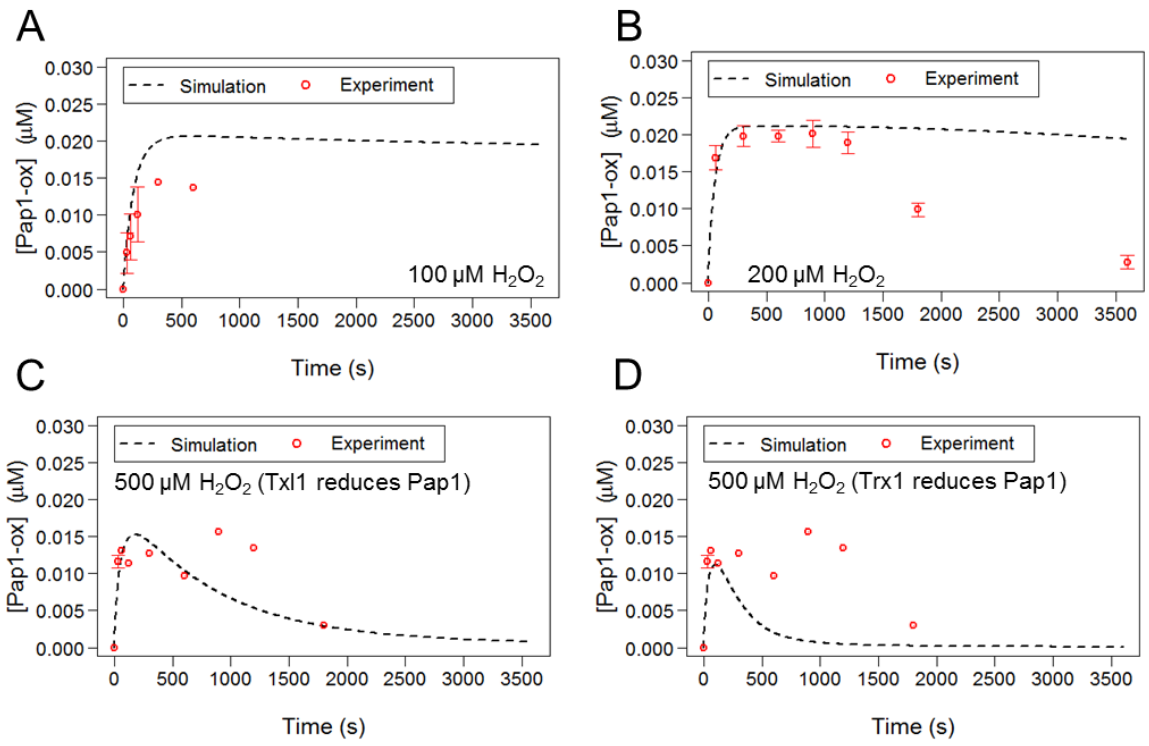

Figure 4.30: The reduction of oxidised Pap1 by Txl1 is better able to simulate the experimentally observed oxidation of Pap1 oxidation after a 0 – 3600 seconds exposure to 500 µM H_2O_2.

The computer model of Pap1 reduction by Txl1 was used to simulate changes in the concentration of oxidised Pap1 (Pap1-ox) 0 – 3600 seconds after exposure to (A) 100 µM, (B) 200 µM and (C) 500 µM. The experimental data for the concentration of Pap1-ox (red circles) was plotted on the same axis as the simulation data (black dashed line). Error bars represent the standard deviation of repeated measurements (0 µM n = 9, 100 µM n = 3, 200 µM, n = 3 and 500 µM n = 3). Data points without error bars indicate that no repeat measurements were made. (D) The simulation data for a 0 – 3600 seconds exposure to 500 µM using Pap1 model B (Pap1 is reduced by Trx1) (Table 4.6, Figure 4.22, Figure 4.23) is also displayed.

4.6 The effect of mutations to the thioredoxin system on Pap1 oxidation

The computer model of Pap1 oxidation by Tpx1 and subsequent reduction by Txl1 was still unable to accurately simulate the experimentally observed oxidation of Pap1. This suggests that the oxidation and reduction of Pap1 is influenced by factors not represented in the computer model. To gain more insight into the role of Tpx1 and the thioredoxin system in the regulation of Pap1, Pap1 oxidation was measured in *S. pombe* mutant strains engineered with genetic perturbations to components of the thioredoxin system.

4.6.1 Trx1 and Txl1 are required to maintain Pap1 in a soluble and regulatable state

The H_2O_2 induced oxidation of Pap1 was almost completely inhibited in Δ*trx1*Δ*txl1* cells (Figure 4.31A). Furthermore, repeat experiments indicated that the amount of oxidised Pap1 in unstressed Δ*trx1*Δ*txl1* cells varied between experiments (compare Figure 4.31A and C). In one experiment very little oxidised Pap1 was detected before and after exposure to H_2O_2 in Δ*trx1*Δ*txl1* cells (Figure 4.31A), whilst in another experiment 50% of Pap1 was oxidised in the same cells (Figure 4.31C). This result indicates that Δ*trx1*Δ*txl1* cells contain a pool of reduced Pap1 this is insensitive to H_2O_2. Moreover, although Pap1 is constitutively nuclear in Δ*trx1*Δ*txl1* cells, Pap1 dependent gene expression was not fully activated and Pap1 mRNA levels were increased (data not shown). This suggests that Pap1 is not fully functional in Δ*trx1*Δ*txl1* cells. Pap1 was constitutively oxidised in Δ*trr1* cells, independent from H_2O_2 concentration (Figure 4.31B). Interestingly, this constitutive oxidation was independent from Tpx1 since Pap1 was also constitutively oxidised in Δ*trr1*Δ*tpx1* cells (Figure 4.31B). These findings demonstrate that Pap1 can be oxidised independently of Tpx1 and H_2O_2 in cells lacking Trr1. Pap1 was only partially oxidised in Δ*trr1*Δ*trx1*Δ*txl1* cells, indicating that Trx1 and Txl1 are required for the complete oxidation of Pap1 in Δ*trr1* cells (Figure 4.31C). This suggests that Trx1 and/or Txl1 have another role in the regulation of Pap1 oxidation. Thioredoxins can also act as chaperones maintaining oxidation sensitive proteins in a reduced and folded state (Durigon et al., 2012). Hence, the solubility of Pap1 was measured in Δ*trx1*Δ*txl1* cells. Western blot analysis of soluble and whole cell lysates revealed that, despite

being detected at similar levels to wild-type in whole cell lysates, Pap1 was not detected in the soluble fractions of lysates from Δ*trx1*Δ*txl1* cells (Figure 4.32). Taken together these data suggest Δ*trx1*Δ*txl1* cells contain a pool of insoluble Pap1 that is resistant to oxidation.

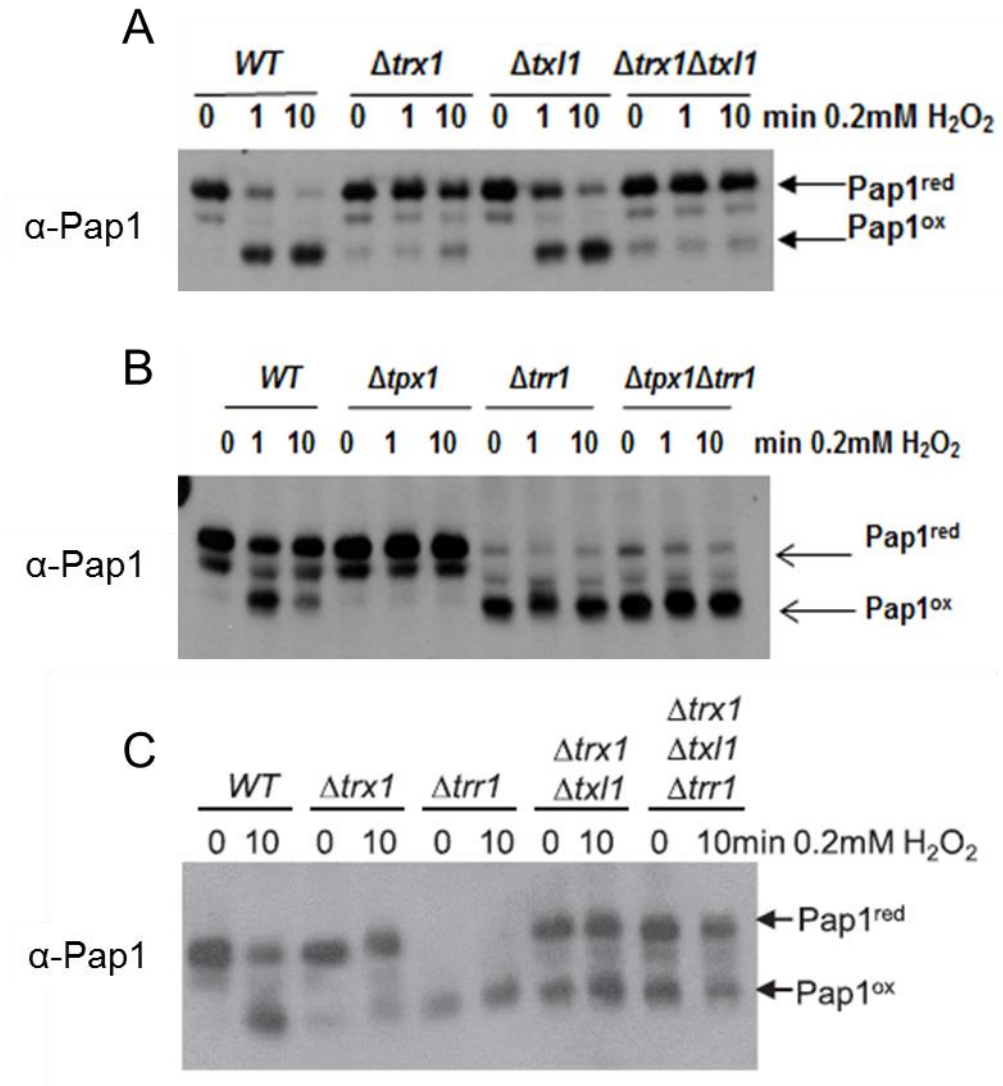

Figure 4.31: Effects of thioredoxin system mutations on Pap1 oxidation before and after 10 min exposure to 200 µM H_2O_2.

Western blot analysis, using α-Pap1 antibodies, of IAA-treated protein extracts from wild-type and mutant cells before and after a 10 min exposure to 200 µM H_2O_2. The mutant strains tested were (B) Δ*tpx1*, (A & C) Δ*trx1*, (A) Δ*txl1*, (A & C) Δ*txl1*Δ*trx1*, (B & C) Δ*trr1*, (B) Δ*tpx1*Δ*trr1* and (C) Δ*txl1*Δ*trx1*Δ*trr1* cells. (Data provided by Dr Alison M Day and Dr Jonathon Brown.)

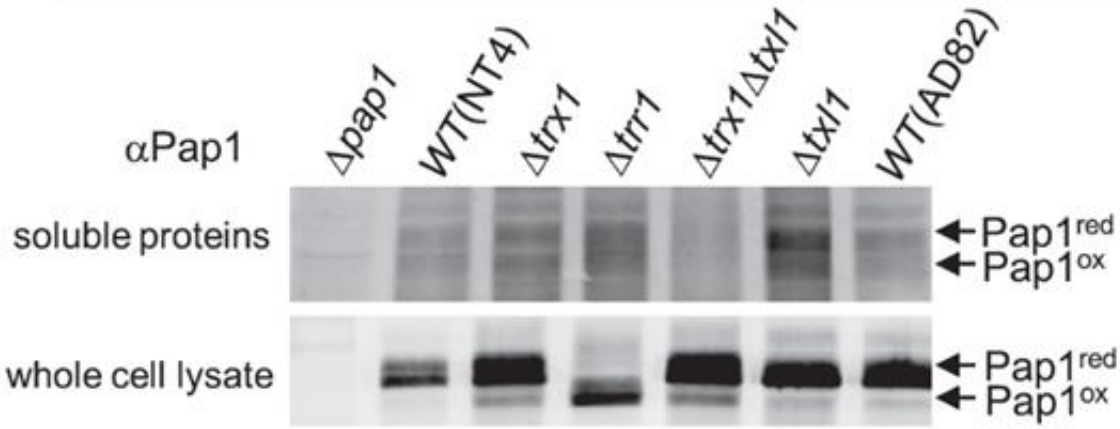

Figure 4.32: Pap1 is insoluble in Δ*txl1*Δ*trx1* cells.

Western blot analysis, using α-Pap1 antibodies, of NEM-treated protein extracts from non-stressed wild-type (NT4 & AD82) and mutant cells (Δ*trx1* (EV68), Δ*txl1*Δ*trx1* (AD140), Δ*trr1* (AD81), Δ*txl1* (EV75)). Proteins were extracted using either lysis-buffer (soluble proteins) or acid-lysis (whole cell lysates).

4.7 Discussion

It is well established that the thiol-peroxidases Gpx3 and Tsa1 act as H_2O_2-receptors and transducers for the H_2O_2-induced oxidation of the *S. cerevisiae* stress response transcription Yap1 (Okazaki et al., 2007, Delaunay et al., 2002). It is also well established the thioredoxin-peroxidase activity of Tpx1 is required for the H_2O_2-induced activation of the *S. pombe* Yap1 homolog Pap1 (Bozonet et al., 2005, Veal et al., 2004, Vivancos et al., 2005). However, at the commencement of these studies it was not clear if the role of Tpx1 in the activation of Pap1 is as a H_2O_2-receptor/transducer or to inhibit the reduction of Pap1 by Thioredoxin or an alternative mechanism.

A quantitative data set representing the changes in the availability of Trx1-red in response to a range of H_2O_2 was used, as well as the data for Tpx1 oxidation collected in chapter 3, to build a computer model representing the oxidation of Tpx1 and Trx1. This model accurately simulated the oxidation of Tpx1 and was also reasonably able simulate the changes in the availability of reduced Trx1 in response to H_2O_2 (Figure 4.13). Since the experimental measurements used to create the quantitative data set for Trx1-red availability were only performed once, it could be argued this it is difficult to make a robust assessment of the accuracy of the model in simulating Trx1 oxidation. However, the model was clearly able to simulate the experimental observation that Tpx1 hyperoxidation would increase the availability of reduced Trx1 (Figure 4.13). This particular relationship between Tpx1 and Trx1 is well-established based on published data (Day et al., 2012). Thus, since the model was able to simulate this well-established relationship between Trx1 and Tpx1 the model can be said to be an accurate representation of Trx1 and Tpx1 oxidation. It is unlikely that re-parameterising the model using more data would dramatically impact this specific behaviour of the model.

This model of Tpx1 and Trx1 oxidation was adapted to create three models each representing an alternative mechanism for the oxidation of Pap1. One of these models assumed that Pap1 is oxidised directly by H_2O_2 (Figure 4.20), a mechanism which is well established for the bacterial stress response transcription factor OxyR (for review see (Storz and Tartaglia, 1992). However, this model was unable to simulate the experimental data for the early oxidation

of Pap1 (Figure 2.21). In particular, this model predicted that increasing concentration of extracellular H_2O_2 would always result in the increased oxidation of Pap1 (Figure 2.21), despite the increased availability of Trx1-red. This model therefore suggested that direct oxidation of Pap1 by H_2O_2 and subsequent reduction by Trx1 are unlikely to be the mechanisms regulating Pap1 oxidation.

A computer model which assumed that Pap1 behaves as a disulphide reductase, a mechanism that has been proposed in a recent publication (Calvo et al, 2014), was better able to simulate the experimentally observed early oxidation of Pap1 (Figure 4.24 & 4.25). However, this model incorrectly predicted that the concentration of Pap1-ox would peak after treatment with 100 µM H_2O_2 rather than 200 µM H_2O_2 as was indicated by the experimental data (Figure 4.25). This result therefore suggests that the Pap1-mediated reduction of Tpx1 disulphides is not the main mechanism involved in H_2O_2-induced activation of Pap1.

Instead, of the three Pap1 regulation models tested, the model in which Pap1 is directly oxidised by Tpx1-SOH was best able to simulate the experimentally observed features of the early oxidation of Pap1 (Figure 4.22 & 4.23). This suggests that direct oxidation of Pap1 by Tpx1-SOH could be the biological mechanism of H_2O_2-induced Pap1 oxidation. Even so, this model was unable to simulate the experimentally observed changes in Pap1-ox concentration over extended periods of time (Figure 4.26). This suggested that although direct oxidation of Pap1 by Tpx1-SOH and subsequent reduction by Trx1 could be responsible for the activation of Pap1 shortly after H_2O_2 exposure, the oxidation and reduction of Pap1 is likely to be influenced by other biochemical processes not represented in this model.

Indeed, the detection of a complex between Txl1 and Pap1 in $Tpx1^{C169S}$ cells (Figure 4.27A & B), and the experimental observation that deletion of Txl1 restores the H_2O_2-induced oxidation of Pap1 in these cells (Figure 4.27B), is a strong indication that Txl1, and not Trx1, is responsible for the reduction of oxidised Pap1. Preliminary findings of a computer model in which Pap1 is oxidised by Tpx1-SOH and reduced by Txl1 suggested that this model was better able to simulate the extended changes in Pap1-ox after exposure to 500 µM H_2O_2 (Figure 4.30) further indicating that Pap1-ox is reduced by Txl1 *in vivo*. However, this model was still unable to accurately simulate all of the experimentally

observed features of Pap1 oxidation. This suggests that the *in vivo* oxidation of Pap1 is also influenced by biochemical factors not represented in this computer model. For example, the role Trx1 and/or Txl1 in maintaining the solubility of Pap1 was not taken into account in any of the computer models tested (Figure 4.33). The influence of the chaperone function of Trx1/Txl1 in maintaining Pap1 solubility could be included in a future model.

Another important aspect of the *S. pombe* response to H_2O_2 that has not been represented in any of these models are H_2O_2-induced changes in gene expression. Indeed it is well established that, in response to H_2O_2, *S. pombe* cells undergo alterations in the intracellular concentrations of gene transcripts and protein expression levels (Chen et al., 2008, Lackner et al., 2012). Although H_2O_2-induced gene expression change will probably have little effect on the oxidation of Pap1, Tpx1, Trx1 and Txl1 shortly after H_2O_2 exposure, it is highly probable that gene expression change will influence the oxidation of these proteins at later time points. Furthermore, this model does not take into account the levels of Srx1, which can reduce hyperoxidised Tpx1 and is induced in response to H_2O_2 (Chen et al., 2008, Bozonet et al., 2005, Vivancos et al., 2005). A computer model built to take into account H_2O_2-induced gene expression is likely to provide a deeper understanding of how H_2O_2-induced gene expression change could influence the oxidation of Pap1 over a longer time course. It remains possible that inclusion of H_2O_2-induced gene expression could fully explain all of the experimentally observed features of Pap1 oxidation.

However, based on the results of the computer models of Pap1 regulation, and the experimental evidence that Txl1 is a substrate for Trr1 (Figure 4.28), the work presented in this chapter suggests that the most likely explanation for the activation of Pap1 in response to H_2O_2 is that Pap1 is directly oxidised by Tpx1-SOH and reduced by Txl1 (Figure 4.29). Furthermore, the experimental observation that Txl1 is present in the nucleus and cytoplasm, whereas Trx1 is a cytoplasmic protein, make reduction of Pap1 by Txl1 a more likely mechanism (Matsuyama et al., 2006). The experimental observation that Pap1 is oxidised in response to H_2O_2 to a lesser extent in Δ*trx1* cells could be explained if Trx1 and Txl1 directly compete for the same pool of Trr1. This would mean that the H_2O_2-induced oxidation of Trx1, due to the Trx1-mediated reduction of Tpx1 disulphides, would inhibit the reduction of Txl1 by Trr1 due to direct competition

between Trx1 and Txl1 for Trr1. This inhibition of Txl1 reduction would result in accumulation of oxidised Txl1 and therefore inhibit the Txl1-mediated reduction of oxidised Pap1. Deletion of Trx1 would release the inhibition of Trr1-mediated Txl1 reduction, this would increase the availability of reduced Txl1 and therefore inhibit the H_2O_2-induced oxidation of Pap1.

Finally, it is important to note that not all of the experimental data presented in this chapter is consistent with this proposed model of Pap1 regulation (Figure 4.33). Although the experimental observation that Pap1 is constitutively oxidised in Δ*trr1* cells could be explained by this model, the finding that Pap1 is also constitutively oxidised in Δ*tpx1*Δ*trr1* cells suggests that Pap1 regulation is oxidised via a Tpx1-independent mechanism in these cells (Figure 4.30). It has been argued that in Δ*trr1* cells the redox balance of the cell is so unregulated that Pap1 oxidation in these cells does not represent Pap1 regulation in healthy wild-type cells (Garcia-Santamarina et al., 2013). Alternatively, the constitutive activation of Pap1 in these cells means that expression of other components of this model are very different from wild-type cells. For example, Δ*trr1* cells contain more Trx1 than wild-type cells (Brown et al., 2013). This further complicates the interpretation of the Pap1 oxidation measurements collected using Δ*trr1* cells. Similarly, the finding that Pap1 is in an insoluble H_2O_2-resistant reduced state in Δ*trx1*Δ*txl1* cells (Figure 4.32) also highlights the complications of interpreting experiments performed in different genetic mutants where gene-deletion often influences multiple biological processes. An advantage of computer modelling approaches is their ability to infer information about the structure of a system based on the dynamics of wild-type time course data, a useful complement to potentially misleading experiments using mutant strains.

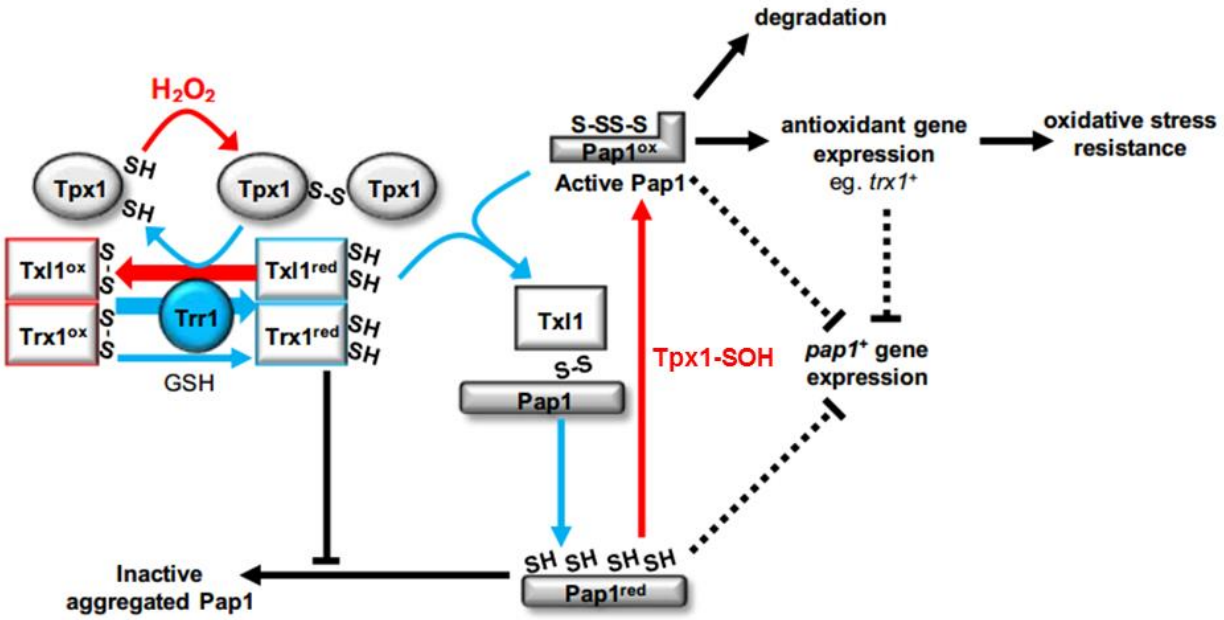

Figure 4.33: Extended model depicting how the H_2O_2-dependent regulation of Trx1 and Txl1 by the Tpx1, contributes to the regulation of Pap1 activity and oxidative stress resistance.

Tpx1 disulphides are rapidly generated in response to H_2O_2. The reduction of these Tpx1 disulphides by thioredoxin family proteins (Trx1 and Txl1) overcomes the capacity of thioredoxin reductase (Trr1) to regenerate reduced Trx1 and Txl1. Hence, Trx1 and Txl1 become oxidized. This is important to prevent Txl1 from directly reducing active, oxidized Pap1. Trx1 and/or Txl1 are important to maintain Pap1 in a soluble form that can be activated by H_2O_2. Accordingly, the elevated *pap1*$^+$ mRNA levels in Δ*trx1*Δ*txl1* mutant cells suggest the existence of a feedback mechanism/s (dashed lines) monitoring the levels of soluble Pap1 and/or thioredoxin that inhibits *pap1*$^+$ gene expression. As indicated (Tpx1-SOH), our computer modelling approach suggests that Tpx1-SOH most likely initiates the oxidation of Pap1. Oxidized Pap1 accumulates in the nucleus where it activates the expression of antioxidant genes and is reduced by Txl1 and/or targeted for degradation by the proteasome.

Chapter 5. Investigating the effects of H_2O_2- and quiescence-induced changes in gene expression on cell responses to H_2O_2

5.1 Introduction

In chapters 3 and 4 computational models were constructed to examine how the oxidation of peroxiredoxins and thioredoxin system components influences cells' responses to H_2O_2. In chapter 1 the principle of the oxidative stress response (OSR) was discussed (see 1.4). As part of this response, cells exposed to an oxidant, such as H_2O_2, will increase the expression of antioxidant and repair genes (see section 1.4). Activation of the OSR in bacteria and yeast species has been demonstrated to improve the resistance of the organism to a subsequent exposure to H_2O_2 (Christman et al., 1985, Demple and Halbrook, 1983, Quinn et al., 2002). However, how the OSR increases the H_2O_2-resistance of an organism or affects future responses to H_2O_2 is not fully understood. For example, it is not clear whether increased antioxidant enzyme levels protect cellular components from H_2O_2-induced damage by reducing the levels of H_2O_2 in the environment more rapidly as well as by preventing increases in the intracellular H_2O_2 concentration. It is also unclear how OSR-induced increases in antioxidant enzyme levels influence the sensitivity of cell-signalling pathways to H_2O_2 and whether this contributes to the protective effect of these responses.

In *S. pombe* it is well established that exposure to H_2O_2 causes the increased expression of a multitude of genes many of which encode detoxification enzymes. These include Trx1, Trr1, Tpx1 and Srx1 (Chen et al., 2003, Chen et al, 2008, Quinn et al., 2002, Lackner et al., 2012). As Tpx1 is required for the H_2O_2-induced activation of Pap1 and Sty1 (Bozonet et al., 2005, Veal et al., 2004), as well as increasing the cells' ability to remove peroxide, H_2O_2-induced gene expression changes may have more complex effects on the cells' ability to initiate future responses to H_2O_2.

Genome-wide quantification of gene expression in exponentially growing and quiescent *S. pombe* cells has indicated that many proteins show markedly different levels of expression in stationary phase cells (Marguerat et al., 2012). This also includes the expression of antioxidant genes such as *tpx1*$^+$, *trr1*$^+$ and

ctt1^{+}. It is therefore likely that the ability of cells to remove H_2O_2 from the environment and resist increases in intracellular H_2O_2 concentration will also be altered in stationary phase cells compared to exponentially growing cells. Furthermore, these changes could potentially affect the sensitivity of Pap1 and Sty1 to H_2O_2-dependent activation.

The aim of this chapter was to investigate the potential effects of H_2O_2- and quiescence-induced gene expression on the ability of cells to (i) buffer intracellular H_2O_2, (ii) remove H_2O_2 from the environment and (iii) on the sensitivity of signalling pathways (Pap1 and Sty1) to H_2O_2-dependent activation.

5.2 Building a simple computer model representing H_2O_2 metabolism by multiple peroxidase processes

In chapter 3 a simple computer model was used to demonstrate how a Michaelis-Menten peroxidase process would inhibit changes in intracellular H_2O_2 in response to low extracellular doses of H_2O_2 (Figure 3.6). This model demonstrated that the concentration of extracellular H_2O_2 required to cause a change in the intracellular H_2O_2 concentration was dependent on the maximum rate of this peroxidase process (V_{max}), its affinity for H_2O_2 (K_m) and the permeability of the cell membrane/wall ($k_{H2O2perm}$) (Figure 3.7). However, this model only contained one peroxidase process. Cells actually contain multiple peroxidase processes, each with different K_m and V_{max} values all of which will influence the ability of the cell to buffer intracellular increases in H_2O_2.

A preliminary model, discussed in chapter 4, demonstrated how a system of redox couples, such as the thiol-proteome, could inhibit increases in intracellular H_2O_2 (Figure 4.1 & 4.2). In this model, the concentration of extracellular H_2O_2 required to cause an increase in the intracellular H_2O_2 concentration was dependent on the rate constant for the reduction of Trx1 by Trr1 (Figure 4.2). This relationship between the activity of Trr1 and the inhibition of increases in the intracellular H_2O_2 concentration is analogous to changing the V_{max} of the Michaelis-Menten peroxidase process discussed in chapter 3 that acts to buffer low levels of H_2O_2 (Figure 3.5 & 3.6). This demonstrates that the effect of changes in Trr1 expression on the peroxidase capacity of the thiol-proteome can be

effectively modelled by changing the V_{max} in a Michaelis-Menten peroxidase reaction. This is in agreement with a published mathematical analysis of a single-cycle redoxin system which indicated that the apparent k_{cat} of a redox couple is proportional to the rate of Trx reduction (Pillay et al., 2009).

Based on this principle a new computer model was built representing the metabolism of H_2O_2 due to three different peroxidase processes (Table 5.1 & 5.2, Figure 5.1). We used the different parameter sets for this model, each representing either log-phase, H_2O_2-induced or quiescence-induced gene expression. The parameters used to represent log-phase gene expression were as follows. H_2O_2 metabolism by the thiol-proteome was represented using a Michaelis-Menten peroxidase reaction with a V_{max} of 59 µM s^{-1} ($V_{max\_thiol\_pro}$) and a $K_{m\_thiol\_pro}$ of 0.007 µM, as was estimated in chapter 3 (Table 3.7, $V_{max\_H2O2\_metab}$, $K_{m\_H2O2\_metab}$). H_2O_2 metabolism due to glutathione (GSH) and GSH dependent processes was represented by a Michaelis-Menten peroxidase reaction (Table 5.1). The V_{max} of this reaction was assumed to be entirely dependent on the rate of GSSG reduction by the *S. pombe* glutathione-reductase, Pgr1. As discussed in chapter 3 (see 3.6) the k_{cat} for the *S. cerevisiae* glutathione reductase Glr1 is 900 s^{-1} (Yu and Zhou, 2007) and the intracellular concentration of *S. pombe* Pgr1 is around 0.3 µM (Marguerat et al., 2012). The V_{max} for the reaction representing H_2O_2-metabolism by GSH dependent processes was therefore estimated to be equal to 270 µM s^{-1} (k_{cat} x [Pgr1] = 900 s^{-1} x 0.3 µM = 270 µM s^{-1}). An estimate of the K_m for this reaction will be difficult to calculate, since it will be inversely proportional to all of the processes which contribute to the oxidation of GSH (Pillay et al., 2009), and was therefore arbitrarily set to 10 µM (Table 5.2). H_2O_2 metabolism due to catalase was also modelled using Michaelis-Menten kinetics with K_m and k_{cat} values of 38 mM and 54,000 s^{-1} respectively (Switala and Loewen, 2002).

In order to select a parameter set representing H_2O_2-induced gene expression and quiescence induced gene expression, we used data from Lackner et al (2012) and Marguerat et al, (2012) respectively. The Lackner (2012) data demonstrates that Trr1 protein levels increase 2.9 fold following a 3 hour exposure to 200 µM H_2O_2 (Lackner et al., 2012). Hence, to represent the effect that H_2O_2-induced increase in Trr1 levels will have on thiol-proteome dependent H_2O_2 metabolism, the rate constant $V_{max\_thiol\_pro}$ was multiplied by 2.9 (59 µM s^{-1}

x 2.9 = 168 µM s^{-1}). In contrast, according to Marguerat et al (2012), the amount of Trr1 protein in quiescent cells is around half (~ 0.46 times) that of exponentially growing cells. Therefore, in the model for quiescent cells, the value for $V_{max\_thiol\_pro}$ was decreased to 27 µM s^{-1} (Table 5.2).

Table 5.1 Reaction equations and rate laws for the computer model of H_2O_2 metabolism

Reaction description	Reaction equation	Rate law
H_2O_2 influx	$H_2O_2(ex) \rightarrow H_2O_2(int)$	$k_{H2O2\_perm} \cdot Vol_{ex} \cdot [H_2O_2]_{ex}$
H_2O_2 efflux	$H_2O_2(int) \rightarrow H_2O_2(ex)$	$k_{H2O2\_perm} \cdot (Vol_{ex}/Vol_{int}) \cdot [H_2O_2]_{int} \cdot Vol_{int}$
Thiol-proteome dependent H_2O_2 metabolism	$H_2O_2(int) \rightarrow$	$V_{max\_thiol\_pro} \cdot [H_2O_2]_{int}/K_{m\_thiol\_prob} + [H_2O_2]_{int}$
Glutathion-dependent H_2O_2 metabolism	$H_2O_2(int) \rightarrow$	$k_{cat\_GSH\_metab} \cdot [Pgr1] \cdot [H_2O_2]_{int}/K_{m\_GSH\_metab} + [H_2O_2]_{int}$
Catalase-dependent H_2O_2 metabolism	$H_2O_2(int) \rightarrow$	$k_{cat\_ctt1} \cdot [Ctt1] \cdot [H_2O_2]_{int}/K_{m\_ctt1} + [H_2O_2]_{int}$

Table 5.1: Reaction equations and rate laws used in the computer model of H_2O_2 metabolism by multiple peroxidase processes.

Table displays the reaction equations and rate laws used for the computer model of H_2O_2 metabolism by multiple peroxidase processes. A description of each reaction is displayed in the left hand column. The movement of H_2O_2 between the extracellular and intracellular environment (H_2O_2 influx & H_2O_2 efflux) was modelled using mass action kinetics. All of the H_2O_2 metabolism reactions were modelled using Michaelis-Menten kinetics.

Table 5.2 Parameters values used for the computer model of H_2O_2 metabolism

Parameter	Log-phase Value	H_2O_2-induced Value[1]	Quiescent Value[2]	Units	ref
$[H_2O_2]_{ex}$	0	0	0	µM	NA
$[H_2O_2]_{int}$	0	0	0	µM	NA
[Ctt1]	0.07	0.292	0.27	µM	Marguerat et al, 2012; Lackner et al, 2012
[Pgr1]	0.3	0.3	0.3	µM	Marguerat et al, 2012; Lackner et al, 2012
k_{H2O2_perm}	3.44×10^{-4}	3.44×10^{-4}	3.44×10^{-4}	$l^{-1}\ s^{-1}$	Parameter Estimation (see Table 3.7)
Vol_{ex}	0.05	0.05	0.05	l	Measured (see 2.6.2)
Vol_{int}	5.2×10^{-5}	5.2×10^{-5}	5.2×10^{-5}	l	Measured (see 2.6.2)
$V_{max\_thiol\_pro}$	59	168	27	µM s^{-1}	see Table 3.7 and section 5.2
$K_{m\_thiol\_pro}$	0.007	0.007	0.007	µM	see Table 3.7
$k_{cat\_GSH\_metab}$	900	900	900	s^{-1}	Yu and Zhou, 2007
$K_{m\_GSH\_metab}$	10	10	10	µM	Arbitrary
k_{cat_ctt1}	54,000	54,000	54,000	s^{-1}	Switala & Loewen, 2002
K_{m_ctt1}	38,000	38,000	38,000	µM	Switala & Loewen, 2002

[1] After a 3 hour exposure to 200 µM H_2O_2 (Lackner et al., 2012).
[2] After 24 hours nitrogen starvation (Marguerat et al, 2012).

Table 5.2: Parameters used for the computer model of H_2O_2 metabolism by multiple peroxidase processes.

Table displays the values used for each of the parameters used in the computer model of H_2O_2 metabolism by multiple peroxidase processes. The parameter values for [Ctt1] and $V_{max\_H2O2\_metab}$ used to represent H_2O_2 metabolism in H_2O_2-pretreated and stationary phase cells are also displayed. For details on how they were calculated see 5.2, 5.3 and 5.4.

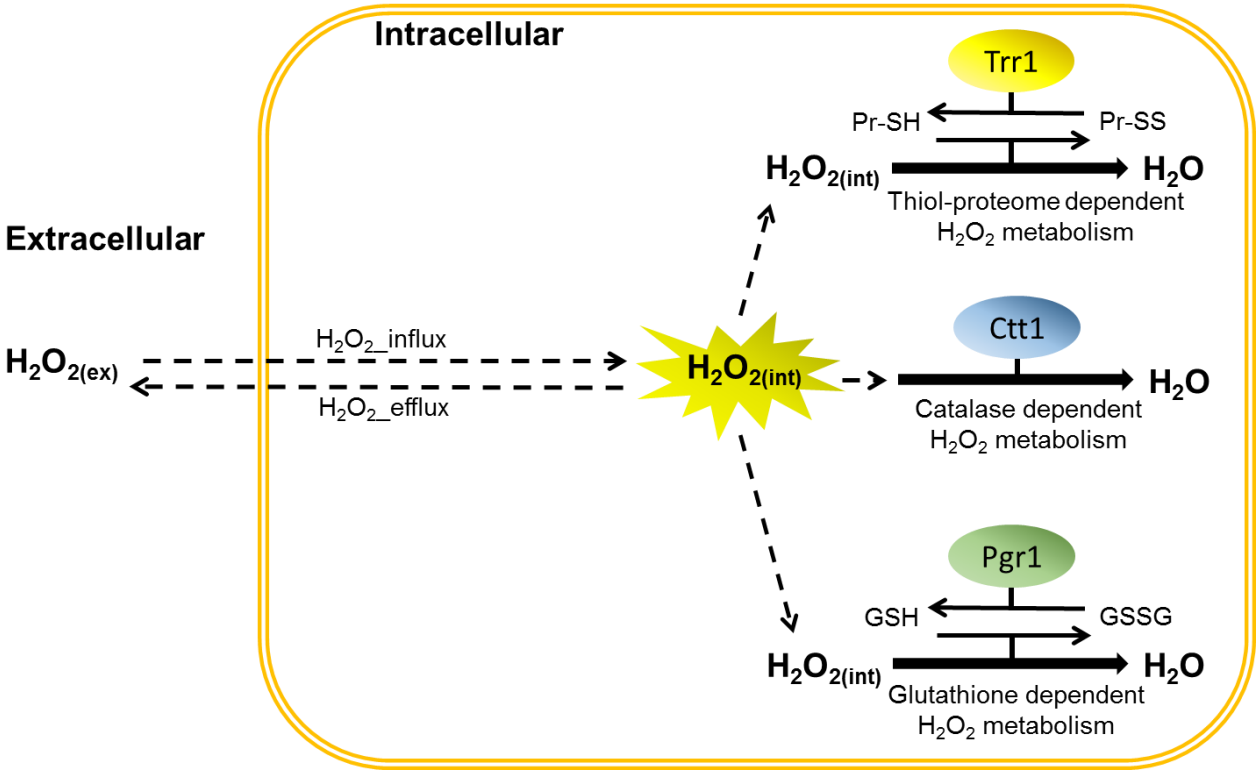

Figure 5.1: Diagram for the model of H_2O_2 metabolism by multiple peroxidase processes.

The diagram displays the compartments (Intracellular & Extracellular) and reactions used to model H2O2 metabolism by multiple peroxidase processes. The reactions H_2O_2_influx and H_2O_2_efflux represent the movement of H_2O_2 between the extracellular and intracellular space. The other three reactions represent H_2O_2 metabolism by the thiol-proteome, catalase and glutathione dependent processes.

5.3 Model predictions for the effect of gene expression change on the H_2O_2 buffering capacity of the cell

The model of H_2O_2 metabolism by multiple peroxidase processes was used to simulate the $[H_2O_2]_{int}$ after a 60 second exposure to 0 – 6 mM H_2O_2 (Figure 5.2). The model predicted that as $[H_2O_2]_{ex}$ is increased from 0 to ~200 µM there will be very little change in the intracellular H_2O_2 concentration (Figure 5.2). However treatment with $[H_2O_2]_{ex}$ between 200 – 800 µM will cause an increase in $[H_2O_2]_{int}$ (Figure 5.2). In the model, this increase in $[H_2O_2]_{int}$ is due to the saturation of the Trr1-mediated peroxidase process, which represents peroxide metabolism due to the thiol-proteome. This reaction becomes saturated at the lowest H_2O_2 concentrations because it has the lowest V_{max} and K_m value. The model predicted that H_2O_2-induced expression of Trr1 (3 hours 200 µM, (Lackner et al., 2012)) increases the ability of the thiol-proteome to inhibit increases in $[H_2O_2]_{int}$ such that a $[H_2O_2]_{ex}$ concentration of ~500 µM would be required to overcome this buffering capacity and cause an increase in $[H_2O_2]_{int}$ (Figure 5.2A). This suggests that H_2O_2-induced increases in Trr1 expression will increase the buffering capacity of the thiol-proteome making cells more resistant to increases in intracellular H_2O_2. In contrast the model predicted that, in quiescent *S. pombe* cells, where Trr1 protein levels are lower, a lower concentration of $[H_2O_2]_{ex}$ would be required to cause an increase in the intracellular H_2O_2 concentration (Figure 5.2B).

The model predicted that, in exponentially growing cells, exposure to extracellular H_2O_2 concentrations between ~200 – 800 µM causes only a modest increase in the intracellular H_2O_2 concentration (Figure 5.2C & D) compared with extracellular H_2O_2 concentrations greater than 800 µM which cause much sharper increases in intracellular H_2O_2 (Figure 5.2C - F). Our model predicts that the increase in the intracellular H_2O_2 concentration is only modest after exposure to ~200 – 800 µM H_2O_2 due to the effects of GSH-dependent H_2O_2 metabolism (Figure 5.2C). The model predicts that, exposure to an extracellular H_2O_2 concentration of 200 µM is sufficient to saturate the thiol-proteome and cause a rise in intracellular H_2O_2 (Figure 5.2A & B). However, this increase in intracellular H_2O_2 is small compared the increase predicted after 800 µM H_2O_2 treatment (Figure 5.2A & B). This sharp increase in the intracellular H_2O_2 concentration after treatment with 800 µM H_2O_2 is due to the saturation of the glutathione-dependent

peroxidases reaction (Figure 5.2A & B). No changes in H_2O_2- and quiescence-induced Pgr1 levels have been detected (Lackner et al., 2012). However, the model did predict that the extracellular H_2O_2 concentration required to saturate GSH-dependent peroxidase processes would be higher in H_2O_2-pretreated cells due to the effects of increased Trr1 expression (Figure 5.2C).

The model predicted that, catalase dependent H_2O_2-metabolism will be the only peroxidase process inhibiting increases in intracellular H_2O_2 concentration in cells exposed to extracellular H_2O_2 concentrations greater than 800 µM (Figure 5.2E & F). The high K_m of catalase for H_2O_2 (38,000 µM) means that catalase is not very effective at buffering low concentrations of intracellular H_2O_2. However, the model does predict that H_2O_2- and quiescence-induced increases in Ctt1 levels will cause a substantial decrease in the intracellular H_2O_2 concentration in cells exposed to high extracellular H_2O_2 concentrations (above 1,000 µM) (Figure 5.2E & F). This indicates that catalase can still have a substantial influence on the intracellular H_2O_2 concentration, despite its low affinity for H_2O_2. The model predicts that catalase dependent H_2O_2 metabolism will not become saturated even after treatment with H_2O_2 concentrations as high as 6000 µM (Figure 5.2E & F). This suggests that catalase is the last line of defence against H_2O_2 which continues to reduce the intracellular H_2O_2 concentration when all other peroxidase processes have become saturated.

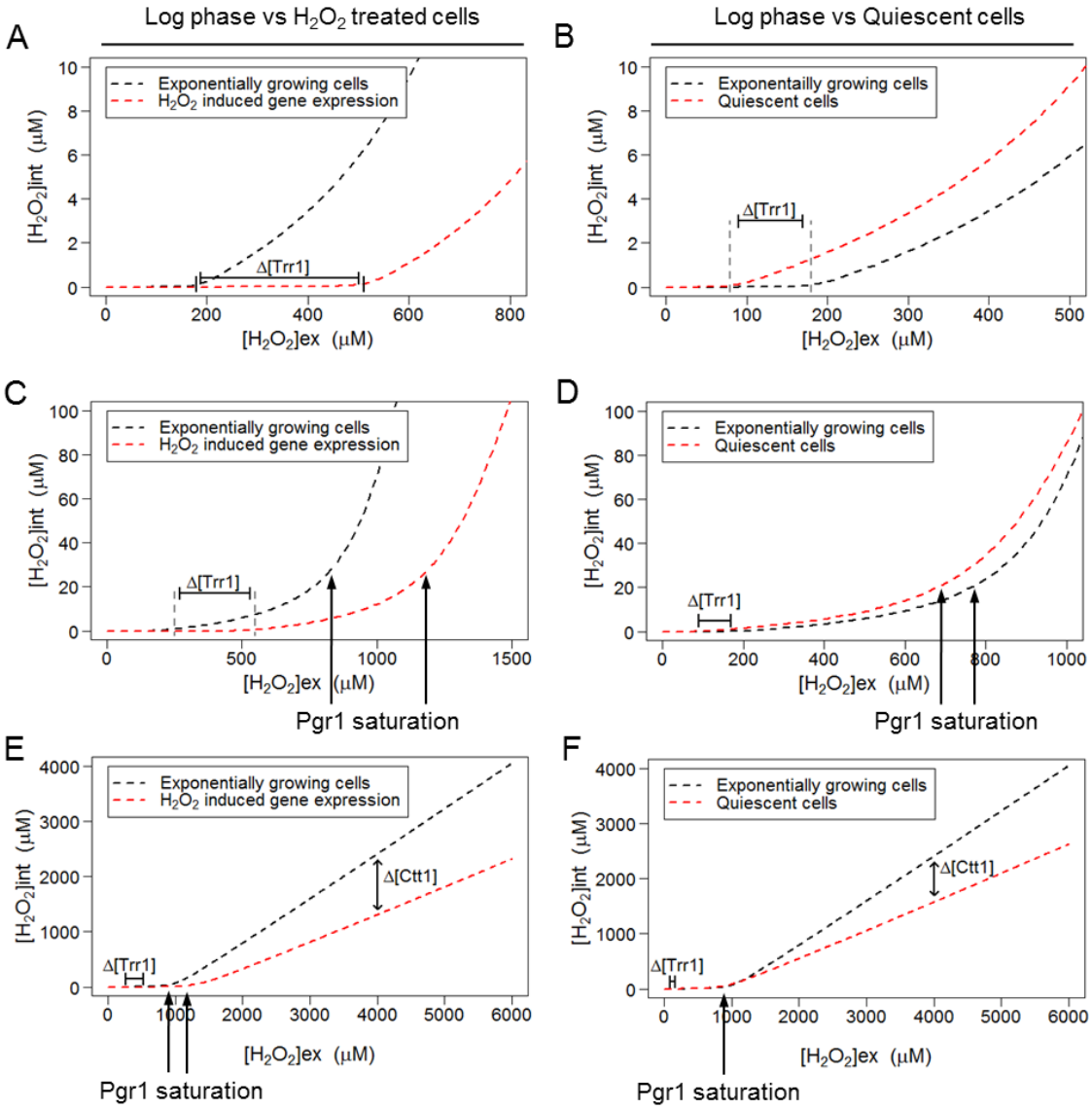

Figure 5.2: Model predictions for the effect of gene expression changes on intracellular H_2O_2 concentration.

The model of H_2O_2 metabolism by multiple peroxidase processes (Table 5.1 & 5.2) was used to predict the effect that increasing the extracellular H_2O_2 concentration ($[H_2O_2]_{ex}$) would have on the intracellular H_2O_2 concentration ($[H_2O_2]_{int}$) in non-stressed log-phase cells (A - F), cells pre-treated with 200 µM H_2O_2 for 3 hours (A - C) and quiescent cells (D - F) (indicated in legends). The predicted changes in H_2O_2 dynamics due to altered expression of Trr1 and ctt1 are indicated (Δ[Trr1] & Δ[Ctt1] respectively). The $[H_2O_2]_{int}$ when Pgr1 mediated H_2O_2 metabolism has become saturated is also indicated (Pgr1 saturation).

5.4 Predicting the effects of gene expression change on the removal of H_2O_2 from the extracellular environment

The computer model of H_2O_2 metabolism by multiple peroxidase processes was used to simulate the removal of 100 – 6000 µM H_2O_2 from the extracellular space (Figure 5.3). The simulations were performed using the parameter sets representing log-phase cells, H_2O_2-pretreated cells and quiescent cells (Figure 5.3). Interestingly, the model predicted that even without H_2O_2- and quiescence-induced gene expression changes, the removal of 100 – 1000 µM H_2O_2 from the extracellular space occurs quite rapidly, with changes in Trr1 and Ctt1 levels having little effect (Figure 5.3A - C). In contrast, the predicted effects of H_2O_2-induced gene expression on the intracellular H_2O_2 concentration were predicted to be quite substantial (Figure 5.2). This suggests that any increased H_2O_2 resistance caused by H_2O_2-induced gene expression is due to the ability of the cells to resist increases in the intracellular H_2O_2 concentration rather than decrease the time for which they are exposed to extracellular H_2O_2. However, the model did predict that both quiescence- and H_2O_2-induced gene expression would increase the rate at which 6000 µM H_2O_2 was removed from the extracellular space. This suggests that the levels of antioxidant enzymes in exponentially growing cells are sufficient to rapidly remove H_2O_2 from the extracellular space and only become saturated at very high concentrations of H_2O_2 (6000 µM). Nevertheless, our model indicates that the changes in Trr1 and particularly Ctt1 levels do allow quiescent and H_2O_2-pretreated cells to clear very high concentrations of H_2O_2 from the environment more effectively than untreated exponentially growing cells.

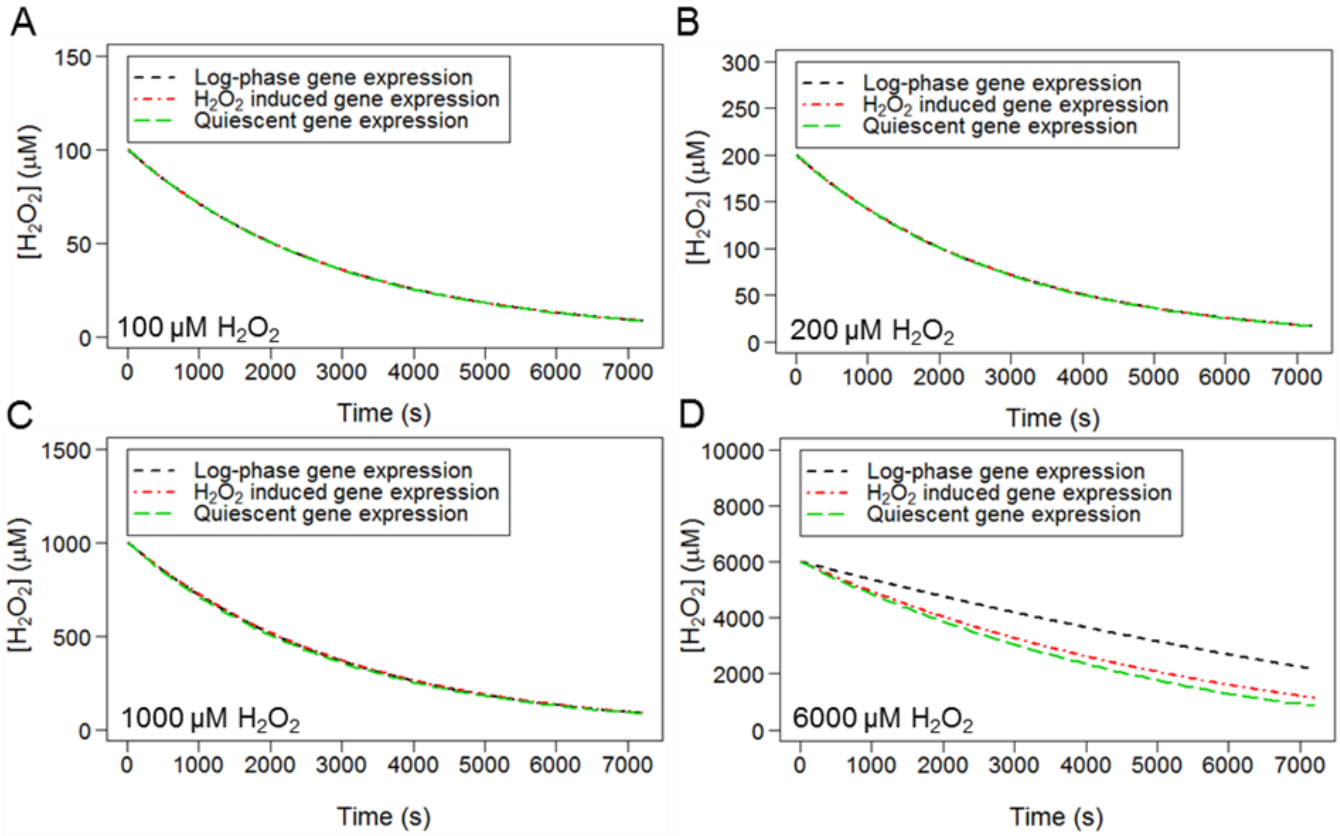

Figure 5.3: Model predictions for the effect of gene expression changes on the removal of H_2O_2 from the extracellular environment.

The model of H_2O_2 metabolism by multiple peroxidase processes (Table 5.1 & 5.2) was used to predict the removal of (A) 100 μM, (B) 200 μM, (C) 500 μM and (D) 1000 μM H_2O_2 from the extracellular environment. For each H_2O_2 concentration simulations were performed using parameters sets representing either normal log-phase gene expression (black), H_2O_2-induced gene expression (red) or quiescence-induced gene expression (green).

5.5 Examining whether H_2O_2-induced increases in Srx1 protein levels could contribute to cell responses to H_2O_2

Sulphiredoxin (Srx1) reduces hyperoxidised Prx (Prx-SOOH). The majority of organisms with hyperoxidation-sensitive Prx also contain Srx1 (see 1.3.4). However, intriguingly, the levels of Srx1 appear to be tightly regulated. For example, in *S. cerevisiae*, pre-stress levels of *SRX1* mRNA are very low but exposure to 400 µM H_2O_2 causes a very large increase in *SRX1* mRNA levels (Biteau et al., 2003). Moreover, there is additional post-transcriptional regulation of Srx1 protein levels through a PKA-dependent block in *SRX1* mRNA translation (Molin et al 2011). In *S. pombe*, H_2O_2 has also been demonstrated to dramatically increase the levels of *srx1*$^+$ mRNA, which appear to be extremely low under normal growth conditions (Chen et al., 2003; Bozonet et al., 2005). However, the levels of Srx1 protein in exponentially growing cells or following exposure to H_2O_2 have not been determined previously. Genome wide quantification of the *S. pombe* proteome detected very low levels of Srx1 protein (less than 0.5 copies per cell) in exponentially growing or quiescent cells (Marguerat et al., 2012). Moreover, a similar genome-wide relative quantification of H_2O_2-induced gene expression detected no significant increase in Srx1 (Lackner et al., 2012). This is surprising considering that treatment with H_2O_2 causes a 20 – 30 fold increase in *srx1*$^+$ mRNA levels and suggested that, as in *S. cerevisiae*, there may be some post-transcriptional regulation of Srx1 protein levels (Chen et al., 2003; Bozonet et al., 2005). In order to determine *S. pombe* Srx1 protein levels in exponentially growing cells, and in response to H_2O_2, an *S. pombe* strain was made expressing N-terminally tagged FLAG-Srx1 from its natural locus. Dilution assays showed that *FLAG-srx1* cells grow with a similar colony number and colony size to wild-type cells when grown on YE5S (Figure 5.4). This indicates that the FLAG-epitope tag does not affect normal cell growth. Furthermore, whereas Δ*srx1* cells were highly sensitive to H_2O_2, *FLAG-srx1* cells had wild-type levels of H_2O_2 resistance (Figure 5.4). This suggests that the FLAG tag has not affected the normal function of Srx1.

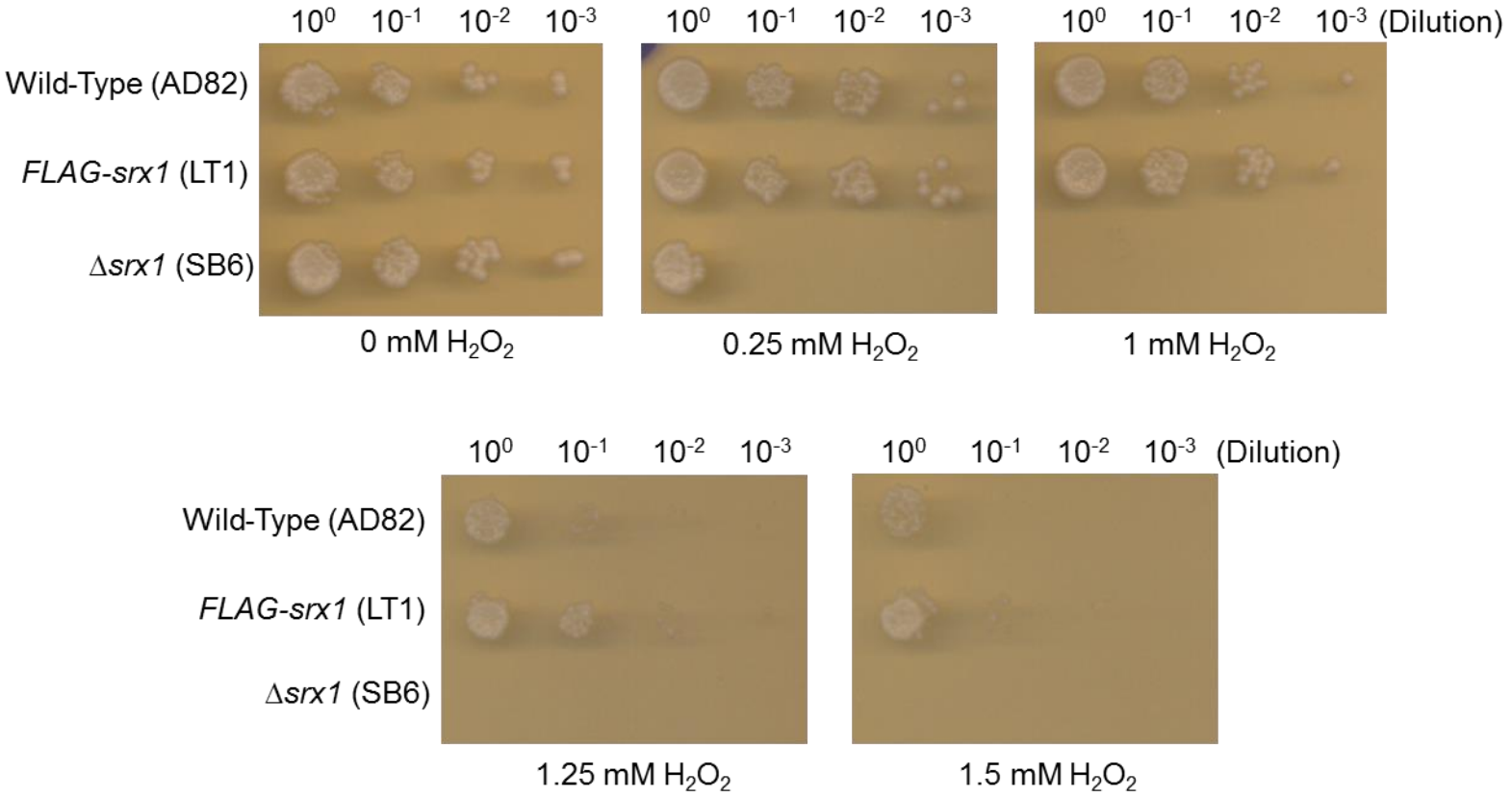

Figure 5.4: *FLAG-srx1* cells display wild-type levels of H_2O_2 resistance.

Serial 10-fold dilutions of wild-type (AD82), *FLAG-srx1* (LT1) and Δ*srx1* (SB6) cells were spotted onto YE5S agar plates containing the indicated concentrations of H_2O_2.

5.5.1 Srx1 protein levels are increased in response to H_2O_2

FLAG-srx1 cells were exposed to 200 µM H_2O_2 for up to 40 min and protein extracts were treated with NEM and analysed by western blot using anti-FLAG antibodies (Figure 5.5). Before addition of H_2O_2 a band was detected with a mobility between the 15 and 22 kDa molecular weight marker (Figure 5.5). This band was absent from cells expressing FLAG-Trx1 or Δ*srx1* mutant cells indicating that this band represents FLAG-Srx1 (Figure 5.5). The molecular weight of this band was slightly higher than expected, based on the predicted molecular weight of Srx1 (~13 kDa), even when the additional molecular weight of the FLAG-epitope tag (~1 kDa) was taken into account (Figure 5.4). This suggests that FLAG-Srx1 may undergo some form of post-translational modification (Figure 5.5). The intensity of the FLAG-Srx1 band remained unchanged for up to 20 min after H_2O_2 exposure, after which it increased reaching around 12-fold by 40 min (Figure 5.5). When this experiment was repeated, an increase in the levels of Srx1 was again observed 20 min after exposure to 200 µM H_2O_2, but this time only increased by around 5-fold 40 min after H_2O_2 exposure (Figure 5.6). In this experiment (Figure 5.6) the levels of FLAG-Srx1 before addition of H_2O_2 appeared higher compared with FLAG-TRX1 than in the first experiment (Fig. 5.5) suggesting that other factors may regulate the intracellular concentration of Srx1 independently from H_2O_2 treatment. Intriguingly, in the repeat experiment, the increase in the intensity of the FLAG-Srx1 band was coupled with the appearance of two new bands with similar mobility to the 40 kDa and kDa molecular weight markers (Figure 5.6). Although no follow up work was done to identify these bands, they most likely represent disulphide complexes between FLAG-Srx1 and other proteins. An increase in the intensity of the FLAG-Srx1 band was also detected 20 min after exposure to 50 µM H_2O_2 (Figure 5.7). This suggests that the timing of the H_2O_2-induced increase in FLAG-Srx1 is the same for 50 µM and 200 µM H_2O_2 treatments (Figure 5.5, 5.6 & 5.7).

Based on all three experiments an estimate for the intracellular concentration of FLAG-Srx1 in exponentially growing *S. pombe* cells was made by comparing the intensity of the FLAG-Srx1 band in the untreated cells to the intensity of the FLAG-Trx1 band detected in the untreated *FLAG-trx1* cells (see 2.6.5). This

estimate found that the intracellular concentration of FLAG-Srx1 in untreated cells was 0.15 ± 0.1 µM. Quantitative data for the changes in intracellular Srx1 concentration after H_2O_2-exposure was also calculated for each experiment (see 2.6.5) (Figure 5.8). This data revealed a marked difference in the H_2O_2-induced changes in Srx1 between experiments (Figure 5.8). In one experiment, exposure to 200 µM H_2O_2 resulted in the intracellular concentration of Srx1 increasing from ~0.04 to ~0.47 µM (Figure 5.5, 5.8). However, in another experiment, treatment with the same H_2O_2 concentration caused Srx1 levels to increase from 0.27 to 1.29 µM (Figure 5.6, 5.8). Treatment with 50 µM H_2O_2 resulted in the intracellular Srx1 concentration increasing from 0.14 to 0.69 µM (Figure 5.7, 5.8). It has been demonstrated in *S. cerevisiae* that calorie restriction results in the increased accumulation of Srx1 (Molin et al., 2011). Perhaps the variation in the pre-H_2O_2 levels of Srx1 between each experiment could reflect changes in the amount of glucose present in the cell culture when the protein samples were collected.

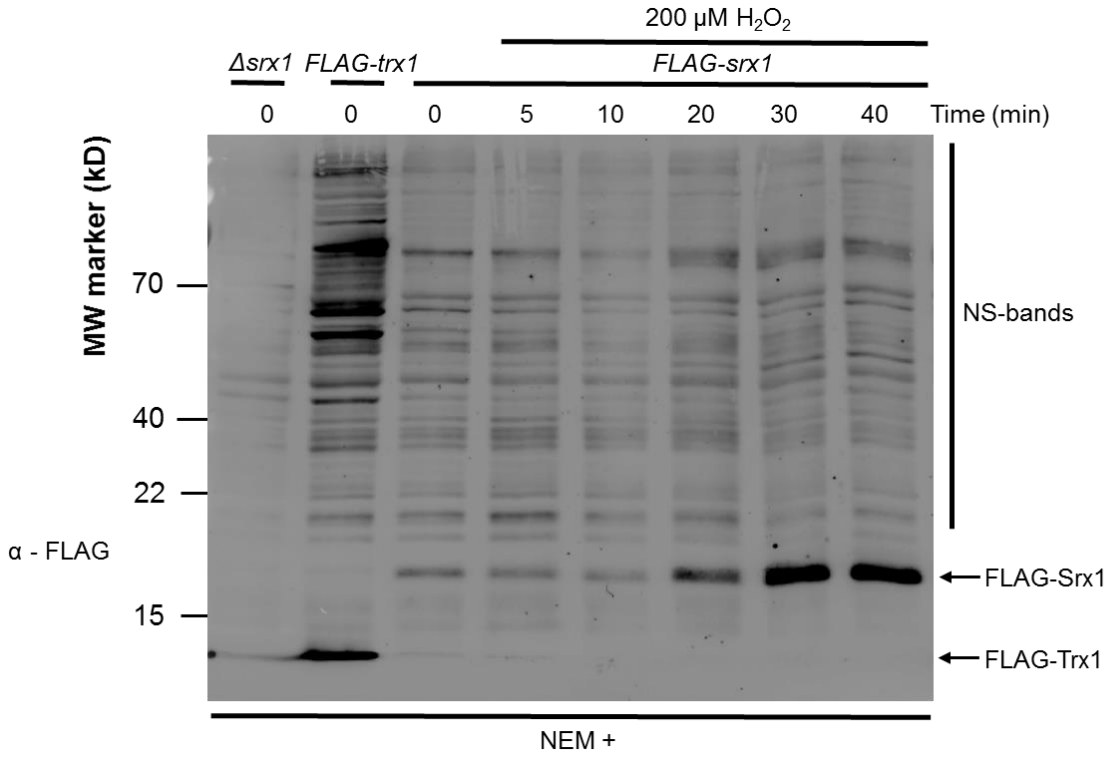

Figure 5.5: Measuring increases in FLAG-Srx1 protein levels in response to 200 µM H_2O_2.

Western blot analysis, using α-FLAG antibodies, of NEM-treated protein extracts from *FLAG-srx1* (LT1), *FLAG-trx1* (JB35) and Δ*srx1* (SB6) cells treated with 200 µM H_2O_2 for up to 40 min. Bands containing FLAG-Srx1 and FLAG-Trx1 are indicated, as well as non-specific bands (NS).

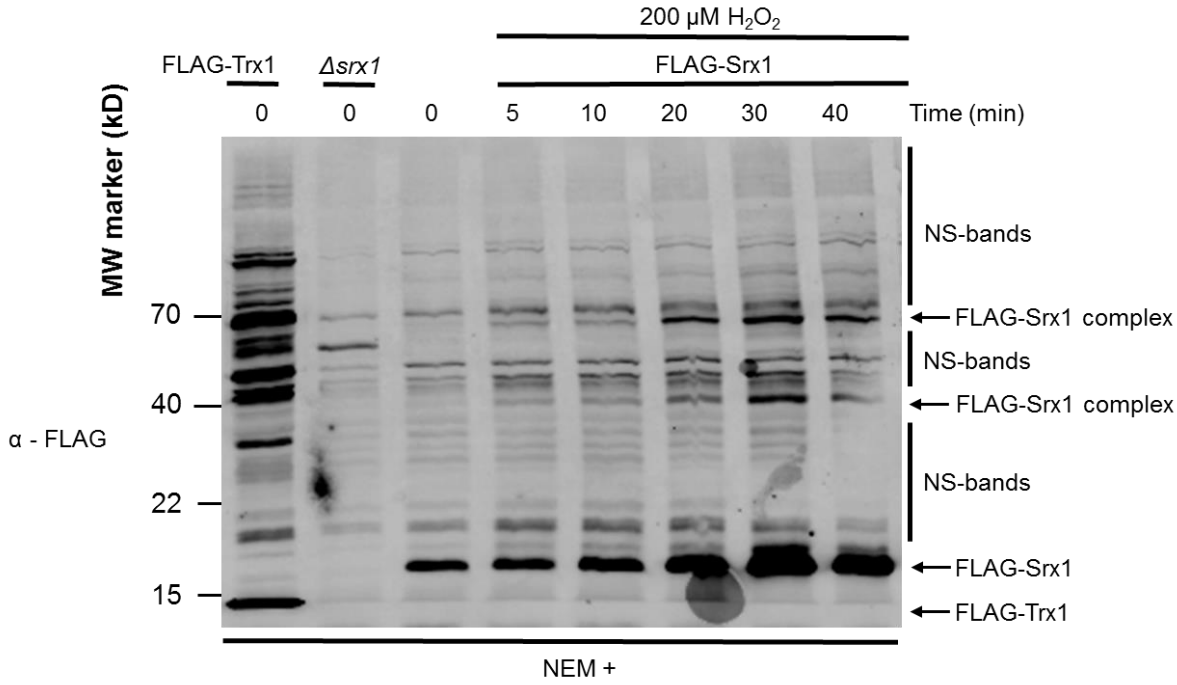

Figure 5.6: Measuring increases in FLAG-Srx1 protein levels in response to 200 µM H_2O_2.

Western blot analysis, using α-FLAG antibodies, of NEM-treated protein extracts from *FLAG-srx1* (LT1), *FLAG-trx1* (JB35) and Δ*srx1* (SB6) cells treated with 200 µM H_2O_2 for up to 40 min. Bands containing FLAG-Srx1 and FLAG-Trx1 are indicated, as well as non-specific bands (NS).

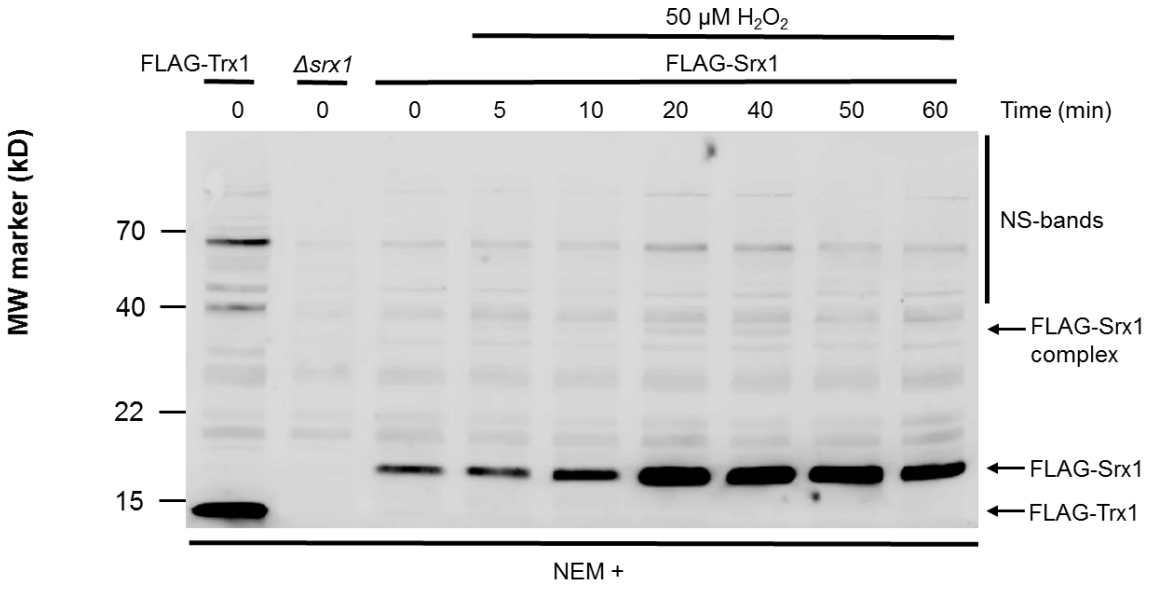

Figure 5.7: Measuring increases in FLAG-Srx1 protein levels in response to 50 µM H_2O_2.

Western blot analysis, using α-FLAG antibodies, of NEM-treated protein extracts from *FLAG-srx1* (LT1), *FLAG-trx1* (JB35) and Δ*srx1* (SB6) cells treated with 50 µM H_2O_2 for up to 40 min. Bands containing FLAG-Srx1 and FLAG-Trx1 are indicated, as well as non-specific bands (NS).

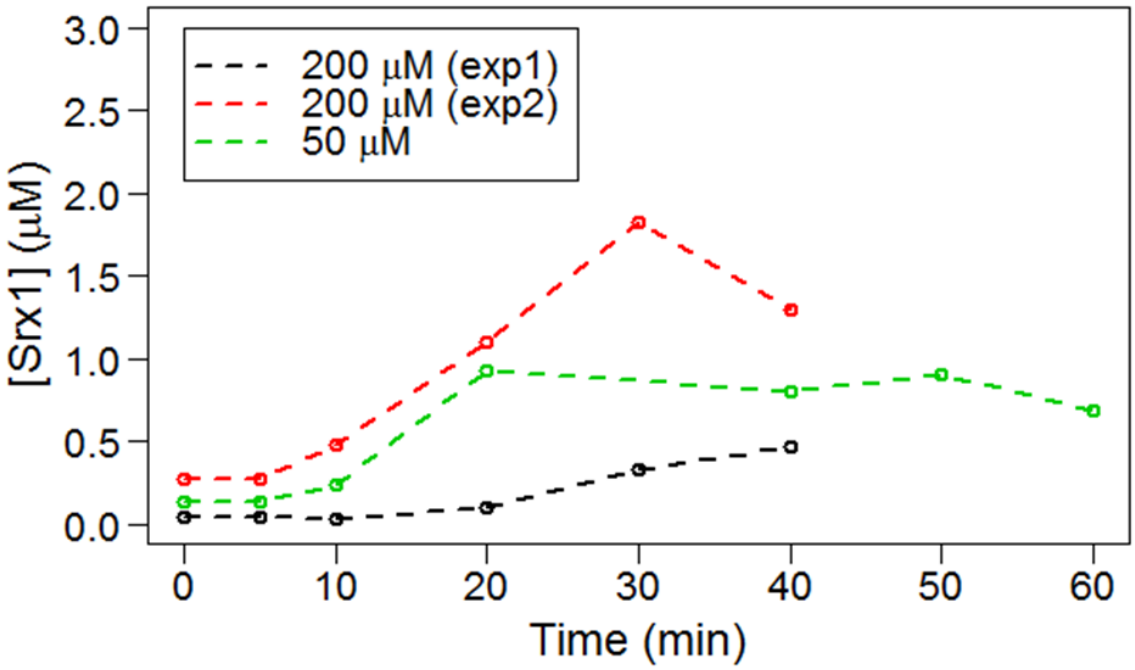

Figure 5.8: Quantification of the intracellular Srx1 concentration before and after H_2O_2 exposure.

The western blot data measuring changes in FLAG-Srx1 levels in response to H_2O_2 (Figure 5.4, 5.5 & 5.6) was used to create quantitative data sets for the changes in the intracellular concentration of Srx1 (see 2.6.5). The quantitative data calculated from each individual experiment was plotted.

5.6 Discussion

In this chapter a computer model of H_2O_2 metabolism by multiple peroxidase processes was used to predict the effects that H_2O_2- and quiescence-induced gene expression changes will have on subsequent cell responses to H_2O_2. Firstly, the computer model predicted that the H_2O_2-induced expression of Trr1 will increase the peroxide buffering capacity of the thiol-proteome (Figure 5.2A). The model predicted that due to this increased buffering capacity, cells pre-treated with H_2O_2 will be able to inhibit increases in intracellular H_2O_2 concentration after exposure to up to 500 µM extracellular H_2O_2 (Figure 5.2A). This is around two-fold higher than non-pre-treated cells which will experience increases in the intracellular H_2O_2 concentration after exposure to 200 µM H_2O_2 (Figure 5.2A). This prediction could be tested by using PF3 to measure the rate of intracellular H_2O_2 accumulation (see 2.3.3) in H_2O_2-pretreated and non-pre-treated cells. If this experiment found that the rate of PF3 fluorescence increased disproportionately faster after treatment with ~500 µM H_2O_2, rather than after ~150 µM as was observed for non-pre-treated cells in chapter 3 (Figure 3.27), it would be a strong indication that H_2O_2-induced gene expression increases the peroxide removal capacity of the thiol-proteome. In this context, the role of H_2O_2 induced gene expression is to limit increases in the intracellular H_2O_2 concentration. Indeed, the model predicted that H_2O_2-induced gene expression would have very little effect on the ability of the cell to remove H_2O_2 from the extracellular space, except for at very high H_2O_2 concentrations (Figure 5.3). This further suggests that the changes in gene expression induced by exposure to 200 µM H_2O_2 improve the ability of the cell to limit increases in the intracellular H_2O_2 concentration, but have little effect on the rate at which cells are able to completely remove H_2O_2 from the extracellular environment.

Although in the lab, exponentially growing cells are used for most experimental investigations, in their natural environment yeast are likely to spend most of their time in environments which are non-favourable for growth and division. Hence a well-defined programme of gene expression is initiated which allows *S. pombe* to withstand long periods in nutrient-limited conditions. The length of time for which cells can survive in this ‘quiescent’ state can be defined as the yeast cell lifespan and certain genes, including Sty1, have been found to be important for this

lifespan (Zuin et al., 2010). Here we have investigated how the changes in levels of Trr1 and catalase are predicted to influence cell responses to H_2O_2. Intriguingly, the model predicted that quiescent cells are less able to prevent increases in intracellular H_2O_2 concentration during exposure to low concentrations (100 – 1000 µM) of extracellular H_2O_2 than exponentially growing cells (Figure 5.2D & E). However, due to the increased expression of catalase, quiescent cells were predicted to be better able to inhibit increases in the intracellular H_2O_2 concentration after exposure to high H_2O_2 concentrations (> 1000 µM) than log-phase cells (Figure 5.2F). Furthermore, quiescent cells were better able to remove high concentrations of H_2O_2 from the extracellular environment compared to log-phase cells.

This prediction suggests that quiescence-induced gene expression does not limit, and could even facilitate, increases in intracellular H_2O_2 after exposure to low concentrations of H_2O_2. This would cause Tpx1 to become hyperoxidised at a lower H_2O_2 concentration in quiescent cells and would therefore promote the activation of Sty1 rather Pap1. This suggests that one of the roles of quiescence-induced gene expression is to promote the activation of Sty1 in response to H_2O_2 and could therefore explain the importance of Sty1 in the chronological lifespan of *S. pombe* (Zuin et al., 2010).

It is worth noting that there appears to be some limitations regarding the mass spectrometry methods used for the genome-wide quantification of the *S. pombe* proteome (Marguerat et al, 2012). For example, this method failed to detect any Srx1 protein in exponentially growing cells (less than 0.5 copies per cell) (Marguerat et al., 2012). The detection of FLAG-Srx1 in exponentially growing cells suggests that Srx1 is expressed even before H_2O_2-treatment (Figure 5.5, 5.6 & 5.7) although it was possible that the FLAG-epitope tag increases Srx1 protein levels by promoting the translation or stabilising Srx1. However, dilution growth assays indicated that the sensitivity of the FLAG-Srx1 cells to H_2O_2 was the same as wild-type cells suggesting that Srx1 protein levels are not dramatically different in these cells (Figure 5.4). This finding suggests that the mass-spec methods used for the genome-wide quantification of the *S. pombe* proteome are not suitable for detecting Srx1. Indeed, as Srx1 is only 13 kDa in size it is likely that peptide identification may be more difficult. The detection of

increased FLAG-Srx1 protein levels 20 min after exposure to H_2O_2 in FLAG-Srx1 cells (Figure 5.4, 5.5, 5.6 & 5.8) contradicts the genome-wide quantification of H_2O_2-induced protein level changes (Lackner et al., 2012). This study also used a mass-spec based method and detected no significant increase in the levels of Srx1 up to 3 hours after 200 µM H_2O_2 exposure (Lackner et al., 2012). This further suggests that the mass spec methods used in previous studies is not suitable for the detection of Srx1. Since Srx1 is the protein responsible for reducing hyperoxidised Tpx1 (see 1.3.4), it could have potential impacts on the regulation of H_2O_2-dependent signalling processes. Therefore it will be important to have accurate information on the intracellular concentration of Srx1 to ensure that the predictions of future computer models will be accurate.

Chapter 6. Discussion

The research outlined in this thesis has provided novel insights into the complex relationship between the peroxiredoxins, the thioredoxin system, the activation of H_2O_2-dependent transcription factors and changes in the peroxide buffering capacity of the cell. The wider impact of these insights regarding the biological role of the peroxiredoxins and the mitochondrial theory of ageing is discussed below.

6.1 The biological role of peroxiredoxin hyperoxidation

The floodgate hypothesis proposes that the biological role of 2-Cys Prx hyperoxidation is to allow increases in the intracellular H_2O_2 concentration, in order to activate H_2O_2-activated signalling proteins (Wood et al., 2003b). The findings of this study disagree with the floodgate hypothesis. Firstly, our computer model predicted that increases in the intracellular H_2O_2 concentration in response to H_2O_2 are required to actually cause Prx hyperoxidation (Figure 3.25). This is in direct contrast to the flood gate hypothesis which proposes increased intracellular H_2O_2 is a consequence of Prx hyperoxidation, rather than its cause. Furthermore, measuring intracellular H_2O_2 changes in Δ*tpx1* and hyperoxidation resistant *tpx1*$^{1\text{-}181}$ cells suggested that Tpx1 plays very little role in the inhibition of intracellular H_2O_2 increases (Figure 3.27 & 3.29). Instead the evidence described in this thesis suggests, in agreement with published work, that the major role of the peroxiredoxins is H_2O_2-induced signal transduction (Jang et al., 2004, Phalen et al., 2006, Turner-Ivey et al., 2013, Peskin et al., 2013).

As described in Chapter 1 (see 1.4 & 1.5) the fission yeast *S. pombe* has been demonstrated to respond to H_2O_2 with the two distinct, but overlapping, transcriptional responses, in a concentration dependent manner (Chen et al., 2008). These responses are activated by Pap1 at low H_2O_2 concentrations and by Sty1/Atf1 mediated signalling at higher H_2O_2 concentrations, both of which require Tpx1 (Bozonet et al., 2005, Vivancos et al., 2005). The principles outlined in this thesis offer an explanation for why *S. pombe* cells would need to respond

differently to low and high doses of H_2O_2 with distinct transcriptional responses. For example, exposure to low doses of H_2O_2 will not cause an increase in the intracellular H_2O_2 concentration, and therefore is unlikely to cause much damage to cellular components (Figure 3.26). At these low H_2O_2 concentrations it will be more beneficial for the cell to increase the expression of genes that will limit increases in the intracellular H_2O_2 concentration. However, exposure to high concentrations of H_2O_2, sufficient to saturate the cells peroxide buffering capacity, will cause an increase in the intracellular H_2O_2 concentration and therefore irreversible oxidative damage to cellular components.

At these high H_2O_2 concentrations it will be more appropriate for the cell to increase the expression of genes involved in the repair of damaged proteins and DNA. In this context the role of peroxiredoxin hyperoxidation is to inform the cell that the H_2O_2 buffering capacity has been saturated, in response to this the cell will initiate repair processes to reverse ROS-induced damage that may result from the breach of the cells' antioxidant defence. Indeed, Prx hyperoxidation has been demonstrated to facilitate the repair of oxidised proteins by methionine sulphoxide reductase (Mxr1) by increasing the availability of Trx1 (Day et al., 2012). Furthermore, Prx hyperoxidation has been shown to facilitate the protein chaperone function of the Prxs (Moon et al., 2005). Both of these observations are consistent with the hypothesis that the role of Prx hyperoxidation is to switch the cellular response to H_2O_2 from being predominantly geared towards limiting increases in the intracellular H_2O_2 concentration to being more geared towards the repair of ROS-induced damage.

6.2 Impact of this research in terms of the mitochondrial theory of ageing

As discussed in chapter 1 (see 1.2) the mitochondrial theory of ageing proposes that as an organism ages, the accumulation of oxidative damage to mitochondrial proteins and DNA will inhibit healthy mitochondrial function and increase mitochondrial ROS production. This increased mitochondrial ROS production will further accelerate the accumulation of oxidative damage resulting in a vicious cycle eventually resulting in the rapid decline of mitochondrial function and increased mitochondrial ROS production with age.

The research in this thesis has demonstrated that in response to an exposure to extracellular H_2O_2 there will be two possible outcomes regarding its effect on the intracellular H_2O_2 concentration. Firstly, if the extracellular H_2O_2 concentration is below a certain threshold, the rate at which H_2O_2 enters the cell will be slow enough that the cells' peroxide buffering capacity will limit increases in the intracellular H_2O_2 concentration. Under these circumstances there will be very little net change in the intracellular H_2O_2 concentration. However, if the extracellular H_2O_2 concentration is above this threshold, the rate at which H_2O_2 enters the cytoplasm will be faster than the V_{max} of the peroxide removal reactions which will result in an increase in the intracellular H_2O_2 concentration. This relationship between the intracellular and extracellular H_2O_2 concentration was predicted using computer modelling approaches and was also confirmed experimentally in *S. pombe* and human cell lines (Figure 3.6, 3.24, 3.26 & 3.27).

It seems unlikely that mitochondrial ROS will be sufficient to saturate the cells anti-oxidant defences and cause Prx hyperoxidation. However, these low levels of mitochondrial ROS production, especially in aged mitochondria, would be sufficient to oxidise Prx and initiate the Prx catalytic cycle. In *S. pombe* catalytically active Tpx1 is required for the H_2O_2-induced activation of Pap1 (Day et al., 2012). It can therefore be reasoned that Pap1 will be activated in response to mitochondrial ROS production, resulting in the increased expression of Pap1 dependent genes. As discussed in chapter 5 a computer model of H_2O_2 metabolism by multiple peroxidase processes predicted that H_2O_2-induced gene expression would increase the ability of the cell to inhibit increases in intracellular H_2O_2 concentration (Figure 5.1). This model was based on published H_2O_2-induced gene expression data measured in response to treatment with 200 µM

H_2O_2 (Lackner et al., 2012). Due to our experimental observation that Pap1 is fully oxidised for up to an hour after exposure to 200 µM, it is not unreasonable to assume that the H_2O_2-induced gene expression described by Lackner et al (2012) will be, at least partly, due to the activation of Pap1-dependent gene expression. Therefore the predictions of the model in chapter 5 suggest that the expression of Pap1-dependent genes in response to mitochondrial ROS production will improve the peroxide buffering capacity of the cell. This will protect the cell from future increases in mitochondrial ROS production by limiting the ability of mitochondrial derived ROS, and other sources of ROS, to cause major damage to cellular components. This sequence of events is consistent with the principle of mitochondrial hormesis (see 1.2) (for a review see (Ristow and Schmeisser, 2014) which proposes that an initial exposure to low levels of ROS will result in increased resistance to subsequent ROS exposures. Furthermore, due to the evidence that Pap1 is activated by Tpx1-SOH (Figure 4.23), the Pap1-mediated increase in Tpx1 protein levels would be expected to further facilitate the activation of Pap1 in response to H_2O_2. In this context, the increased expression of Prx in response to H_2O_2 is not only to limit increases in intracellular H_2O_2, but also to facilitate Prx-mediated signalling, a principle that could hold true for mammalian cells as well as yeast.

This study demonstrated that Srx1 protein levels will increase in response to H_2O_2, even at low concentrations such as 50 µM, which is too low to hyperoxidise Tpx1 (Figure 5.6). This H_2O_2-induced increase in the level of Srx1 could be sufficient to maintain Tpx1 in an active state at H_2O_2 concentrations that would cause hyperoxidation in non-H_2O_2 pre-treated cells. This hypothesis could be tested using a computer model, similar to the models described in this study. If correct this would facilitate the activation of signalling pathways which require catalytically Prx, such as Pap1 in *S. pombe*, but would likely activate similar pathways in mammals.

These findings together support a scenario whereby cells respond to mitochondrial-ROS by activating Prx-mediated signalling pathways. These pathways would result in the increased expression of genes which not only limit increases in the intracellular ROS concentration but also facilitate future activation of Prx mediated signalling. As the cell ages, and mitochondrial ROS

production increases, the cell will have to increase the levels of antioxidant genes higher and higher to offset the increased ROS production. Since many of these proteins, such as Trx and Prx ultimately require NADPH the cell would eventually reach a point at which the demand on NADPH outweighs NADPH production. This sequence of events could explain the experimental observation that levels of NADPH start to decrease in chronologically ageing *S. cerevisiae* (Brandes et al., 2013).

6.3 Final summary and future perspectives

In this study the combination of computer modelling approaches and experimental data have strongly suggested that peroxiredoxin hyperoxidation occurs when the peroxide buffering capacity becomes saturated by H_2O_2. Furthermore, and in agreement with a previously published computer model (Adimora et al., 2010), evidence in this study has suggested that the peroxide buffering capacity responsible for inhibiting Prx hyperoxidation is the thiol-proteome. This strongly suggests that Prx hyperoxidation acts as a mechanism to signal the moment that the thiol-proteome becomes saturated by H_2O_2.

Based on this principle a computer model predicted that, H_2O_2-induced gene expression, due to the Tpx1-mediated activation of Pap1, will act to increase the peroxide buffering capacity of the thiol-proteome and limit the ability of subsequent, higher doses of H_2O_2 to increase the intracellular H_2O_2 concentration. The predictions of this model, although consistent with the theory of mitochondrial hormesis, were not confirmed experimentally. In order to confirm the predictions of this model future work should aim to measure the ability of H_2O_2-pre-treated cells to inhibit increases in the intracellular H_2O_2 concentration. Furthermore, to support the hypothesis that Tpx1 hyperoxidation will gear the cell towards protein and DNA repair, the computer models described in this thesis could be adapted to represent Sty1/Atf1 induced gene expression changes to predict the effect this will have on the ability of the cell to inhibit increases in intracellular H_2O_2 and repair oxidatively damaged proteins.

In Chapter 4 we built several computer models representing possible mechanisms for the oxidation of Pap1 by Tpx1 in response to H_2O_2 and tested

their ability to simulate experimentally observed features of Pap1 oxidation. This analysis suggested that oxidation of Pap1 by Tpx1-SOH was the most feasible mechanism. However, there were several limitations to this analysis that would need to be overcome in order to draw a firmer conclusion. This first limitation is regarding the data sets used to parameterise this model. For example, although a very robust Tpx1 data set was used (n = 2-5), the data set for changes in the oxidation of Trx1 was not so thorough and had not been repeated (see Figure 4.13). To build on this work, and cement our conclusions, a more robust Trx1 data set should be collected and used to re-parameterise this model. Another limitation of the analysis of the Pap1 models in Chapter 4 was the observation that, despite adding Txl1 to the model, the model was still unable to accurately simulate changes in Pap1 oxidation over extended time periods (Figure 4.30).

To move forward with this research, an adaptation to the Pap1 model needs to found that will enable the model to accurately simulate the extended oxidation of Pap1. If such an adaptation can be made to the model, this would allow a much firmer conclusion to be drawn regarding the mechanisms of Pap1 oxidation and reduction. Several model adaptations could be tested in the future and could include the incorporation of Pap1-dependent gene expression change, the addition of other Trx1 substrates and the addition of a nuclear compartment. If any of these adaptations, along with accompanying experimental data, were able to improve the ability of the model to simulate the long term changes in Pap1 oxidation, this would greatly improve our confidence that Tpx1-SOH is responsible for the initial oxidation of Pap1 in response to H_2O_2.

APPENDIX

Appendix A: Estimating the concentration of the thiol-proteome.

Systematic.name	Common.name	Cytoplasmic concentration (uM)
SPAC13D6.02c	byr3	0.605165288
SPBC16D10.06	zrt1	0.126144969
SPAC24H6.10c	SPAC24H6.10c	0.663311995
SPCC1827.06c	SPCC1827.06c	0.598289076
SPAC1250.03	ubc14	0.047013969
SPAP8A3.07c	SPAP8A3.07c	0.953643202
SPBC32F12.11	tdh1	9.186645029
SPCC576.03c	tpx1	3.963669925
SPAC1783.07c	pap1	0.024472994
SPAC4H3.07c	SPAC4H3.07c	0.176620017
SPAC1F7.05	cdc22	0.322837837
SPAC1556.02c	sdh1	0.467948422
SPCC330.06c	SPCC330.06c	2.404518776
SPAC22E12.04	ccs1	0.016562395
SPAC7D4.07c	trx1	0.722074243
SPCC191.07	cyc1	0.518624318
SPBC32F12.03c	gpx1	0.611484813
SPAC5D6.01	rps2202	1.013444442
SPAC13G7.06	met16	0.152491308
SPAC25B8.12c	SPAC25B8.12c	2.02448133
SPAC1805.12c	uep1	0
SPAC9E9.03	leu2	0.641502195
SPBC2G2.05	rpl1603	0.029167955
SPCC13B11.01	adh1	7.576317715
SPBC31A8.01c	rtn1	0.440453415
SPAC6G10.11c	ubi3	1.319354297
SPAC222.17	SPAC222.17	0
SPAC3G9.03	rpl2301	1.76727094
SPCC1223.05c	rpl3702	0.625332018
SPAC23A1.08c	rpl3401	1.424249583
SPBP4H10.13	rps2302	0.633546191
SPBC4.06	SPBC4.06	0.147427329
SPBP8B7.03c	rpl402	0.83576106
SPAC23C11.05	SPAC23C11.05	1.193141536
SPBC18E5.06	rps21	1.109888149
SPCC24B10.21	tpi1	0.66885891
SPCC364.07	SPCC364.07	1.041375356
SPBC2G2.04c	mmf1	0.941963888
SPCC962.04	rps1201	2.990780191
SPBC1734.11	mas5	0.374525283
SPAC4H3.10c	pyk1	4.531684895
SPBC19C2.07	fba1	9.257425821
SPAC4F10.20	grx1	0.936128293
SPBC14F5.05c	sam1	3.300007508

SPBC1685.09	rps29	4.787099842
SPAC1296.02	cox4	0.328976374
SPBC3B9.19	mge1	0.102602554
SPAC1F5.02	SPAC1F5.02	0.183533149
SPBP4G3.02	pho1	0.46780643
SPAC6C3.02c	SPAC6C3.02c	0.108733688
SPBC16C6.08c	qcr6	0.353808276
SPAC222.03c	tim10	0.104895648
SPCC24B10.05	tim9	0.161393779
SPAC57A10.11c	tim40	0.0471352
SPAC13G6.04	tim8	0.286470148
SPAC24H6.04	hxk1	0.812001549
SPAC4A8.08c	vrs2	0.005888131
SPAC9E9.09c	SPAC9E9.09c	1.178729791
SPAC19G12.10c	cpy1	0.129584925
SPAC3C7.11c	cnx1	0.871930429
SPAC821.10c	sod1	2.246698822
SPBC16C6.11	rpl3201	0.261454549
SPAC1002.09c	dld1	0.566081235
SPAC1805.13	rpl14	0.754698944
SPAC607.03c	snu13	0.91418968
SPBC21C3.08c	car2	1.049527063
	total	82.10884708

Table lists all of the proteins shown to become oxidised in response to 200 µM H_2O_2, based on the data from Garcia-Santamarina et al., 2013. The table displays the systematic name and the common name for each gene. The table also displays the estimated intracellular concentration of each protein based on the data published in Marguerat et al., 2012. The total concentration of each protein is displayed and was used as an estimate for the concentration of the thiol-proteome (see 4.2.1).

Appendix B: Data sets used for parameter estimation.

Extracellular H2O2 data (Exp1)

Time	H2O2ex_Exp1	H2O2initial
0	50	50
60	48	50
120	48	50
300	43	50
600	40	50
900	38	50
1200	34	50
1500	29	50
1800	24	50

Extracellular H2O2 data (Exp2)

Time	H2O2ex_Exp2	H2O2initial
0	50	50
60	49	50
120	49	50
300	47	50
600	42	50
900	38	50
1200	34	50
1500	30	50
1800	27	50

Intracellular H2O2 data

Time	H2O2ex	H2O2int
0	0	0.001
10	0	0.001
60	0	0.001

100 µM Tpx1 Time course data (Exp1)

Time	Tpx1SH	Tpx1ox2	Tpx1ox1	Tpx1oxSOOH	Tpx1SOOH	H2O2ex
0	4	0	0	0	0	100
30	2.439	0.385	0.396	0	0	100
60	2.528	0.365	0.371	0	0	100
120	2.396	0.379	0.422	0	0	100
300	1.578	0.495	0.716	0	0	100
600	1.746	0.525	0.602	0	0	100

Steady State

Time	Tpx1SH	Tpx1ox2	Tpx1ox1	Tpx1oxSOOH	Tpx1SOOH	H2O2ex
0	4	0	0	0	0	0

20	3.95	0	0.025	0	0	0
60	3.95	0	0.025	0	0	0

100 µM Tpx1 Time course data (Exp2)

Time	Tpx1SH	Tpx1ox2	Tpx1ox1	Tpx1oxSOOH	Tpx1SOOH	H2O2ex
0	4	0	0	0	0	100
20	0.978	0.523	0.988	0	0	100
40	1.002	0.475	1.024	0	0	100
60	1.144	0.466	0.961	0	0	100

Steady State

Time	Tpx1SH	Tpx1ox2	Tpx1ox1	Tpx1oxSOOH	Tpx1SOOH	H2O2ex
0	4	0	0	0	0	0
20	3.3184	0	0.3408	0	0	0
60	3.3184	0	0.3408	0	0	0

100 µM Tpx1 Time course data (Exp3)

Time	Tpx1SH	Tpx1ox2	Tpx1ox1	Tpx1oxSOOH	Tpx1SOOH	H2O2ex
0	4	0	0	0	0	100
60	0.999	0.598	0.903	0	0	100
300	1.13	0.43	1.005	0	0	100
600	2.07	0.25	0.715	0	0	100

Steady State

Time	Tpx1SH	Tpx1ox2	Tpx1ox1	Tpx1oxSOOH	Tpx1SOOH	H2O2ex
0	4	0	0	0	0	0
20	3.4872	0	0.5128	0	0	0
60	3.4872	0	0.5128	0	0	0

100 µM Tpx1 Time course data (Exp4)

Time	Tpx1SH	Tpx1ox2	Tpx1ox1	Tpx1oxSOOH	Tpx1SOOH	H2O2ex
0	4	0	0	0	0	100
60	0.127	0.64	1.297	0	0	100
300	0.423	0.393	1.396	0	0	100
600	0.85	0.306	1.269	0	0	100

Steady State

Time	Tpx1SH	Tpx1ox2	Tpx1ox1	Tpx1oxSOOH	Tpx1SOOH	H2O2ex
0	4	0	0	0	0	0
20	3.1964	0.0616	0.4018	0	0	0
60	3.1964	0.0616	0.4018	0	0	0

200 µM Tpx1 Time course (Exp1)

Time	Tpx1SH	Tpx1ox2	Tpx1oxSOOH	Tpx1ox1	Tpx1SOOH	H2O2
0	4	0	0	0	0	200

20	0.07	0.91	0.28	0.77	0	200
40	0.09	0.81	0.31	0.84	0	200
60	0.03	0.9	0.26	0.83	0	200
120	0	0.76	0.32	0.71	0.43	200
240	0	0.44	0.2	0.52	1.69	200
360	0	0.5	0.33	0.77	0.82	200
480	0	0.41	0.31	0.68	1.2	200
600	0	0.43	0.35	0.75	0.95	200

Steady State

Time	Tpx1SH	Tpx1ox2	Tpx1oxSOOH	Tpx1ox1	Tpx1SOOH	H2O2
0	4	0	0	0	0	0
20	3.09	0	0	0.227	0	0
60	3.09	0	0	0.227	0	0

200 µM Time course data (Exp2)

Time	Tpx1SH	Tpx1ox2	Tpx1oxSOOH	Tpx1ox1	Tpx1SOOH	H2O2
0	4	0	0	0	0	200
20	0.185	0.72	0.349	0.838	0	200
40	0.195	0.631	0.357	0.914	0	200
60	0.198	0.592	0.419	0.89	0	200
120	0	0.234	0.259	0.632	1.749	200
240	0	0.047	0.065	0.197	3.382	200
360	0	0.045	0.111	0.23	3.228	200
480	0	0.061	0.117	0.32	3.003	200
600	0	0.044	0.201	0.211	3.088	200

Steady State

Time	Tpx1SH	Tpx1ox2	Tpx1oxSOOH	Tpx1ox1	Tpx1SOOH	H2O2
0	4	0	0	0	0	0
20	3.304	0	0	0.348	0	0
60	3.304	0	0	0.348	0	0

200 µM Time course data (Exp3)

Time	Tpx1SH	Tpx1ox2	Tpx1oxSOOH	Tpx1ox1	Tpx1SOOH	H2O2
0	4	0	0	0	0	200
600	0	0.334	0.209	0.829	1.256	200

Steady State

Time	Tpx1SH	Tpx1ox2	Tpx1oxSOOH	Tpx1ox1	Tpx1SOOH	H2O2
0	4	0	0	0	0	0
20	3.492	0	0	0.254	0	0
60	3.492	0	0	0.254	0	0

200 µM Tpx1 Time course data (Exp4)

Time	Tpx1SH	Tpx1ox2	Tpx1oxSOOH	Tpx1ox1	Tpx1SOOH	H2O2

0	4	0	0	0	0	200
20	0.0592	0.8176	0.2682	0.8848	0	200
40	0.0736	0.8752	0.2096	0.8784	0	200
60	0	0.8938	0.1888	0.9174	0	200
120	0	0.8656	0.2758	0.755	0.2072	200
240	0	0.5096	0.2308	0.8218	0.8752	200
360	0	0.4876	0.1978	0.7414	1.1464	200
480	0	0.3452	0.1516	0.654	1.6988	200
600	0	0.2448	0.2186	0.6148	1.8436	200

Steady State

Time	Tpx1SH	Tpx1ox2	Tpx1oxSOOH	Tpx1ox1	Tpx1SOOH	H2O2
0	4	0	0	0	0	0
20	3.2296	0	0	0.3852	0	0
60	3.2296	0	0	0.3852	0	0

200 µM Tpx1 Time course data (Exp5)

Time	Tpx1SH	Tpx1ox2	Tpx1oxSOOH	Tpx1ox1	Tpx1SOOH	H2O2
0	4	0	0	0	0	200
30	0.0372	0.7852	0.2766	0.8534	0.1324	200
60	0	0.5828	0.2154	0.8456	0.712	200
120	0	0.3964	0.1434	0.5908	1.7392	200
240	0	0.2348	0	0.2014	3.1276	200
360	0	0.2132	0	0.4276	2.7188	200
480	0	0.204	0	0.3408	2.9104	200
600	0	0.1632	0	0.4216	2.8304	200

Steady State

Time	Tpx1SH	Tpx1ox2	Tpx1oxSOOH	Tpx1ox1	Tpx1SOOH	H2O2
0	4	0	0	0	0	0
20	3.366	0.2188	0	0.4152	0	0
60	3.366	0.2188	0	0.4152	0	0

Tpx1 20 seconds after 0 - 6000 µM H2O2 (exp1)

Time	H2O2	Tpx1SH	Tpx1SOOH	Tpx1ox2	Tpx1oxSOOH	Tpx1ox1
0	0	4	0	0	0	0
20	0	3.04	0	0	0	0.48

Time	H2O2	Tpx1SH	Tpx1SOOH	Tpx1ox2	Tpx1oxSOOH	Tpx1ox1
0	50	4	0	0	0	0
20	50	1.3292	0	0.2036	0	1.1318

Time	H2O2	Tpx1SH	Tpx1SOOH	Tpx1ox2	Tpx1oxSOOH	Tpx1ox1
0	100	4	0	0	0	0
20	100	0.0708	0	1.0862	0	0.8784

Time	H2O2	Tpx1SH	Tpx1SOOH	Tpx1ox2	Tpx1oxSOOH	Tpx1ox1

0	200	4	0	0	0	0
20	200	0	0	1.318	0.2434	0.4388

Time	H2O2	Tpx1SH	Tpx1SOOH	Tpx1ox2	Tpx1oxSOOH	Tpx1ox1
0	300	4	0	0	0	0
20	300	0	0	1.2006	0.4322	0.3672

Time	H2O2	Tpx1SH	Tpx1SOOH	Tpx1ox2	Tpx1oxSOOH	Tpx1ox1
0	500	4	0	0	0	0
20	500	0	0	0.9796	0.7018	0.3188

Time	H2O2	Tpx1SH	Tpx1SOOH	Tpx1ox2	Tpx1oxSOOH	Tpx1ox1
0	1000	4	0	0	0	0
20	1000	0	0	0.9254	0.8264	0.2482

Time	H2O2	Tpx1SH	Tpx1SOOH	Tpx1ox2	Tpx1oxSOOH	Tpx1ox1
0	6000	4	0	0	0	0
20	6000	0	1.0412	0	1.4794	0

Tpx1 20 seconds after 0 - 6000 µM H2O2 (exp2)

Time	H2O2	Tpx1SH	Tpx1SOOH	Tpx1ox2	Tpx1oxSOOH	Tpx1ox1
0	0	4	0	0	0	0
20	0	3.71	0	0	0	0.145

Time	H2O2	Tpx1SH	Tpx1SOOH	Tpx1ox2	Tpx1oxSOOH	Tpx1ox1
0	50	4	0	0	0	0
20	50	1.35	0	0.175	0	1.155

Time	H2O2	Tpx1SH	Tpx1SOOH	Tpx1ox2	Tpx1oxSOOH	Tpx1ox1
0	100	4	0	0	0	0
20	100	1.26	0	0.165	0	1.2

Time	H2O2	Tpx1SH	Tpx1SOOH	Tpx1ox2	Tpx1oxSOOH	Tpx1ox1
0	200	4	0	0	0	0
20	200	0	0	0.965	0.47	0.56

Time	H2O2	Tpx1SH	Tpx1SOOH	Tpx1ox2	Tpx1oxSOOH	Tpx1ox1
0	300	4	0	0	0	0
20	300	0	0	1.04	0.475	0.485

Time	H2O2	Tpx1SH	Tpx1SOOH	Tpx1ox2	Tpx1oxSOOH	Tpx1ox1
0	500	4	0	0	0	0
20	500	0	0.04	0.955	0.715	0.31

Time	H2O2	Tpx1SH	Tpx1SOOH	Tpx1ox2	Tpx1oxSOOH	Tpx1ox1
0	1000	4	0	0	0	0

20	1000	0	0.14	1.225	0.705	0

Time	H2O2	Tpx1SH	Tpx1SOOH	Tpx1ox2	Tpx1oxSOOH	Tpx1ox1
0	6000	4	0	0	0	0
20	6000	0	2.08	0	0.96	0

100 µM Tpx1 Time course data with Tpx1Trx1 (Exp1)

Time	Tpx1SH	Tpx1ox#2	Tpx1ox#1	Tpx1Trx1	Tpx1oxSOOH	Tpx1SOOH	H2O2
0	4	0	0	0	0	0	100
20	0.8964	0.479	0.9052	0.1678	0	0	100
40	0.938	0.4446	0.9578	0.1284	0	0	100
60	1.05	0.4278	0.882	0.1652	0	0	100

Steady State

Time	Tpx1SH	Tpx1ox2	Tpx1oxSOOH	Tpx1Trx1	Tpx1ox1	Tpx1SOOH	H2O2
0	4	0	0	0	0	0	0
20	3.298	0	0	0	0.351	0	0
60	3.298	0	0	0	0.351	0	0

100 µM Tpx1 Time course data with Tpx1Trx1 (Exp2)

Time	Tpx1SH	Tpx1ox#2	Tpx1ox#1	Trx1Txl1	Tpx1oxSOOH	Tpx1SOOH	H2O2
0	4	0	0	0	0	0	100
60	0.12	0.6	1.215	0.13	0	0	100
300	0.4	0.375	1.335	0.09	0	0	100
600	0.81	0.29	1.215	0.09	0	0	100

Steady State

Time	Tpx1SH	Tpx1ox2	Tpx1oxSOOH	Trx1Txl1	Tpx1ox1	Tpx1SOOH	H2O2
0	4	0	0	0	0	0	0
20	3.17	0	0	0	0.415	0	0
60	3.17	0	0	0	0.415	0	0

100 µM Tpx1 Time course data with Tpx1Trx1 (Exp3)

Time	Tpx1SH	Tpx1ox#2	Tpx1ox#1	Trx1Txl1	Tpx1oxSOOH	Tpx1SOOH	H2O2
0	4	0	0	0	0	0	100
60	0.94	0.565	0.85	0.11	0	0	100
300	1.08	0.41	0.96	0.09	0	0	100
600	1.98	0.24	0.685	0.09	0	0	100

Steady State

Time	Tpx1SH	Tpx1ox2	Tpx1ox1	Trx1Txl1	Tpx1oxSOOH	Tpx1SOOH	H2O2ex
0	4	0	0	0	0	0	0
20	3.47	0	0.265	0	0	0	0

60	3.47	0	0.265	0	0	0	0

100 µM Tpx1 Time course data with Tpx1Trx1 (Exp4)

Time	Tpx1SH	Tpx1ox#2	Tpx1ox#1	Trx1Txl1	Tpx1oxSOOH	Tpx1SOOH	H2O2
0	4	0	0	0	0	0	100
30	2.34	0.37	0.38	0.085	0	0	100
60	2.42	0.35	0.355	0.08	0	0	100
120	2.27	0.36	0.4	0.1	0	0	100
300	1.45	0.455	0.66	0.16	0	0	100
600	1.6	0.48	0.55	0.17	0	0	100

Steady State

Time	Tpx1SH	Tpx1ox2	Tpx1ox1	Trx1Txl1	Tpx1oxSOOH	Tpx1SOOH	H2O2ex
0	4	0	0	0	0	0	0
20	3.95	0	0.025	0	0	0	0
60	3.95	0	0.025	0	0	0	0

200 µM Tpx1 Time course data with Tpx1Trx1 (Exp1)

Time	Tpx1SH	Tpx1ox2	Tpx1oxSOOH	Tpx1ox1	Trx1Tpx1	Tpx1SOOH	H2O2
0	4	0	0	0	0	0	200
20	0.1488	0.602	0.293	0.6958	0.2546	0.1604	200
40	0.1772	0.5182	0.2778	0.7328	0.2592	0.2464	200
60	0.1716	0.508	0.3492	0.752	0.1282	0.3532	200
120	0.312	0.2044	0.2222	0.5358	0.153	1.4572	200
240	0	0.0474	0.0634	0.1966	0	3.3852	200
360	0	0.048	0.1058	0.2246	0	3.2432	200
480	0	0.0766	0.1118	0.3234	0	2.9764	200
600	0	0.0704	0.1556	0.2212	0	3.1052	200

Steady State

Time	Tpx1SH	Tpx1ox2	Tpx1oxSOOH	Tpx1ox1	Tpx1Trx1	Tpx1SOOH	H2O2
0	4	0	0	0	0	0	0
20	3.2	0	0	0.4	0	0	0
60	3.2	0	0	0.4	0	0	0

200 µM Tpx1 Time course data with Tpx1Trx1 (Exp2)

Time	Tpx1SH	Tpx1ox2	Tpx1oxSOOH	Tpx1ox1	Tpx1Trx1	Tpx1SOOH	H2O2
0	4	0	0	0	0	0	200
20	0.07	0.825	0.255	0.7	0.19	0	200
40	0.07	0.705	0.265	0.725	0.265	0	200
60	0.02	0.845	0.24	0.77	0.13	0	200
480	0	0.845	0.435	0.195	0	1.69	200
600	0	0.41	0.495	0.33	0	0.82	200

Steady State

Time	Tpx1SH	Tpx1ox2	Tpx1oxSOOH	Tpx1ox1	Trx1Txl1	Tpx1SOOH	H2O2
0	4	0	0	0	0	0	0
20	3.09	0	0	0.455	0	0	0

60	3.09	0	0	0.455	0	0	0

200 µM Tpx1 Time course data with Tpx1Trx1 (Exp4)

Time	Tpx1SH	Tpx1ox2	Tpx1oxSOOH	Tpx1ox1	Tpx1SOOH	Trx1Tpx1	H2O2
0	4	0	0	0	0	0	200
30	0	0.6836	0.2408	0.7428	0.1152	0.2752	200
60	0	0.5186	0.1918	0.7526	0.6336	0.2202	200
120	0	0.3778	0.1366	0.563	1.6576	0.0938	200
240	0	0.2286	0	0.1962	3.0456	0.0524	200
360	0	0.2086	0	0.4184	2.6604	0.0428	200
480	0	0.1994	0	0.333	2.8436	0.0458	200
600	0	0.1584	0	0.4094	2.7492	0.0576	200

Steady State

Time	Tpx1SH	Tpx1ox2	Tpx1oxSOOH	Tpx1ox1	Trx1Txl1	Tpx1SOOH	H2O2
0	4	0	0	0	0	0	0
20	3.56	0	0	0.2195	0	0	0
60	3.56	0	0	0.2195	0	0	0

Tpx1 20 seconds after 0 - 1000 µM with Tpx1Trx1 H2O2 (exp1)

Time	H2O2	Tpx1SH	Tpx1SOOH	Tpx1ox2	Tpx1oxSOOH	Tpx1ox1	Tpx1Trx1
0	0	4	0	0	0	0	0
20	0	3.04	0	0	0	0.48	0

Time	H2O2	Tpx1SH	Tpx1SOOH	Tpx1ox2	Tpx1oxSOOH	Tpx1ox1	Tpx1Trx1
0	50	4	0	0	0	0	0
20	50	1.2668	0	0.194	0	1.0784	0.0942

Time	H2O2	Tpx1SH	Tpx1SOOH	Tpx1ox2	Tpx1oxSOOH	Tpx1ox1	Tpx1Trx1
0	100	4	0	0	0	0	0
20	100	0.0644	0	0.9894	0	0.8	0.1784

Time	H2O2	Tpx1SH	Tpx1SOOH	Tpx1ox2	Tpx1oxSOOH	Tpx1ox1	Tpx1Trx1
0	200	4	0	0	0	0	0
20	200	0	0	1.1992	0.2214	0.3992	0.1802

Time	H2O2	Tpx1SH	Tpx1SOOH	Tpx1ox2	Tpx1oxSOOH	Tpx1ox1	Tpx1Trx1
0	300	4	0	0	0	0	0
20	300	0	0	1.0892	0.3922	0.3332	0.1854

Time	H2O2	Tpx1SH	Tpx1SOOH	Tpx1ox2	Tpx1oxSOOH	Tpx1ox1	Tpx1Trx1
0	500	4	0	0	0	0	0
20	500	0	0	0.8966	0.6424	0.2918	0.1694

Time	H2O2	Tpx1SH	Tpx1SOOH	Tpx1ox2	Tpx1oxSOOH	Tpx1ox1	Tpx1Trx1
0	1000	4	0	0	0	0	0
20	1000	0	0	0.9336	0.9216	0	0.1448

Tpx1 20 seconds after 0 - 1000 µM with Tpx1Trx1 H2O2 (exp2)

Time	H2O2	Tpx1SH	Tpx1SOOH	Tpx1ox2	Tpx1oxSOOH	Tpx1ox1	Tpx1Trx1
0	0	4	0	0	0	0	0
20	0	3.7096	0	0	0	0.1452	0

Time	H2O2	Tpx1SH	Tpx1SOOH	Tpx1ox2	Tpx1oxSOOH	Tpx1ox1	Tpx1Trx1
0	50	4	0	0	0	0	0
20	50	1.2764	0	0.1634	0	1.0904	0.108

Time	H2O2	Tpx1SH	Tpx1SOOH	Tpx1ox2	Tpx1oxSOOH	Tpx1ox1	Tpx1Trx1
0	100	4	0	0	0	0	0
20	100	1.196	0	0.1572	0	1.1386	0.1062

Time	H2O2	Tpx1SH	Tpx1SOOH	Tpx1ox2	Tpx1oxSOOH	Tpx1ox1	Tpx1Trx1
0	200	4	0	0	0	0	0
20	200	0	0	0.7886	0.3852	0.4576	0.3688

Time	H2O2	Tpx1SH	Tpx1SOOH	Tpx1ox2	Tpx1oxSOOH	Tpx1ox1	Tpx1Trx1
0	300	4	0	0	0	0	0
20	300	0	0	0.911	0.4164	0.4242	0.2484

Time	H2O2	Tpx1SH	Tpx1SOOH	Tpx1ox2	Tpx1oxSOOH	Tpx1ox1	Tpx1Trx1
0	500	4	0	0	0	0	0
20	500	0	0.0352	0.8596	0.6456	0.2806	0.1968

Time	H2O2	Tpx1SH	Tpx1SOOH	Tpx1ox2	Tpx1oxSOOH	Tpx1ox1	Tpx1Trx1
0	1000	4	0	0	0	0	0
20	1000	0	0.13	0.9254	0.6782	0	0.0764

Reduced Trx1 (Trx1red) data

Time	H2O2	Trx1red
0	50	0.7
60	50	0.318
300	50	0.647
600	50	0.459

Time	H2O2	Trx1red
0	70	0.7
60	70	0.2

300	70	0.318
600	70	0.231

Time	H2O2	Trx1red
0	100	0.7
60	100	0.102
300	100	0.156
600	100	0.429

Time	H2O2	Trx1red
0	200	0.7
60	200	0.211
300	200	0.505
600	200	0.468

Time	H2O2	Trx1red
0	500	0.7
60	500	0.528
300	500	0.7
600	500	0.476

Time	H2O2	Trx1red
0	1000	0.7
60	1000	0.372
300	1000	0.699
600	1000	0.475

100 µM H2O2 Pap1 (0 - 600 sec)

Time	Pap1red	Pap1ox	H2O2
0	0.0245	0	100
30	0.015756	0.008744	100
60	0.013024	0.011476	100
120	0.010699	0.013801	100
300	0.010067	0.014433	100
600	0.010802	0.013698	100

Steady State

Time	Pap1red	Pap1ox	H2O2
0	0.0245	0	0
30	0.0238	0.0016	0
60	0.0238	0.0016	0

100 µM H2O2 Pap1 (0 - 60 sec)

Time	Pap1red	Pap1ox	H2O2
0	0.0245	0	100
30	0.0224	0.003	100
60	0.0208	0.0046	100

Steady State

Time	Pap1red	Pap1ox	H2O2
0	0.0245	0	0
30	0.024057	0.000443	0
60	0.024057	0.000443	0

100 µM H2O2 Pap1 (0 - 120 sec)

Time	Pap1red	Pap1ox	H2O2
0	0.0245	0	100
30	0.0216	0.0029	100
60	0.0194	0.0051	100
120	0.0181	0.0064	100

Steady State

Time	Pap1red	Pap1ox	H2O2
0	0.0245	0	0
30	0.0225	0.002	0
60	0.0225	0.002	0
120	0.0225	0.002	0

200 µM H2O2 Pap1 (0 - 600 sec)

Time	Pap1red	Pap1ox	H2O2
0	0.0245	0	200
60	0.0076	0.0169	200
300	0.0047	0.0198	200
600	0.0047	0.0198	200

Steady State

Time	Pap1red	Pap1ox	H2O2
0	0.0245	0	0
60	0.0219	0.0026	0

500 µM H2O2 Pap1 (0 - 60 sec)

Time	Pap1red	Pap1ox	H2O2
0	0.0245	0	500
30	0.0132	0.0122	500
60	0.0115	0.0139	500

Steady State

Time	Pap1red	Pap1ox	H2O2
0	0.0245	0	0
30	0.0229	0.0025	0
60	0.0229	0.0025	0

100 µM H2O2 Pap1 (0 - 3600 sec)

Time	Pap1red	Pap1ox	H2O2
0	0.0245	0	200
60	0.0053	0.0192	200
300	0.0022	0.0223	200
600	0.0032	0.0213	200
900	0.0031	0.0214	200
1200	0.0046	0.0199	200
1800	0.0139	0.0106	200
3600	0.0223	0.0022	200

Steady State

Time	Pap1red	Pap1ox	H2O2
0	0.0245	0	0
60	0.0233	0.0012	0

200 µM H2O2 Pap1 (0 - 3600 sec)

Time	Pap1red	Pap1ox	H2O2
0	0.0245	0	200
60	0.0084	0.0161	200
300	0.0046	0.0199	200
600	0.0043	0.0202	200
900	0.0057	0.0188	200
1200	0.0066	0.0179	200
1800	0.0152	0.0093	200
3600	0.021	0.0035	200

Steady State

Time	Pap1red	Pap1ox	H2O2
0	0.0245	0	0
60	0.0214	0.0031	0

500 µM H2O2 Pap1 (0 - 120 sec)

Time	Pap1red	Pap1ox	H2O2
0	0.0245	0	500
30	0.0135	0.011	500
60	0.0122	0.0123	500
120	0.0131	0.0114	500

Steady State

Time	Pap1red	Pap1ox	H2O2
0	0.0245	0	0
30	0.0223	0.0022	0
60	0.0223	0.0022	0

500 µM H2O2 Pap1 (0 - 1800 sec)

Time	Pap1red	Pap1ox	H2O2
0	0.0245	0	500
60	0.0115	0.013	500
300	0.0118	0.0127	500
300	0.0118	0.0127	500
900	0.0089	0.0156	500
1200	0.011	0.0135	500
1800	0.0215	0.003	500

Steady State

Time	Pap1red	Pap1ox	H2O2
0	0.0245	0	0
30	0.0218	0.0027	0
60	0.0218	0.0027	0

The tables display the quantitative data for $[H_2O_2]$ex, $[H_2O_2]$int, Tpx1, Trx1 and Pap1 used for parameter estimation (see 2.6). All data sets were calculated based on experimental data apart from the “Intracellular H_2O_2 data”, which was based on data from the literature (see 2.6). Each table is formatted in the correct

style required for use in parameter estimation. All data in the “Time” columns has units of seconds, and all other data has units of μM.

Reference list.

ADIMORA, N. J., JONES, D. P. & KEMP, M. L. 2010. A model of redox kinetics implicates the thiol proteome in cellular hydrogen peroxide responses. *Antioxid Redox Signal,* 13**,** 731-43.

AKAIKE, H. J. 1973. Information theory and an extension of the maximum likelihood principle. Akademiai Kiado, Budapest: Petrov, B. N. and Caski, F. (Eds.). pp. 267–281.

ALI, M. H., MUNGAI, P. T. & SCHUMACKER, P. T. 2006. Stretch-induced phosphorylation of focal adhesion kinase in endothelial cells: role of mitochondrial oxidants. *Am J Physiol Lung Cell Mol Physiol,* 291**,** L38-45.

ALON, U. 2007. Network motifs: theory and experimental approaches. *Nat Rev Genet,* 8**,** 450-61.

ANDZIAK, B., O'CONNOR, T. P., QI, W., DEWAAL, E. M., PIERCE, A., CHAUDHURI, A. R., VAN REMMEN, H. & BUFFENSTEIN, R. 2006. High oxidative damage levels in the longest-living rodent, the naked mole-rat. *Aging Cell,* 5**,** 463-471.

AVERY, A. M. & AVERY, S. V. 2001. Saccharomyces cerevisiae expresses three phospholipid hydroperoxide glutathione peroxidases. *J Biol Chem,* 276**,** 33730-5.

AZEVEDO, D., TACNET, F., DELAUNAY, A., RODRIGUES-POUSADA, C. & TOLEDANO, M. B. 2003. Two redox centers within Yap1 for H_2O_2 and thiol-reactive chemicals signaling. *Free Radic Biol Med,* 35**,** 889-900.

BAE, S. H., SUNG, S. H., CHO, E. J., LEE, S. K., LEE, H. E., WOO, H. A., YU, D.-Y., KIL, I. S. & RHEE, S. G. 2011. Concerted action of sulfiredoxin and peroxiredoxin I protects against alcohol-induced oxidative injury in mouse liver. *Hepatology,* 53**,** 945-953.

BAE, S. H., WOO, H. A., SUNG, S. H., LEE, H. E., LEE, S. K., KIL, I. S. & RHEE, S. G. 2008. Induction of Sulfiredoxin via an Nrf2-dependent pathway and hyperoxidation of Peroxiredoxin III in the Lungs of Mice exposed to hyperoxia. *Antioxidants & Redox Signaling,* 11**,** 937-948.

BAKER, L. M. & POOLE, L. B. 2003. Catalytic mechanism of thiol peroxidase from Escherichia coli. sulfenic acid formation and overoxidation of essential CYS61. *J Biol Chem,* 278**,** 9203-11.

BAO, R., ZHANG, Y., ZHOU, C. Z. & CHEN, Y. 2009. Structural and mechanistic analyses of yeast mitochondrial thioredoxin Trx3 reveal putative function of its additional cysteine residues. *Biochim Biophys Acta,* 1794**,** 716-21.

BASU, M. K. & KOONIN, E. V. 2005. Evolution of Eukaryotic Cysteine sulfinic scid reductase, Sulfiredoxin (Srx), from bacterial chromosome partitioning protein ParB. *Cell Cycle,* 4**,** 947-952.

BENHAR, M., ENGELBERG, D. & LEVITZKI, A. 2002. ROS, stress-activated kinases and stress signaling in cancer. *EMBO Rep,* 3**,** 420-5.

BISHOP, N. A. & GUARENTE, L. 2007. Genetic links between diet and lifespan: shared mechanisms from yeast to humans. *Nat Rev Genet,* 8**,** 835-44.

BITEAU, B., LABARRE, J. & TOLEDANO, M. B. 2003. ATP-dependent reduction of cysteine-sulphinic acid by S. cerevisiae sulphiredoxin. *Nature,* 425**,** 980-984.

BOKOV, A., CHAUDHURI, A. & RICHARDSON, A. 2004. The role of oxidative damage and stress in aging. *Mechanisms of Ageing and Development,* 125**,** 811-826.

BOSCHI-MULLER, S., AZZA, S. & BRANLANT, G. 2001. E. coli methionine sulfoxide reductase with a truncated N terminus or C terminus, or both, retains the ability to reduce methionine sulfoxide. *Protein Sci*, 10, 2272-2279.

BOSCHI-MULLER, S., OLRY, A., ANTOINE, M. & BRANLANT, G. 2005. The enzymology and biochemistry of methionine sulfoxide reductases. *Biochim Biophys Acta*, 1703, 231-238.

BOVERIS, A. & CHANCE, B. 1973. The mitochondrial generation of hydrogen peroxide. General properties and effect of hyperbaric oxygen. *Biochem J,* 134**,** 707-16.

BOZONET, S. M., FINDLAY, V. J., DAY, A. M., CAMERON, J., VEAL, E. A. & MORGAN, B. A. 2005. Oxidation of a Eukaryotic 2-Cys Peroxiredoxin Is a molecular switch controlling the

transcriptional response to Increasing levels of Hydrogen Peroxide. *Journal of Biological Chemistry,* 280**,** 23319-23327.

BRANDES, N., TIENSON, H., LINDEMANN, A., VITVITSKY, V., REICHMANN, D., BANERJEE, R. & JAKOB, U. 2013. Time line of redox events in aging postmitotic cells. *Elife,* 2**,** e00306.

BROWN, J. D., DAY, A. M., TAYLOR, S. R., TOMALIN, L. E., MORGAN, B. A. & VEAL, E. A. 2013. A peroxiredoxin promotes H_2O_2 signaling and oxidative stress resistance by oxidizing a thioredoxin family protein. Cell Rep, 5, 1425-35.

BRUNER, S. D., NORMAN, D. P. & VERDINE, G. L. 2000. Structural basis for recognition and repair of the endogenous mutagen 8-oxoguanine in DNA. *Nature,* 403**,** 859-66.

BUCK, V., QUINN, J., SOTO PINO, T., MARTIN, H., SALDANHA, J., MAKINO, K., MORGAN, B. A. & MILLAR, J. B. 2001. Peroxide sensors for the fission yeast stress-activated mitogen-activated protein kinase pathway. *Mol Biol Cell,* 12**,** 407-19.

BUTLER, J. & HOEY, B. M. 1993. The one-electron reduction potential of several substrates can be related to their reduction rates by cytochrome P-450 reductase. *Biochim Biophys Acta,* 1161**,** 73-8.

CALVO, I. A., AYTE, J. & HIDALGO, E. 2013. Reversible thiol oxidation in the H_2O_2-dependent activation of the transcription factor Pap1. *J Cell Sci,* 126**,** 2279-84.

CALVO, I. A., GARCIA, P., AYTE, J. & HIDALGO, E. 2012. The transcription factors Pap1 and Prr1 collaborate to activate antioxidant, but not drug tolerance, genes in response to H_2O_2. *Nucleic Acids Res,* 40**,** 4816-24.

CAO, Z., SUBRAMANIAM, S. & BULLEID, N. J. 2014. Lack of an efficient endoplasmic reticulum-localized recycling system protects peroxiredoxin IV from hyperoxidation. *J Biol Chem,* 289**,** 5490-8.

CARMEL-HAREL, O., STEARMAN, R., GASCH, A. P., BOTSTEIN, D., BROWN, P. O. & STORZ, G. 2001. Role of thioredoxin reductase in the Yap1p-dependent response to oxidative stress in Saccharomyces cerevisiae. *Mol Microbiol,* 39**,** 595-605.

CASTILLO, E. A., VIVANCOS, A. P., JONES, N., AYTE, J. & HIDALGO, E. 2003. Schizosaccharomyces pombe cells lacking the Ran-binding protein Hba1 show a multidrug resistance phenotype due to constitutive nuclear accumulation of Pap1. *J Biol Chem,* 278**,** 40565-72.

CHAE, H. Z., CHUNG, S. J. & RHEE, S. G. 1994a. Thioredoxin-dependent peroxide reductase from yeast. *Journal of Biological Chemistry,* 269**,** 27670-27678.

CHAE, H. Z., KIM, H. J., KANG, S. W. & RHEE, S. G. 1999. Characterization of three isoforms of mammalian peroxiredoxin that reduce peroxides in the presence of thioredoxin. *Diabetes Res Clin Pract,* 45**,** 101-12.

CHAE, H. Z., ROBISON, K., POOLE, L. B., CHURCH, G., STORZ, G. & RHEE, S. G. 1994b. Cloning and sequencing of thiol-specific antioxidant from mammalian brain: alkyl hydroperoxide reductase and thiol-specific antioxidant define a large family of antioxidant enzymes. *Proceedings of the National Academy of Sciences,* 91**,** 7017-7021.

CHAE, H. Z., UHM, T. B. & RHEE, S. G. 1994c. Dimerization of thiol-specific antioxidant and the essential role of cysteine 47. *Proceedings of the National Academy of Sciences,* 91**,** 7022-7026.

CHAMBERS, J. M. 1992. *Linear models.* Chapter 4 of *Statistical Models in S* eds J. M. Chambers and T. J. Hastie, Wadsworth & Brooks/Cole.

CHANCE, B., SIES, H. & BOVERIS, A. 1979. Hydroperoxide metabolism in mammalian organs. *Physiol Rev,* 59**,** 527-605.

CHANG, T.-S., JEONG, W., WOO, H. A., LEE, S. M., PARK, S. & RHEE, S. G. 2004. Characterization of mammalian sulfiredoxin and its reactivation of hyperoxidized Peroxiredoxin through reduction of cysteine sulfinic acid in the active site to cysteine. *Journal of Biological Chemistry,* 279**,** 50994-51001.

CHAUDIÈRE, J. & FERRARI-ILIOU, R. 1999. Intracellular Antioxidants: from chemical to biochemical mechanisms. *Food and Chemical Toxicology,* 37**,** 949-962.

CHELIKANI, P., FITA, I. & LOEWEN, P. C. 2004. Diversity of structures and properties among catalases. *Cell Mol Life Sci,* 61**,** 192-208.

CHEN, D., TOONE, W. M., MATA, J., LYNE, R., BURNS, G., KIVINEN, K., BRAZMA, A., JONES, N. & BAHLER, J. 2003. Global transcriptional responses of fission yeast to environmental stress. Mol Biol Cell, 14, 214-29.

CHEN, D., WILKINSON, C. R., WATT, S., PENKETT, C. J., TOONE, W. M., JONES, N. & BAHLER, J. 2008. Multiple pathways differentially regulate global oxidative stress responses in fission yeast. *Mol Biol Cell,* 19**,** 308-17.

CHEN, Q., VAZQUEZ, E. J., MOGHADDAS, S., HOPPEL, C. L. & LESNEFSKY, E. J. 2003. Production of reactive oxygen species by Mitochondria. *Journal of Biological Chemistry,* 278**,** 36027-36031.

CHEN, R. E. & THORNER, J. 2007. Function and regulation in MAPK signaling pathways: lessons learned from the yeast Saccharomyces cerevisiae. *Biochim Biophys Acta,* 1773**,** 1311-40.

CHIARUGI, P., PANI, G., GIANNONI, E., TADDEI, L., COLAVITTI, R., RAUGEI, G., SYMONS, M., BORRELLO, S., GALEOTTI, T. & RAMPONI, G. 2003. Reactive oxygen species as essential mediators of cell adhesion: the oxidative inhibition of a FAK tyrosine phosphatase is required for cell adhesion. *J Cell Biol,* 161**,** 933-44.

CHOI, H. J., KANG, S. W., YANG, C. H., RHEE, S. G. & RYU, S. E. 1998. Crystal structure of a novel human peroxidase enzyme at 2.0 A resolution. *Nat Struct Biol,* 5**,** 400-6.

CHOI, M. H., LEE, I. K., KIM, G. W., KIM, B. U., HAN, Y. H., YU, D. Y., PARK, H. S., KIM, K. Y., LEE, J. S., CHOI, C., BAE, Y. S., LEE, B. I., RHEE, S. G. & KANG, S. W. 2005. Regulation of PDGF signalling and vascular remodelling by peroxiredoxin II. *Nature,* 435**,** 347-53.

CHRISTMAN, M. F., MORGAN, R. W., JACOBSON, F. S. & AMES, B. N. 1985. Positive control of a regulon for defenses against oxidative stress and some heat-shock proteins in Salmonella typhimurium. *Cell,* 41**,** 753-62.

COLEMAN, S. T., EPPING, E. A., STEGGERDA, S. M. & MOYE-ROWLEY, W. S. 1999. Yap1p activates gene transcription in an oxidant-specific fashion. *Mol Cell Biol,* 19**,** 8302-13.

COLLINSON, E. J., WHEELER, G. L., GARRIDO, E. O., AVERY, A. M., AVERY, S. V. & GRANT, C. M. 2002. The yeast glutaredoxins are active as glutathione peroxidases. *J Biol Chem,* 277**,** 16712-7.

COLLINSON, L. P. & DAWES, I. W. 1992. Inducibility of the response of yeast cells to peroxide stress. *J Gen Microbiol,* 138**,** 329-335.

CONWAY, J. P. & KINTER, M. 2006. Dual role of peroxiredoxin I in macrophage-derived foam cells. *J Biol Chem,* 281**,** 27991-8001.

COX, A. G., PESKIN, A. V., PATON, L. N., WINTERBOURN, C. C. & HAMPTON, M. B. 2009. Redox potential and peroxide reactivity of human peroxiredoxin 3. *Biochemistry,* 48**,** 6495-501.

CRAVEN, R. A., GRIFFITHS, D. J., SHELDRICK, K. S., RANDALL, R. E., HAGAN, I. M. & CARR, A. M. 1998. Vectors for the expression of tagged proteins in Schizosaccharomyces pombe. *Gene,* 221**,** 59-68.

CUDDIHY, S. L., WINTERBOURN, C. C. & HAMPTON, M. B. 2011. Assessment of redox changes to hydrogen peroxide-sensitive proteins during EGF signaling. *Antioxid Redox Signal,* 15**,** 167-74.

CULLINAN, S. B., GORDAN, J. D., JIN, J., HARPER, J. W. & DIEHL, J. A. 2004. The Keap1-BTB protein is an adaptor that bridges Nrf2 to a Cul3-based E3 ligase: oxidative stress sensing by a Cul3-Keap1 ligase. *Mol Cell Biol,* 24**,** 8477-86.

DANGOOR, I., PELED-ZEHAVI, H., WITTENBERG, G. & DANON, A. 2012. A chloroplast light-regulated oxidative sensor for moderate light intensity in Arabidopsis. *Plant Cell,* 24**,** 1894-906.

DAVIES, J. M., LOWRY, C. V. & DAVIES, K. J. 1995. Transient adaptation to oxidative stress in yeast. *Arch Biochem Biophys,* 317**,** 1-6.

DAY, ALISON M., BROWN, JONATHON D., TAYLOR, SARAH R., RAND, JONATHAN D., MORGAN, BRIAN A. & VEAL, ELIZABETH A. 2012. Inactivation of a Peroxiredoxin by hydrogen peroxide is critical for Thioredoxin-Mediated repair of oxidized proteins and Cell Survival. *Molecular Cell,* 45**,** 398-408.

DAY, A. M. & VEAL, E. A. 2010. Hydrogen peroxide-sensitive cysteines in the Sty1 MAPK regulate the transcriptional response to oxidative stress. *J Biol Chem,* 285**,** 7505-16.

DEGOLS, G., SHIOZAKI, K. & RUSSELL, P. 1996. Activation and regulation of the Spc1 stress-activated protein kinase in Schizosaccharomyces pombe. *Mol Cell Biol,* 16**,** 2870-7.

DELAUNAY, A., ISNARD, A. D. & TOLEDANO, M. B. 2000. H_2O_2 sensing through oxidation of the Yap1 transcription factor. *EMBO J,* 19**,** 5157-66.

DELAUNAY, A., PFLIEGER, D., BARRAULT, M. B., VINH, J. & TOLEDANO, M. B. 2002. A thiol peroxidase is an H2O2 receptor and redox-transducer in gene activation. *Cell,* 111**,** 471-81.

DEMPLE, B. & HALBROOK, J. 1983. Inducible repair of oxidative DNA damage in Escherichia coli. *Nature,* 304**,** 466-8.

DEYULIA, G. J., JR. & CARCAMO, J. M. 2005. EGF receptor-ligand interaction generates extracellular hydrogen peroxide that inhibits EGFR-associated protein tyrosine phosphatases. *Biochem Biophys Res Commun,* 334**,** 38-42.

DEYULIA, G. J., JR., CARCAMO, J. M., BORQUEZ-OJEDA, O., SHELTON, C. C. & GOLDE, D. W. 2005. Hydrogen peroxide generated extracellularly by receptor-ligand interaction facilitates cell signaling. *Proc Natl Acad Sci U S A,* 102**,** 5044-9.

DHAKSHINAMOORTHY, S., JAIN, A. K., BLOOM, D. A. & JAISWAL, A. K. 2005. Bach1 competes with Nrf2 leading to negative regulation of the antioxidant response element (ARE)-mediated NAD(P)H:quinone oxidoreductase 1 gene expression and induction in response to antioxidants. *J Biol Chem,* 280**,** 16891-900.

DHILLON, A. S., HAGAN, S., RATH, O. & KOLCH, W. 2007. MAP kinase signalling pathways in cancer. *Oncogene,* 26**,** 3279-90.

DICKINSON, B. C. & CHANG, C. J. 2008. A targetable fluorescent probe for imaging hydrogen peroxide in the mitochondria of living cells. *J Am Chem Soc,* 130**,** 9638-9.

DICKINSON, B. C., HUYNH, C. & CHANG, C. J. 2010. A palette of fluorescent probes with varying emission colors for imaging hydrogen peroxide signaling in living cells. *J Am Chem Soc,* 132**,** 5906-15.

DIRMEIER, R., O'BRIEN, K. M., ENGLE, M., DODD, A., SPEARS, E. & POYTON, R. O. 2002. Exposure of yeast cells to anoxia induces transient oxidative stress. Implications for the induction of hypoxic genes. *J Biol Chem,* 277**,** 34773-84.

DOONAN, R., MCELWEE, J. J., MATTHIJSSENS, F., WALKER, G. A., HOUTHOOFD, K., BACK, P., MATSCHESKI, A., VANFLETEREN, J. R. & GEMS, D. 2008. Against the oxidative damage theory of aging: superoxide dismutases protect against oxidative stress but have little or no effect on life span in Caenorhabditis elegans. *Genes Dev,* 22**,** 3236-41.

DROGE, W. 2002. Free radicals in the physiological control of cell function. *Physiol Rev,* 82**,** 47-95.

DURIGON, R., WANG, Q., CEH PAVIA, E., GRANT, C. M. & LU, H. 2012. Cytosolic thioredoxin system facilitates the import of mitochondrial small Tim proteins. EMBO Rep, 13, 916-22.

ERUSLANOV, E. & KUSMARTSEV, S. 2010. Identification of ROS using oxidized DCFDA and flow-cytometry. *Methods Mol Biol,* 594**,** 57-72.

FAULKNER, M. J. & HELMANN, J. D. 2011. Peroxide stress elicits adaptive changes in bacterial metal ion homeostasis. *Antioxid Redox Signal,* 15**,** 175-89.

FAY, A. J., QIAN, X., JAN, Y. N. & JAN, L. Y. 2006. SK channels mediate NADPH oxidase-independent reactive oxygen species production and apoptosis in granulocytes. *Proc Natl Acad Sci U S A,* 103**,** 17548-53.

FOREMAN, J., DEMIDCHIK, V., BOTHWELL, J. H., MYLONA, P., MIEDEMA, H., TORRES, M. A., LINSTEAD, P., COSTA, S., BROWNLEE, C., JONES, J. D., DAVIES, J. M. & DOLAN, L. 2003. Reactive oxygen species produced by NADPH oxidase regulate plant cell growth. *Nature,* 422**,** 442-6.

FRIDOVICH, I. 1986. Biological effects of the superoxide radical. *Arch Biochem Biophys,* 247**,** 1-11.

FUJINO, G., NOGUCHI, T., MATSUZAWA, A., YAMAUCHI, S., SAITOH, M., TAKEDA, K. & ICHIJO, H. 2007. Thioredoxin and TRAF family proteins regulate reactive oxygen species-dependent activation of ASK1 through reciprocal modulation of the N-terminal homophilic interaction of ASK1. *Mol Cell Biol,* 27**,** 8152-63.

GARCIA-SANTAMARINA, S., BORONAT, S., CALVO, I. A., RODRIGUEZ-GABRIEL, M., AYTE, J., MOLINA, H. & HIDALGO, E. 2013. Is oxidized thioredoxin a major trigger for cysteine oxidation? Clues from a redox proteomics approach. *Antioxid Redox Signal,* 18**,** 1549-56.

GARCIA-SANTAMARINA, S., BORONAT, S., ESPADAS, G., AYTE, J., MOLINA, H. & HIDALGO, E. 2011. The oxidized thiol proteome in fission yeast--optimization of an ICAT-based method to identify H_2O_2-oxidized proteins. *J Proteomics,* 74**,** 2476-86.

GOBLIRSCH, B., KURKER, R. C., STREIT, B. R., WILMOT, C. M. & DUBOIS, J. L. 2011. Chlorite dismutases, DyPs, and EfeB: 3 microbial heme enzyme families comprise the CDE structural superfamily. *J Mol Biol,* 408**,** 379-98.

GOTH, L., RASS, P. & PAY, A. 2004. Catalase enzyme mutations and their association with diseases. *Mol Diagn,* 8**,** 141-9.

GRANT, C. M. 2001. Role of the glutathione/glutaredoxin and thioredoxin systems in yeast growth and response to stress conditions. *Molecular Microbiology,* 39**,** 533-541.

GRANT, C. M., COLLINSON, L. P., ROE, J. H. & DAWES, I. W. 1996. Yeast glutathione reductase is required for protection against oxidative stress and is a target gene for yAP-1 transcriptional regulation. *Mol Microbiol,* 21**,** 171-9.

GUARENTE, L. & KENYON, C. 2000. Genetic pathways that regulate ageing in model organisms. *Nature,* 408**,** 255-262.

GULSHAN, K., ROVINSKY, S. A., COLEMAN, S. T. & MOYE-ROWLEY, W. S. 2005. Oxidant-specific folding of Yap1p regulates both transcriptional activation and nuclear localization. *J Biol Chem,* 280**,** 40524-33.

GUTSCHER, M., SOBOTTA, M. C., WABNITZ, G. H., BALLIKAYA, S., MEYER, A. J., SAMSTAG, Y. & DICK, T. P. 2009. Proximity-based protein thiol oxidation by H_2O_2-scavenging peroxidases. *J Biol Chem,* 284**,** 31532-40.

HALLIWELL, B. & GUTTERIDGE, J. M. 1985. The importance of free radicals and catalytic metal ions in human diseases. *Mol Aspects Med,* 8**,** 89-193.

HANUKOGLU, I., RAPOPORT, R., WEINER, L. & SKLAN, D. 1993. Electron leakage from the mitochondrial NADPH-adrenodoxin reductase-adrenodoxin-P450scc (cholesterol side chain cleavage) system. *Arch Biochem Biophys,* 305**,** 489-98.

HARIDAS, V., NI, J., MEAGER, A., SU, J., YU, G. L., ZHAI, Y., KYAW, H., AKAMA, K. T., HU, J., VAN ELDIK, L. J. & AGGARWAL, B. B. 1998. TRANK, a novel cytokine that activates NF-kappa B and c-Jun N-terminal kinase. *J Immunol,* 161**,** 1-6.

HARMAN, D. 1956. Aging: a theory based on free radical and radiation chemistry. *J Gerontol,* 11**,** 298-300.

HARMAN, D. 1972. The biologic clock: the mitochondria? *J Am Geriatr Soc,* 20**,** 145-7.

HART, Y., ANTEBI, Y. E., MAYO, A. E., FRIEDMAN, N. & ALON, U. 2012. Design principles of cell circuits with paradoxical components. *Proc Natl Acad Sci U S A,* 109**,** 8346-51.

HAYES, J. D. & MCLELLAN, L. I. 1999. Glutathione and glutathione-dependent enzymes represent a co-ordinately regulated defence against oxidative stress. *Free Radic Res,* 31**,** 273-300.

HAYNES, A. C., QIAN, J., REISZ, J. A., FURDUI, C. M. & LOWTHER, W. T. 2013. Molecular basis for the resistance of human mitochondrial 2-Cys peroxiredoxin 3 to hyperoxidation. *J Biol Chem,* 288**,** 29714-23.

HE, X. J. & FASSLER, J. S. 2005. Identification of novel Yap1p and Skn7p binding sites involved in the oxidative stress response of Saccharomyces cerevisiae. *Mol Microbiol,* 58**,** 1454-67.

HE, X. J., MULFORD, K. E. & FASSLER, J. S. 2009. Oxidative stress function of the Saccharomyces cerevisiae Skn7 receiver domain. *Eukaryot Cell,* 8**,** 768-78.

HOLMGREN, A. & LU, J. 2010. Thioredoxin and thioredoxin reductase: Current research with special reference to human disease. *Biochemical and Biophysical Research Communications,* 396**,** 120-124.

HONDA, Y. & HONDA, S. 1999. The daf-2 gene network for longevity regulates oxidative stress resistance and Mn-superoxide dismutase gene expression in Caenorhabditis elegans. *The FASEB Journal,* 13**,** 1385-1393.

HOOPS, S., SAHLE, S., GAUGES, R., LEE, C., PAHLE, J., SIMUS, N., SINGHAL, M., XU, L., MENDES, P. & KUMMER, U. (2006). COPASI: a COmplex PAthway SImulator. *Bioinformatics* 22, 3067-74.

INOUE, Y., MATSUDA, T., SUGIYAMA, K., IZAWA, S. & KIMURA, A. 1999. Genetic analysis of glutathione peroxidase in oxidative stress response of Saccharomyces cerevisiae. *J Biol Chem,* 274**,** 27002-9.

ISHIKAWA, M., NUMAZAWA, S. & YOSHIDA, T. 2005. Redox regulation of the transcriptional repressor Bach1. *Free Radic Biol Med,* 38**,** 1344-52.

ISOYAMA, T., MURAYAMA, A., NOMOTO, A. & KUGE, S. 2001. Nuclear import of the yeast AP-1-like transcription factor Yap1p is mediated by transport receptor Pse1p, and this import step is not affected by oxidative stress. *J Biol Chem,* 276**,** 21863-9.

ITOH, K., CHIBA, T., TAKAHASHI, S., ISHII, T., IGARASHI, K., KATOH, Y., OYAKE, T., HAYASHI, N., SATOH, K., HATAYAMA, I., YAMAMOTO, M. & NABESHIMA, Y. 1997. An Nrf2/small Maf heterodimer mediates the induction of phase II detoxifying enzyme genes through antioxidant response elements. *Biochem Biophys Res Commun,* 236**,** 313-22.

ITOH, K., WAKABAYASHI, N., KATOH, Y., ISHII, T., IGARASHI, K., ENGEL, J. D. & YAMAMOTO, M. 1999. Keap1 represses nuclear activation of antioxidant responsive elements by Nrf2 through binding to the amino-terminal Neh2 domain. *Genes Dev,* 13**,** 76-86.

IZAWA, S., MAEDA, K., SUGIYAMA, K., MANO, J., INOUE, Y. & KIMURA, A. 1999. Thioredoxin deficiency causes the constitutive activation of Yap1, an AP-1-like transcription factor in Saccharomyces cerevisiae. *J Biol Chem,* 274**,** 28459-65.

JAMIESON, D. J. 1998. Oxidative stress responses of the yeast Saccharomyces cerevisiae. *Yeast,* 14**,** 1511-1527.

JANG, H. H., LEE, K. O., CHI, Y. H., JUNG, B. G., PARK, S. K., PARK, J. H., LEE, J. R., LEE, S. S., MOON, J. C., YUN, J. W., CHOI, Y. O., KIM, W. Y., KANG, J. S., CHEONG, G. W., YUN, D. J., RHEE, S. G., CHO, M. J. & LEE, S. Y. 2004. Two enzymes in one; two yeast peroxiredoxins display oxidative stress-dependent switching from a peroxidase to a molecular chaperone function. *Cell,* 117**,** 625-35.

JANG, Y. C., PÉREZ, V. I., SONG, W., LUSTGARTEN, M. S., SALMON, A. B., MELE, J., QI, W., LIU, Y., LIANG, H., CHAUDHURI, A., IKENO, Y., EPSTEIN, C. J., VAN REMMEN, H. & RICHARDSON, A. 2009. Overexpression of Mn Superoxide Dismutase does not increase life span in Mice. *The Journals of Gerontology Series A: Biological Sciences and Medical Sciences,* 64A**,** 1114-1125.

JARA, M., VIVANCOS, A. P., CALVO, I. A., MOLDON, A., SANSO, M. & HIDALGO, E. 2007. The peroxiredoxin Tpx1 is essential as a H2O2 scavenger during aerobic growth in fission yeast. *Mol Biol Cell,* 18**,** 2288-95.

JARVELA, S., RANTALA, I., RODRIGUEZ, A., KALLIO, H., PARKKILA, S., KINNULA, V. L., SOINI, Y. & HAAPASALO, H. 2010. Specific expression profile and prognostic significance of peroxiredoxins in grade II-IV astrocytic brain tumors. *BMC Cancer,* 10**,** 104.

JARVIS, R. M., HUGHES, S. M. & LEDGERWOOD, E. C. 2012. Peroxiredoxin 1 functions as a signal peroxidase to receive, transduce, and transmit peroxide signals in mammalian cells. *Free Radic Biol Med,* 53**,** 1522-30.

JEONG, W., PARK, S. J., CHANG, T.-S., LEE, D.-Y. & RHEE, S. G. 2006. Molecular Mechanism of the reduction of cysteine sulfinic acid of Peroxiredoxin to cysteine by Mammalian Sulfiredoxin. *Journal of Biological Chemistry,* 281**,** 14400-14407.

JOHNSON, N. L., KOTZ, S. & BALAKRISHNAN, N. 1995. Continuous univariate distributions, volume 2, chapters 27 and 30. Wiley, New York.

JONSSON, T. J., JOHNSON, L. C. & LOWTHER, W. T. 2008. Structure of the sulphiredoxin-peroxiredoxin complex reveals an essential repair embrace. *Nature,* 451**,** 98-101.

JÖNSSON, T. J., JOHNSON, L. C. & LOWTHER, W. T. 2009. Protein engineering of the quaternary Sulfiredoxin·Peroxiredoxin enzyme·substrate complex reveals the molecular basis for cysteine sulfinic acid phosphorylation. *Journal of Biological Chemistry,* 284**,** 33305-33310.

JÖNSSON, T. J., MURRAY, M. S., JOHNSON, L. C., POOLE, L. B. & LOWTHER, W. T. 2005. Structural basis for the retroreduction of inactivated Peroxiredoxins by Human Sulfiredoxin†,‡. *Biochemistry,* 44**,** 8634-8642.

KANG, D. H., LEE, D. J., LEE, K. W., PARK, Y. S., LEE, J. Y., LEE, S. H., KOH, Y. J., KOH, G. Y., CHOI, C., YU, D. Y., KIM, J. & KANG, S. W. 2011. Peroxiredoxin II is an essential antioxidant enzyme that prevents the oxidative inactivation of VEGF receptor-2 in vascular endothelial cells. *Mol Cell,* 44**,** 545-58.

KANG, S. W., CHANG, T. S., LEE, T. H., KIM, E. S., YU, D. Y. & RHEE, S. G. 2004. Cytosolic peroxiredoxin attenuates the activation of Jnk and p38 but potentiates that of Erk in Hela cells stimulated with tumor necrosis factor-alpha. *J Biol Chem,* 279**,** 2535-43.

KARIHTALA, P., MANTYNIEMI, A., KANG, S. W., KINNULA, V. L. & SOINI, Y. 2003. Peroxiredoxins in breast carcinoma. *Clin Cancer Res,* 9**,** 3418-24.

KIL, I. S., LEE, S. K., RYU, K. W., WOO, H. A., HU, M. C., BAE, S. H. & RHEE, S. G. 2012. Feedback control of adrenal steroidogenesis via H_2O_2-dependent, reversible inactivation of peroxiredoxin III in mitochondria. *Mol Cell,* 46**,** 584-94.

KIM, D. U., HAYLES, J., KIM, D., WOOD, V., PARK, H. O., WON, M., YOO, H. S., DUHIG, T., NAM, M., PALMER, G., HAN, S., JEFFERY, L., BAEK, S. T., LEE, H., SHIM, Y. S., LEE, M., KIM, L., HEO, K. S., NOH, E. J., LEE, A. R., JANG, Y. J., CHUNG, K. S., CHOI, S. J., PARK, J. Y., PARK, Y., KIM, H. M., PARK, S. K., PARK, H. J., KANG, E. J., KIM, H. B., KANG, H. S., PARK, H. M., KIM, K., SONG, K., SONG, K. B., NURSE, P. & HOE, K. L. 2010. Analysis of a genome-wide set of gene deletions in the fission yeast Schizosaccharomyces pombe. *Nat Biotechnol,* 28**,** 617-23.

KIM, S. Y., KIM, T. J. & LEE, K. Y. 2008. A novel function of peroxiredoxin 1 (Prx-1) in apoptosis signal-regulating kinase 1 (ASK1)-mediated signaling pathway. *FEBS Lett,* 582**,** 1913-8.

KOBAYASHI, M. & YAMAMOTO, M. 2006. Nrf2-Keap1 regulation of cellular defense mechanisms against electrophiles and reactive oxygen species. *Adv Enzyme Regul,* 46**,** 113-40.

KOO, K. H., LEE, S., JEONG, S. Y., KIM, E. T., KIM, H. J., KIM, K., SONG, K. & CHAE, H. Z. 2002. Regulation of Thioredoxin Peroxidase activity by C-terminal truncation. *Archives of Biochemistry and Biophysics,* 397**,** 312-318.

KUDO, N., TAOKA, H., TODA, T., YOSHIDA, M. & HORINOUCHI, S. 1999. A novel nuclear export signal sensitive to oxidative stress in the fission yeast transcription factor Pap1. *J Biol Chem,* 274**,** 15151-8.

KUGE, S., ARITA, M., MURAYAMA, A., MAETA, K., IZAWA, S., INOUE, Y. & NOMOTO, A. 2001. Regulation of the yeast Yap1p nuclear export signal is mediated by redox signal-induced reversible disulfide bond formation. *Mol Cell Biol,* 21**,** 6139-50.

KUGE, S. & JONES, N. 1994. YAP1 dependent activation of TRX2 is essential for the response of Saccharomyces cerevisiae to oxidative stress by hydroperoxides. *EMBO J,* 13**,** 655-64.

KUGE, S., JONES, N. & NOMOTO, A. 1997. Regulation of yAP-1 nuclear localization in response to oxidative stress. *EMBO J,* 16**,** 1710-20.

KUMSTA, C. & JAKOB, U. 2009. Redox-regulated chaperones. *Biochemistry,* 48**,** 4666-76.

KYRIAKIS, J. M. & AVRUCH, J. 2001. Mammalian mitogen-activated protein kinase signal transduction pathways activated by stress and inflammation. *Physiol Rev,* 81**,** 807-69.

LACKNER, D. H., SCHMIDT, M. W., WU, S., WOLF, D. A. & BAHLER, J. 2012. Regulation of transcriptome, translation, and proteome in response to environmental stress in fission yeast. *Genome Biol,* 13**,** R25.

LAEMMLI, U. K. 1970. Cleavage of structural proteins during the assembly of the head of bacteriophage T4. *Nature,* 227**,** 680-5.

LAWRENCE, C. L., JONES, N. & WILKINSON, C. R. 2009. Stress-Induced phosphorylation of *S. pombe* Atf1 abrogates its interaction with F Box protein Fbh1. *Curr Biol,* 282**,** 1907-7.

LAWRENCE, C. L., MAEKAWA, H., WORTHINGTON, J. L., REITER, W., WILKINSON, C. R. & JONES, N. 2007. Regulation of Schizosaccharomyces pombe Atf1 protein levels by Sty1-mediated phosphorylation and heterodimerization with Pcr1. *J Biol Chem,* 282**,** 5160-70.

LEBOVITZ, R. M., ZHANG, H., VOGEL, H., CARTWRIGHT, J., DIONNE, L., LU, N., HUANG, S. & MATZUK, M. M. 1996. Neurodegeneration, myocardial injury, and perinatal death in mitochondrial superoxide dismutase-deficient mice. *Proceedings of the National Academy of Sciences,* 93**,** 9782-9787.

LEE, D.-Y., PARK, S. J., JEONG, W., SUNG, H. J., OHO, T., WU, X., RHEE, S. G. & GRUSCHUS, J. M. 2006. Mutagenesis and modeling of the Peroxiredoxin (Prx) complex with the NMR Structure of ATP-bound Human Sulfiredoxin implicate aspartate 187 of Prx I as the catalytic residue in ATP Hydrolysis‡. *Biochemistry,* 45**,** 15301-15309.

LEE, S., KIM, S. M. & LEE, R. T. 2013. Thioredoxin and thioredoxin target proteins: from molecular mechanisms to functional significance. *Antioxid Redox Signal,* 18**,** 1165-207.

LI, Y., HUANG, T.-T., CARLSON, E. J., MELOV, S., URSELL, P. C., OLSON, J. L., NOBLE, L. J., YOSHIMURA, M. P., BERGER, C., CHAN, P. H., WALLACE, D. C. & EPSTEIN, C. J. 1995. Dilated cardiomyopathy and neonatal lethality in mutant mice lacking manganese superoxide dismutase. *Nat Genet,* 11**,** 376-381.

LILLIG, C. H., BERNDT, C. & HOLMGREN, A. 2008. Glutaredoxin systems. *Biochim Biophys Acta,* 1780**,** 1304-17.

LIU, X. P., LIU, X. Y., ZHANG, J., XIA, Z. L., LIU, X., QIN, H. J. & WANG, D. W. 2006. Molecular and functional characterization of sulfiredoxin homologs from higher plants. *Cell Res,* 16**,** 287-96.

LONGO, V. D., GRALLA, E. B. & VALENTINE, J. S. 1996. Superoxide Dismutase activity is essential for stationary phase survival in Saccharomyces cerevisiae. *Journal of Biological Chemistry,* 271**,** 12275-12280.

LONGO, V. D., LIOU, L.-L., VALENTINE, J. S. & GRALLA, E. B. 1999. Mitochondrial Superoxide Decreases yeast survival in stationary phase. *Archives of Biochemistry and Biophysics,* 365**,** 131-142.

MA, L. H., TAKANISHI, C. L. & WOOD, M. J. 2007. Molecular mechanism of oxidative stress perception by the Orp1 protein. *J Biol Chem,* 282**,** 31429-36.

MAKINO, N., MISE, T. & SAGARA, J. 2008. Kinetics of hydrogen peroxide elimination by astrocytes and C6 glioma cells analysis based on a mathematical model. *Biochim Biophys Acta,* 1780**,** 927-36.

MANIATIS, T., FRITSCH, E. and Sambrook, J. 1982. Molecular cloning, a laboratory manual. Cold Spring Harbour, New York, Cold Spring Harbour Laboratory Press.

MARGUERAT, S., SCHMIDT, A., CODLIN, S., CHEN, W., AEBERSOLD, R. & BAHLER, J. 2012. Quantitative analysis of fission yeast transcriptomes and proteomes in proliferating and quiescent cells. *Cell,* 151**,** 671-83.

MARIOTTI, M., RIDGE, P. G., ZHANG, Y., LOBANOV, A. V., PRINGLE, T. H., GUIGO, R., HATFIELD, D. L. & GLADYSHEV, V. N. 2012. Composition and evolution of the vertebrate and mammalian selenoproteomes. *PLoS One,* 7**,** e33066.

MARQUARDT, D. W. 1963. An algorithm for least squares estimation of nonlinear parameters. *Siam Journal on Algebraic and Discrete Methods,* 11**,** 431-441.

MATSUYAMA, A., ARAI, R., YASHIRODA, Y., SHIRAI, A., KAMATA, A., SEKIDO, S., KOBAYASHI, Y., HASHIMOTO, A., HAMAMOTO, M., HIRAOKA, Y., HORINOUCHI, S. & YOSHIDA, M. 2006. ORFeome cloning and global analysis of protein localization in the fission yeast Schizosaccharomyces pombe. *Nat Biotechnol,* 24**,** 841-7.

MILLER, E. W., DICKINSON, B. C. & CHANG, C. J. 2010. Aquaporin-3 mediates hydrogen peroxide uptake to regulate downstream intracellular signaling. *Proc Natl Acad Sci U S A,* 107**,** 15681-6.

MISSALL, T. A., CHERRY-HARRIS, J. F. & LODGE, J. K. 2005. Two glutathione peroxidases in the fungal pathogen Cryptococcus neoformans are expressed in the presence of specific substrates. *Microbiology,* 151**,** 2573-81.

MOLIN, M., YANG, J., HANZÉN, S., TOLEDANO, MICHEL B., LABARRE, J. & NYSTRÖM, T. 2011. Life span extension and H_2O_2 resistance elicited by caloric restriction require the Peroxiredoxin Tsa1 in Saccharomyces cerevisiae. *Molecular Cell,* 43**,** 823-833.

MOON, J. C., HAH, Y.-S., KIM, W. Y., JUNG, B. G., JANG, H. H., LEE, J. R., KIM, S. Y., LEE, Y. M., JEON, M. G., KIM, C. W., CHO, M. J. & LEE, S. Y. 2005. Oxidative stress-dependent structural and functional switching of a Human 2-Cys Peroxiredoxin Isotype II that enhances HeLa Cell resistance to H_2O_2-induced cell death. *Journal of Biological Chemistry,* 280**,** 28775-28784.

MORENO, S., KLAR, A. & NURSE, P. 1991. Molecular genetic analysis of fission yeast Schizosaccharomyces pombe. *Methods Enzymol,* 194**,** 795-823.

MORGAN, B. A., BANKS, G. R., TOONE, W. M., RAITT, D., KUGE, S. & JOHNSTON, L. H. 1997. The Skn7 response regulator controls gene expression in the oxidative stress response of the budding yeast Saccharomyces cerevisiae. *EMBO J,* 16**,** 1035-44.

MOTOORI, S., MAJIMA, H. J., EBARA, M., KATO, H., HIRAI, F., KAKINUMA, S., YAMAGUCHI, C., OZAWA, T., NAGANO, T., TSUJII, H. & SAISHO, H. 2001. Overexpression of Mitochondrial Manganese Superoxide Dismutase protects against radiation-induced cell death in the human hepatocellular carcinoma cell line HLE. *Cancer Research,* 61**,** 5382-5388.

MOYE-ROWLEY, W. S., HARSHMAN, K. D. & PARKER, C. S. 1989. Yeast YAP1 encodes a novel form of the jun family of transcriptional activator proteins. *Genes Dev,* 3**,** 283-92.

MULFORD, K. E. & FASSLER, J. S. 2011. Association of the Skn7 and Yap1 transcription factors in the Saccharomyces cerevisiae oxidative stress response. *Eukaryot Cell,* 10**,** 761-9.

MURPHY, C. T., MCCARROLL, S. A., BARGMANN, C. I., FRASER, A., KAMATH, R. S., AHRINGER, J., LI, H. & KENYON, C. 2003. Genes that act downstream of DAF-16 to influence the lifespan of Caenorhabditis elegans. *Nature,* 424**,** 277-283.

NAGY, P., KARTON, A., BETZ, A., PESKIN, A. V., PACE, P., O'REILLY, R. J., HAMPTON, M. B., RADOM, L. & WINTERBOURN, C. C. 2011. Model for the exceptional reactivity of peroxiredoxins 2 and 3 with hydrogen peroxide: a kinetic and computational study. *J Biol Chem,* 286**,** 18048-55.

NAKAGAWA, C. W., YAMADA, K. & MUTOH, N. 2000. Role of Atf1 and Pap1 in the induction of the catalase gene of fission yeast schizosaccharomyces pombe. *J Biochem,* 127**,** 233-8.

NAVROT, N., COLLIN, V., GUALBERTO, J., GELHAYE, E., HIRASAWA, M., REY, P., KNAFF, D. B., ISSAKIDIS, E., JACQUOT, J. P. & ROUHIER, N. 2006. Plant glutathione peroxidases are functional peroxiredoxins distributed in several subcellular compartments and regulated during biotic and abiotic stresses. *Plant Physiol,* 142**,** 1364-79.

NGUYEN, A. N., LEE, A., PLACE, W. & SHIOZAKI, K. 2000. Multistep phosphorelay proteins transmit oxidative stress signals to the fission yeast stress-activated protein kinase. *Mol Biol Cell,* 11**,** 1169-81.

NUMAZAWA, S., ISHIKAWA, M., YOSHIDA, A., TANAKA, S. & YOSHIDA, T. 2003. Atypical protein kinase C mediates activation of NF-E2-related factor 2 in response to oxidative stress. *Am J Physiol Cell Physiol,* 285**,** C334-42.

O'BRIEN, M. L. & TEW, K. D. 1996. Glutathione and related enzymes in multidrug resistance. *Eur J Cancer,* 32A**,** 967-78.

OGATA, M. 1991. Acatalasemia. *Hum Genet,* 86**,** 331-40.

OHMIYA, R., KATO, C., YAMADA, H., AIBA, H. & MIZUNO, T. 1999. A fission yeast gene (prr1(+)) that encodes a response regulator implicated in oxidative stress response. *J Biochem,* 125**,** 1061-6.

OHMIYA, R., YAMADA, H., KATO, C., AIBA, H. & MIZUNO, T. 2000. The Prr1 response regulator is essential for transcription of ste11^{+} and for sexual development in fission yeast. *Mol Gen Genet,* 264**,** 441-51.

OKAZAKI, S., NAGANUMA, A. & KUGE, S. 2005. Peroxiredoxin-mediated redox regulation of the nuclear localization of Yap1, a transcription factor in budding yeast. *Antioxid Redox Signal,* 7**,** 327-34.

OKAZAKI, S., TACHIBANA, T., NAGANUMA, A., MANO, N. & KUGE, S. 2007. Multistep disulfide bond formation in Yap1 is required for sensing and transduction of H_2O_2 stress signal. *Mol Cell,* 27**,** 675-88.

OLAHOVA, M., TAYLOR, S. R., KHAZAIPOUL, S., WANG, J., MORGAN, B. A., MATSUMOTO, K., BLACKWELL, T. K. & VEAL, E. A. 2008. A redox-sensitive peroxiredoxin that is important for longevity has tissue- and stress-specific roles in stress resistance. *Proc Natl Acad Sci U S A,* 105**,** 19839-44.

OLIVEIRA, M. A., DISCOLA, K. F., ALVES, S. V., MEDRANO, F. J., GUIMARAES, B. G. & NETTO, L. E. 2010. Insights into the specificity of thioredoxin reductase-thioredoxin interactions. A structural and functional investigation of the yeast thioredoxin system. *Biochemistry,* 49**,** 3317-26.

PARK, S. G., CHA, M. K., JEONG, W. & KIM, I. H. 2000. Distinct physiological functions of thiol peroxidase isoenzymes in Saccharomyces cerevisiae. *J Biol Chem,* 275**,** 5723-32.

PARTRIDGE, L. & GEMS, D. 2002. Mechanisms of aging: public or private? *Nat Rev Genet,* 3**,** 165-175.

PASCUAL, M. B., MATA-CABANA, A., FLORENCIO, F. J., LINDAHL, M. & CEJUDO, F. J. 2010. Overoxidation of 2-Cys peroxiredoxin in prokaryotes: cyanobacterial 2-Cys peroxiredoxins sensitive to oxidative stress. *J Biol Chem,* 285**,** 34485-92.

PAULO, E., GARCIA-SANTAMARINA, S., CALVO, I. A., CARMONA, M., BORONAT, S., DOMENECH, A., AYTE, J. & HIDALGO, E. 2014. A genetic approach to study H2O2 scavenging in fission yeast--distinct roles of peroxiredoxin and catalase. *Mol Microbiol,* 92**,** 246-57.

PEKOVIC-VAUGHAN, V., GIBBS, J., YOSHITANE, H., YANG, N., PATHIRANAGE, D., GUO, B., SAGAMI, A., TAGUCHI, K., BECHTOLD, D., LOUDON, A., YAMAMOTO, M., CHAN, J., VAN DER HORST, G. T., FUKADA, Y. & MENG, Q. J. 2014. The circadian clock regulates rhythmic activation of the NRF2/glutathione-mediated antioxidant defense pathway to modulate pulmonary fibrosis. *Genes Dev,* 28**,** 548-60.

PESKIN, A. V., DICKERHOF, N., POYNTON, R. A., PATON, L. N., PACE, P. E., HAMPTON, M. B. & WINTERBOURN, C. C. 2013. Hyperoxidation of peroxiredoxins 2 and 3: rate constants for the reactions of the sulfenic acid of the peroxidatic cysteine. *J Biol Chem,* 288**,** 14170-7.

PESKIN, A. V., LOW, F. M., PATON, L. N., MAGHZAL, G. J., HAMPTON, M. B. & WINTERBOURN, C. C. 2007. The high reactivity of peroxiredoxin 2 with H_2O_2 is not reflected in its reaction with other oxidants and thiol reagents. *J Biol Chem,* 282**,** 11885-92.

PETZOLD, L. 1983. Automatic selection of methods for solving stiff and nonstiff systems of ordinary differential-equations. *Siam Journal on Scientific and Statistical Computing,* 4**,** 136-148.

PHALEN, T. J., WEIRATHER, K., DEMING, P. B., ANATHY, V., HOWE, A. K., VAN DER VLIET, A., JONSSON, T. J., POOLE, L. B. & HEINTZ, N. H. 2006. Oxidation state governs structural transitions in peroxiredoxin II that correlate with cell cycle arrest and recovery. *J Cell Biol,* 175**,** 779-89.

PILLAY, C., HOFMEYR, J.-H. & ROHWER, J. 2011. The logic of kinetic regulation in the thioredoxin system. *BMC Systems Biology,* 5**,** 15.

PILLAY, C. S., HOFMEYR, J. H., OLIVIER, B. G., SNOEP, J. L. & ROHWER, J. M. 2009. Enzymes or redox couples? The kinetics of thioredoxin and glutaredoxin reactions in a systems biology context. *Biochem J,* 417**,** 269-75.

PINEYRO, M. D., ARCARI, T., ROBELLO, C., RADI, R. & TRUJILLO, M. 2011. Tryparedoxin peroxidases from Trypanosoma cruzi: high efficiency in the catalytic elimination of hydrogen peroxide and peroxynitrite. *Arch Biochem Biophys,* 507**,** 287-95.

PIPER, M. D. & BARTKE, A. 2008. Diet and aging. *Cell Metab,* 8**,** 99-104.

POOLE, L. B. 1996. Flavin-dependent alkyl hydroperoxide reductase from Salmonella typhimurium. 2. Cystine disulfides involved in catalysis of peroxide reduction. *Biochemistry,* 35**,** 65-75.

QUINN, J., FINDLAY, V. J., DAWSON, K., MILLAR, J. B., JONES, N., MORGAN, B. A. & TOONE, W. M. 2002. Distinct regulatory proteins control the graded transcriptional response to increasing H_2O_2 levels in fission yeast Schizosaccharomyces pombe. Mol Biol Cell, 13, 805-16.

QUINN, J., MALAKASI, P., SMITH, D. A., CHEETHAM, J., BUCK, V., MILLAR, J. B. & MORGAN, B. A. 2011. Two-component mediated peroxide sensing and signal transduction in fission yeast. *Antioxid Redox Signal,* 15**,** 153-65.

RHEE, S. G. & WOO, H. A. 2011. Multiple functions of peroxiredoxins: peroxidases, sensors and regulators of the intracellular messenger H_2O_2, and protein chaperones. *Antioxid Redox Signal,* 15**,** 781-94.

RHEE, S. G., WOO, H. A., KIL, I. S. & BAE, S. H. 2012. Peroxiredoxin functions as a peroxidase and a regulator and sensor of local peroxides. *J Biol Chem,* 287**,** 4403-10.

RISTOW, M. & SCHMEISSER, K. 2014. Mitohormesis: promoting health and lifespan by increased levels of reactive oxygen species (ROS). *Dose Response,* 12**,** 288-341.

RISTOW, M. & ZARSE, K. 2010. How increased oxidative stress promotes longevity and metabolic health: The concept of mitochondrial hormesis (mitohormesis). *Exp Gerontol,* 45**,** 410-8.

RODRIGUEZ-GABRIEL, M. A., BURNS, G., MCDONALD, W. H., MARTIN, V., YATES, J. R., 3RD, BAHLER, J. & RUSSELL, P. 2003. RNA-binding protein Csx1 mediates global control of gene expression in response to oxidative stress. *EMBO J,* 22**,** 6256-66.

ROSS, S. J., FINDLAY, V. J., MALAKASI, P. & MORGAN, B. A. 2000. Thioredoxin peroxidase is required for the transcriptional response to oxidative stress in budding yeast. *Mol Biol Cell,* 11**,** 2631-42.

SAITOH, M., NISHITOH, H., FUJII, M., TAKEDA, K., TOBIUME, K., SAWADA, Y., KAWABATA, M., MIYAZONO, K. & ICHIJO, H. 1998. Mammalian thioredoxin is a direct inhibitor of apoptosis signal-regulating kinase (ASK) 1. *EMBO J,* 17**,** 2596-606.

SALVADOR, A., SOUSA, J. & PINTO, R. E. 2001. Hydroperoxyl, superoxide and pH gradients in the mitochondrial matrix: a theoretical assessment. *Free Radic Biol Med,* 31**,** 1208-15.

SAMBROOK, I., FRITSCH, E. and MANIATIS, T. 1989. Molecular biology: a laboratory manual, Cold Spring Harbour, New York, Cold Spring Harbour Laboratory Press.

SAMEJIMA, I., MACKIE, S. & FANTES, P. A. 1997. Multiple modes of activation of the stress-responsive MAP kinase pathway in fission yeast. *EMBO J,* 16**,** 6162-70.

SCHABER, J. 2012. Easy parameter identifiability analysis with COPASI. *Biosystems,* 110**,** 183-5.

SCHABER, J. & KLIPP, E. 2011. Model-based inference of biochemical parameters and dynamic properties of microbial signal transduction networks. *Curr Opin Biotechnol,* 22**,** 109-16.

SCHNELL, N. & ENTIAN, K. D. 1991. Identification and characterization of a Saccharomyces cerevisiae gene (PAR1) conferring resistance to iron chelators. *Eur J Biochem,* 200**,** 487-93.

SCHNELL, N., KREMS, B. & ENTIAN, K. D. 1992. The PAR1 (YAP1/SNQ3) gene of Saccharomyces cerevisiae, a c-jun homologue, is involved in oxygen metabolism. *Curr Genet,* 21**,** 269-73.

SCHRINER, S. E., LINFORD, N. J., MARTIN, G. M., TREUTING, P., OGBURN, C. E., EMOND, M., COSKUN, P. E., LADIGES, W., WOLF, N., VAN REMMEN, H., WALLACE, D. C. & RABINOVITCH, P. S. 2005. Extension of murine life span by overexpression of catalase targeted to mitochondria. *Science,* 308**,** 1909-11.

SCHULZ, T. J., ZARSE, K., VOIGT, A., URBAN, N., BIRRINGER, M. & RISTOW, M. 2007. Glucose restriction extends Caenorhabditis elegans life span by inducing mitochondrial respiration and increasing oxidative stress. *Cell Metab,* 6**,** 280-93.

SEGAL, A. W. & SHATWELL, K. P. 1997. The NADPH oxidase of phagocytic leukocytes. *Ann N Y Acad Sci,* 832**,** 215-22.

SEN, C. K. & ROY, S. 2008. Redox signals in wound healing. *Biochim Biophys Acta,* 1780**,** 1348-61.

SHIEH, J. C., MARTIN, H. & MILLAR, J. B. 1998. Evidence for a novel MAPKKK-independent pathway controlling the stress activated Sty1/Spc1 MAP kinase in fission yeast. *J Cell Sci,* 111 (Pt 18)**,** 2799-807.

SHIOZAKI, K. & RUSSELL, P. 1996. Conjugation, meiosis, and the osmotic stress response are regulated by Spc1 kinase through Atf1 transcription factor in fission yeast. *Genes Dev,* 10**,** 2276-88.

SILVA, J. P., SHABALINA, I. G., DUFOUR, E., PETROVIC, N., BACKLUND, E. C., HULTENBY, K., WIBOM, R., NEDERGAARD, J., CANNON, B. & LARSSON, N.-G. 2005. SOD2 overexpression: enhanced mitochondrial tolerance but absence of effect on UCP activity. *EMBO J,* 24**,** 4061-4070.

ST-PIERRE, J., BUCKINGHAM, J. A., ROEBUCK, S. J. & BRAND, M. D. 2002. Topology of superoxide production from different sites in the mitochondrial electron transport chain. *J Biol Chem,* 277**,** 44784-90.

STANGHERLIN, A. & REDDY, A. B. 2013. Regulation of circadian clocks by redox homeostasis. *J Biol Chem,* 288**,** 26505-11.

STEPHEN, D. W., RIVERS, S. L. & JAMIESON, D. J. 1995. The role of the YAP1 and YAP2 genes in the regulation of the adaptive oxidative stress responses of Saccharomyces cerevisiae. *Mol Microbiol,* 16**,** 415-23.

STOCK, A. M., ROBINSON, V. L. & GOUDREAU, P. N. 2000. Two-component signal transduction. *Annu Rev Biochem,* 69**,** 183-215.

STONE, J. R. & YANG, S. 2006. Hydrogen peroxide: a signaling messenger. *Antioxid Redox Signal,* 8**,** 243-70.

STORZ, G. & TARTAGLIA, L. A. 1992. OxyR: a regulator of antioxidant genes. *J Nutr,* 122**,** 627-30.

SUN, J., FOLK, D., BRADLEY, T. J. & TOWER, J. 2002. Induced overexpression of Mitochondrial Mn-Superoxide Dismutase extends the life span of adult Drosophila melanogaster. *Genetics,* 161**,** 661-672.

SWITALA, J. & LOEWEN, P. C. 2002. Diversity of properties among catalases. *Arch Biochem Biophys,* 401**,** 145-54.

TACHIBANA, T., OKAZAKI, S., MURAYAMA, A., NAGANUMA, A., NOMOTO, A. & KUGE, S. 2009. A major peroxiredoxin-induced activation of Yap1 transcription factor is mediated by reduction-sensitive disulfide bonds and reveals a low level of transcriptional activation. *J Biol Chem,* 284**,** 4464-72.

TAKEUCHI, T., MIYAHARA, K., HIRATA, D. & MIYAKAWA, T. 1997. Mutational analysis of Yap1 protein, an AP-1-like transcriptional activator of Saccharomyces cerevisiae. *FEBS Lett,* 416**,** 339-43.

TAYLOR, S.R. 2009. *The Role of 2-Cys Peroxiredoxins in regulating responses to peroxide.* Ph.D. Thesis. Newcastle University: UK

THIERBACH, R., SCHULZ, T. J., ISKEN, F., VOIGT, A., MIETZNER, B., DREWES, G., VON KLEIST-RETZOW, J. C., WIESNER, R. J., MAGNUSON, M. A., PUCCIO, H., PFEIFFER, A. F.,

STEINBERG, P. & RISTOW, M. 2005. Targeted disruption of hepatic frataxin expression causes impaired mitochondrial function, decreased life span and tumor growth in mice. *Hum Mol Genet,* 14**,** 3857-64.

TODA, T., SHIMANUKI, M., SAKA, Y., YAMANO, H., ADACHI, Y., SHIRAKAWA, M., KYOGOKU, Y. & YANAGIDA, M. 1992. Fission yeast pap1-dependent transcription is negatively regulated by an essential nuclear protein, crm1. *Mol Cell Biol,* 12**,** 5474-84.

TOONE, W. M., KUGE, S., SAMUELS, M., MORGAN, B. A., TODA, T. & JONES, N. 1998. Regulation of the fission yeast transcription factor Pap1 by oxidative stress: requirement for the nuclear export factor Crm1 (Exportin) and the stress-activated MAP kinase Sty1/Spc1. *Genes Dev,* 12**,** 1453-63.

TRUJILLO, M., CLIPPE, A., MANTA, B., FERRER-SUETA, G., SMEETS, A., DECLERCQ, J. P., KNOOPS, B. & RADI, R. 2007. Pre-steady state kinetic characterization of human peroxiredoxin 5: taking advantage of Trp84 fluorescence increase upon oxidation. *Arch Biochem Biophys,* 467**,** 95-106.

TURNER-IVEY, B., MANEVICH, Y., SCHULTE, J., KISTNER-GRIFFIN, E., JEZIERSKA-DRUTEL, A., LIU, Y. & NEUMANN, C. A. 2013. Role for Prdx1 as a specific sensor in redox-regulated senescence in breast cancer. *Oncogene,* 32**,** 5302-14.

VALKO, M., IZAKOVIC, M., MAZUR, M., RHODES, C. J. & TELSER, J. 2004. Role of oxygen radicals in DNA damage and cancer incidence. *Molecular and Cellular Biochemistry,* 266**,** 37-56.

VALKO, M., RHODES, C. J., MONCOL, J., IZAKOVIC, M. & MAZUR, M. 2006. Free radicals, metals and antioxidants in oxidative stress-induced cancer. *Chemico-Biological Interactions,* 160**,** 1-40.

VAN RAAMSDONK, J. M. & HEKIMI, S. 2012. Superoxide dismutase is dispensable for normal animal lifespan. *Proceedings of the National Academy of Sciences,* 109**,** 5785-5790.

VEAL, E. & DAY, A. 2011. Hydrogen peroxide as a signaling molecule. *Antioxid Redox Signal,* 15**,** 147-51.

VEAL, E. A., FINDLAY, V. J., DAY, A. M., BOZONET, S. M., EVANS, J. M., QUINN, J. & MORGAN, B. A. 2004. A 2-Cys Peroxiredoxin regulates peroxide-induced oxidation and activation of a Stress-Activated MAP Kinase. *Molecular Cell,* 15**,** 129-139.

VEAL, E. A., ROSS, S. J., MALAKASI, P., PEACOCK, E. & MORGAN, B. A. 2003. Ybp1 is required for the hydrogen peroxide-induced oxidation of the Yap1 transcription factor. *J Biol Chem,* 278**,** 30896-904.

VINSON, C., ACHARYA, A. & TAPAROWSKY, E. J. 2006. Deciphering B-ZIP transcription factor interactions in vitro and in vivo. *Biochim Biophys Acta,* 1759**,** 4-12.

VINSON, C., MYAKISHEV, M., ACHARYA, A., MIR, A. A., MOLL, J. R. & BONOVICH, M. 2002. Classification of human B-ZIP proteins based on dimerization properties. *Mol Cell Biol,* 22**,** 6321-35.

VIVANCOS, A. P., CASTILLO, E. A., BITEAU, B., NICOT, C., AYTE, J., TOLEDANO, M. B. & HIDALGO, E. 2005. A cysteine-sulfinic acid in peroxiredoxin regulates H_2O_2-sensing by the antioxidant Pap1 pathway. *Proc Natl Acad Sci U S A,* 102**,** 8875-80.

WAKABAYASHI, N., ITOH, K., WAKABAYASHI, J., MOTOHASHI, H., NODA, S., TAKAHASHI, S., IMAKADO, S., KOTSUJI, T., OTSUKA, F., ROOP, D. R., HARADA, T., ENGEL, J. D. & YAMAMOTO, M. 2003. Keap1-null mutation leads to postnatal lethality due to constitutive Nrf2 activation. *Nat Genet,* 35**,** 238-45.

WHEELER, G. L. & GRANT, C. M. 2004. Regulation of redox homeostasis in the yeast Saccharomyces cerevisiae. *Physiol Plant,* 120**,** 12-20.

WILKINSON & ROGERS, C. E. 1973. Symbolic Description of Factorial Models for Analysis of Variance. *Journal of the Royal Statistical Society Series C-Applied Statistics,* 22**,** 392-399.

WILKINSON, M. G., SAMUELS, M., TAKEDA, T., TOONE, W. M., SHIEH, J. C., TODA, T., MILLAR, J. B. & JONES, N. 1996. The Atf1 transcription factor is a target for the Sty1 stress-activated MAP kinase pathway in fission yeast. *Genes Dev,* 10**,** 2289-301.

WINTERBOURN, C. C. & HAMPTON, M. B. 2008. Thiol chemistry and specificity in redox signaling. *Free Radical Biology and Medicine,* 45**,** 549-561.

WONG, C. M., SIU, K. L. & JIN, D. Y. 2004. Peroxiredoxin-null yeast cells are hypersensitive to oxidative stress and are genomically unstable. *J Biol Chem,* 279**,** 23207-13.

WONG, C. M., ZHOU, Y., NG, R. W., KUNG HF, H. F. & JIN, D. Y. 2002. Cooperation of yeast peroxiredoxins Tsa1p and Tsa2p in the cellular defense against oxidative and nitrosative stress. *J Biol Chem,* 277**,** 5385-94.

WOO, H. A., JEONG, W., CHANG, T.-S., PARK, K. J., PARK, S. J., YANG, J. S. & RHEE, S. G. 2005. Reduction of cysteine Sulfinic acid by Sulfiredoxin is specific to 2-Cys Peroxiredoxins. *Journal of Biological Chemistry,* 280**,** 3125-3128.

WOO, H. A., YIM, S. H., SHIN, D. H., KANG, D., YU, D. Y. & RHEE, S. G. 2010. Inactivation of peroxiredoxin I by phosphorylation allows localized H_2O_2 accumulation for cell signaling. *Cell,* 140**,** 517-28.

WOOD, M. J., ANDRADE, E. C. & STORZ, G. 2003a. The redox domain of the Yap1p transcription factor contains two disulfide bonds. *Biochemistry,* 42**,** 11982-91.

WOOD, Z. A., POOLE, L. B. & KARPLUS, P. A. 2003b. Peroxiredoxin evolution and the regulation of hydrogen peroxide signaling. *Science,* 300**,** 650-3.

WU, A., WEMMIE, J. A., EDGINGTON, N. P., GOEBL, M., GUEVARA, J. L. & MOYE-ROWLEY, W. S. 1993. Yeast bZip proteins mediate pleiotropic drug and metal resistance. *J Biol Chem,* 268**,** 18850-8.

WU, A. L. & MOYE-ROWLEY, W. S. 1994. GSH1, which encodes gamma-glutamylcysteine synthetase, is a target gene for yAP-1 transcriptional regulation. *Mol Cell Biol,* 14**,** 5832-9.

XIANG, H., ZHANG, R., LI, N. & VOSSBRINCK, C. R. 2014. Searching for convergent evolution in manganese superoxidase dismutase using hydrophobic cluster analysis. *Genet Mol Biol,* 37**,** 460-74.

YAMAMOTO, T., SUZUKI, T., KOBAYASHI, A., WAKABAYASHI, J., MAHER, J., MOTOHASHI, H. & YAMAMOTO, M. 2008. Physiological significance of reactive cysteine residues of Keap1 in determining Nrf2 activity. *Mol Cell Biol,* 28**,** 2758-70.

YAN, C., LEE, L. H. & DAVIS, L. I. 1998. Crm1p mediates regulated nuclear export of a yeast AP-1-like transcription factor. *EMBO J,* 17**,** 7416-29.

YANG, K.-S., KANG, S. W., WOO, H. A., HWANG, S. C., CHAE, H. Z., KIM, K. & RHEE, S. G. 2002. Inactivation of Human Peroxiredoxin I during catalysis as the result of the oxidation of the catalytic site cysteine to cysteine-sulfinic acid. *Journal of Biological Chemistry,* 277**,** 38029-38036.

YANG, W. & HEKIMI, S. 2010. A Mitochondrial Superoxide signal triggers increased longevity in *Caenorhabditis elegans*. *PLoS Biol,* 8**,** e1000556.

YU, J. & ZHOU, C. Z. 2007. Crystal structure of glutathione reductase Glr1 from the yeast Saccharomyces cerevisiae. *Proteins,* 68**,** 972-9.

ZAMOCKY, M., FURTMULLER, P. G. & OBINGER, C. 2008a. Evolution of catalases from bacteria to humans. *Antioxid Redox Signal,* 10**,** 1527-48.

ZAMOCKY, M., JAKOPITSCH, C., FURTMULLER, P. G., DUNAND, C. & OBINGER, C. 2008b. The peroxidase-cyclooxygenase superfamily: Reconstructed evolution of critical enzymes of the innate immune system. *Proteins,* 72**,** 589-605.

ZUIN, A., CARMONA, M., MORALES-IVORRA, I., GABRIELLI, N., VIVANCOS, A. P., AYTE, J. & HIDALGO, E. 2010. Lifespan extension by calorie restriction relies on the Sty1 MAP kinase stress pathway. EMBO J, 29, 981-91.

COMMUNICATIONS